Atmospheric Reactive Trace Gas Observations in Field and Chamber Studies using CF_3O^- Chemical Ionization Mass Spectrometry

Thesis by

John D. Crounse

In Partial Fulfillment of the Requirements

for the Degree of

Doctor of Philosophy
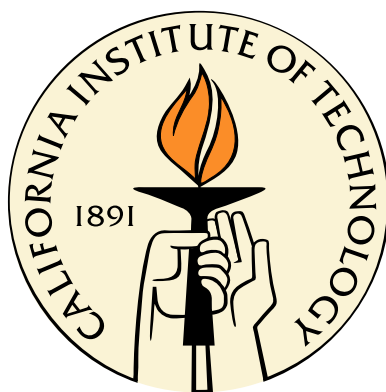
California Institute of Technology

Pasadena, California

2011

(Defended December 6, 2010)

To Kimberly and Leif, and to my Parents, Virginia and Robert

Acknowledgments

I thank Prof. Paul Wennberg for countless ideas, discussions, and (seemingly) endless opportunities for conducting exciting research throughout my time at Caltech, and for serving as my academic and research advisor. It has been a very rewarding experience to work closely with Paul during my graduate studies. In addition to being a brilliant scientist, Paul also takes a personal interest in the well-being of his students. This has created an enjoyable and productive working environment.

I also express gratitude to Prof. Mitchio Okumura, Prof. Geoff Blake, and Prof. John Seinfeld for their collaborations, insight, and direction, and also for serving as my thesis committee.

I fondly recall stimulating interactions with the diverse group of people with whom I have shared office space during my time at Caltech: Drs. David Shuster, Julianne Fry, and Julie O'Leary, William Amidon, as well as (future Drs.), Anna Beck, and Xavier Levine. The practice of having people with widely diverse backgrounds sharing office space is, in my opinion, a very good thing.

I thank Dr. Coleen Roehl for her ready and willing support in wide ranging areas, including custom chemical syntheses, chemical analyzes, ordering materials and chemicals, fabrication of instrument cables and electronics boxes, and much help with packing and preparing for field experiments. Without such assistance, this work would not be possible.

I must thank Sergey Nizkorodov, the leading postdoctoral scholar in the lab when I arrived, who taught me much about experimental laboratory techniques, including the dangers of trapping ozone. He is an exceptional scientist, and was a great mentor to me as a new graduate student.

A special thanks to Drs. Karena McKinney, David McCabe, Jason St. Clair, Andreas Kürten and Melinda Beaver – postdoctoral scholars with whom I had the distinct pleasure of working closely with in the development and field deployment of the CIMS instrumentation which forms the basis of this research; and fellow graduate students Alan (#1) Kwan, Kathleen Spencer, and Fabien Paulot – all of whom have shared in extensive field work and its associated joys and sorrows.

I have benefited greatly from working closely with fellow graduate student Fabien Paulot. I have learned much from his insight into chemical reaction mechanisms. His exceeding computer

coding and chemical modeling (and Teflon bag making) abilities coupled with his zeal for complete understanding have been a tremendous boon to myself and to the larger Wennberg group.

It has been very good to work closely with Jason St. Clair and Melinda Beaver. These recent postdocs in the Wennberg group have taught me that in science, patience is a virtue. I have benefited from Jason's broad knowledge on all manner of things, and Melinda's thoughtful insight.

David McCabe and I spent two very memorable field campaigns (INTEX-B and TC4) deploying (and building) our instrumentation. While, at the time, these were quite stressful situations, now, I have fond memories of these experiences. Amongst many other things, David taught me that steadfast perseverance can overcome large obstacles.

Thanks also to the many experiences shared with fellow Wennbergers – Rebecca Washenfelder, Yang Zhonghua, Julianne Fry, Gretchen Keppel-Aleks, and almost Wennbergers – Shabari Basu, Kate Cambell, and Anna Beck. Also, thanks to Zsuzsa Marka and Yael Yavin for assistance in getting our CIMS instruments ready for field operations.

I have had the pleasure of fruitful collaborations with Bob Yokelson (U. Montana, and co-workers) on several projects relating to emissions from biomass burning and chemistry thereof. He has taught me much about the atmospheric chemistry of forest fire emissions.

Many thanks to the members of the Seinfeld group Jesse Kroll, Sally Ng, Arthur Chan, Puneet Chhabra, Beth Kautzman, Jason Surratt, Man Nin Chan, Christine Loza, and Lindsay Yee, with whom we have worked with closely in carrying out the chamber experiments. Without the experimental collaboration with the Seinfeld roof lab, much of the research reported in this thesis would not have been possible.

I thank Jim Oliver (mechanical engineer), Norton Allen (software engineer), Ricardo Paniagua (machinist), Joseph Haggerty (machinist), Michael Roy (machinist), Chris Baumgartner (electronics engineer), Suresh Dhaniyala (aeronautical engineer), Urs Steiner (mass spectrometry expert, Varian Inc.), Tommy Thompson (RF engineer), and Dave Tanner (CIMS expert) for their involvement in design, and implementation/fabrication of the CIMS instruments, electronics, software, and hardware required for the integration of these instruments onto research aircraft. These people do the real work of transforming ideas into reality – without their support this science would not be possible.

I would also like to acknowledge my uncle, Ray Gustafson. Ray and I share a common interest

in science and engineering. I have enjoyed our conversations about science and life in general. Our interactions influenced my decision to study physical science, and I thank him for that.

Finally, I thank my wife, Kimberly, my son, Leif, and family who have encouraged and supported me throughout my graduate work. You have endured the trials beside me, and for this I am very thankful. My brother James, and sister-in-law Shallena, have provided local support and encouragement during my graduate studies. It has been very nice to have family nearby during this journey. My parents, Virginia and Robert Crounse, have nurtured my sense of curiosity since a young age, placing a high value on education. They have continually provided material, emotional, and spiritual support. For this I am eternally grateful.

Abstract

This dissertation describes the development of chemical ionization mass spectrometry (CIMS) instrumentation and methods utilizing the CF_3O^- reagent ion for the sensitive, specific, and direct detection of many oxygenated volatile organic compounds (OVOC) and inorganic reactive trace gases in the atmosphere. These species include HNO_3, HONO, HO_2NO_2, SO_2, HCN, H_2O_2, CH_3OOH, $CH_3C(O)OOH$, $HC(O)OH$, $CH_3C(O)OH$, $HC(O)CH_2OH$, $CH_3C(O)CH_2OH$, organic hydroperoxides (ROOH), and many multifunctional species (e.g., hydroxynitrates, hydroxycarbonyls, hydroxy-hydroperoxides, carbonylnitrates, carbonylhydroperoxides, etc.). CF_3O^- tandem mass spectrometry (MSMS) is demonstrated to be useful for distinguishing and individual quantification of certain isobaric compounds, as well as solving instrumental background problems for certain species. This technology is applied in field studies conducted from aircraft and ground-based platforms and to chamber studies investigating VOC oxidation and organic aerosol formation mechanisms. Comparisons with simultaneous observations from other instrumentation for several species show good agreement with CIMS observations.

CF_3O^--CIMS observations of HCN (a biomass burning tracer) from aircraft are used to quantify the impact of biomass burning emissions to the Mexico City region in March 2006. Biomass burning emissions are shown to contribute significantly to a number of gas and aerosol phase pollutants even in the midst of the large anthropogenic pollution emissions from Mexico City. The analysis of the photochemical aging of a fire plume over the Yucatan Peninsula (March 2006) is also reported. Observations indicate intense chemistry occurring within the fire plume evidenced by high OH levels, fast production of H_2O_2 and conversion of NO and NO_2 (NO_x) into peroxyacetylnitrate (PAN) and aerosol nitrate. This rapid chemistry is likely driven by photolysis of HONO, which is observed to be emitted in high amounts from these fires.

The CIMS methods are applied to studies of VOC oxidation and organic aerosol formation conducted in chamber experiments. Specifically, new insights gained from the study of isoprene oxidation under high and low NO_x conditions are reported. We quantify the formation of small

carboxylic acids as well as C_5-nitrates from the oxidation of isoprene under high NO_x conditions. Under low NO_x conditions, we show that C_5-hydroxyhydroperoxides are formed in high yield. Subsequent oxidation of these hydroxyhydroperoxides is shown to occur through a unique HO_x neutral mechanism that generates C_5-epoxydiols, a likely precursor to organic aerosol.

We utilize the high sensitivity and specificity of CF_3O^--CIMS to study novel intermolecular hydrogen-shift isomerization processes in peroxy radicals formed during isoprene oxidation. We find these rates to be substantially slower than recent theoretical predictions; however, we find these isomerization rates to be fast enough to be important for atmospheric isoprene oxidation in regions where RO_2 lifetimes become long. Globally, we estimate 8-11% of isoprene peroxy radicals react through 1,6-H-shift isomerization reactions.

Contents

List of Figures

xvii

List of Tables

List of Schemes

Chapter 1

Introduction

1.1 Overview

Atmospheric chemistry research encompases the study of the composition of and the chemical reactions occurring within and at the interfaces of planetary atmospheres. For more than the past half century, extensive work in this field has resulted in a substantial body of knowledge about the composition and chemistry of Earth's atmosphere, and, in particular, how both are impacted by natural and anthropogenic activities or processes. Still, there remain significant gaps in our understanding. Specifically, mechanisms for the gas-phase degradation of certain larger (i.e., C$\geq$4) volatile organic compounds (VOC) under low to moderate nitric oxide (NO) conditions (relevant for much of Earth's atmosphere) are poorly understood. Also, the mechanistic understanding of secondary organic aerosol (SOA) formation from the oxidation of VOC remains elusive. In many cases, the uncertainties in the gas-phase oxidation processes of VOC are directly related to uncertainties in SOA formation mechanisms. These uncertainties translate into incomplete understanding of ozone and organic aerosol production degrading our ability to improve air quality. From the perspective of climate change these uncertainties also influence our understanding of Earth's global radiative forcing budget and hence our predictions of future climate. The reduction of some of these uncertainties has been the goal of this thesis.

The gas-phase photooxidation of VOC in Earth's atmosphere result eventually in either conversion of the constituent carbon and hydrogen atoms into CO_2 and H_2O, respectively, or the loss of some intermediate product(s) to the surface by wet or dry deposition. This oxidation process can involve various oxidants (for most VOC, OH radical is dominant), many oxidation steps, and numerous intermediate products for each VOC.

The intermediate oxygenated volatile organic compounds (OVOC) produced in the oxidation of VOC are often multifunctional and, depending on their size and volatility, can partition to aerosol and participate in heterogeneous chemistry. Continued oxidation of OVOC generally result in more highly oxidized species. Corresponding vapor pressures for the OVOC intermediates either decrease as compounds become larger and/or more functionalized, or increase if fragmentation via C-C bond scission occurs (Kroll and Seinfeld, 2008; Kroll et al., 2009). For a given parent VOC, the combination of these processes (functionalization and fragmentation) often leads to minimum in OVOC volatilities at some intermediate oxidation step. Thus it is logical to expect these intermediate OVOC to play an important role in SOA formation.

The detection and quantification of gas-phase OVOC through traditional analytical methods (e.g., gas chromatography (GC), high performance liquid chromatography (HPLC), derivatization-

HPLC, Fourier transform spectroscopy (FTS), mass spectrometry (MS), and combination thereof) poses substantial analytical challenges. As noted above, many OVOC contain multiple functionalities, including hydroxy, hydroperoxy, nitrooxy, carbonyl, acid, and peracid groups. These compounds often tend to be quite reactive (even unstable), such that collection in the condensed phase, or even gas-phase exposure to GC columns result in irreversible loss and often conversion to other species. Spectroscopic detection methods (e.g., FTS) while having the benefits of being very specific and not requiring significant sample handling, are generally less sensitive and thus require high analyte concentrations (or very long pathlengths) to achieve reasonable signal-to-noise levels as well as quality reference spectra for product identification and quantification. Futhermore, such reference spectra are generally not available for more complex OVOC. MS, while very sensitive and requiring little sample handling (if used alone), is generally not very specific. Traditional ionization methods (electron impact ionization (EI)) involve high ionization energies, which usually result in substantial fragmentation of the analyte species. The lack of sensitive, specific, and quantitative methods for detecting and monitoring these reactive intermediate OVOC species is a major impediment to the reduction in uncertainties related to atmospheric VOC oxidation and SOA formation mechanisms.

The focus of this thesis is the development and application of advanced mass spectrometry instrumentation capable of sensitive, specific, and quantitative detection of many reactive intermediate OVOC (and other important inorganic photochemical species). As summarized below, chapters 2 and 3 describe the development of the chemical ionization mass spectrometry (CIMS) instruments used in this work. Chapters 4 and 5 discuss the deployment of these instruments on research aircraft for making observations of trace gases in the atmosphere, particularly focusing on the importance of emissions from biomass burning (BB) to atmospheric chemistry and composition. Finally, Chapters 6, 7, and 8 discuss the application of this technology to environmental chamber studies for the detection of reactive OVOC intermediates formed during the oxidation of biogenic VOC illustrating how such OVOC detection enables elucidation of VOC oxidation and SOA formation mechanisms.

1.2 Instrumentation

Chemical ionization mass spectrometry (CIMS) differs from traditional electron impact ionization mass spectrometry (EI-MS) in that the neutral analyte is ionized through reaction with an ionized atomic or molecular species, generally termed reagent ion. The reaction energy for these ion – neutral molecule reactions is substantially less than that required for electron impact ionization. This typically results in the ionization of neutral species with no (or little) fragmentation – markedly

different from electron impact ionization. Given this, chemical ionization typically allows for much greater specificity in the detection of neutral species than does electron impact ionization. However, the choice of reagent ion often limits the species that can be detected and the environments within which they can be detected due to the reactivities (or lack thereof) of the reagent ion with the analyte of interest and with other gases that may be present (e.g. O_3, H_2O, etc). Owing to the high sensitivity inherent in MS techniques, and high specificity achieved through soft ionization, CIMS methods can quantify trace gases directly in ambient air (providing the reagent ion is unreactive to the major atmospheric gases) often with detection limits of a few 10's of pptv for sub-second integration periods. In recent years CIMS methods (including proton-transfer-reaction mass spectrometry (PTR-MS)) have been shown to be very powerful tools for quantifying trace gases in Earth's atmosphere (Viggiano (1993); Huey (2007); de Gouw and Warneke (2007), and references contained within).

Chapters 2 and 3 describe two chemical ionization mass spectrometry (CIMS) instruments and methodologies which have been developed as part of this thesis. Both instruments utilize CF_3O^- ion chemistry, differing only in the ion mass filtering part of the instruments. CF_3O^- has proven to be a very special reagent ion with many applications for monitoring *in situ* atmospheric trace gases due to its low reactivity with O_3 and H_2O and its high reactivity with many atmospheric species of interest. The ion chemistry of CF_3O^- has been investigated previously in the laboratory for potential detection of several inorganic and small organic acids (Huey et al., 1996; Amelynck et al., 2000a,b). Prior to this work, however, CF_3O^- has not seen extensive application.

Chapter 2 describes the first instrument (as deployed on the NASA DC-8 aircraft for the INTEX-NA experiment) referred to here as the single quadrupole instrument. This instrument was originally constructed to fly aboard the NASA ER-2 aircraft and did so during the SOLVE campaign measuring HNO_3 in both the gas and particle phase. In 2003 this instrument was overhauled and fitted for deployment on the NASA DC-8. Along with refitting the instrument to the DC-8, the instrumental sensitivity was improved and the suite of detectable species was broadened. In particular, the discovery of CF_3O^- clustering chemistry with H_2O_2, PAA, and other hydroperoxides was an important step for continued field deployment of this instrument. The single quadrupole instrument was deployed on the NASA DC-8 aircraft during the Intercontinental Chemical Transport Experiment – North America (INTEX-NA) in the summer of 2004. CIMS observations of HNO_3, H_2O_2, HCN and peroxyacetic acid ($CH_3C(O)OOH$, PAA) were reported for this mission. Comparisons with NO_3^- observations from a mist chamber instrument (`http://www-air.larc.nasa.gov/TAbMEP2_icartt.html`)

and HPLC-derivative-fluorescence observations of H_2O_2 and PAA (Chapter 2) were possible throughout the entire campaign as all instruments were located on the same platform. In general, the comparisons were quite good, demonstrating the ability of this CIMS technique to make robust trace gas observations from aircraft platforms. PAA was shown to be ubiquitous throughout the troposphere often present at levels exceeding 100 pptv during the INTEX-NA campaign. Observations of methyl hydrogen peroxide (MHP, CH_3OOH) while demonstrated in the laboratory under dry conditions were not possible in the field due to interferences present under humid conditions at the cluster ion detection mass ($m/z = 133$).

Chapter 3 describes a second CIMS instrument consisting of a modified commercial instrument (Varian triple quadrupole), and differing from the single quadrupole in that it contains three quadrupole ion guides, allowing for tandem mass spectrometry (MSMS). The primary motivation for the development of this instrument was the inability to detect MHP with the single quadrupole instrument due to background interferences. MSMS provides a viable method for the separation of isobaric ions so long as the fragment ion spectra produced under the collision induced dissociation (CID) of parent ions are distinct. For the MHP product ion and isobaric background ions this is indeed the case, such that MSMS-MHP has virtually no instrumental backgrounds. This has been demonstrated through the *in situ* observations of MHP, which have been reported for subsequent field campaigns (the second part of INTEX-B, TC4, and ARCTAS).

The added benefits that MSMS brings to CF_3O^- ion chemistry have only just begun to be exploited. Chapter 7 describes the separation and quantification of isobaric hydroxyhydroperoxides and dihydroxyepoxides that are formed in the oxidation of isoprene. It also describes a characteristic daughter ion ($m/z = 63$) that appears to be to originate from clusters of CF_3O^- with hydroperoxide compounds, but not other multifunctional compounds (i.e., hydroxycarbonyls, hydroxynitrates, etc.)

This instrument also has the ability to switch rapidly between negative ion mode (CF_3O^- chemistry) and positive ion mode ($H^+ \cdot (H_2O)_n$ chemistry (PTR-MS)). The PTR-MS ion chemistry allows for detection of simple alcohols, carbonyls, and other VOC compounds that are not detectable using CF_3O^- ion chemistry. PTR-MS mode has not been used in field experiments due to the need to generate quasi-continuous data for species observed in negative ion mode, but has been used successfully in chamber studies, where analyte concentrations change slowly enough to allow for switching between negative and positive modes.

The combination of MSMS–CF_3O^- ion chemistry and positive ion chemistry make the triple quadrupole instrument a very powerful tool for the investigation of oxidation mechanisms of VOC.

1.3 Field observations of biomass burning emmisions

Emissions from the combustion of non-fossilized vegetative material often termed biomass burning (BB) are estimated to comprise the largest source of carbon-containing aerosol particles and the second largest source of atmospheric trace gasses to the atmosphere (Andreae and Merlet, 2001; Bond et al., 2004; Guenther et al., 2006). The photochemistry within these BB plumes can be quite intense due to high concentrations of reactive species and seemingly ample sources of oxidant. Much is still unknown about the chemical composition and chemistry of BB plumes with only $\sim$50% of the carbon being identified as specific species. The unidentified fraction is thought to consist of primarily of high molecular weight OVOC species.

Chapters 4 and 5 report findings from the analysis of data collected during the Megacity Initiative: Local and Global Research Observations (MILAGRO) science campaign, conducted in March 2006. The MILAGRO campaign involved a very large number of scientists and instruments operating from several ground locations and a number of airborne (aircraft and balloon) platforms in and around Mexico City. The primary goal of this research intensive was to characterize the emissions from a mega-city and monitor the photochemical aging of these emissions as they are transported away from the city to the regional and global scales.

The two Caltech CIMS instruments operated from the NSF/NCAR C-130 aircraft, which was stationed in Veracruz, Mexico. The C-130 made 12 local sorties from Veracruz, most of which aimed at intercepting the Mexico City plume at various distances from the city. One flight targeted the emissions from large fires burning on the Yucatan Peninsula. Chemical species monitored by the CIMS instruments for this research campaign include: HNO_3, peroxynitric acid (PNA, HO_2NO_2), HONO , SO_2, HCN, H_2O_2, peroxyacetic acid (PAA, $CH_3C(O)OOH$), and formic ($HC(O)OH$), acetic ($CH_3C(O)OH$), and propionic ($CH_3CH_2C(O)OH$) acids.

Elevated levels of HCN, a tracer for BB emissions (Li et al., 2000), were observed over the entire Mexico City region for much of this research campaign. Using HCN and acetylene (C_2H_2) as biomass burning and urban emissions tracers, respectively, Chapter 4 describes an analysis of the impact of biomass burning emissions within the Mexico City region during March 2006. From the tracer analysis of the aircraft data we estimate that biomass burning contributed approximately 1/3 of the elevated CO, benzene (C_6H_6), and NO_y. Such emissions we associate with 2/3 of the organic aerosol (OA), and sub-micron scattering. Fire season in the Mexico City region generally intensifies from March–June, peaking in May. Fires during March 2006 were closer to the climatological average for the month of May. The fire impact inferred from ground-based observations within Mexico City are

somewhat smaller than those determined from the aircraft data (Molina et al., 2007; Bravo et al., 2002; Salcedo et al., 2006; Yokelson et al., 2007b; Stone et al., 2008; Moffet et al., 2008; Aiken et al., 2009, 2010; DeCarlo et al., 2010). This effect is likely due to the separation of sources, with fires occurring primarily on the sides of the mountains surrounding Mexico City, and the anthropogenic emissions occurring predominantly on the basin floor within Mexico City. Even so, biomass burning emissions during fire season substantially impact pollution and visibility levels in and around Mexico City in spite of large anthropogenic pollution emissions.

Chapter 5 reports emissions for a large number of species observed from the Yucatan fires during March 2006. These emissions were observed by instrumentation located on two aircraft platforms, the NSF C-130 and the University of Montana/US Forest Service Twin Otter. Emission ratios (relative to CO) are reported for several species which have never (or rarely) been measured from fires previously, including: OH, PAA, propionic acid, H_2O_2, methane sulfonic acid, and sulfuric acid. Also reported is a rare study of the photochemical aging of a fire plume. The C-130 aircraft flew inside of the fire plume downwind from the fire, sampling the aged BB emissions. Rapid production of several species, including H_2O_2, O_3, PAN, organic and inorganic aerosol – all indicate intense photochemistry occurring within the plume. Of particular interest is the observation that $\Delta PM_{2.5}/\Delta CO$ more than doubled over this time period. This fast photochemistry is likely fueled by the photolysis HONO, which is emitted in large amounts ($\sim$10% of NO_y) from these fires. It is now being recognized that HONO emissions from fire are generally abundant (3–30% of NO_y) (Trentmann et al., 2005; Keene et al., 2006; Yokelson et al., 2007a; Burling et al., 2010; Roberts et al., 2010) and HONO photolysis is an important source of OH during the initial stages of photochemical aging during daylight periods (Trentmann et al., 2005; Alvarado and Prinn, 2009).

1.4 Atmospheric oxidation mechanisms of biogenic compounds

Approximately 500 Tg of isoprene (C_5H_8, 2-methyl-1,3-butadiene) synthesized by plants are released to the atmosphere each year (Guenther et al., 2006). This single emission dominates the release of non-methane hydrocarbons (NMHC) to the atmosphere. Current research continues to reveal new aspects of isoprene chemistry that have important implications for our understanding of Earth's atmospheric photochemistry and formation of secondary organic aerosol. Driven primarily by discrepancies between observed and modeled OH levels under high isoprene conditions (Tan et al., 2001; Thornton et al., 2002; Ren et al., 2008; Lelieveld et al., 2008), and by evidence that, in certain regions of the atmosphere, a large fraction of the SOA is attributable to isoprene chemistry (Claeys

et al., 2004; Surratt et al., 2006), the study of the atmospheric chemistry of isoprene through both experimental and theoretical means is being revisited.

Chapter 6 details an in-depth analysis of the gas-phase products formed in the oxidation of isoprene under high NO_x conditions. Important findings include the observation of significant yields for both formic and acetic acids, and an estimation for the yield of isoprene nitrates near the high end of the range of previous determinations ($\sim$12% molar yield). In addition we find that the C_5-isoprene nitrates have a short atmospheric lifetime and, upon oxidation, appear to recycle NO_x with substantial yield. Propanone nitrate was determined to be formed in the course of this chemistry in $\sim$1% molar yield, and, due to its long lifetime, is likely to have the largest impact in terms of atmospheric reactive nitrogen transport of all the isoprene nitrates.

A surprising and important discovery pertaining to low NO_x isoprene oxidation is described in Chapter 7. C_5-hydroxyhydroperoxides are formed in high yield ($>$70%) as first generation products. Through the combination of MSMS-CF_3O^- ion chemistry and use of isotopically labeled oxidants, we show that these C_5-hydroxyhydroperoxides are catalytically converted (by the OH radical) to C_5-dihydroxyepoxides in high yield ($>$75%). This unique mechanism explains a portion (but not all) of the modeled–versus–observed OH discrepancy described above. Several theoretical-based predictions have been put forward which may help resolve more of the remaining discrepancy. Perhaps even more important is the now experimentally confirmed (Surratt et al., 2010; Chan et al., 2010) prediction that these dihydroxyepoxides should efficiently undergo heterogeneous reactive uptake to form C_5-tetrols and related species that have previously been shown to comprise a large fraction of SOA attributed to isoprene under low-moderate NO_x conditions (Claeys et al., 2004; Surratt et al., 2008).

Chapter 8 presents experimental constraints for the 1,6-H-shift isomerization rates of 1,4-OH-OO- and 4,1-OH-OO-isoprene peroxy radicals. The isomerization rates are experimentally determined to be ~50 times slower than the recent theoretical predictions of Peeters et al. (2009). Despite this slow rate ($k_{1,6\text{-isom}}^{295} = 0.002$ s^{-1}), this isomerization reaction is predicted to substantially impact the atmospheric chemistry of isoprene (Archibald et al., 2010). The full impact on atmospheric HOx levels is not yet known due to uncertainty in the fate of the isomerization products. The rates for the 1,5-H-shifts (from alcohol) for 1,2-OH-OO and 4,3-OH-OO β-isoprene peroxy radicals, also predicted through theoretical calculations by Peeters et al. (2009) and da Silva et al. (2010), were not well-constrained through our experiments, but observations were consistent with the rate calculated by da Silva et al. (2010) ($k_{1,5\text{-isom}}^{318} = 0.005$ s^{-1}).

Bibliography

Aiken, A. C., Salcedo, D., Cubison, M. J., Huffman, J. A., DeCarlo, P. F., Ulbrich, I. M., Docherty, K. S., Sueper, D., Kimmel, J. R., Worsnop, D. R., Trimborn, A., Northway, M., Stone, E. A., Schauer, J. J., Volkamer, R. M., Fortner, E., de Foy, B., Wang, J., Laskin, A., Shutthanandan, V., Zheng, J., Zhang, R., Gaffney, J., Marley, N. A., Paredes-Miranda, G., Arnott, W. P., Molina, L. T., Sosa, G., and Jimenez, J. L.: Mexico City aerosol analysis during MILAGRO using high resolution aerosol mass spectrometry at the urban supersite (T0) - Part 1: Fine particle composition and organic source apportionment, Atmos. Chem. Phys., 9, 6633–6653, 2009.

Aiken, A. C., de Foy, B., Wiedinmyer, C., DeCarlo, P. F., Ulbrich, I. M., Wehrli, M. N., Szidat, S., Prevot, A. S. H., Noda, J., Wacker, L., Volkamer, R., Fortner, E., Wang, J., Laskin, A., Shutthanandan, V., Zheng, J., Zhang, R., Paredes-Miranda, G., Arnott, W. P., Molina, L. T., Sosa, G., Querol, X., and Jimenez, J. L.: Mexico City aerosol analysis during MILAGRO using high resolution aerosol mass spectrometry at the urban supersite (T0) - Part 2: Analysis of the biomass burning contribution and the non-fossil carbon fraction, Atmos. Chem. Phys., 10, 5315–5341, doi:10.5194/acp-10-5315-2010, 2010.

Alvarado, M. J. and Prinn, R. G.: Formation of ozone and growth of aerosols in young smoke plumes from biomass burning: 1. Lagrangian parcel studies, J. Geophys. Res.-Atmos., 114, doi:10.1029/2008JD011144, 2009.

Amelynck, C., Schoon, N., and Arijs, E.: Gas phase reactions of CF_3O^- and $CF_3O^- \cdot H_2O$ with nitric, formic, and acetic acid, Int. J. Mass. Spectrom., 203, 165–175, 2000a.

Amelynck, C., Van Bavel, A. M., Schoon, N., and Arijs, E.: Gas phase reactions of CF_3O^- and $CF_3O^- \cdot H_2O$ and their relevance to the detection of stratospheric HCl, Int. J. Mass. Spectrom., 202, 207–216, 2000b.

Andreae, M. and Merlet, P.: Emission of trace gases and aerosols from biomass burning, Global Biogeochem. Cy., 15, 955–966, 2001.

Archibald, A. T., Cooke, M. C., Utembe, S. R., Shallcross, D. E., Derwent, R. G., and Jenkin, M. E.: Impacts of mechanistic changes on HO_x formation and recycling in the oxidation of isoprene, Atmos. Chem. Phys., 10, 8097–8118, doi:10.5194/acp-10-8097-2010, URL http://www.atmos-chem-phys.net/10/8097/2010/, 2010.

Blin-Simiand, N., Jorand, F., Keller, K., Fiderer, M., and Sahetchian, K.: Ketohydroperoxides and ignition delay in internal combustion engines, Combust. Flame, 112, 278–282, 1998.

Blin-Simiand, N., Jorand, F., Sahetchian, K., Brun, M., Kerhoas, L., Malosse, C., and Einhorn, J.: Hydroperoxides with zero, one, two or more carbonyl groups formed during the oxidation of n-dodecane, Combust. Flame, 126, 1524–1532, 2001.

Bond, T., Streets, D., Yarber, K., Nelson, S., Woo, J., and Klimont, Z.: A technology-based global inventory of black and organic carbon emissions from combustion, J. Geophys. Res.-Atmos., 109, doi:10.1029/2003JD003697, 2004.

Bravo, A. H., Sosa, E. R., Sanchez, A. P., Jaimes, P. M., and Saavedra, R. M. I.: Impact of wildfires on the air quality of Mexico City, 1992–1999, Environ. Pollut., 117, 243–253, 2002.

Burling, I. R., Yokelson, R. J., Griffith, D. W. T., Johnson, T. J., Veres, P., Roberts, J. M., Warneke, C., Urbanski, S. P., Reardon, J., Weise, D. R., Hao, W. M., and de Gouw, J.: Laboratory measurements of trace gas emissions from biomass burning of fuel types from the Southeastern and Southwestern United States, Atmos. Chem. Phys. Discuss., 10, 16 425–16 473, doi:10.5194/acpd-10-16425-2010, URL http://www.atmos-chem-phys-discuss.net/10/16425/2010/, 2010.

Chan, M. N., Surratt, J. D., Claeys, M., Edgerton, E. S., Tanner, R. L., Shaw, S. L., Zheng, M., Knipping, E. M., Eddingsaas, N. C., Wennberg, P. O., and Seinfeld, J. H.: Characterization and quantification of isoprene-derived epoxydiols in ambient aerosol in the Southeastern United States, Environ. Sci. Technol., 44, 4590–4596, doi:10.1021/es100596b, 2010.

Claeys, M., Graham, B., Vas, G., Wang, W., Vermeylen, R., Pashynska, V., Cafmeyer, J., Guyon, P., Andreae, M., Artaxo, P., and Maenhaut, W.: Formation of secondary organic aerosols through photooxidation of isoprene, Science, 303, 1173–1176, 2004.

Da Silva, G., Graham, C., and Wang, Z.-F.: Unimolecular beta-Hydroxyperoxy Radical Decomposition with OH Recycling in the Photochemical Oxidation of Isoprene, Environ. Sci. Technol., 44, 250–256, doi:10.1021/es900924d, 2010.

de Gouw, J. and Warneke, C.: Measurements of volatile organic compounds in the earths atmosphere using proton-transfer-reaction mass spectrometry, Mass Spectrom. Rev., 26, 223–257, doi:10.1002/mas.20119, 2007.

DeCarlo, P. F., Ulbrich, I. M., Crounse, J., de Foy, B., Dunlea, E. J., Aiken, A. C., Knapp, D., Weinheimer, A. J., Campos, T., Wennberg, P. O., and Jimenez, J. L.: Investigation of the sources and processing of organic aerosol over the Central Mexican Plateau from aircraft measurements during MILAGRO, Atmos. Chem. Phys., 10, 5257–5280, doi:10.5194/acp-10-5257-2010, 2010.

Guenther, A., Karl, T., Harley, P., Wiedinmyer, C., Palmer, P. I., and Geron, C.: Estimates of global terrestrial isoprene emissions using MEGAN (Model of Emissions of Gases and Aerosols from Nature), Atmos. Chem. Phys., 6, 3181–3210, 2006.

Huey, L., Villalta, P., Dunlea, E., Hanson, D., and Howard, C.: Reactions of CF_3O^- with atmospheric trace gases, J. Phys. Chem., 100, 190–194, 1996.

Huey, L. G.: Measurement of trace atmospheric species by chemical ionization mass spectrometry: Speciation of reactive nitrogen and future directions, Mass Spectrom. Rev., 26, 166–184, doi: 10.1002/mas.20118, 2007.

Jorand, F., Heiss, A., Sahetchian, K., Kerhoas, L., and Einhorn, J.: Identification of an unexpected peroxide formed by successive isomerization reactions of the n-butoxy radical in oxygen, J. Chem. Soc. Faraday T., 92, 4167–4171, 1996.

Jorand, F., Kerhoas, L., Heiss, A., Einhorn, J., and Sahetchian, K.: Determination of the ultra violet absorption cross section of hexyl-ketohydroperoxides in solution in acetonitrile, J. Photoch. Photobio. A, 134, 119–125, 2000.

Keene, W. C., Lobert, R. M., Crutzen, P. J., Maben, J. R., Scharffe, D. H., Landmann, T., Hely, C., and Brain, C.: Emissions of major gaseous and particulate species during experimental burns of southern African biomass, J. Geophys. Res.-Atmos., 111, doi:10.1029/2005JD006319, 2006.

Kroll, J. H. and Seinfeld, J. H.: Chemistry of secondary organic aerosol: Formation and evolution of low-volatility organics in the atmosphere, Atmos. Environ., 42, 3593–3624, doi:10.1016/j.atmosenv.2008.01.003, 2008.

Kroll, J. H., Smith, J. D., Che, D. L., Kessler, S. H., Worsnop, D. R., and Wilson, K. R.: Measurement of fragmentation and functionalization pathways in the heterogeneous oxidation of oxidized organic aerosol, Phys. Chem. Chem. Phys., 11, 8005–8014, doi:10.1039/b905289e, 2009.

Lelieveld, J., Butler, T. M., Crowley, J. N., Dillon, T. J., Fischer, H., Ganzeveld, L., Harder, H., Lawrence, M. G., Martinez, M., Taraborrelli, D., and Williams, J.: Atmospheric oxidation capacity sustained by a tropical forest, Nature, 452, 737–740, doi:10.1038/nature06870, 2008.

Li, Q., Jacob, D., Yantosca, R., Heald, C., Singh, H., Koike, M., Zhao, Y., Sachse, G., and Streets, D.: A global three-dimensional model analysis of the atmospheric budgets of HCN and CH_3CN: Constraints from aircraft and ground measurements, J. Geophys. Res.-Atmos., 108, doi:10.1029/2002JD003075, 2003.

Li, Q. B., Jacob, D. J., Bey, I., Yantosca, R. M., Zhao, Y. J., Kondo, Y., and Notholt, J.: Atmospheric hydrogen cyanide (HCN): Biomass burning source, ocean sink?, Geophys. Res. Lett., 27, 357–360, 2000.

Moffet, R. C., de Foy, B., Molina, L. T., Molina, M. J., and Prather, K. A.: Measurement of ambient aerosols in northern Mexico City by single particle mass spectrometry, Atmos. Chem. Phys., 8, 4499–4516, 2008.

Molina, L. T., Kolb, C. E., de Foy, B., Lamb, B. K., Brune, W. H., Jimenez, J. L., Ramos-Villegas, R., Sarmiento, J., Paramo-Figueroa, V. H., Cardenas, B., Gutierrez-Avedoy, V., and Molina, M. J.: Air quality in North America's most populous city - overview of the MCMA-2003 campaign, Atmos. Chem. Phys., 7, 2447–2473, 2007.

Peeters, J. and Muller, J.-F.: HO_x radical regeneration in isoprene oxidation via peroxy radical isomerisations. II: experimental evidence and global impact, Phys. Chem. Chem. Phys., 12, 14 227–14 235, doi:10.1039/c0cp00811g, 2010.

Peeters, J., Nguyen, T. L., and Vereecken, L.: HO_x radical regeneration in the oxidation of isoprene, Phys. Chem. Chem. Phys., 11, 5935–5939, doi:10.1039/b908511d, 2009.

Perrin, O., Heiss, A., Doumenc, F., and Sahetchian, K.: Homogeneous and heterogeneous reactions of the $n-C_5H_{11}O$, $n-C_5H_{10}OH$ and $OOC_5H_{10}OH$ radicals in oxygen. Analytical steady state solution by use of the Laplace transform, J. Chem. Soc. Faraday T., 94, 2323–2335, 1998a.

Perrin, O., Heiss, A., Sahetchian, K., Kerhoas, L., and Einhorn, J.: Determination of the isomerization rate constant $HOCH_2CH_2CH_2CH(OO^{\cdot})CH_3 \rightarrow HOC^{\cdot}HCH_2CH_2CH(OOH)CH_3$. Importance of intramolecular hydroperoxy isomerization in tropospheric chemistry, Int. J. Chem. Kinet., 30, 875–887, 1998b.

Ren, X., Olson, J. R., Crawford, J. H., Brune, W. H., Mao, J., Long, R. B., Chen, Z., Chen, G., Avery, M. A., Sachse, G. W., Barrick, J. D., Diskin, G. S., Huey, L. G., Fried, A., Cohen, R. C., Heikes, B., Wennberg, P. O., Singh, H. B., Blake, D. R., and Shetter, R. E.: HO_x chemistry

during INTEX-A 2004: Observation, model calculation, and comparison with previous studies, J. Geophys. Res.-Atmos., 113, doi:10.1029/2007JD009166, 2008.

Roberts, J. M., Veres, P., Warneke, C., Neuman, J. A., Washenfelder, R. A., Brown, S. S., Baasandorj, M., Burkholder, J. B., Burling, I. R., Johnson, T. J., Yokelson, R. J., and de Gouw, J.: Measurement of HONO, HNCO, and other inorganic acids by negative-ion proton-transfer chemical-ionization mass spectrometry (NI-PT-CIMS): application to biomass burning emissions, Atmos. Meas. Tech., 3, 981–990, doi:10.5194/amt-3-981-2010, 2010.

Salcedo, D., Onasch, T. B., Dzepina, K., Canagaratna, M. R., Zhang, Q., Huffman, J. A., DeCarlo, P. F., Jayne, J. T., Mortimer, P., Worsnop, D. R., Kolb, C. E., Johnson, K. S., Zuberi, B., Marr, L. C., Volkamer, R., Molina, L. T., Molina, M. J., Cardenas, B., Bernabe, R. M., Marquez, C., Gaffney, J. S., Marley, N. A., Laskin, A., Shutthanandan, V., Xie, Y., Brune, W., Lesher, R., Shirley, T., and Jimenez, J. L.: Characterization of ambient aerosols in Mexico City during the MCMA-2003 campaign with Aerosol Mass Spectrometry: results from the CENICA Supersite, Atmos. Chem. Phys., 6, 925–946, 2006.

Stone, E. A., Snyder, D. C., Sheesley, R. J., Sullivan, A. P., Weber, R. J., and Schauer, J. J.: Source apportionment of fine organic aerosol in Mexico City during the MILAGRO experiment 2006, Atmos. Chem. Phys., 8, 1249–1259, 2008.

Surratt, J. D., Murphy, S. M., Kroll, J. H., Ng, a. L. N., Hildebrandt, L., Sorooshian, A., Szmigielski, R., Vermeylen, R., Maenhaut, W., Claeys, M., Flagan, R. C., and Seinfeld, J. H.: Chemical composition of secondary organic aerosol formed from the photooxidation of isoprene, J. Phys. Chem. A, 110, 9665–9690, doi:10.1021/jp061734m, 2006.

Surratt, J. D., Gomez-Gonzalez, Y., Chan, A. W. H., Vermeylen, R., Shahgholi, M., Kleindienst, T. E., Edney, E. O., Offenberg, J. H., Lewandowski, M., Jaoui, M., Maenhaut, W., Claeys, M., Flagan, R. C., and Seinfeld, J. H.: Organosulfate formation in biogenic secondary organic aerosol, J. Phys. Chem. A, 112, 8345–8378, doi:10.1021/jp802310p, 2008.

Surratt, J. D., Chan, A. W. H., Eddingsaas, N. C., Chan, M., Loza, C. L., Kwan, A. J., Hersey, S. P., Flagan, R. C., Wennberg, P. O., and Seinfeld, J. H.: Reactive intermediates revealed in secondary organic aerosol formation from isoprene, P. Natl. Acad. Sci. USA, 107, 6640–6645, doi:10.1073/pnas.0911114107, 2010.

Tan, D., Faloona, I., Simpas, J., Brune, W., Shepson, P., Couch, T., Sumner, A., Carroll, M., Thornberry, T., Apel, E., Riemer, D., and Stockwell, W.: HO_x budgets in a deciduous forest: Results from the PROPHET summer 1998 campaign, J. Geophys. Res.-Atmos., 106, 24 407–24 427, 2001.

Thornton, J. A., Wooldridge, P. J., Cohen, R. C., Martinez, M., Harder, H., Brune, W. H., Williams, E. J., Roberts, J. M., Fehsenfeld, F. C., Hall, S. R., Shetter, R. E., Wert, B. P., and Fried, A.: Ozone production rates as a function of NO_x abundances and HO_x production rates in the Nashville urban plume, J. Geophys. Res.-Atmos., 107, doi:10.1029/2001JD000932, 2002.

Trentmann, J., Yokelson, R. J., Hobbs, P. V., Winterrath, T., Christian, T. J., Andreae, M. O., and Mason, S. A.: An analysis of the chemical processes in the smoke plume from a savanna fire, J. Geophys. Res.-Atmos., 110, doi:10.1029/2004JD005628, 2005.

Viggiano, A. A.: In-situ mass-spectrometry and ion chemistry in the stratosphere and troposphere, Mass Spectrom. Rev., 12, 115–137, 1993.

Yokelson, R. J., Karl, T., Artaxo, P., Blake, D. R., Christian, T. J., Griffith, D. W. T., Guenther, A., and Hao, W. M.: The Tropical Forest and Fire Emissions Experiment: overview and airborne fire emission factor measurements, Atmos. Chem. Phys., 7, 5175–5196, 2007a.

Yokelson, R. J., Urbanski, S. P., Atlas, E. L., Toohey, D. W., Alvarado, E. C., Crounse, J. D., Wennberg, P. O., Fisher, M. E., Wold, C. E., Campos, T. L., Adachi, K., Buseck, P. R., and Hao, W. M.: Emissions from forest fires near Mexico City, Atmos. Chem. Phys., 7, 5569–5584, 2007b.

Chapter 2

Measurement of gas-phase hydroperoxides by chemical ionization mass spectrometry*

2.1   Abstract

A new method for the detection of gas-phase hydroperoxides is described. The clustering chemistry of CF_3O^- is exploited to produce speciated measurements of several hydroperoxides with high sensitivity and fast time response. Correspondence of airborne observations made with this technique and the established HPLC method is illustrated. CF_3O^- appears to be a highly versatile reagent ion for measurements of both weak and strong acids in the atmosphere.

2.2   Introduction

Hydroperoxides (ROOHs) are important components of the Earth's atmosphere. Depending on the nature of R, they have widely varying atmospheric lifetimes and impacts. In general, the larger and less polar organic hydroperoxides (e.g., $R = CH_3$ or CH_3CH_2) can be transported by atmospheric motion without significant loss to cloud. Thus, these compounds serve as reservoirs of HO_x (OH and HO_2) whose subsequent photochemistry (photolysis or oxidation by OH) can release radicals, oftentimes in areas distant from where they are initially formed. Such transport, for example, to the upper troposphere, can significantly alter gas-phase oxidation rates and radical budgets (Wennberg et al., 1998; Jaegle et al., 2000). Peroxides with high solubility (e.g., $R = H$, $HOCH_2$) are often lost by uptake onto aerosol and cloud droplets where they promote heterogeneous oxidation of many compounds such as SO_2 (Penkett et al., 1979) and may play a role in the formation of secondary organic aerosol (Claeys et al., 2004).

Hydrogen peroxide, H_2O_2, is formed in the atmosphere almost exclusively through the self-reaction of HO_2:

$$HO_2 + HO_2 \rightarrow H_2O_2 \tag{R2.1}$$

Organic peroxides generally form in the atmosphere via OH mediated oxidation of saturated hydrocarbons,

$$R{-}H + OH \rightarrow R\cdot + H_2O \tag{R2.2}$$

$$R\cdot + O_2 + M \rightarrow RO_2\cdot + M \tag{R2.3}$$

$$RO_2\cdot + HO_2\cdot \rightarrow ROOH + O_2 \tag{R2.4}$$

or unsaturated hydrocarbons,

$$(R_1)(R_2)C{=}C(R_3)(R_4) + OH \rightarrow (R_1)(R_2)C(OH){-}C{\cdot}(R_3)(R_4) \tag{R2.5}$$

$$(R_1)(R_2)C(OH){-}C{\cdot}(R_3)(R_4) + O_2 + M \rightarrow (R_1)(R_2)C(OH){-}C(R_3)(R_4)O_2{\cdot}{+}M \tag{R2.6}$$

$$(R_1)(R_2)C(OH){-}C(R_3)(R_4)O_2{\cdot} + HO_2{\cdot} \rightarrow (R_1)(R_2)C(OH){-}C(R_3)(R_4)OOH + O_2 \tag{R2.7}$$
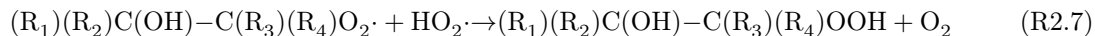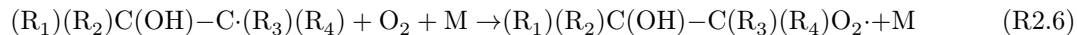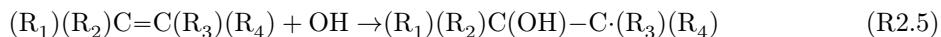
where R is an organic substituent (e.g., CH_3), and $R_1{-}R_4$ are either H-atom or organic substituents. Peroxides can also be produced by the ozonolysis of alkenes under high-humidity conditions (Gab et al., 1995). Because $RO_2{\cdot}$ reacts quickly with NO, the efficiency of peroxide formation tends to decrease at high NO_x, although in highly polluted environments, such as Mexico City, peroxides are predicted to be highly elevated despite the high NO_x due to very high hydrocarbon concentrations (Madronich, 2005).

To date, most atmospheric peroxide measurements have required extensive sample handling (Kok et al., 1989; Lee et al., 2000). Typically, sampled air is passed through water, stripping soluble peroxides into the aqueous phase. The aqueous-phase peroxides are detected using a derivatization/fluorescence technique, sometimes after separation by high-performance liquid chromatography (HPLC) (Lee et al., 2000; Heikes et al., 1987; Penkett et al., 1995; Lee et al., 1995). While these methods have been tested and refined for some time, they are limited by the solubility of ROOH, potential artifacts from aqueous-phase chemistry, and the ability to separate and preserve ROOH on the HPLC column. In addition, time response can be rather long (a few minutes). Direct measurements of peroxides have been performed with tunable diode lasers, but these methods suffer from poor sensitivity and "optical noise" effects (Slemr et al., 1986; Kormann et al., 2002).

Chemical ionization mass spectrometry (CIMS) has been shown to be a versatile and fast measurement technique for a wide variety of atmospheric trace gases. Airplane measurements by CIMS have focused on HNO_3 (Fahey et al., 2001; Furutani and Akimoto, 2002; Miller et al., 2000; Neuman et al., 2002; Zondlo et al., 2003; Marcy et al., 2005; Reiner et al., 1998), with some measurements of peroxy radicals (Cantrell et al., 2003), SO_2 (Miller et al., 2000; Reiner et al., 1998), HCN (Miller et al., 2000; Viggiano et al., 2002), DMSO (Nowak et al., 2001), OH, H_2SO_4, and MSA (Mauldin et al., 2003), and $ClONO_2$ and HCl (Marcy et al., 2005), but the technique has also been explored for a suite of other species including CH_3COOH and HCOOH (Amelynck et al., 2000a), NH_3 (Nowak et al., 2002), and HNO_4 (Slusher et al., 2001), using a wide range of ionization schemes and other conditions. For many compounds, detection limits of 10 pptv can be obtained with subsecond inte-

gration time. The fast response time allows for high temporal resolution, which is particularly useful for airborne measurements.

To our knowledge, peroxides have been detected by CIMS on three occasions. H_2O_2 and CH_3OOH clusters with F^- have been demonstrated in laboratory studies (Messer et al., 2000), a cluster tentatively identified as $CO_3^- \cdot H_2O_2$ was observed in aircraft-borne observations over Germany during a 1991 aircraft campaign aboard the DLR Falcon (Reiner et al., 1998), and a product ion at 101 amu was assigned to isoprenehydroxy-hydroperoxides detected using a proton-transfer reaction mass spectrometer, which made measurements over a tropical rain forest (Warneke et al., 2001). In this paper, we describe the use of the negative ion cluster chemistry of CF_3O^-, which has previously been shown to be useful for measurement of inorganic and organic acids (Amelynck et al., 2000b,a; Huey et al., 1996), for sensitive and selective airborne measurement of ROOH species H_2O_2 and $CH_3C(O)OOH$ (peroxyacetic acid, PAA). We also report the results of an intercomparison between our technique and the established HPLC method (Lee et al., 1995) performed on the NASA DC-8 during the Intercontinental Chemical Transport Experiment-North America (INTEX-NA, summer 2004), which shows these two methods to be in good agreement.

2.3 Instrument description

The Caltech CIMS instrument was built in 1998 through a joint collaboration with the National Center for Atmospheric Research (NCAR) to measure polar stratospheric HNO_3 on the NASA ER2 aircraft (Fahey et al., 2001). It was retrofitted in 2003 to fly aboard the NASA DC-8 aircraft and the suite of compounds quantified has been broadened. The instrument components, described below, are depicted in Figure 2.1.

Ambient air is sampled through a custom, partially stopped, aluminum inlet (A and B in Figure 2.1), which directs a fraction of the flow perpendicularly toward the instrument and serves as a virtual impactor to discriminate against particles of diameter > 0.3 μm from the sample flow. Upon redirection, the sample air flows through a glass tube (C), coated with a thin layer of Teflon (Fluoropel PFC 801A, Cytonix Corp.) to minimize surface hydrophilicity, which is particularly problematic for HNO_3. Wall effects are further mitigated because flow through the glass tube is fast (40 m/s), and only the center of the flow passes through the adjustable aperture (G) into the ion flow tube (J), while the rest is exhausted through the arms of the aluminum y-block (F).

The reagent ion is produced by flowing a 10 ppmv mixture of CF_3OOCF_3 in N_2 at a rate of 400 standard cubic centimeters per minute (sccm) at 35 hPa total pressure through a cylindrical

A. Inlet shroud
B. Partial plug
C. Teflon coated glass inlet tube (high flow).
D. Teardrop-shaped inlet tube pylon.
E. Wall of aircraft
F. Y-block.
G. Ajustable sampling aperture.
H. Calibration gas line.
I. Zero gas line.
J. Teflon coated glass flow tube
K. Ion/molecule reaction region
L. Critical orifice, connects to scroll pump
M. Ion source cup, lined with Po-210 foil

N. Ion source cap
O. Pinhole plate
P. Lens 1
Q. Octopole ion guide
R. Turbo pump 1
S. Lens 2, seperates octopole chamber from quadrupole chamber
T. Lens 3
U. Lens 4
V. Lens 5
W. Lens 6
X. Quadrupole mass filter
Y. Turbo pump 2
Z. Channel electron multiplier

Figure 2.1 – Schematic of the Caltech CIMS instrument as utilized on the NASA DC-8.

ion source cup (M) lined with a nickel foil containing a layer of polonium-210 and sealed with a gold coating (NRD LLC-initially 4.5 mCu activity). Polonium-210 ejects α particles, which start the series of reactions leading to formation of CF_3O^-:

$$^{210}\text{Po} \rightarrow \alpha + {}^{206}\text{Pb} \tag{R2.8}$$

$$\alpha + N_2 \rightarrow N_2^+ + e^- + \alpha \tag{R2.9}$$

$$e^- + CF_3OOCF_3 \rightarrow CF_3O^- + CF_3O\cdot \tag{R2.10}$$

The CF_3OOCF_3 was prepared by Dr. Darryl DesMarteau of Clemson University. Careful storage and handling of the CF_3OOCF_3 is required to produce a clean CF_3O^- source. We highly recommend use of an all-metal storage system. Small amounts of silicone from O-rings and grease in valves, regulators, and tubing within the gas handling system lead to unacceptably high impurity ions such as $Si(CH_3)_3F_2^-$ (m/z 111), $Si(CH_3)_2F_3^-$ (m/z 115), $Si(CH_3)F_4^-$ (m/z 119), and SiF_5^- (m/z 123), which presumably are ions formed from the reaction of CF_3O^- with fluorinated silicon molecules ($Si(CH_3)_3F$, $Si(CH_3)_2F_2$, $Si(CH_3)F_3$, and SiF_4, respectively). These fluorinated silicon molecules seem to form through the reaction of CF_3OOCF_3 (or some degradation product thereof) with silicone

present in the system. The removal of all silicone compounds from the system virtually eliminates these impurities.

Transport of the ions out of the source is enhanced by applying an electric potential between the source cup and the source cap (N). The cup and cap are typically held at –250 and –240 V, respectively, with respect to the pinhole orifice plate (O). There is essentially no pressure drop between the ion source and the ion/molecule reaction region (K) in the ion flow tube (J). As the ions enter the ion-molecule reaction region, they are accelerated toward the pinhole, perpendicular to the sample flow, by the electric field between the source cap and the pinhole orifice plate (100 V/cm). In this region, the ions react with trace gases in the sample air to form selective product ions (described below in Ion Chemistry and Water Dependence). The adjustable orifice (G) is adjusted using a computer-controlled stepper motor to maintain a constant flow tube pressure (35 hPa). A critical orifice (L) located just after the ion-molecule reaction region ensures a constant mass flow (2 L/min) through the flow tube. Temperature throughout the flow tube is close to 20°C but varies somewhat with the temperature outside the aircraft and the temperature of the aircraft cabin.

The average ion-molecule reaction time in the flow tube is 1 ms. This is determined by monitoring the ratio of $[\mathrm{HF} \cdot \mathrm{NO}_3^-]$ to $[\mathrm{CF}_3\mathrm{O}^-]$ as a function of $[\mathrm{HNO}_3]$ and using the established rate constant for the reaction $\mathrm{HNO}_3 + \mathrm{CF}_3\mathrm{O}^- \rightarrow \mathrm{HF} \cdot \mathrm{NO}_3^- + \mathrm{CF}_2\mathrm{O}$ (Amelynck et al., 2000a; Huey et al., 1996). The reaction time estimated in this manner is somewhat longer than the transit time calculated for an electric field of 100 V/cm over the flow tube diameter of 2.5 cm at 35 hPa, possibly due to the non-uniform electric field produced across the flow tube.

After formation, the product ions are sampled into the high vacuum system through a 260 μm pinhole on the orifice plate (O). They are then directed through lens 1 (P) and enter the octopole ion guide (Q) composed of 0.635 cm (diameter) precision ground stainless steel rods arranged in a circle with i.d. of 1.78 cm and held together by two Teflon mounting rings. The octopole power supply is a simple resonant circuit, composed of an air core transformer whose primary is driven by switching transistors. The power supply operates at 1.2 MHz and is tuned into resonance by adjusting the frequency. The typical rf amplitude is 200 V peak to peak. The pinhole and lens 1 are normally held at aircraft ground, while the octopole bias is set to +1.5 V to optimize ion throughput while minimizing fragmentation of weakly bound clusters such as $\mathrm{CF}_3\mathrm{O}^- \cdot \mathrm{H}_2\mathrm{O}_2$. The octopole chamber is maintained at $\sim 10^{-3}$ hPa under the typical gas load (gas flow of 20 sccm at a flow tube pressure of 35 hPa and 20°C) by turbopump 1 (R, Varian V-250).

As the ions exit the octopole, they pass through lens 2 (S), set at +18 V, into the quadrupole

chamber. The quadrupole chamber is differentially pumped by a second turbopump (Y, Varian V-250) to a pressure of 1×10^{-5} hPa under gas load; this turbopump exhausts into the low-pressure side of turbopump 1 to reduce power consumption and heat production. In the quadrupole chamber, the ions pass through a series of four lenses (T-W) held at –40, +220, –100, and +30 V, respectively, to focus and energetically prepare the ions for the mass filter (X), a commercial 19-mm quadrupole (Extrel). The quadrupole power supply (QSC Systems) enables selective filtering of masses ranging from 10 to 250 amu with unit mass resolution and consumes 30 W of power. The ions of a selected mass exit the quadrupole, and are detected using a channel electron multiplier (Z, K&M 7550m) operated in pulse counting mode with a preamp/discriminator (Amptek A-101) allowing for single ion detection and count rates up to 4 MHz. All instrument control and data collection are conducted with a PC-104 computer through data acquisition boards (Diamond Systems) running a real-time operating system (QNX 4.25) using custom control software.

2.4   Ion chemistry and water dependence

In the first laboratory study of CF_3O^- chemistry, Huey et al. identified fluoride ion transfer as the primary reaction pathway of CF_3O^- with strong acids, i.e., $CF_3O^- + HX \rightarrow HF \cdot X^- + CF_2O$ (Huey et al., 1996). Amelynck et al. later showed that for weaker acids, such as $HC(O)OH$ and $CH_3C(O)OH$, CF_3O^- often reacts via clustering chemistry, i.e., $CF_3O^- + HX \rightarrow CF_3O^- \cdot HX$ (Amelynck et al., 2000a). While investigating the ion reaction chemistry of CF_3O^- with peroxynitric acid (HNO_4; which also reacts both by fluoride transfer and clustering), we discovered that CF_3O^- clustered efficiently with H_2O_2, which is a reagent (and impurity) in the synthesis of HNO_4. Further experimentation with additional hydroperoxides (CH_3OOH, $CH_3C(O)OOH$, and $HOCH_2OOH$) showed that many other compounds of this type cluster efficiently with CF_3O^-.

The efficiency of the clustering of CF_3O^- with a particular ROOH is highly dependent on the water vapor mixing ratio. To quantify this dependence in the laboratory, we introduced a known quantity of ROOH into the flow tube and monitored instrument sensitivity as a function of flow tube humidity, which we controlled.

H_2O_2 was introduced to the humidity-controlled flow tube by flowing dry N_2 over urea hydrogen peroxide (UHP) held at constant temperature. Constant outputs of other hydroperoxides came from temperature-controlled diffusion vials. PAA and UHP are available commercially (Sigma-Aldrich) while methyl hydrogen peroxide (MHP) (Vaghjiani and Ravishankara, 1989) and hydroxymethyl hydrogen peroxide (HMHP) (Marklund, 1971) were synthesized in the laboratory, using established
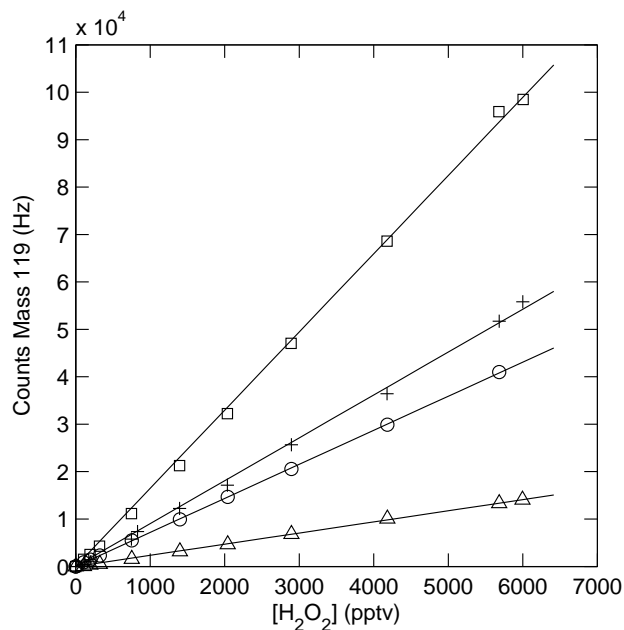
Figure 2.2 – Sensitivity to H_2O_2 (mass 119), dependent on water (stars, 10000 ppmv H_2O; circles, 100 ppmv H_2O) due to reduced sensitivity and increase in the background. For the mass scans illustrated here, the H_2O_2 mixing ratio is 5000 (closed stars), 500 (closed circles), or < 50 pptv (open symbols).

methods. While we had no incidents, extreme care must be taken synthesizing these peroxides as they have been know to explode unexpectedly.

We controlled the humidity with mass flow controllers, adjusting the proportion of water vapor saturated air to dry zero air (Air Liquide) entering the flow tube. The saturated air was provided by a series of two atmospheric pressure (1013 hPa) H_2O bubblers submerged in a temperature-controlled bath held at 40°C. After the second bubbler, the saturated air flowed through an orifice to reduce the pressure and avoid water condensation in the flow tube, even at high water vapor mixing ratios and reduced temperature. The measured rate of mass loss of the water in the double bubbler system was consistent with complete saturation of the air exiting the bubbler.

Figure 2.2 illustrates mass scans in the region of the $CF_3O^- \cdot H_2O_2$ cluster (m/z 119). At high concentrations of H_2O, the CF_3O^- is present as $CF_3O^- \cdot H_2O$ (m/z 103), $CF_3O^- \cdot (H_2O)_2$ (m/z 121), and higher clusters–$CF_3O^- \cdot (H_2O)_n$. This decreases the sensitivity to H_2O_2 (and other peroxides) and increases the backgrounds due to the hydrolysis of CF_3O^- by H_2O to $F^- \cdot (H_2O)_n$ ions.

While the thermodynamics of the reaction mechanism are beyond the scope of this paper, the following reactions are likely responsible for the changing sensitivity in response to varying [H_2O]:

$$CF_3O^- + ROOH + M \leftrightarrow CF_3O^- \cdot ROOH + M \qquad \text{(R2.11)}$$

$$CF_3O^- \cdot H_2O + ROOH \rightarrow CF_3O^- \cdot ROOH + H_2O \qquad (R2.12)$$

$$CF_3O^- \cdot ROOH + H_2O \rightarrow CF_3O^- \cdot H_2O + ROOH \qquad (R2.13)$$
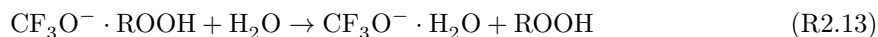
For H_2O_2, R2.11 (forward) is somewhat slower than R2.12, so the sensitivity improves as $[H_2O]$ increases to 0.1% before decreasing at higher water mixing ratios. For other peroxides (e.g., MHP), the sensitivity decreases with increasing H_2O for all H_2O concentrations. The ratio of R2.13 to R2.12 sets how quickly the sensitivity declines with $[H_2O]$. For relatively strong clusters (e.g., $CF_3O^- \cdot H_2O_2$ or $CF_3O^- \cdot PAA$), the falloff is less steep than for weaker ones (e.g., $CF_3O^- \cdot CH_3OOH$ or $CF_3O^- \cdot CH_3CH_2OOH$). Thus, for accurate quantification, each individual compound must be calibrated separately; in addition, the curves shown in Figure 2.3 will be specific to the conditions in the ion flow tube (pressure, temperature, interaction time). The heat of formation of $CF_3O^- \cdot H_2O_2$ has not been measured, but the binding energy is greater than that of $CF_3O^- \cdot H_2O$ (51 kJ mol^{-1} (Amelynck et al., 2000b)), as evidenced by reaction R2.12. *Ab initio* calculations and thermodynamic discussions of the clustering chemistry will be addressed in a separate paper.

2.5 Field operation

2.5.1 Calibration

In addition to the laboratory calibrations, the instrument was calibrated hourly during flight using standard additions of gas-phase H_2O_2, HNO_3, $HC(O)OH$, and $H_3CC(O)OH$ to the flow tube. The nitric acid and organic acid standards are isotopically labeled and evolve from permeation tubes held at constant temperature (Washenfelder et al., 2003). The H_2O_2 calibration standard is produced by flowing dry N_2 over UHP held at a constant temperature of 0°C in a glass U-tube. At 0°C, UHP has a H_2O_2 vapor pressure of 1.4×10^{-3} hPa (determined by collecting the output in water and analyzing with a standard colorimetric technique (Bioxytech H_2O_2-560, Bio-Stat Research). Maintaining the pressure (2000 hPa) and flow (80 sccm) constant, one produces a standard of 700 ppbv H_2O_2. A fraction of this flow (22 sccm) is injected into the flow tube and diluted by the either scrubbed ambient air or zero air (1800 sccm) to give a concentration of 8 ppbv H_2O_2 in the ion flow tube. This source produces a constant ($\pm 10\%$) mass flow of H_2O_2 over several months, without need to refresh the UHP. The sensitivity for other species (e.g., HCN and PAA) was inferred from laboratory determination of the relative calibration factors for these compounds compared to the standards used in flight.
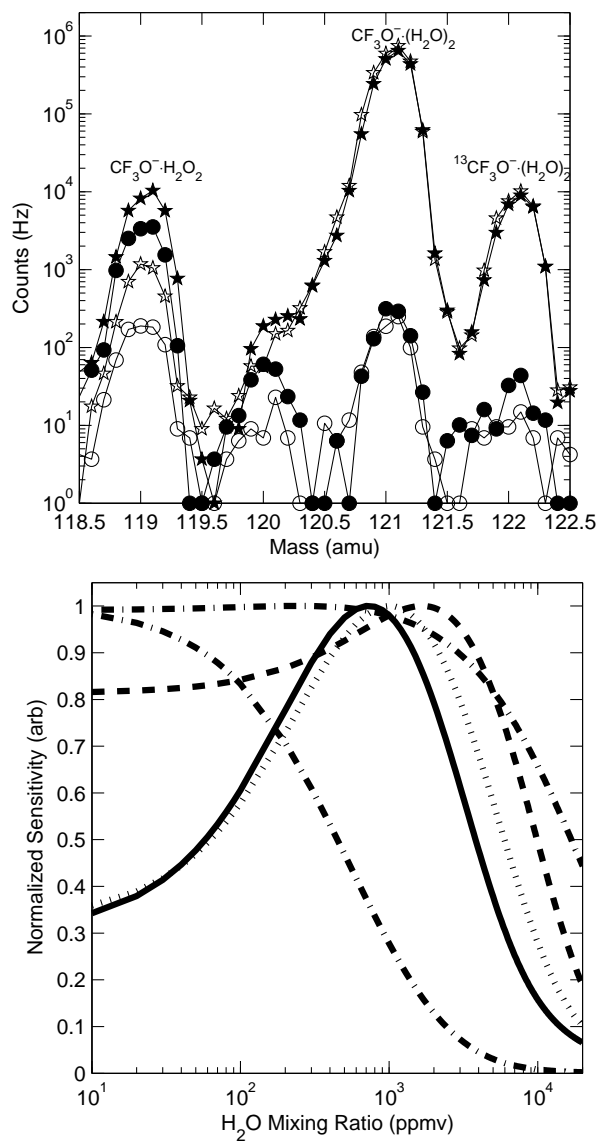
Figure 2.3 – (Top) Mass 119 signal as a function of $[H_2O_2]$ for several H_2O concentrations: plus $[H_2O]$) 10 ppmv, square $[H_2O]$) 1000 ppmv, circle $[H_2O]$) 5000 ppmv, and triangle $[H_2O]$) 10000 ppmv. (Bottom) Normalized signal for mass 119 (solid-thick), 161 (dotted), 112 (dashed), 82 (dash-dot), and mass 133 (solid-thin) signal as a function of $[H_2O]$, for a constant addition of H_2O_2, PAA, HCN, HNO_3, and MHP, respectively.

2.5.2 Water sensitivity

Accounting for the change in sensitivity with variation in the water vapor mixing ratio is critical for accurate measurements. During INTEX-NA, the ion flow tube air was essentially undiluted ambient air. Water vapor mixing ratios varied from more than 3% to as low as 10 ppmv, resulting in very large changes in the sensitivity for all analytes. We account for these changes in sensitivity by using a combination of the periodic calibrations and measurements of the ambient H_2O mixing ratio by a separate instrument on the DC-8, the tunable diode laser hygrometer (Podolske et al., 2003). In the future, we plan to use a 1:4 mix of ambient air to dry nitrogen to avoid H_2O mixing ratios greater than 1%. Above 1% humidity, we observe substantial hydrolysis of our reagent ion. The hydrolysis of the reagent ion yields many product ions that clutter the mass spectrum.

2.5.3 Backgrounds

Even in the absence of analytes, ion signals are often present at masses of interest. These arise from interferences from mass analogs as well as H_2O clusters of other ions present in the flow. We use two methods in flight to estimate these background signals. In the first, ambient air is "scrubbed" by passing it through a two-stage filter composed of (1) alumina pellets coated with palladium (Sigma-Aldrich) and (2) nylon wool coated with sodium bicarbonate before entering the flow tube. This filter quantitatively removes H_2O_2 and organic peroxides (as well as most acids). In the second, high-purity zero air from a cylinder (Air Liquide) is added to the flow tube instead of ambient air. Neither method is ideal. Although the filter scrubs targeted analytes from the air, it may also scrub the species which cause mass analog background signals. The bottled air measures the instrument background signal but does not give any information about mass analog backgrounds in ambient air. Also, both methods, generally, alter the humidity in the flow tube, which, as discussed above, directly affects the sensitivity for these gases. Fortunately, for many analytes, including H_2O_2 and PAA, these backgrounds tend to be relatively constant (at a given water vapor concentration). For CH_3OOH, backgrounds at mass 133 ($Si(CH_3)_2F_3^- \cdot H_2O$) coupled with low sensitivity due to high water concentrations in the flow tube prevented us from making make usable measurements of this compound during INTEX-NA (see Table 2.1, Supporting Information, for a summary of sensitivities and backgrounds).

2.5.4 Measurement of additional compounds using CF_3O^-

In addition to its clustering with ROOH, CF_3O^- clusters efficiently with other compounds that have historically been difficult to detect and quantify. During INTEX-NA, our instrument measured HCN and HNO_3 as well as H_2O_2 and PAA, while organic acids, though quantifiable in principle, could not be measured effectively due to background issues. In addition, preliminary work in our laboratory demonstrates that many of the products of isoprene oxidation can be measured with high sensitivity using CF_3O^- clustering chemistry. These include isoprene-hydroxy-hydroperoxide, isoprene-hydroxy-nitrate, and hydroxy-acetone. Additional laboratory tests have confirmed this method to be sensitive for measuring compounds of the form $RCH(OOH)CH_2(OH)$, $RC(O)CH_2OH$, and $RCH(ONO_2)CH_2OH$. A paper describing these experiments on isoprene oxidation products will be forthcoming.

2.6 Comparison with HPLC method

During the INTEX-NA field campaign, the CIMS instrument measured H_2O_2 and PAA with an approximate 7 and 3% duty cycle, respectively. The remainder of the time the instrument measured other compounds (e.g., HNO_3 and HCN), backgrounds, standards, and the reagent ion and its water clusters, which are necessary for data reduction. This field experiment provided over 28 h of direct comparison of this new peroxide technique with observations from the University of Rhode Island HPLC-fluorescence instrument (Lee et al., 1995). These flights spanned conditions from the polluted boundary layer to the remote free troposphere and lower stratosphere.

Figure 2.4 shows the comparison for H_2O_2 and PAA from these two instruments. Overall, agreement is quite good for both species. A total of 89 and 92% of the observations for H_2O_2 and PAA, respectively, lie within experimental uncertainty. The correlation for the PAA comparison ($r^2 = 0.60$) is somewhat less than for H_2O_2 ($r^2 = 0.82$), possibly due to the following: (1) There were 45% fewer comparisons for PAA than H_2O_2. (2) The dynamic range was significantly smaller for PAA than H_2O_2. (3) The HPLC detection limit was significantly higher for PAA than for H_2O_2. The uncertainty in CIMS measurements during INTEX-NA were 35% for H_2O_2 and 35% for PAA and are primarily determined by uncertainties in backgrounds and our water sensitivity determination. Agreement at both low– and high–humidity demonstrates that our parametrization of the humidity dependence of the instrument's sensitivity is adequate for water mixing ratios ranging from less than 10 ppmv up to 2% (see Figure 2.5).
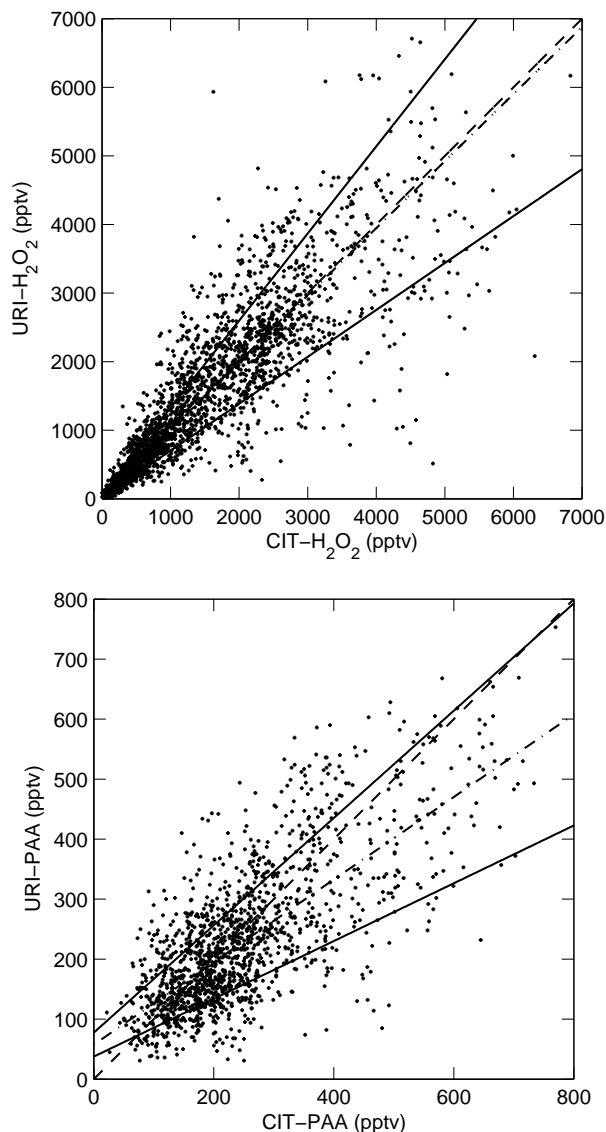
Figure 2.4 – (Top) University of Rhode Island H_2O_2 vs. Caltech CIMS H_2O_2 both measured aboard NASA DC-8 during INTEX-NA. A total of 89% of the measurements agree within uncertainties after averaging the faster measurement to the slower time base for a total of 2793 comparable observations. The dash-dot line is the Matlab robust fit ($y = mx + b$) to filtered data (+) with $m = 0.98$, $b = 32$ pptv, and $r^2 = 0.82$, and the dashed line is 1-1 line. Solid lines are error limits about dash-dot line. The data were filtered (open circles, rejected [8%], plus symbols [+], accepted [91%]) using a first-derivative cutoff (17 pptv/s) in the time domain for each set of data to remove outliers. The reasons for using the derivative cutoff are 2-fold: (1) there are errors associated with averaging the fast time base to the slower one, and these are more prevalent when the analyte concentration is changing rapidly, and (2) the Caltech CIMS measurements occasionally were affected by short periods of electronic noise. Both error sources are captured by the derivative cutoff. (Bottom) Same comparison as (A), but for PAA measurements. A total of 92% of measurements lie within uncertainties for the 1504 comparable observations. The first derivative cutoff (6 pptv/s) removed 1% of the data. Solid lines are error limits about dash-dot line; the dash-dot line is Matlab robust fit ($y = mx + b$) to the filtered data (+) with $m = 0.69$, $b = 56$ pptv, and $r^2 = 0.60$. The dashed line is 1-1 line.

Table 2.1 – Typical sensitivities and backgrounds for several hydroperoxides measured by the Caltech CIMS at several water levels.

	Sensitivity (cts s^{-1} pptv^{-1})			Background (cts s^{-1})		
Ambient [H$_2$O] (ppmv)	H$_2$O$_2$	PAA	MHP	H$_2$O$_2$	PAA	MHP
10^2	15	15	12	120	80	640
10^3	25	17	4	400	120	1000
10^4	4	9	0.1	1000	200	1500

2.7   Conclusions and summary

CIMS using CF$_3$O$^-$ as a reagent ion has been successfully demonstrated to measure hydroperoxides H$_2$O$_2$ and PAA with good sensitivity (25 pptv for H$_2$O$_2$, 25 pptv for PAA) and time resolution ($<$ 1 s). This fast technique will enhance studies of heterogeneous air masses and is particularly useful for airborne sampling. High temporal resolution aircraft measurements of hydroperoxides will contribute to the study of many important atmospheric processes including convective transport, cloud processing, and aerosol aging. Further development of this method should increase its applicability to other important compounds, such as CH$_3$OOH, HMHP, and the products of isoprene oxidation.

2.8   Supporting information

As supporting information we present Table 2.1 containing information regarding the average sensitivities and backgrounds for the CIMS technique at several water levels as well as Figure 2.5 showing the ratio of the URI(H$_2$O$_2$)/CIT(H$_2$O$_2$) measurements from INTEX-NA as a function of water mixing ratio.

2.9   Acknowledgments

Figure 2.5 – Ratio of URI-H_2O_2/CIT-H_2O_2 as a function of water. The dash-dot line is robust fit to data ($m = 0.00$, $b = 1.07$)

by the EPA. The views expressed in this document are solely those of the authors and the EPA does not endorse any products or commercial services mentioned in this publication.

Bibliography

Amelynck, C., Schoon, N., and Arijs, E.: Gas phase reactions of CF_3O^- and $CF_3O^- \cdot H_2O$ with nitric, formic, and acetic acid, Int. J. Mass. Spectrom., 203, 165–175, 2000a.

Amelynck, C., Van Bavel, A. M., Schoon, N., and Arijs, E.: Gas phase reactions of CF_3O^- and $CF_3O^- \cdot H_2O$ and their relevance to the detection of stratospheric HCl, Int. J. Mass. Spectrom., 202, 207–216, 2000b.

Cantrell, C. A., Edwards, G. D., Stephens, S., Mauldin, L., Kosciuch, E., Zondlo, M., and Eisele, F.: Peroxy radical observations using chemical ionization mass spectrometry during TOPSE, J. Geophys. Res.-Atmos., 108, doi:10.1029/2002JD002715, 2003.

Claeys, M., Wang, W., Ion, A. C., Kourtchev, I., Gelencser, A., and Maenhaut, W.: Formation of secondary organic aerosols from isoprene and its gas-phase oxidation products through reaction with hydrogen peroxide, Atmos. Environ., 38, 4093–4098, doi:10.1016/j.atmosenv.2004.06.001, 2004.

Fahey, D. W., Gao, R. S., Carslaw, K. S., Kettleborough, J., Popp, P. J., Northway, M. J., Holecek, J. C., Ciciora, S. C., McLaughlin, R. J., Thompson, T. L., Winkler, R. H., Baumgardner, D. G., Gandrud, B., Wennberg, P. O., Dhaniyala, S., McKinney, K., Peter, T., Salawitch, R. J., Bui, T. P., Elkins, J. W., Webster, C. R., Atlas, E. L., Jost, H., Wilson, J. C., Herman, R. L., Kleinbohl, A., and von Konig, M.: The detection of large HNO_3-containing particles in the winter arctic stratosphere, Science, 291, 1026–1031, 2001.

Furutani, H. and Akimoto, H.: Development and characterization of a fast measurement system for gas-phase nitric acid with a chemical ionization mass spectrometer in the marine boundary layer, J. Geophys. Res.-Atmos., 107, doi:10.1029/2000JD000269, 2002.

Gab, S., Turner, W. V., Wolff, S., Becker, K. H., Ruppert, L., and Brockmann, K. J.: Formation of alkyl and hydroxyalkyl hydroperoxides on ozonolysis in water and in air, Atmos. Environ., 29, 2401–2407, 1995.

Heikes, B. G., Kok, G. L., Walega, J. G., and Lazrus, A. L.: H_2O_2, O_3 and SO_2 measurements in the lower troposphere over the eastern-United-States during Fall, J. Geophys. Res.-Atmos., 92, 915–931, 1987.

Huey, L. G., Villalta, P. W., Dunlea, E. J., Hanson, D. R., and Howard, C. J.: Reactions of CF_3O^- with atmospheric trace gases, J. Phys. Chem., 100, 190–194, 1996.

Jaegle, L., Jacob, D. J., Brune, W. H., Faloona, I., Tan, D., Heikes, B. G., Kondo, Y., Sachse, G. W., Anderson, B., Gregory, G. L., Singh, H. B., Pueschel, R., Ferry, G., Blake, D. R., and Shetter, R. E.: Photochemistry of HO_x in the upper troposphere at northern midlatitudes, J. Geophys. Res.-Atmos., 105, 3877–3892, 2000.

Kok, G. L., Heikes, B. G., Lind, J. A., and Lazrus, A. L.: A brief survey of methods for the measurement of gas-phase hydrogen-peroxide, Atmos. Environ., 23, 283, 1989.

Kormann, R., Fischer, H., Gurk, C., Helleis, F., Klupfel, T., Kowalski, K., Konigstedt, R., Parchatka, U., and Wagner, V.: Application of a multi-laser tunable diode laser absorption spectrometer for atmospheric trace gas measurements at sub-ppbv levels, Spectrochim. Acta A, 58, 2489–2498, 3rd International Conference on Tunable Diode Laser Spectroscopy, Zermatt, Switzerlandp, JUL 08-12, 2001, 2002.

Lee, M., Noone, B. C., O'Sullivan, D., and Heikes, B. G.: Method for the collection and HPLC analysis of hydrogen-peroxide and C_1 and C_2 hydroperoxides in the atmosphere, J. Atmos. Ocean. Tech., 12, 1060–1070, 1995.

Lee, M. H., Heikes, B. G., and O'Sullivan, D. W.: Hydrogen peroxide and organic hydroperoxide in the troposphere: A review, Atmos. Environ., 34, 3475–3494, 2000.

Madronich, S.: Personal communication, nCAR, 2005.

Marcy, T. P., Gao, R. S., Northway, M. J., Popp, P. J., Stark, H., and Fahey, D. W.: Using chemical ionization mass spectrometry for detection of HNO_3, HOl, and $CIONO_2$ in the atmosphere, Int. J. Mass. Spectrom., 243, 63–70, doi:10.1016/j.ijms.2004.11.012, 2005.

Marklund, S.: Simultaneous determination of bis(hydroxymethyl)-peroxide (BHMP), hydroxymethylhydroperoxide (HMP), and (H_2O_2) with titanium IV – Equilibria between peroxides and stabilities of HMP and BHMP at physiological conditions, Acta Chem. Scand., 25, 3517, 1971.

Mauldin, R. L., Cantrell, C. A., Zondlo, M. A., Kosciuch, E., Ridley, B. A., Weber, R., and Eisele, F. E.: Measurements of OH, H_2SO_4, and MSA during Tropospheric Ozone Production About the Spring Equinox (TOPSE), J. Geophys. Res.-Atmos., 108, doi:10.1029/2002JD002295, 2003.

Messer, B. M., Stielstra, D. E., Cappa, C. D., Scholtens, K. W., and Elrod, M. J.: Computational and experimental studies of chemical ionization mass spectrometric detection techniques for atmospherically relevant peroxides, Int. J. Mass. Spectrom., 197, 219–235, 2000.

Miller, T. M., Ballenthin, J. O., Meads, R. F., Hunton, D. E., Thorn, W. F., Viggiano, A. A., Kondo, Y., Koike, M., and Zhao, Y. J.: Chemical ionization mass spectrometer technique for the measurement of HNO_3 in air traffic corridors in the upper troposphere during the SONEX campaign, J. Geophys. Res.-Atmos., 105, 3701–3707, 2000.

Neuman, J. A., Huey, L. G., Dissly, R. W., Fehsenfeld, F. C., Flocke, F., Holecek, J. C., Holloway, J. S., Hubler, G., Jakoubek, R., Nicks, D. K., Parrish, D. D., Ryerson, T. B., Sueper, D. T., and Weinheimer, A. J.: Fast-response airborne in situ measurements of HNO_3 during the Texas 2000 Air Quality Study, J. Geophys. Res.-Atmos., 107, doi:10.1029/2001JD001437, 2002.

Nowak, J. B., Davis, D. D., Chen, G., Eisele, F. L., Mauldin, R. L., Tanner, D. J., Cantrell, C., Kosciuch, E., Bandy, A., Thornton, D., and Clarke, A.: Airborne observations of DMSO, DMS, and OH at marine tropical latitudes, Geophys. Res. Lett., 28, 2201–2204, 2001.

Nowak, J. B., Huey, L. G., Eisele, F. L., Tanner, D. J., Mauldin, R. L., Cantrell, C., Kosciuch, E., and Davis, D. D.: Chemical ionization mass spectrometry technique for detection of dimethylsulfoxide and ammonia, J. Geophys. Res.-Atmos., 107, doi:10.1029/2001JD001058, 2002.

Penkett, S. A., Jones, B. M. R., Brice, K. A., and Eggleton, A. E. J.: Importance of atmospheric ozone and hydrogen-peroxide in oxidizing sulfur-dioxide in cloud and rainwater, Atmos. Environ., 13, 123–137, 1979.

Penkett, S. A., Bandy, B. J., Reeves, C. E., McKenna, D., and Hignett, P.: Measurements of peroxides in the atmosphere and their relevance to the understanding of global tropospheric chemistry, Faraday Discuss., 100, 155–174, Faraday Disussions on Atmospheric Chemistry – Measurements, Mechanics and Models, E. Anglia, England, Apr 19–21, 1995.

Podolske, J. R., Sachse, G. W., and Diskin, G. S.: Calibration and data retrieval algorithms for the NASA Langley/Ames Diode Laser Hygrometer for the NASA Transport and Chemical Evolution Over the Pacific (TRACE-P) mission, J. Geophys. Res.-Atmos., 108, doi:10.1029/2002JD003156, 2003.

Reiner, T., Mohler, O., and Arnold, F.: Improved atmospheric trace gas measurements with an

aircraft-based tandem mass spectrometer: Ion identification by mass-selected fragmentation studies, J. Geophys. Res.-Atmos., 103, 31 309–31 320, 1998.

Slemr, F., Harris, G. W., Hastie, D. R., Mackay, G. I., and Schiff, H. I.: Measurement of gas-phase hydrogen-peroxide in air by tunable diode-laser absorption-spectroscopy, J. Geophys. Res.-Atmos., 91, 5371–5378, 1986.

Slusher, D. L., Pitteri, S. J., Haman, B. J., Tanner, D. J., and Huey, L. G.: A chemical ionization technique for measurement of pernitric acid in the upper troposphere and the polar boundary layer, Geophys. Res. Lett., 28, 3875–3878, 2001.

Vaghjiani, G. L. and Ravishankara, A. R.: Kinetics and mechanism of OH reaction with CH_3OOH, J. Phys. Chem., 93, 1948–1959, 1989.

Viggiano, A. A., Hunton, D. E., Miller, T. M., and Ballenthin, J. O.: *In situ* measurements of hydrogen cyanide in the upper troposphere/lower stratosphere during Arctic Spring 2000, J. Geophys. Res.-Atmos., 108, doi:10.1029/2001JD001033, 2002.

Warneke, C., Holzinger, R., Hansel, A., Jordan, A., Lindinger, W., Poschl, U., Williams, J., Hoor, P., Fischer, H., Crutzen, P. J., Scheeren, H. A., and Lelieveld, J.: Isoprene and its oxidation products methyl vinyl ketone, methacrolein, and isoprene related peroxides measured online over the tropical rain forest of Surinam in March 1998, J. Atmos. Chem., 38, 167–185, 2001.

Washenfelder, R. A., Roehl, C. M., McKinney, K. A., Julian, R. R., and Wennberg, P. O.: A compact, lightweight gas standards generator for permeation tubes, Rev. Sci. Instrum., 74, 3151–3154, doi:10.1063/1.1570949, 2003.

Wennberg, P. O., Hanisco, T. F., Jaegle, L., Jacob, D. J., Hintsa, E. J., Lanzendorf, E. J., Anderson, J. G., Gao, R. S., Keim, E. R., Donnelly, S. G., Del Negro, L. A., Fahey, D. W., McKeen, S. A., Salawitch, R. J., Webster, C. R., May, R. D., Herman, R. L., Proffitt, M. H., Margitan, J. J., Atlas, E. L., Schauffler, S. M., Flocke, F., McElroy, C. T., and Bui, T. P.: Hydrogen radicals, nitrogen radicals, and the production of O_3 in the upper troposphere, Science, 279, 49–53, 1998.

Zondlo, M. A., Mauldin, R. L., Kosciuch, E., Cantrell, C. A., and Eisele, F. L.: Development and characterization of an airborne-based instrument used to measure nitric acid during the NASA Transport and Chemical Evolution over the Pacific field experiment, J. Geophys. Res.-Atmos., 108, doi:10.1029/2002JD003234, 2003.

Chapter 3

Chemical ionization tandem mass spectrometer for the *in situ* measurement of methyl hydrogen peroxide*

3.1 Abstract

A new approach for measuring gas-phase methyl hydrogen peroxide (MHP, CH_3OOH) utilizing chemical ionization mass spectrometry is presented. Tandem mass spectrometry is used to avoid mass interferences that hindered previous attempts to measure atmospheric CH_3OOH with CF_3O^- clustering chemistry. CH_3OOH has been successfully measured *in situ* using this technique during both airborne and ground-based campaigns. The accuracy and precision for the MHP measurement are a function of water vapor mixing ratio. Typical precision at 500 pptv MHP and 100 ppmv H_2O is 80 pptv 2 sigma for a 1 s integration period. The accuracy at 100 ppmv H_2O is estimated to be better than 40%. Chemical ionization tandem mass spectrometry shows considerable promise for the determination of *in situ* atmospheric trace gas mixing ratios where isobaric compounds or mass interferences impede accurate measurements.

3.2 Introduction

Hydrogen peroxide (H_2O_2) and methyl hydrogen peroxide (MHP, CH_3OOH) are the two most abundant hydroperoxides in the troposphere. The formation of H_2O_2 and CH_3OOH occurs via reactions R3.1 and R3.2.

$$HO_2 + HO_2 \rightarrow H_2O_2 + O_2 \tag{R3.1}$$

$$CH_3O_2 + HO_2 \rightarrow CH_3OOH + O_2 \tag{R3.2}$$
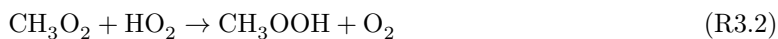
Primary loss mechanisms for both hydroperoxides include photolysis and reaction with OH

$$H_2O_2 + hv \rightarrow 2\,OH \tag{R3.3}$$

$$CH_3OOH + hv \rightarrow CH_3O + OH \tag{R3.4}$$

$$CH_3O + O_2 \rightarrow CH_2O + HO_2 \tag{R3.5}$$

$$H_2O_2 + OH \rightarrow HO_2 + H_2O \tag{R3.6}$$

$$CH_3OOH + OH \rightarrow CH_3OO + H_2O \tag{R3.7}$$

$$CH_3OOH + OH \rightarrow CH_2O + OH + H_2O\,(via\,CH_2OOH) \tag{R3.8}$$
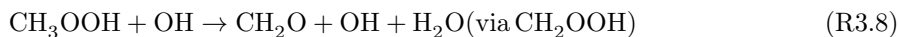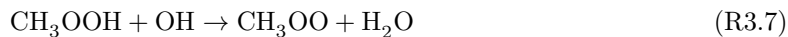
H_2O_2 is also lost via wet and dry deposition (O'Sullivan et al., 1996; Valverde-Canossa et al., 2006). The transport of H_2O_2 and CH_3OOH and the subsequent release of HO_x and CH_2O (a HO_x precursor) necessitates the inclusion of hydroperoxides in HO_x and O_3 budgets, particularly for the upper troposphere (UT) (Jacob et al., 1997; Prather and Jacob, 1997; Jaegle et al., 2001). Convective systems rapidly transport boundary layer air up into the UT, affecting the chemical balance of the UT through enhancements of photochemically active species, including hydroperoxides (Jaegle et al., 2001; Barth et al., 2007). H_2O_2 has a higher removal rate via convective processing than CH_3OOH due to its much larger Henry's Law coefficient 8.33×10^4 and 311 M atm^{-1}, respectively, at 298 K (O'Sullivan et al., 1996). Consequently, an increase in CH_3OOH relative to H_2O_2 can be used to identify recent convective activity (Heikes et al., 1996; Cohan et al., 1999; Kim et al., 2002).

The most common technique for the measurement of atmospheric gas phase H_2O_2 and CH_3OOH involves transferring the hydroperoxides into the aqueous phase followed by chemical derivatization and detection via fluorescence (Lee et al., 2000). Separation of the constituent hydroperoxides by high-performance liquid chromatography is often performed on the aqueous sample before derivatization. Drawbacks to the fluorescence technique include a slow instrumental time response often minutes and the potential for interference from aqueous chemistry, e.g., hydroperoxide reaction with SO_2 (Lee et al., 2000). We have successfully utilized the chemical ionization mass spectrometry (CIMS) for the *in situ* detection of H_2O_2 as described in Crounse et al. (2006) with an instrument time response of 1 s and a possible data rate of 8 Hz or higher. The measurement of H_2O_2 and other trace species by the Caltech single quadrupole CIMS instrument using CF_3O^- negative ion chemistry followed from previous works with similar ion chemistry (Huey et al., 1996; Amelynck et al., 2000b,a). The negative ion cluster chemistry of CF_3O^- with H_2O_2 provides a signal at a mass-to-charge ratio $m/z = 119$, unencumbered by significant mass interferences. However, the detection of CH_3OOH by the same ion chemistry is complicated by a background signal at $m/z = 133$ that is unrelated to CH_3OOH (Crounse et al., 2006).

We have developed a new CIMS instrument for the detection of CH_3OOH and other trace species that utilizes the same ion chemistry while being largely immune to mass interferences described previously (Crounse et al., 2006). The new instrument employs tandem mass spectrometry MS to differentiate isobaric ionized species by decomposing the parent ion into daughter fragments that uniquely identify each species if their respective daughter ion spectra are distinct. The tandem MS or triple quadrupole instrument has participated in three aircraft campaigns: aboard the NSF C-130 during MILAGRO/INTEX-B in 2006, and aboard the NASA DC-8 during TC4 in 2007 and

ARCTAS in 2008 see Fast et al. (2007), Toon et al. (2010), and Jacob et al. (2010), respectively, for mission details. The tandem MS instrument also participated in the ground-based summer 2009 BEARPEX campaign. In this paper, we describe the tandem MS CIMS instrument as well as present *in situ* data showing the benefit of tandem MS for the measurement of methyl hydrogen peroxide by CIMS.

3.3 Instrument description

The Caltech triple quadrupole CIMS instrument consists of a custom chemical ionization source coupled to the mass spectrometer from a commercial Varian 1200 GCMS system Palo Alto, CA. The ion source and ion chemistry have been described previously for the Caltech single quadrupole CIMS instrument (Crounse et al., 2006), so only a brief description is included below. The Varian 1200 contains three quadrupoles: two used for mass filtration and one for collision-induced dissociation. The instrument can be operated in single MS or tandem MS (MSMS) mode, although in flight, it is typically run only in MSMS mode due to the time required to switch between the two modes. The instrument can also be operated in a positive ion mode similar to a proton transfer reaction mass spectrometer, though this ability has only been exploited in the laboratory (Paulot et al., 2009b) and not in field experiments.

A schematic of the Caltech triple quadrupole CIMS instrument is shown in Fig. 3.1. The DC-8 aircraft inlet is described in Crounse et al. (2006) and is shown schematically in Fig. 3.1 (A–C). The triple quadrupole CIMS samples from one of the two bypass flows from the single quadrupole instrument Y-block (Crounse et al., 2006, Fig. 1D). From the Y-block, the flow travels through 1.57 m of 2.54 cm outer diameter OD Teflon perfluoroalkoxy polymer PFA tubing (Fig. 3.1, E) at a flow of 10 standard liters per second to a T-block (Fig. 3.1, F) mounted atop the mass spectrometer. The majority of the flow into the T-block exits as bypass flow through two ports on opposite sides of the block, as only a small portion 600 standard cubic centimeters per minute SCCM is analytically sampled. The sample flow enters the flow tube through an adjustable pinhole orifice plate (Fig. 3.1, G) that regulates the flow via software control of a stepper motor to maintain a constant 35 hPa pressure and approximately constant analytical sample mass flow in the flow tube. The 2.54 cm OD, 11.7 cm long glass flow tube (Fig. 3.1, H) connects the T-block to the ion source block, delivering the sample flow to the ion/molecule reaction region (Fig. 3.1, J). The flow tube is coated with a fluoropolymer (Fluoropel PFC 801A, Cytonix, Beltsville, MD) to minimize the wall uptake and release of water and other analytes. The analytical flow is diluted 1:2 by the addition of a
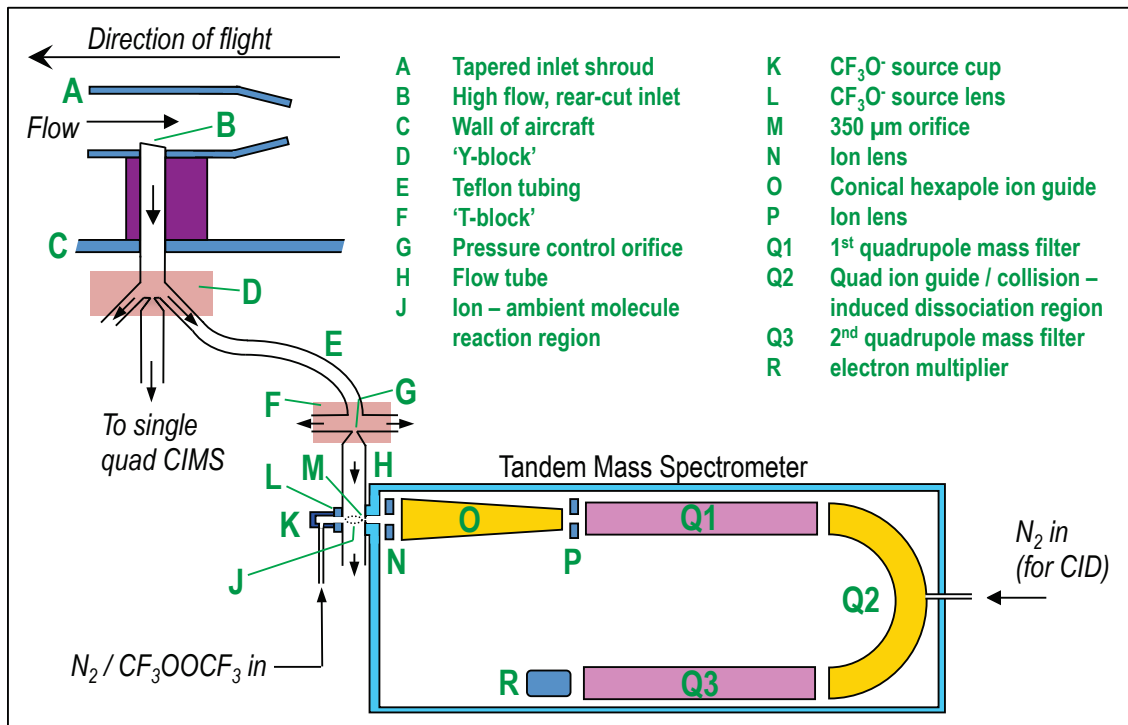
Figure 3.1 – Triple quadrupole CIT CIMS instrument schematic aboard the NASA DC-8.

constant 1.2 standard liters per minute flow of ultrahigh purity (UHP) N_2 on the low-pressure side of the T-block. The decrease in water mixing ratio upon dilution improves the instrument sensitivity for MHP, which exhibits monotonically decreasing sensitivity with increasing water and decreases instrumental backgrounds from water clusters. Calibration gases are also introduced at the lowpressure side of the T-block during calibration cycles. All flow controllers used in the instrument are piezoelectricactuated with all-metal seals (HORIBA STEC, Austin, TX).

The reagent ion for the chemical ionization is produced by flowing 400 SCCM of 10 ppmv CF_3OOCF_3 in UHP N_2 into a cylindrical source cup (Fig. 3.1, K) lined with a foil containing Po-210 (NRD LLC, 4.5 mCi). Alpha particles emitted by the Po-210 begin a series of reactions that ultimately yield the reagent ion CF_3O^-. A 30 V potential between the source cup and source lens (Fig. 3.1, L) accelerates CF_3O^- ions into the ion/molecule reaction region where they can react with analytes. CH_3OOH forms a cluster with the reagent ion

$$CF_3O^- + CH_3OOH + M \rightarrow CF_3O^- \cdot CH_3OOH + M, \qquad (R3.9)$$

where M is a N_2 or an O_2 molecule. Typical voltages for the source cup and source lens are 330

and 300 V, respectively, with the orifice into the mass spectrometer at 0 V. The potential between the source lens and the orifice directs ions toward the orifice, moving the ions perpendicular to the sample flow. Note that all voltages listed below are relative to ground rather than to adjacent ion optics.

Product ions enter the mass spectrometer through the 350 μm orifice (Fig. 3.1, M), passing through a lens (Fig. 3.1, N) before reaching the conical hexapole ion guide (Fig. 3.1, O). The lens serves to shield the orifice from the hexapole and both the lens and the orifice are held at 0 V. The hexapole is mounted in the chamber that originally housed the ionization source for the commercial instrument. The conical hexapole is driven at 1.638 MHz by the radio frequency (RF) supply used to operate the original hexapole ion guide in the Varian 1200 and typically is biased by +1.2 V.

The conical hexapole is composed of six 16.6 cm long conical stainless steel rods with end diameters of 7.1 and 2.4 mm. The rods are arranged in a circular pattern that begins with an inner diameter (ID) of 14.2 mm for the larger diameter rod ends near the lens. The ID of the hexapole narrows to 4.8 mm at the smaller diameter rod ends. The ion beam exits the hexapole chamber via a 4 mm aperture (Fig. 3.1, P), held at +2.4 V for $m/z = 133 \rightarrow$ m/z=85, as are all of the subsequent ion optic voltages. The pressure in the hexapole chamber is typically 4.7×10^{-3} hPa.

The first mass selection is performed by the first quadrupole mass filter (Fig. 3.1, Q1). Q1 is usually set to a 0.7 amu full-width half maximum FWHM mass resolution with an average potential of +3.4 V. Ions that are selected by Q1 pass through to the collision-induced dissociation CID chamber (Fig. 3.1, Q2), consisting of a partially enclosed rf-only quadrupole with a small flow of N_2 that yields a CID pressure of 2.7×10^{-3} hPa. Collisions of ions with N_2 in Q2 cause fragmentation of the analyte ions with the fragment yield dependent on the CID pressure and the collision energetics. The third quadrupole (Fig. 3.1, Q3), with a typical mass resolution of 1.5 amu FWHM, filters for a specific daughter ion produced by the CID. The voltage between Q1 and Q2 is adjusted to optimize the yield of the desired daughter ion. In the case of CH_3OOH, Q2 is set to +6.4 V. CID decomposes the ion cluster

$$CF_3O^- \cdot CH_3OOH(m/z = 133) + M \rightarrow CF_3O^-(m/z = 85) + CH_3OOH + M, \qquad (R3.10)$$

with Q3 passing $m/z = 85$ to the electron multiplier detector (Fig. 3.1, R). Q3 is held at +7.0 V and the voltage across the electron multiplier is 2 kV. The pressure in the main chamber is 6.7×10^{-5} hPa while the CID gas is flowing. The pumping on the hexapole chamber and the main chamber is performed by a split flow Edwards EXT200/200H turbomolecular pump (Tewksbury, MA).

Data for the triple quadrupole CIMS instrument are collected on two computer systems. Control and data collection for the mass spectrometer are conducted by the software provided by Varian, along with supplemental scripts written in-house. Gas flows, ion source voltages, pump and valve controls, and environmental parameters are controlled and recorded by a Diamond Systems Hercules II (Mountain View, CA) running the QNX real-time operating system version 4.25 with custom software. Communication between the two computer systems, necessary for synchronizing data collection, is achieved via 3 bits from QNX to Windows that enable/disable MS data collection, select source polarity, and select scan or hop mode for m/z selection; 2 bits from Windows to QNX indicate the status of MS data collection.

3.4   Instrument operation

The data collection rate for a given m/z is dependent on the number of other masses monitored and the amount of time spent on each mass. The time spent on a given mass varies from mass to mass, between 0.125 and 1 s in multiples of 0.125 s, and was chosen in consideration of the signal to noise ratio at that mass. For example, CH_3OOH data might be collected for 1 s every 30 s. The base unit of 0.125 s is arbitrary. It is important to note that data reported from instruments operated in this manner contain no information about a given mass in the air sampled while the instrument is not measuring that mass.

The electron multiplier in the Varian 1200 provides an analog signal to an analog-to-digital converter ADC for data collection, in contrast to the single quadrupole CIMS instrument where the electron multiplier is operated in pulse counting mode. Each 0.125 s segment is comprised of 1531 samples of the ADC one every 82 s, which are averaged to give the analog signal in millivolts. The instrument requires the data to be collected over a scan, so the 1531 samples span a 0.1 amu Q3 window centered on the daughter m/z.

A software ion-counting method is used to improve the sensitivity of the instrument at low signal levels. The signal for each of the 1531 samples is compared in the software to a preset threshold and if the signal exceeds the threshold, then a count is recorded. The two subsequent samples are ignored to avoid double-counting the same ion. The number of counts tallied over the 1531 samples is recorded as the raw digital signal per 1/8 s. This digital signal and the analog signal are subjected to postflight data processing before being combined into one data set, as described below.

3.4.1 Backgrounds and in-flight calibrations

The measurement of MHP by single MS is hindered by $m/z = 133$ signal from ions (e.g., $CF_3CO_2^- \cdot HF$ and $Si(CH_3)_2F_3^- \cdot H_2O$) that are produced in the ion source from impurities in the reagent gas CF_3OOCF_3 flow. The measurement of MHP by tandem MS is largely immune from significant instrumental backgrounds because the interfering ions do not yield $m/z = 85$ upon collision-induced dissociation. Instrumental backgrounds are measured on a regular basis with a dry zero every 110 min and an ambient zero every 20 min. During a dry zero, the T-block orifice closes to end sampling of ambient air and the dilution N_2 flow is increased in compensation to maintain 35 hPa in the flow tube. During the ambient zero, the balance of flow is instead provided with ambient air that is first passed through a scrubber consisting of Pd-coated alumina pellets and an annular glass substrate coated with $NaHCO_3$. The scrubber quantitatively removes peroxides while passing H_2O. In-flight calibrations are typically performed every 45 min with an ambient zero flow and every 110 min with a dry zero flow. The in-flight calibration system is described in Crounse et al. (2006). The calibration species typically included are H_2O_2, CH_3OOH, peroxyacetic acid $CH_3C(O)OOH$, and isotopically labeled nitric, formic, and acetic acids (Washenfelder et al., 2003).

3.5 Data analysis

The analog and the digital count data require postcollection processing before the data are analyzed. A counting correction is applied to the digital count data to account for multiple ions arriving at the detector within the same counting window. The analog signal is corrected for detector baseline drift by subtracting a baseline from the analog data. The baseline is obtained by interpolating the analog signal measured when the digital count rate is zero. The data carried forward in the analysis are a combination of the analog and digital count data: digital count data are used up to 200 counts per 1/8 s and the analog data are used when the count rate is higher. Data with 200 counts per 1/8 s are fit to a line and the slope is applied as a scaling factor to the higher-signal analog data before combining the analog and digital data into a single data set, expressed as an ion count. Consecutive 1/8 s data points with the same m/z 8 data points for MHP are then averaged using the combined analog/ digital data. As a consequence, all count rates presented for the tandem MS instrument are in 1/8 s time units.

The data are normalized to the ^{13}C reagent ion signal, taken as $^{13}CF_3O^-(m/z = 86) + {}^{13}CF_3O^- \cdot H_2O(m/z = 104)$. Signal levels at the ^{12}C reagent ion masses ($m/z = 85$ and $m/z = 103$) are too

high to safely measure without decreasing the detector gain. Typical rates for $m/z = 86 \rightarrow m/z=86$ in dry air are 1500 cts per 1/8 s. Normalizing to the reagent ion signal is necessary to correct for changes in reagent ion mixing ratio in the flow tube, as well as changes in instrumental ion throughput (generally $\leq \pm 7\%$). "Normalized ion counts" refer to the data after this correction is applied.

The periodic dry and ambient zero data are used to obtain a background signal for each analyte. The approach used to obtain the background for a given species varies, depending on factors such as the efficiency of the ambient scrubber in removing the species and whether the background signal exhibits a water dependence. For MHP measured by tandem MS, the background signal is small and stable enough that an interpolation of the zero data is sufficient to represent the instrument background. After the background is subtracted, the water-dependent sensitivity curve for the analyte is applied using the water cluster masses $m/z = 104$ and $m/z = 121(^{12}\text{CF}_3\text{O}^- \cdot (\text{H}_2\text{O})_2)$ or the water measurement available for the flight (e.g., the NASA Langley Diode Laser Hygrometer DLH (Podolske et al., 2003)), with a dilution factor applied to account for the decrease from ambient to flow tube humidity. The calculated analyte flow tube mixing ratio is then corrected for dilution to obtain the ambient mixing ratio.

3.6   Laboratory calibrations

Laboratory calibrations for CH_3OOH and H_2O_2 are performed by introducing the output of a stable peroxide source and measuring the ion signal as a function of flow tube water mixing ratio. Figure 3.2 shows the CH_3OOH and H_2O_2 sensitivity curves for the tandem instrument, with ion signal plotted as a function of flow tube water mixing ratio. The ion signal is shown normalized to the ^{13}C reagent ion signal as explained in Sec. 3.5. The details of the peroxide calibrations are enumerated in Crounse et al. (2006). In-flight calibrations are performed using a temperature-controlled diffusion vial as the CH_3OOH source and urea hydrogen peroxide as the H_2O_2 source. The same peroxide sources are used for laboratory calibrations. Additional laboratory calibrations for CH_3OOH are performed with a larger source consisting of CH_3OOH in a 6.4 mm OD glass vial held at room temperature. Dry N_2 is passed over top of the vial and into a single pass optical cell for mixing ratio determination by Fourier transform–IR absorption (Niki et al., 1983). The output of the optical cell is then diluted and introduced into the CIMS flow tube. The output of all CH_3OOH and H_2O_2 sources are determined by a colorimetric technique (Bioxytech H_2O_2-560, Bio-Stat Research).
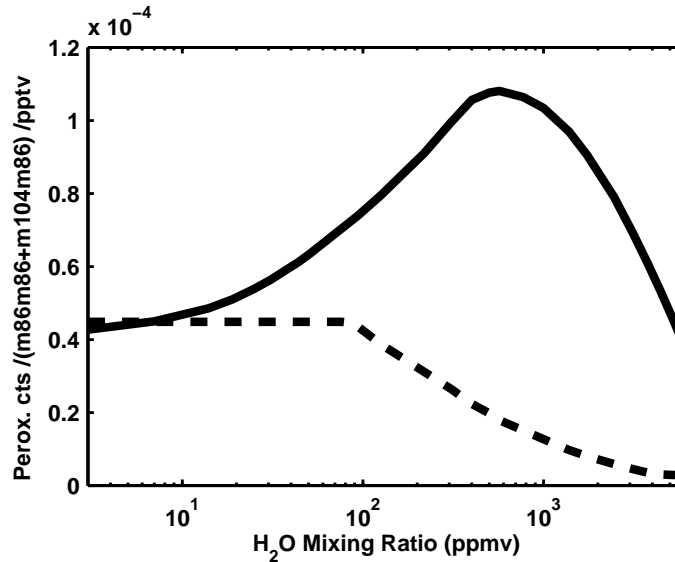
Figure 3.2 – Sensitivity curves for CH_3OOH ($m/z = 133 \rightarrow m/z = 85$) dashed line and H_2O_2 ($m/z = 119 \rightarrow m/z = 85$) solid line as a function of the water mixing ratio in the instrument flow tube.

3.7   Field data

To illustrate the benefit of tandem MS in reducing signal backgrounds, Fig. 3.3 displays the $m/z = 133$ normalized ion counts from both Caltech CIMS instruments and MHP mixing ratios from the tandem MS instrument for one flight April 19, 2008, during the spring ARCTAS campaign. Figures 3.3(a) and 3.3(b) show the normalized counts for $m/z = 133$ (single quadrupole CIMS) and $m/z = 133 \rightarrow m/z=85$ (triple quadrupole CIMS), with the ambient data shown as the line and the zeros shown as dark points (dry zero) and light points (ambient zero). The single quadrupole CIMS collected data at $m/z = 133$ for 1/8 s every 15 s while the triple quadrupole CIMS collected data at $m/z = 133 \rightarrow m/z=85$ for 1 s every 8 s. The zeros for the single quadrupole CIMS are substantial in comparison to the ambient data signal and they vary over the duration of the flight. The zeros for the triple quadrupole CIMS instrument, in contrast, are consistently an order of magnitude lower than the ambient data signal. The difference in the relative magnitude of the zeros for the two instruments makes determining MHP mixing ratios straightforward for the triple quadrupole CIMS and very difficult for the single quadrupole instrument. Triple quadrupole CIMS MHP data for the flight, determined by subtraction of the zeros and application of the water-dependent sensitivity curve, is also shown in Fig. 3.3 (c). Aircraft altitude is included for reference.
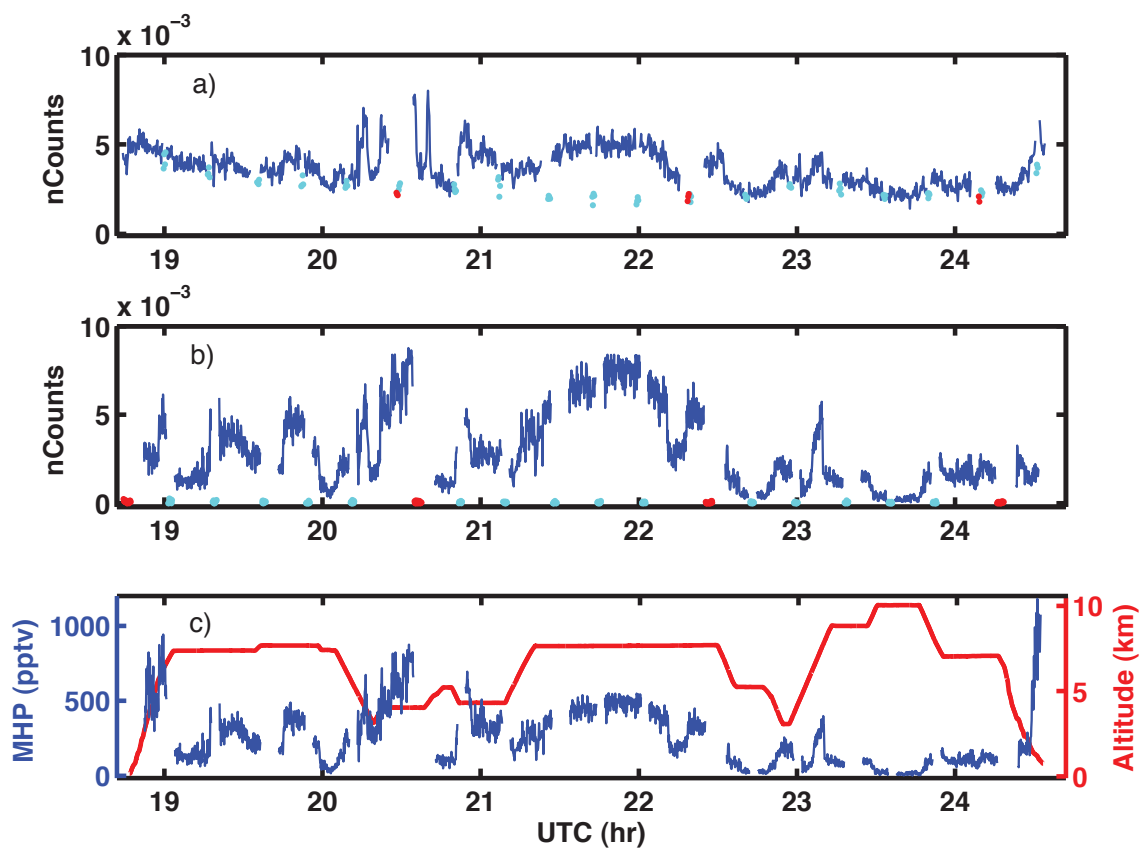
Figure 3.3 – ARCTAS flight of April 19, 2008. Top panel: normalized counts of $m/z = 133$ for the single quadrupole CIMS. The line is data, dark points are dry zero, and light points are ambient zero. Middle panel: normalized counts of $m/z = 133{\rightarrow}m/z = 85$ for the triple quadrupole CIMS. Bottom panel: MHP mixing ratio as determined by the triple quadrupole CIMS thin line and aircraft altitude thick line.

3.8 Accuracy and precision

The uncertainty in the *in situ* measurement of MHP by the triple quadrupole CIMS instrument is dominated by the uncertainty in the water-dependent sensitivity curve used to calculate MHP mixing ratios. Uncertainty in the sensitivity curve is a combination of instrumental precision, accuracy in the absolute quantification of the MHP calibration source, and accuracy in the quantification of the water mixing ratio in the flow tube during calibration. At high flow tube water mixing ratios, the sensitivity of the instrument to MHP is greatly diminished as seen in Fig. 3.2. The lower sensitivity results in greater uncertainty in $[CH_3OOH]_{ambient}$ at high water mixing ratios. Uncertainty in the determination of the flow tube water mixing ratio, during both calibration and ambient air sampling, contributes to the uncertainty in the MHP measurement because the instrument sensitivity to MHP varies with water and any error in $[H_2O]_{flowtube}$ results in an error in $[CH_3OOH]_{ambient}$. For the ARCTAS campaign, we determined the 95% confidence interval measurement uncertainty to be the following function of ambient H_2O:

$$U_{95\%}(DLH) = 50 \text{ pptv} + \begin{cases} 0.40 \times [\text{MHP}] & \text{if } 0 \leq \text{DLH} \leq 230 \text{ ppmv} \\ \frac{-9.1 + 20.8 \times \log_{10}(\text{DLH})}{100} \times [\text{MHP}] & \text{if DLH} > 230 \text{ ppmv}, \end{cases} \quad (3.1)$$

where "DLH" is the ambient water mixing ratio in ppmv as measured by the DLH instrument. The 50 pptv term is included to account for the possible introduction of a bias by the subtraction of the instrumental background and is only significant at low MHP mixing ratios. At higher MHP mixing ratios, the uncertainty ranges from 40% to 80% at high water. Because the measurement uncertainty is dominated by the accuracy, time-averaging data does not reduce the uncertainty. The precision at 500 pptv MHP and 100 ppmv H_2O is 80 pptv (2σ) for a 1 s integration period.

3.9 Conclusions

MHP can be quantified rapidly and precisely with CF_3O^- CIMS using tandem MS to distinguish MHP signal from mass interferences at $m/z = 133$. Like the single quadrupole CIMS instrument, the tandem MS instrument possesses the high sensitivity and rapid time response that is necessary for high spatial resolution *in situ* sampling from aircraft. In addition, the tandem MS instrument opens up the possibility of measuring atmospheric species that are otherwise not measurable, either by separating mass interferences, differentiating between isobaric compounds, or elucidating chem-

ical structures by analyzing parent-daughter fragmentation patterns. The tandem MS instrument achieves a typical precision of 80 pptv (2σ) at 500 pptv MHP and 100 ppmv H_2O for a 1 s integration period and a measurement accuracy better than 40% at 100 ppmv H_2O.

3.10   Acknowledgments

Bibliography

Amelynck, C., Schoon, N., and Arijs, E.: Gas phase reactions of CF_3O^- and $CF_3O^- \cdot H_2O$ with nitric, formic, and acetic acid, Int. J. Mass. Spectrom., 203, 165–175, 2000a.

Amelynck, C., Van Bavel, A. M., Schoon, N., and Arijs, E.: Gas phase reactions of CF_3O^- and $CF_3O^- \cdot H_2O$ and their relevance to the detection of stratospheric HCl, Int. J. Mass. Spectrom., 202, 207–216, 2000b.

Barth, M. C., Kim, S. W., Skamarock, W. C., Stuart, A. L., Pickering, K. E., and Ott, L. E.: Simulations of the redistribution of formaldehyde, formic acid, and peroxides in the 10 July 1996 Stratospheric-Tropospheric Experiment: Radiation, Aerosols, and Ozone deep convection storm, J. Geophys. Res.-Atmos., 112, doi:10.1029/2006JD008046, 2007.

Cohan, D. S., Schultz, M. G., Jacob, D. J., Heikes, B. G., and Blake, D. R.: Convective injection and photochemical decay of peroxides in the tropical upper troposphere: Methyl iodide as a tracer of marine convection, J. Geophys. Res.-Atmos., 104, 5717–5724, 1999.

Crounse, J. D., McKinney, K. A., Kwan, A. J., and Wennberg, P. O.: Measurement of gas-phase hydroperoxides by chemical ionization mass spectrometry, Anal. Chem., 78, 6726–6732, doi:10.1021/ac0604235, 2006.

Fast, J. D., de Foy, B., Rosas, F. A., Caetano, E., Carmichael, G., Emmons, L., McKenna, D., Mena, M., Skamarock, W., Tie, X., Coulter, R. L., Barnard, J. C., Wiedinmyer, C., and Madronich, S.: A meteorological overview of the MILAGRO field campaigns, Atmos. Chem. Phys., 7, 2233–2257, 2007.

Heikes, B., Lee, M. H., Jacob, D., Talbot, R., Bradshaw, J., Singh, H., Blake, D., Anderson, B., Fuelberg, H., and Thompson, A. M.: Ozone, hydroperoxides, oxides of nitrogen, and hydrocarbon budgets in the marine boundary layer over the South Atlantic, J. Geophys. Res.-Atmos., 101, 24 221–24 234, 1996.

Huey, L. G., Villalta, P. W., Dunlea, E. J., Hanson, D. R., and Howard, C. J.: Reactions of CF_3O^- with atmospheric trace gases, J. Phys. Chem., 100, 190–194, 1996.

Jacob, D. J., Prather, M. J., Rasch, P. J., Shia, R. L., Balkanski, Y. J., Beagley, S. R., Bergmann, D. J., Blackshear, W. T., Brown, M., Chiba, M., Chipperfield, M. P., deGrandpre, J., Dignon, J. E., Feichter, J., Genthon, C., Grose, W. L., Kasibhatla, P. S., Kohler, I., Kritz, M. A., Law,

K., Penner, J. E., Ramonet, M., Reeves, C. E., Rotman, D. A., Stockwell, D. Z., VanVelthoven, P. F. J., Verver, G., Wild, O., Yang, H., and Zimmermann, P.: Evaluation and intercomparison of global atmospheric transport models using Rn-222 and other short-lived tracers, J. Geophys. Res.-Atmos., 102, 5953–5970, 1997.

Jacob, D. J., Crawford, J. H., Maring, H., Clarke, A. D., Dibb, J. E., Emmons, L. K., Ferrare, R. A., Hostetler, C. A., Russell, P. B., Singh, H. B., Thompson, A. M., Shaw, G. E., McCauley, E., Pederson, J. R., and Fisher, J. A.: The Arctic Research of the Composition of the Troposphere from Aircraft and Satellites (ARCTAS) mission: design, execution, and first results, Atmos. Chem. Phys., 10, 5191–5212, doi:10.5194/acp-10-5191-2010, 2010.

Jaegle, L., Jacob, D. J., Brune, W. H., and Wennberg, P. O.: Chemistry of HO_x radicals in the upper troposphere, Atmos. Environ., 35, 469–489, 2001.

Kim, C. H., Kreidenweis, S. M., Feingold, G., Frost, G. J., and Trainer, M. K.: Modeling cloud effects on hydrogen peroxide and methylhydroperoxide in the marine atmosphere, J. Geophys. Res.-Atmos., 107, doi:10.1029/2000JD000285, 2002.

Lee, M. H., Heikes, B. G., and O'Sullivan, D. W.: Hydrogen peroxide and organic hydroperoxide in the troposphere: A review, Atmos. Environ., 34, 3475–3494, 2000.

Niki, H., Maker, P. D., Savage, C. M., and Breitenbach, L. P.: A Fourier-transform infrared study of the kinetics and mechanism for the reaction $HO+CH_3OOH$, J. Phys. Chem., 87, 2190–2193, 1983.

O'Sullivan, D. W., Lee, M. Y., Noone, B. C., and Heikes, B. G.: Henry's law constant determinations for hydrogen peroxide, methyl hydroperoxide, hydroxymethyl hydroperoxide, ethyl hydroperoxide, and peroxyacetic acid, J. Phys. Chem., 100, 3241–3247, 1996.

Paulot, F., Crounse, J. D., Kjaergaard, H. G., Kuerten, A., St Clair, J. M., Seinfeld, J. H., and Wennberg, P. O.: Unexpected Epoxide Formation in the Gas-Phase Photooxidation of Isoprene, Science, 325, 730–733, doi:10.1126/science.1172910, 2009.

Podolske, J. R., Sachse, G. W., and Diskin, G. S.: Calibration and data retrieval algorithms for the NASA Langley/Ames Diode Laser Hygrometer for the NASA Transport and Chemical Evolution Over the Pacific (TRACE-P) mission, J. Geophys. Res.-Atmos., 108, doi:10.1029/2002JD003156, 2003.

Prather, M. J. and Jacob, D. J.: A persistent imbalance in HO_x and NO_x photochemistry of the upper troposphere driven by deep tropical convection, Geophys. Res. Lett., 24, 3189–3192, 1997.

Toon, O. B., Starr, D. O., Jensen, E. J., Newman, P. A., Platnick, S., Schoeberl, M. R., Wennberg, P. O., Wofsy, S. C., Kurylo, M. J., Maring, H., Jucks, K. W., Craig, M. S., Vasques, M. F., Pfister, L., Rosenlof, K. H., Selkirk, H. B., Colarco, P. R., Kawa, S. R., Mace, G. G., Minnis, P., and Pickering, K. E.: Planning, implementation, and first results of the Tropical Composition, Cloud and Climate Coupling Experiment (TC4), J. Geophys. Res.-Atmos., 115, doi:10.1029/2009JD013073, 2010.

Valverde-Canossa, J., Ganzeveld, L., Rappenglueck, B., Steinbrecher, R., Klemm, O., Schuster, G., and Moortgat, G. K.: First measurements of H_2O_2 and organic peroxides surface fluxes by the relaxed eddy-accumulation technique, Atmos. Environ., 40, S55–S67, doi:10.1016/j.atmosenv.2006.03.038, 2006.

Washenfelder, R. A., Roehl, C. M., McKinney, K. A., Julian, R. R., and Wennberg, P. O.: A compact, lightweight gas standards generator for permeation tubes, Rev. Sci. Instrum., 74, 3151–3154, doi:10.1063/1.1570949, 2003.

Chapter 4

Biomass burning and urban air pollution over the Central Mexican Plateau*

4.1   Abstract

Observations during the 2006 dry season of highly elevated concentrations of cyanides in the atmosphere above Mexico City (MC) and the surrounding plains demonstrate that biomass burning (BB) significantly impacted air quality in the region. We find that during the period of our measurements, fires contribute more than half of the organic aerosol mass and submicron aerosol scattering, and one-third of the enhancement in benzene, reactive nitrogen, and carbon monoxide in the outflow from the plateau. The combination of biomass burning and anthropogenic emissions will affect ozone chemistry in the MC outflow.

4.2   Introduction

The 20 million (2005) inhabitants of Mexico City experience some of the worst air quality in the world. The high population density coupled with the topography of the city (2200 m, surrounded on three sides by mountains) leads to the daily buildup of pollutants in the region (Molina and Molina, 2002). Despite growing population and greatly increased automobile use, air quality has improved measurably in the last decade as the federal and city governments implemented a series of air quality regulations broadly similar to those that have been effective in, for example, Los Angeles (Lloyd, 1992). Nevertheless, ozone and particulate matter (PM) in the city often exceed international standards (WHO, 2008) and the city is consistently enveloped in a pall by the large amount of aerosol present.

The pollution from the city has impacts beyond the basin. Aerosols and ozone produce important forcing on regional climate through their interaction with both thermal infrared and visible radiation (Solomon et al., 2007). Indeed, the effluents from megacities, such as Mexico City, are now seen as globally important sources of pollution.

In the last decade, there have been several intensive studies of the air quality in the Mexico City basin. A major study undertaken in the Mexico City Metropolitan Area in spring of 2003 (MCMA-2003) included significant international cooperation (Molina et al., 2007). In the spring of 2006, a consortium of atmospheric scientists expanded significantly on this study, obtaining a large suite of measurements in and around Mexico City in an effort to understand both the controlling chemistry in the basin and the impacts of the outflow pollution on the broader region. Named Megacity Initiative: Local and Global Research Observations (MILAGRO), this campaign involved measurements at several ground sites along the most common outflow trajectory, and from several

aircraft. The National Science Foundation (NSF) C-130 (operated by the National Center for Atmospheric Research (NCAR)), and the US Forest Service Twin Otter, along with several other aircraft operated from Veracruz, Mexico. Here, we focus on observations made from the C-130 aircraft on seven flights above the Central Mexican Plateau. Details about the broader MILAGRO study are reviewed by Fast et al. (2007).

Most efforts to engineer improvements in Mexico City air quality have logically focused on reducing emissions from the transportation and power generation sectors (McKinley et al., 2005) and on new liquefied petroleum gas (LPG) regulations. However, as in Los Angeles, as the emissions from transportation and industrial sectors decline, continued improvement in air quality will require addressing additional sources.

Biomass burning can be a significant contributor to poor air quality in many regions of the world, including Southern California (Muhle et al., 2007). Several previous studies have suggested that fires in and around the Mexico City basin can impact air quality (Molina et al., 2007; Bravo et al., 2002; Salcedo et al., 2006). During the springtime (March–May), many fires occur in the pine forests on the mountains surrounding the city, both inside and outside the basin. These fires are virtually all of human origin. Primarily they originate from accidental means (escaped agricultural/land maintenance fires, escaped campfires, smoking, fireworks, vehicles, etc.), with a smaller number originating from intentional ignition (E. Alvarado, Univ. of Washington, personal communication, 2009). Typically, the biomass burning season intensifies in late March, reaching a maximum in May (Fast et al., 2007; Bravo et al., 2002). The heat from these fires is observable from space by the infrared channels of the moderate resolution imaging spectroradiometer (MODIS) instruments operated from NASA's Aqua and Terra platforms (Giglio et al., 2003). Figure 4.1, for example, shows two visible images from MODIS taken on 5 March (panel a) and 10 March (panel b) 2006. The locations of the detected thermal anomalies are shown as red boxes. The aerosol haze from the fires can be seen covering large areas of land around and above MC, particularly on 5 March. MODIS imagery suggests that the total biomass burning around MC in March 2006 was greater than climatological amounts, and closer to what is normally observed during the month of April.

Using tracers of pollution from biomass burning and urban emissions, we show that fires significantly impacted air quality above and downwind of Mexico City in March 2006. We use aircraft measurements of hydrogen cyanide (HCN) to estimate the contribution of biomass burning to the regional air quality. HCN is produced in the pyrolysis of amino acids (Ratcliff et al., 1974) and has been widely used as an atmospheric tracer of biomass burning emissions (e.g., Li et al., 2003). We
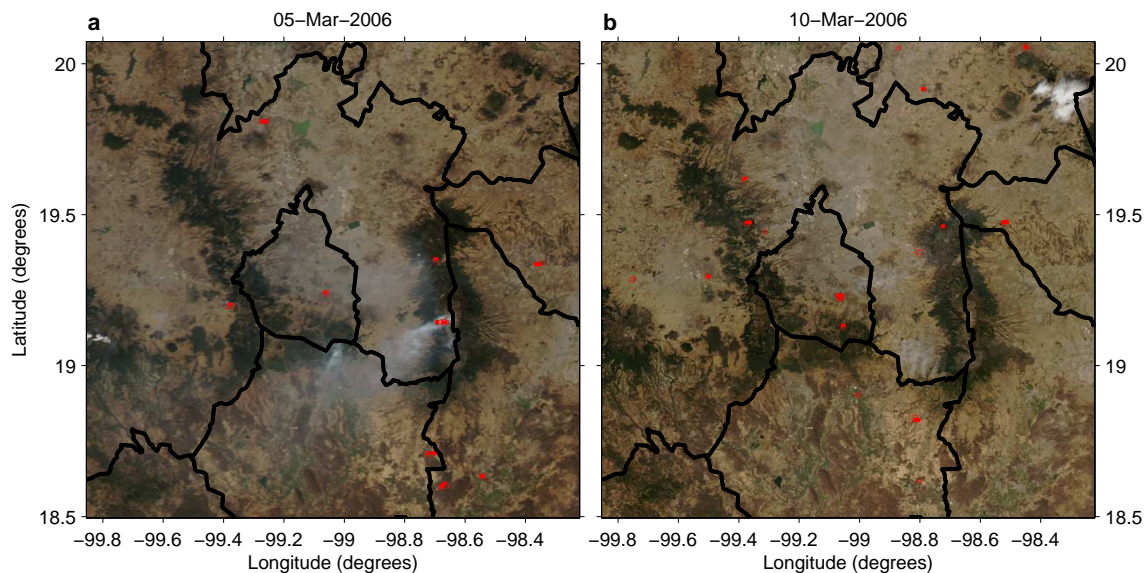
Figure 4.1 – MODIS-Aqua images of the Mexico City basin on (a) 5 March 2006 at 13:35 CST and (b) 10 March 2006 at 13:55 CST, illustrate how large fires in the hillsides surrounding the city can impact visibility. Red boxes are thermal anomalies detected by MODIS. Black lines represent Mexican state boundaries. Images courtesy of MODIS Rapid Response Project at NASA/GSFC.

use simultaneous observations of acetylene (C_2H_2) to characterize the contribution of urban emissions. We show that a simple two end-member mixing model (biomass burning and urban emissions) developed from these tracers can explain most of the observed variability in several pollutants including carbon monoxide, benzene, organic aerosol, reactive nitrogen oxides (NO_y), and the amount of submicron aerosol particles.

4.3   Observations

The NSF C-130 flew through the Mexico City region on eleven flights in March 2006 (Fig. 4.2). Of these flights, three had fewer than ten samples of C_2H_2 within our study area (3×3 degree box centered on MC, shown in Fig. 4.2 and termed Central Mexican Plateau) and one flight did not have HCN observations. These flights are excluded from the calculation of the overall fire impact (4, 12, 26, and 28 March). In Fig. 4.2a, the aircraft flight tracks are colored by the average amount of HCN measured in the air. Acetonitrile (CH_3CN) mixing ratios, which also have been used extensively as a biomass burning tracer, were highly correlated (r^2=0.78) with overall regression slope of 0.39 ($\Delta CH_3CN/\Delta HCN$) (Fig. 4.7), similar to several previous measurements of biomass burning emission ratios (Yokelson et al., 2007a; Singh et al., 2003). The mean mixing ratio of HCN in the study area

(seven flights considered, within the 3×3 degree box) was measured to be 530 pptv, about 390 pptv higher than the background values observed in clean air encountered above the plateau pollution.

Figure 4.2b shows the C-130 flight tracks colored by the mixing ratio of C_2H_2. C_2H_2 is produced in the combustion of both gasoline and diesel fuels. We chose C_2H_2 as our urban tracer because its atmospheric lifetime is quite long. We calculate that with respect to its major loss mechanism (reaction with the hydroxyl radical, OH), the atmospheric lifetime is ten days to two weeks in the Mexico City region. We did not use other tracers of city emissions such as toluene or methyl tert-butyl ether (MTBE) because their shorter atmospheric lifetimes complicate the regional analysis. In fresh city plumes (as determined by the ratio of toluene to C_2H_2), all the urban tracers (e.g., C_2H_2, MTBE, toluene) are highly correlated.

Although the regions of enhanced C_2H_2 and HCN appear geographically coincident in Fig. 4.2, the sources of these gases within the basin are geographically (and temporally) distinct and significant differences in their distribution can be observed on smaller spatial scales. This is illustrated in Fig. 4.3a. On 8 March 2006, the C-130 flew into the Mexico City basin and over a short period encountered air masses significantly enhanced in either HCN, C_2H_2, or both (panel a). Fig. 4.4 shows the flight track corresponding with data shown in Fig. 4.3 on top of the MODIS - Aqua image for March 8th.

To quantify the contribution of both fire and urban emissions to the distribution of a trace gas (or aerosol), Y, we implement a simple two end-member model using the measured excess HCN, $[\text{HCN}]^*$, and measured excess C_2H_2, $[C_2H_2]^*$, as tracers:

$$Y = F_Y(\text{fire}) \times [\text{HCN}]^* + F_Y(\text{urban}) \times [C_2H_2]^* \tag{4.1}$$

where,

$$[\text{HCN}]^* = [\text{HCN}] - S_{\text{HCN}}(\text{urban}) \times [C_2H_2]^* - [\text{HCN}]_{\text{background}} \tag{4.2}$$

$$[C_2H_2]^* = [C_2H_2] - S_{C_2H_2}(\text{fire}) \times [\text{HCN}]^* - [C_2H_2]_{\text{background}} \tag{4.3}$$

F_Y are scalars that relate the emission of Y from fire and urban sources to the emissions of HCN and C_2H_2, respectively (Table 4.1). S_{HCN} and $S_{C_2H_2}$ are the emission ratios of HCN to C_2H_2 and C_2H_2 to HCN for urban and fire emissions, respectively. These cross terms account for the contribution of urban and fire emissions to the excess HCN and C_2H_2, respectively. We also account for the amounts of these tracers advected into the region from afar (backgrounds).

We derive a set of emission ratios, F_Y, for the pollutants using total least squares (TLS) analysis
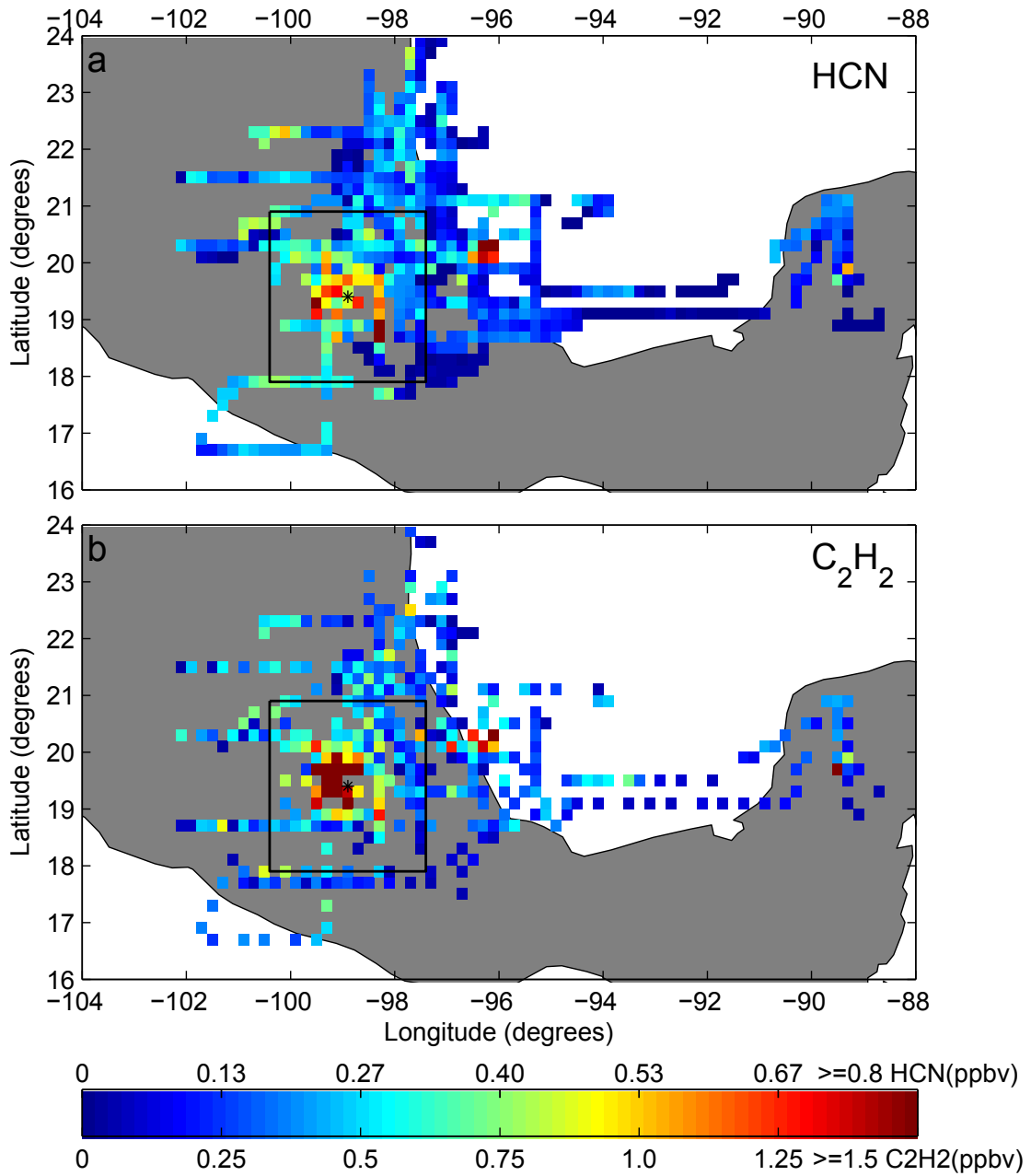
Figure 4.2 – C-130 flight tracks during MILAGRO colored by tracers: (a) observed HCN–HCN$_{\mathrm{background}}$, and (b) observed C$_2$H$_2$. The map has been divided into 0.2×0.2 degree pixels and all observations from the C-130 across the MILAGRO campaign within a given pixel have been averaged together. High-concentration data have been rounded down to capped values of 0.8 and 1.5 ppbv for HCN and C$_2$H$_2$, respectively. Color scales range from 0 ppbv (dark blue) to the capped value (dark red). The black star in each panel is the center of Mexico City, and the black box outlines the 3×3 degree box centered on Mexico City, which is the study area considered for the fire impact analysis.
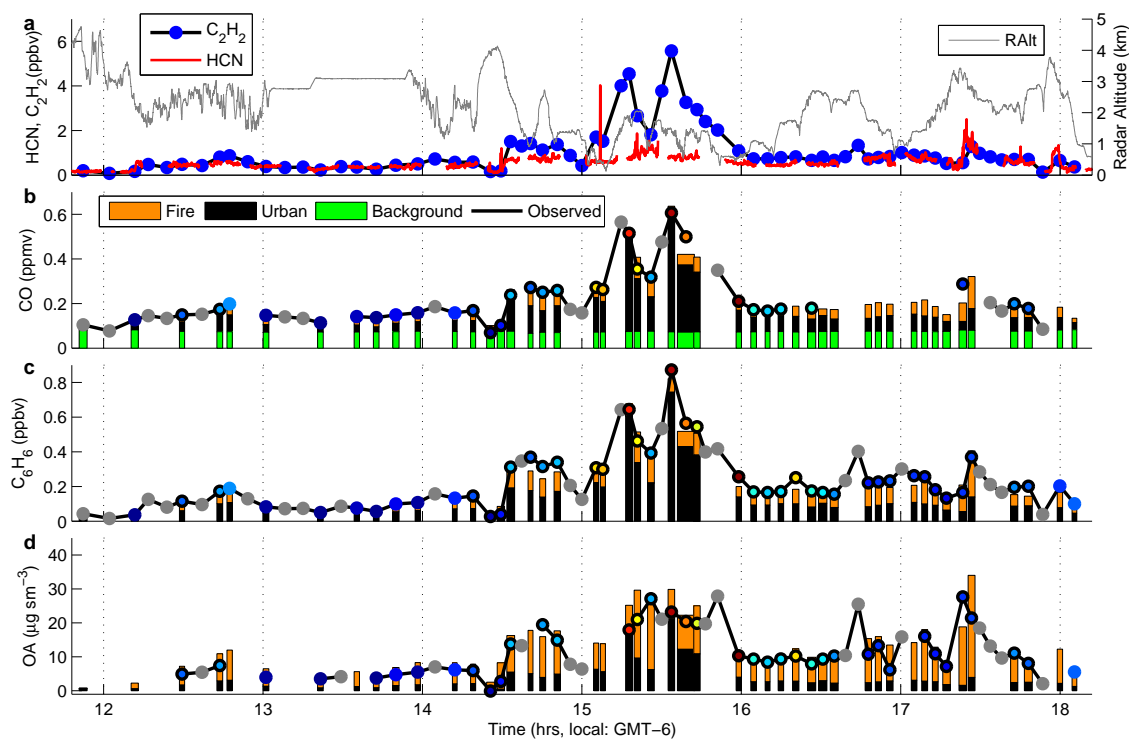
Figure 4.3 – Timeline from the flight of 8 March 2006: (a) measured HCN, C_2H_2, and radar altitude. The observed (dots) and reconstructed (bars) CO, benzene, and organic aerosol concentrations, are shown in panels (b–d), respectively. The bar widths represent the relative bottle sampling time (width has been expanded by $3\times$ for clarity). The measurements in panels (b–d) are colored by $[\text{toluene}]/[C_2H_2]^*$ with color scale ranging from red=1 to blue=0, and grey meaning data was unavailable for this calculation. Data points with black borders in panels (b–d) lie within the 3×3 degree study area.
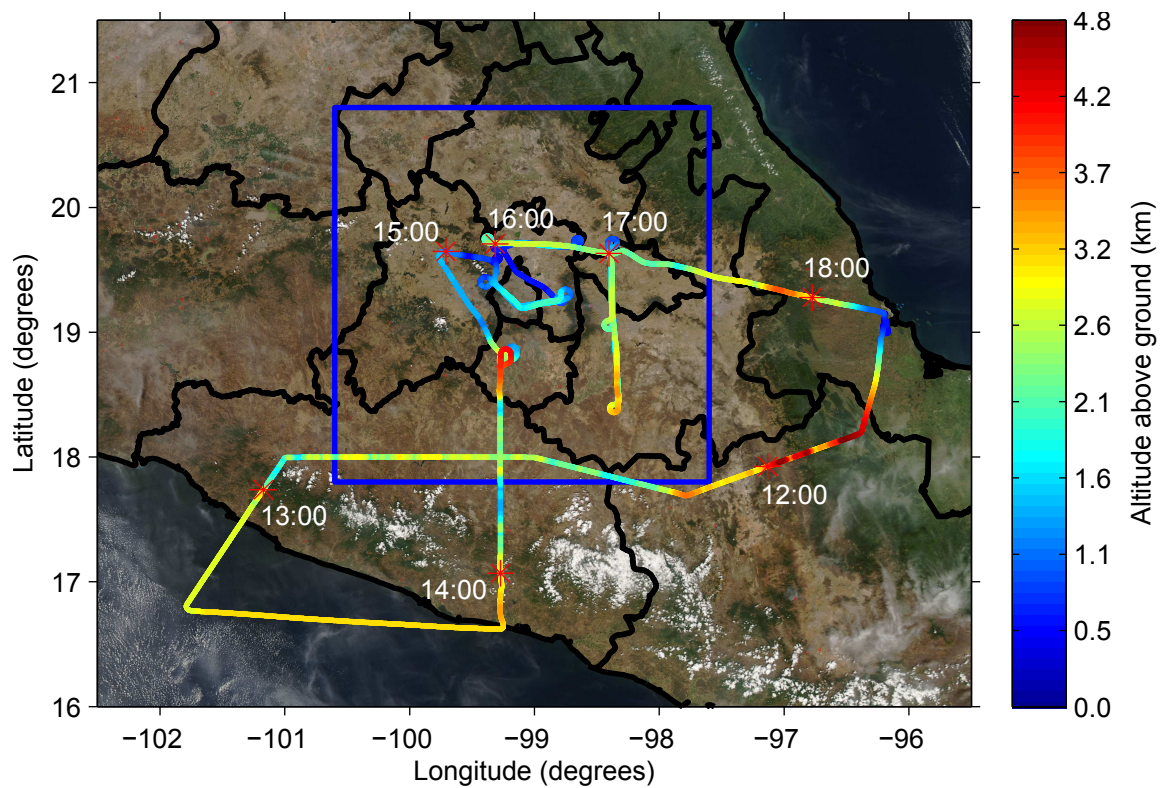
Figure 4.4 – MODIS-Aqua image and C-130 flight track from March 8, 2006, as accompanyment to Figure 4.3. Flight track is colored by aircraft radar altitude (altitude above the ground). Specific times along the flight track are shown as red asterisks, and labeled as local time in hours (GMT-6). The blue box encompasses the 3×3 degree study area.

Table 4.1 – Anthropogenic and biomass burning emission ratios derived here (TLS) and those measured directly in the Mexico City area.

Species	Urban $(\Delta[x]/\Delta[C_2H_2])^a$		Biomass Burning $(\Delta[x]/\Delta[HCN])^a$	
	opt[b]	29 March	opt[b]	fire obs.[d]
CO	$96\pm^3_2$	92	$104\pm^8_9$	117
C_6H_6	$0.137\pm^{0.005}_{0.005}$	0.13	$0.19\pm^{0.01}_{0.01}$	–
NO_y	$4.3\pm^{0.3}_{0.3}$	3.7	$5.4\pm^{1.0}_{1.0}$	7.1[f]
OA	$3.9\pm^{1.0}_{0.6}$	2.9	$22\pm^4_4$	14
scattering[e]	$22\pm^4_3$	22	$75\pm^6_7$	78
HCN	–	0.056[c]	–1–	–1–
C_2H_2	–1–	–1–	–	0.17

[a] Units are mol/mol, except for $\Delta OA/\Delta[y]$ and $\Delta[\text{scattering}]/\Delta[y]$, which have units of μg sm^{-3} ppbv^{-1} and Mm^{-1} ppbv^{-1}, respectively.

[b] Calculated emission ratios determined from TLS anaylsis.

[c] An upper limit for how much HCN comes from urban emissions in MC, derived from data collected from C-130 on 29 March 2007, a day with low BB influence. This factor is not optimized.

[d] Median values for fires sampled by the Twin Otter around Mexico City in March 2006 (Yokelson et al., 2007b).

[e] This refers to submicron scattering measured at 550 nm.

[f] This value is the NO_x/HCN emission ratio, not NO_y/HCN. For this comparison we assume that in the fresh smoke sampled by Yokelson et al. (2007b), $NO_x \approx NO_y$.

(Table 4.1). We weight $[\text{HCN}]^*$ and $[\text{C}_2\text{H}_2]^*$ by estimates of their error determined primarily from uncertainties in the backgrounds and in the variability of the emission ratios. We estimate the uncertainty in the derived emission ratios using a bootstrap method (Efron and Tibshirani, 1993). The bootstrap method creates x alternate data sets by picking n random samples with replacement from the original data set, where n equals the number of samples in the original data set. The TLS analysis is then performed across all alternate data sets, and statistics are computed on the results of all analyses. For this analysis we used $x=1000$. In Table 4.1, we also summarize the emission factors determined independently from measurements made directly in biomass burning plumes measured in the basin during MILAGRO.

Gasoline and diesel engine exhaust contain HCN, though previous measurements of the emissions vary by orders of magnitude (Baum et al., 2007). Automobiles lacking catalytic converters can produce 100 times more HCN than automobiles with functional catalysts (Baum et al., 2007; Harvey et al., 1983). To estimate the appropriate emission ratio for Mexico City, S_{HCN}, we use observations made from the C-130 on 29 March when the C-130 sampled city emissions with what appears to be minimal fire influence (Fast et al., 2007). The measured slope of HCN to C_2H_2 in the city plumes encountered on this day is 0.056 (mol/mol). The ratio of CH_3CN to HCN in the city emissions is 0.5, similar to the ratio measured in both fire plumes and in the region as a whole. This is in contrast to observations from Asia where urban emissions had a much lower ratio of CH_3CN to HCN (Li et al., 2003). Thus it is possible that even on the 29th, some of the HCN is from burning. Given our cross term corrections, and assuming urban fire sources such as garbage, coal, and biofuel burning was no different on 29 March than on other days, emissions from these urban fire sources are counted as urban emissions and not as fire emissions. Using the 0.056 (mol/mol) as an upper limit for the $\text{HCN}/\text{C}_2\text{H}_2$ emission ratio from urban emissions, we estimate that all urban emissions of HCN account for no more than 15% of the total emissions in the basin during March 2006. Other sources of HCN from, for example, coal burning and petrochemical industries are also estimated to be small (see Section 4.6.2).

We use measurements of C_2H_2 and HCN observed in forest fires in and around Mexico City to estimate $S_{\text{C}_2\text{H}_2}$ (Yokelson et al., 2007b). The emission of C_2H_2 from these forest fires was near the low end of the range typically observed for extratropical forest fires (Yokelson et al., 2007b; Andreae and Merlet, 2001). We estimate that the contribution of biomass burning to C_2H_2 accounts for less than 10% of the C_2H_2 in and around Mexico City (see Table 4.1).

To account for the background amounts of C_2H_2 and HCN advected into to the region, we use

our observations in air sampled aloft, away from the Mexico City basin. We use separate HCN and C_2H_2 backgrounds for the gas-phase species and for organic aerosol/scattering, as aerosols have a more variable atmospheric lifetime. For the gas-phase species (CO, benzene, and NO_y), we use a constant value of 140 pptv for the background values of HCN for flights before 21 March. Following a shift in weather on 21–22 March (Fast et al., 2007) (see also Figs. 4.11–4.13, and `http://www.atmos-chem-phys.net/9/4929/2009/acp-9-4929-2009-supplement.pdf` for higher resolution MODIS images), we find higher background concentrations for HCN (220 pptv). C_2H_2 backgrounds are quite small (0–30 pptv), so we have used a constant background value of 0 pptv for the analysis of the gas phase species. For organic aerosol and scattering, we have used a flight-by-flight analysis of the correlation of organic aerosol mass and scattering with HCN and C_2H_2 to define the background HCN and C_2H_2. For flights in early March, the implied background of HCN and C_2H_2 for organic aerosol (the abundance of these gases when the amount of organic aerosol is zero) is very close to the global backgrounds used in the analysis of the gases, but following the rainy period, 20–26 March, the apparent backgrounds for both HCN and C_2H_2 increased more drastically than for the gas phase pollutants; organic aerosol concentrations were near zero at significantly higher concentrations of HCN and C_2H_2 (300 and 150 pptv, respectively). This difference is likely due to removal of aerosol (but not insoluble gases such as HCN, CO, C_2H_2, etc.) in the region during the rain storms.

The variance in the abundance of our fire and urban tracers (HCN and C_2H_2) explains most of the variability in CO and other pollutants. For example, in panels b, c, and d of Fig. 4.3, we show the observations (circles) for CO, benzene, and organic aerosol mass along the C-130 flight track. The observations are averaged to the sampling time of the whole air samples used to determine C_2H_2. The bars show the contributions from fire and urban emissions, estimated from [HCN]* (orange) and acetylene, $[C_2H_2]^*$ (black) using the emission ratios described in Table 4.1 and the mixing model described by Eq. (4.1).

Figure 4.5a shows a scatter plot of the predictions from the two component model and all observations (from all flights) made from the C-130 during MILAGRO for CO. The observations made within the 3×3 degree box surrounding MC, during the seven flights considered in this analysis are highlighted with a black border. CO has a relatively long lifetime in the atmosphere and there is a persistent northern hemispheric background of between 60 and 150 ppbv that varies with season and latitude. To estimate the regional increase in [CO], we assume that the background [CO] is equal to the simulation of background CO taken from the Model for OZone And Related chemical Tracers

(MOZART) chemical transport model (Horowitz et al., 2003), plus a constant 34 ppbv offset (see Fig. 4.3b, green bars). The offset was determined from the bias between MOZART simulations and the observed CO in the cleanest air encountered during MILAGRO – typically aloft and outside the Mexico City basin. Figure 4.5d shows the comparison for benzene. From the tracer analysis, we estimate that biomass burning accounts for $(31\pm3)\%$, $(36\pm3)\%$, and $(34\pm7)\%$ of the CO, benzene, and reactive nitrogen (NO_y). These estimates are the mean of the mass-weighted, daily-averaged fire/excess fractions for observations made within the 3×3 degree box centered on MC, for the seven flights considered in this analysis. The sensitivity of these ratios to the size of the box is described in Table 4.2. Consistent with expectation, the fraction of pollution from biomass burning is lower for a smaller box centered over the city.

Figure 4.6a shows a scatter plot of the predictions from the two component model for organic aerosol. The data are colored by the ratio of toluene to acetylene. High ratios (red colors) are indicative of very fresh emissions with little photochemical processing. A similar figure for submicron aerosol scattering is shown as Fig. 4.9. From the tracer analysis, we estimate that biomass burning accounts for $(66\pm11)\%$, and $(57\pm5)\%$ of the organic aerosol mass and total submicron scattering (which determines visibility). These estimates are the mean of the mass-weighted, daily-averaged fire/excess fractions for observations made within the 3×3 degree box centered on MC for the seven flights considered in this analysis.

4.4 Discussion

In Table 4.1, we compare the emission ratios estimated from the TLS analysis with observations made in the city plume encountered on 29 March (little BB influence) and in fresh fire plumes sampled within the study area by the Twin Otter (Yokelson et al., 2007b). The emission ratios derived here do not change if the data from the 29th are excluded from the least-squares analysis. Note, while (Yokelson et al., 2007b) report emission factors for up to five fires (or groups of fires) as well as the geometric mean of the reported individual emission factors, here we report (Table 4.1) the median values of the individual emission ratios calculated from the emission factors given therein. Median values are reported here because of the high variability of the individual emission factors, and the non-uniform weighting across fires in the geometric mean calculation. In particular, the unusually high modified combustion efficiency (MCE) of the "17 March – Planned Fire" and the group of fires reported as "6 March - Fires 1–4" are given 25% of the weight as the remainder of the fires in calculating the geometric mean. While not as good, the comparison using the mean of the

62
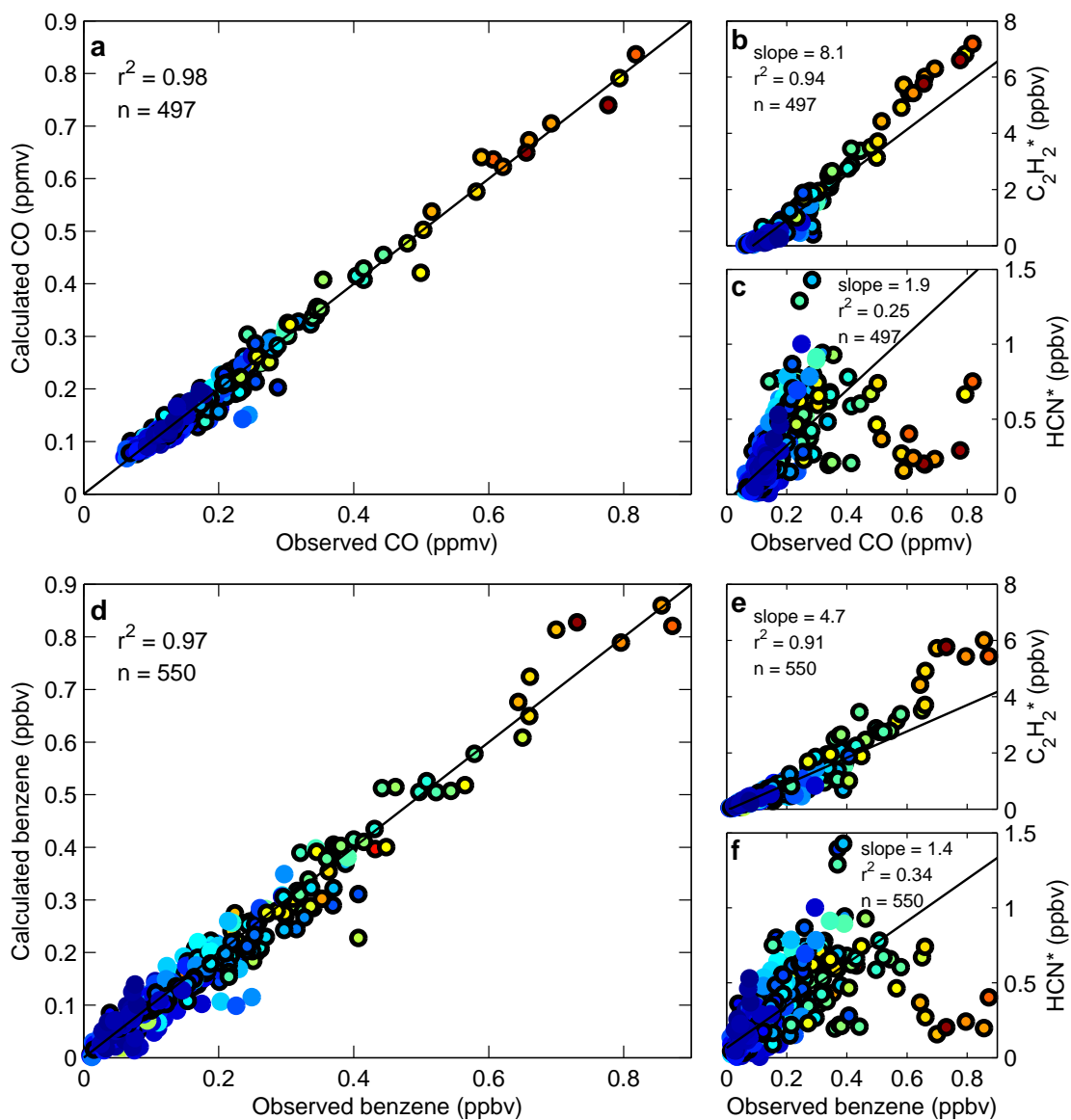
Figure 4.5 – Scatter plots for observed vs. reconstructed CO (a) and benzene (d). Associated scatter plots for CO vs. each tracer, $[C_2H_2]^*$ (b) and $[HCN]^*$ (c) and for benzene vs. each tracer, $[C_2H_2]^*$ (e) and $[HCN]^*$ (f). Lines are best fit to all data using total least squares (TLS) regression. Points are colored by $[toluene]/[C_2H_2]^*$, where red=1 and blue=0. Points with black border lie within the 3×3 degree study area.
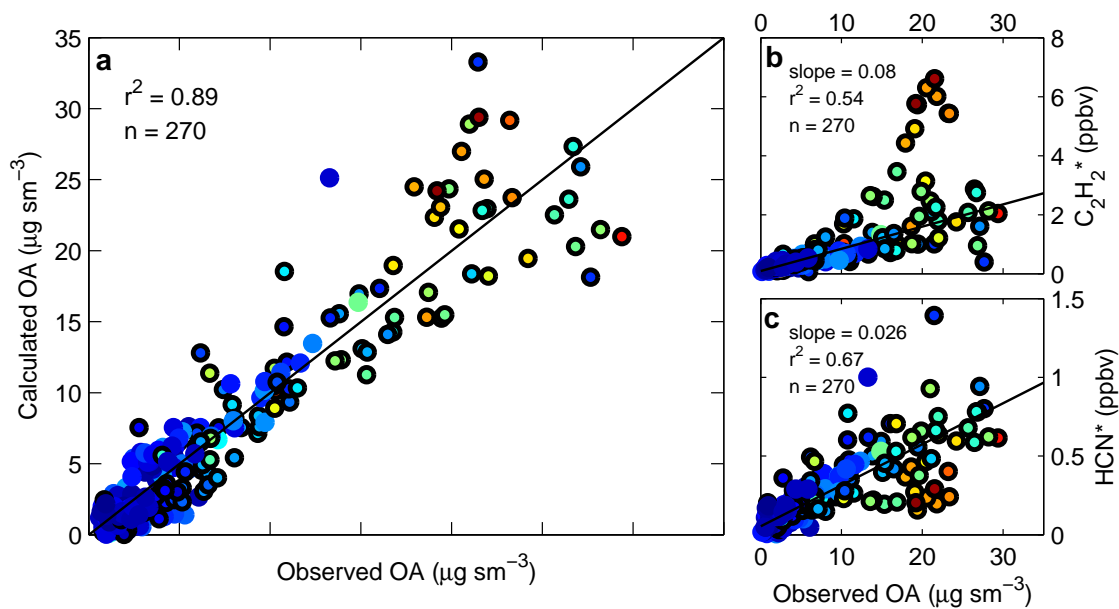
Figure 4.6 – Scatter plot for observed vs. reconstructed OA (a). Associated scatter plots for OA vs. each tracer, $[C_2H_2]^*$ (b) and $[HCN]^*$ (c). Lines are best fit to all data using total least squares (TLS) regression. Points are colored by $[toluene]/[C_2H_2]^*$, where red=1 and blue=0. Points with black border lie within the 3×3 degree study area.

emission ratios derived from (Yokelson et al., 2007b) does not alter the conclusions.

The urban ratio of CO to C_2H_2 measured on 29 March, 92 (mol/mol), is very close to the emission ratio estimate from the total least squares (TLS) analysis, 96 (mol/mol) (Table 4.1). This ratio is lower than typically observed in US (300–500 mol/mol), and Asian cities (220 mol/mol) (Xiao et al., 2007), but comparable to the value observed by Grosjean et al. (1998) in urban air in Brazil. The lower emission ratios in Mexico and Brazil may reflect differences in fuel composition or catalytic converter functionality (Sigsby et al., 1987). The relatively high concentration of C_2H_2 in traffic exhaust combined with the emissions of C_2H_2 from fires near the low end of the typical range makes C_2H_2 a good tracer for the Mexican urban emissions. Observations made during the same period of CO and C_2H_2 at a ground station (T1) in Mexico City and described by de Gouw et al. (2009) show a mean CO to C_2H_2 ratio of 150 mol/mol. It is not known at this time what accounts for this difference, but likely it is due to a difference in calibration factors. The analysis described here is not sensitive to an absolute error in C_2H_2 or CO as the emission ratios are derived internally to the data set. While a calibration error in either CO or C_2H_2 will affect the C_2H_2 emission ratios reported in Table 4.1, it will not change the calculated fire impact for the trace gasses reported in Table 4.2.

The median ratio of CO to HCN observed in biomass burning plumes within the study area, 117 mol/mol (Yokelson et al., 2007b), is close to that derived in the total least squares analysis, 104 mol/mol. As noted by Yokelson et al. (2007b), this ratio is at the low end of the range typically observed for biomass burning. The relatively high emissions of HCN in biomass burning plumes combined with the low emission ratios from urban sources makes HCN a very good tracer for biomass burning in Mexico City.

Biomass burning is a significant global source of benzene and the impact of this source in and around the Mexico City basin is quite apparent in the correlations of benzene with the tracers (Fig. 4.5d–f). From the least squares analysis, we estimate that fires contributed 36% of this pollutant to the atmosphere above the central Mexican Plateau in March 2006. Relative to CO, the benzene emission ratio for biomass burning derived here is similar to those reported in other studies (Andreae and Merlet, 2001). As an aside, measurements of the ratio of benzene to toluene have been used in many previous studies to estimate the aging of an urban airmass as the atmospheric oxidation of toluene occurs much more rapidly than benzene (e.g., Cubison et al., 2006). Because the benzene/toluene emission ratio from fires ($\sim$1–3) is much greater than the same emission ratio from urban emissions (0.2), this method is not appropriate for cities – such as Mexico City during the biomass burning season – that have significant contributions of benzene from fire emissions.

Organic aerosol generally accounts for more than half the mass of fine particulate matter ($PM_{2.5}$) in (Salcedo et al., 2006) and around (DeCarlo et al., 2008) Mexico City. As shown in Fig. 4.6b–c, the amount of organic aerosol is highly correlated with $[HCN]^*$ and $[C_2H_2]^*$, suggestive of large fire and urban emission influences. Using the emission ratios described in Table 4.1, we estimate that biomass burning contributes 66% of the organic aerosol to the study area in March 2006. These estimates are quite uncertain, however, due to complex aerosol chemistry.

Organic aerosol is both formed in and lost from the atmosphere on relatively fast timescales. Although direct (or primary) emissions of organic aerosol from automobiles are quite small ($\sim$5–10 μg per standard (T=273 K, P=1 atm) cubic meter of air (sm^3) per ppmv CO), subsequent atmospheric oxidation of co-emitted hydrocarbons such as toluene and other aromatics, as well as biogenic and biomass burning hydrocarbon emissions, can yield low vapor pressure compounds that condense on the existing particulate forming secondary organic aerosol (SOA) (Kroll and Seinfeld, 2008). The amount of SOA produced from these gas-phase sources over the period of a day substantially exceeds the primary emissions from urban sources (de Gouw et al., 2005; Kleinman et al., 2008; Robinson et al., 2007; Volkamer et al., 2006). The influence of this process is apparent in the aircraft data.

In Fig. 4.6a, the organic aerosol data is colored by the ratio of toluene to acetylene. Toluene is co-emitted with acetylene in urban emissions, but is oxidized in the atmosphere with a lifetime of approximately 12 daylight hours. In samples containing very high toluene (less oxidized), the total least squares analysis tends to over-predict the amount of organic aerosol. For example, the urban emission ratio derived from the least squares analysis ($\sim$39 μg per sm^3 per ppmv CO or $\sim$ 3.9 μg per sm^3 per ppbv of C_2H_2) is greater than the factor derived from the slope of the correlations in the fresh plumes encountered on 29 March.

In addition to aerosol growth, aerosol mass can be lost through several mechanisms. As aerosol is transported away from its source and diluted with clean air, semi-volatile compounds evaporate to the gas phase (Robinson et al., 2007). Dry and wet deposition also remove aerosol from the atmosphere. As mentioned earlier, the changing backgrounds for aerosol relative to insoluble gases observed during late March are likely explained by aerosol loss via wet deposition.

Despite the complexity of the aerosol chemistry, the simple two end-member mixing model does describe much of the variability of organic aerosol mass observed from the C-130. This result may be related to our sampling – most of the observations were made in the afternoon when the city and fire emissions had experienced some aging. The apparent organic aerosol emission ratio for urban emissions derived from the 29 March plume, 32 μg OA per sm^3 per ppmv CO, is not inconsistent with other estimates for organic aerosol from urban emissions aged 3–6 h (de Gouw et al., 2005; Volkamer et al., 2006). The aerosol burden continues to increase as the air masses are further oxidized in the MC outflow (Kleinman et al., 2008); similar to what has been observed in the New York City (de Gouw et al., 2005) and Atlanta plumes (Weber et al., 2007).

The complexity of the mixing of the urban-core aerosol emissions with the regional aerosol emissions (often dominated by fire emissions) as well as mixing with the clean free troposphere precludes strong statements on the aerosol dynamics of these different sources.

The average NO_x/VOC emission ratio for the fires surrounding Mexico City is similar to the urban NO_x/VOC emission ratio for Mexico City. This is due in part to the higher than expected NO_x emission from the fires, which is significantly (2–4$\times$) larger than typical for fires (Yokelson et al., 2007b). As the fire and urban NO_x/VOC emissions are similar, the fire emissions will significantly impact the ozone production in the Mexico City outflow. Modeling of the transport and aging of the MC plume using a 3-D chemical transport model with full chemistry and accurate urban and fire emissions will be required to quantify the full impact of the fire emissions on ozone concentrations.

4.5   Implications for air quality improvement

The implications of this study for air quality engineering in Mexico City are not straightforward. Although visibility within the city and the export of aerosol, ozone, and other trace gases is significantly impacted by biomass burning during the period of our observations, it is not possible to estimate from this data set the long-term impact of such burning on the urban dwellers of Mexico City. Biomass burning in March 2006 was significantly higher than typical for March, though not unlike the amount of burning usually observed in the height of the biomass burning in April/May. During most of the year (June–February), however, these sources are negligible. Thus, annually-averaged, the impact of biomass burning will certainly be much smaller. In addition, because our sampling was from aircraft and primarily in the afternoon, and because the biomass burning was primarily in the forest above the city (Yokelson et al., 2007b), the impact of fire on the air breathed by people within Mexico City will be smaller than the regional impact estimated here. Indeed, we observe that even in the relatively well mixed afternoon planetary boundary layer, the impact of fire increases with altitude (Fig. 4.10). Consistent with this finding, estimates of the impact of fire on air quality at the ground stations within the city suggest a smaller fire influence (Molina et al., 2007; Bravo et al., 2002; Salcedo et al., 2006; Yokelson et al., 2007b; Stone et al., 2008; Moffet et al., 2008; Aiken et al., 2009). A possible method for estimating the impact of fires to people on the ground in Mexico City would be through the use of a high-resolution 3-D chemical transport model constrained by accurate winds and meteorological conditions, accurate fire emissions, and coupled with population maps. For example, an extension of the Fast et al. (2009) study could provide such an estimate, however additional work would be required to properly model the nighttime and early morning boundary layer, as well as an adequate parameterization of SOA growth which considers both anthropogenic and biomass burning precursors. Finally, unlike reducing emissions from the urban sources, reducing fire emissions through fire suppression efforts may have environmental costs as well as benefits; although forest fire suppression in and around the basin would yield improvement in visibility, such fire suppression actions may be inconsistent with proper forest management practices.

4.6 Supporting information

4.6.1 Data sources

HCN was measured on the NCAR C-130 as discrete 0.5 second samples obtained every 5 seconds. The analysis was performed by chemical ionization mass spectrometry (CIMS). While the Caltech CIMS instrument has been described in previously in detail (Crounse et al., 2006), the particular HCN method has not. In brief, HCN reacts rapidly with the CF_3O^- (and $CF_3O^- \cdot H_2O$) anion to form the cluster product ion, $CF_3O^- \cdot HCN$, which is monitored at $m/z = 112$. Instrumental backgrounds were measured once every 15 minutes by passing ambient air through a filter containing nylon wool coated with $NaHCO_3$. In-flight calibrations were performed about once per hour using HNO_3 and H_2O_2 calibration standards and proxied to laboratory calibrations of HCN. Similar to H_2O_2, the sensitivity of the CIMS instrument toward HCN is a function of water vapor. This is corrected for using the aircraft water vapor measurement and a water vapor sensitivity curve for HCN determined in the laboratory. Absolute laboratory calibrations were conducted using HCN permeation tubes (KIN-TEC), whose output was determined through both gravimetric and spectroscopic (FTS) means. Both absolute calibration methods agreed within 10%. Considering uncertainties in the absolute laboratory calibrations and water vapor concentration, the accuracy of the HCN observations is estimated to be better than $\pm 30\%$. The precision is limited mostly by counting statistics (background + signal) and is about 5% (1 standard deviation) at 250 pptv HCN under low to moderate water vapor levels (H_2O mixing ratio ≤ 0.004) for a 0.5 second integration period.

CH_3CN was measured by a cryotrap concentrator coupled to a gas chromatograph mass spectrometer (cryo-GCMS), an instrument similar to the one described by Apel et al. (2003). The cryo-GCMS instrument concentrated ambient air in the cryotrap for 45 seconds prior to a 125 second analysis, yielding one data point every 170 seconds. The accuracy for the cryo-GCMS CH_3CN determination is estimated to be $\pm 20\%$ with a precision of $\pm 3\%$.

C_2H_2, benzene, and toluene were recovered from 2 L canister samples that were periodically filled (approximately 12 samples per hour for the flights into the city). Each canister is filled over a period of 30–120 sec. These samples were analyzed by gas chromatography at UC Irvine (Blake et al., 1997). The detection limit for each of these compounds is 3 pptv, and the accuracy is estimated to be better than $\pm 5\%$ for C_2H_2 and $\pm 10\%$ for benzene and toluene.

NO_y was measured via catalytic reduction of reactive nitrogen species to NO on a gold surface in the presence of a small flow of CO, used as a reducing agent. The resulting NO was measured by the standard chemiluminescence technique. In order to keep the conversion efficiency constant the converter was maintained at a constant pressure using a heated teflon valve just upstream of the converter. The converter was housed in the inlet pylon, extending about 30 cm into the airstream, in order to minimize the length of inlet tubing upstream of the converter. The upstream plumbing (tubing and valve) were limited to a heated length of about 15 cm. The inlet tubing and converter were oriented perpendicular to the airstream with an aft-facing $45°$ cut on the end of the tubing. This configuration minimized particle amplification, and tended to exclude larger particles (1 micron or so). At 1 ppbv, the estimated NO_y precision and accuracy are $\pm 3\%$ and $\pm 15\%$, respectively.

Carbon monoxide was measured continuously with an vacuum ultraviolet (VUV) fluorescence instrument similar to the one developed by Gerbig et al. (1999) with a precision of 3 ppbv and a typical accuracy of $\pm 10\%$ at 100 ppbv CO levels. On several flights, the VUV fluorescence CO measurements were not available and CO concentrations were determined from the canister samples.

Aerosol composition (organic, sulfate, nitrate, ammonium, and chloride) and mass were determined with a high resolution aerosol mass spectrometer (HR-AMS) (DeCarlo et al., 2006, 2008). The HR-AMS detection limit for the organic aerosol is 0.35 μg sm^{-3} for a 12 second integration period, and its accuracy is estimated to be better than $\pm 25\%$. Aerosol scattering coefficients were measured at 450, 550, and 700 nm wavelengths using two TSI-3563 nephelometers. One nephelometer measured submicron scattering employing a 1 μm aerodynamic impactor, and the other measured total scattering (Anderson et al., 2003).

4.6.2   Alternative HCN sources

In addition to biomass burning and gasoline/diesel combustion, other sources of HCN may contribute to the enhanced HCN in the basin. For example, HCN has also been shown to be produced in the pyrolysis of coal from the breakdown of pyrrolic and pyridinic nitrogen (Leppalahti and Koljonen, 1995). Coal burning, however, is minimal in the basin. According to the 1999 Mexico National Emissions Inventory (NEI), 88% of the CO produced in Mexico City, and surrounding states (summing over Distrito-Federal, Mexico, and Morales) comes from mobile sources (NEI, 2008).

We did observe elevated HCN in the plumes from the power plants (fuel-oil fired) and petrochemical complex in Tula, north of Mexico City. The ratio of HCN to CO in the Tula plume is similar to that from fire. The Tula CO emissions are, however, significantly smaller than the CO emissions

from fire in the MC basin suggesting these emissions have minimal influence on the regional HCN budget.

4.6.3   HCN and acetonitrile correlation

A reasonable correlation (r^2=0.78, n=835) exists between HCN and CH_3CN observations, suggesting similar sources (Fig. 4.7). However, on multiple occasions, directly over Mexico City, enhanced CH_3CN was observed without accompanying enhancements in HCN (see Fig. 4.7, data excursions well above the best fit line). Explanations for these CH_3CN plumes could include industrial, non-combustion, sources, or possibly a different compound interfering with the GC-MS CH_3CN measurement. Overall, ΔCH_3CN is 39% of ΔHCN (Fig. 4.7). On 29 March, a day with little fire influence according to HCN levels relative to CO, the slope of CH_3CN to HCN is similar to the overall relationship, indicating that these compounds are emitted from urban sources in about the same ratio as from fire, or that fire is still the dominating source of these compounds even for days without large fires.

4.6.4 NO_y and submicron scattering

Analogous to Figs. 4.5 and 4.6, NO_y (Fig. 4.8), and submicron scattering at 550 nm (Fig. 4.9) reconstructions are shown. The two-component fit for total scattering yielded very similar results as the one for submicron scattering (e.g., fire fraction also equal to 57%), with similar correlation coefficients. Significant amounts of aerosol nitrate were measured in and around Mexico City. For this analysis total NO_y was taken as the sum of measured NO_y and aerosol nitrate. While the NO_y instrument likely measures some of the aerosol nitrate as NO_y, at this time it is not known what fraction of aerosol nitrate was sampled by the NO_y instrument. To the extent aerosol nitrate is sampled by this NO_y instrument, we are double counting the aerosol nitrate. The correlation with the two-component model is significantly better if the aerosol nitrate is added to the NO_y measurement to give total NO_y.

4.6.5   Altitude dependence of fire impact

As observed from the C-130, and inferred by comparing the C-130 data with observations on the ground in Mexico City, the impact of the fires surrounding Mexico City is not as severe on the ground, as it is above the City. This is due in part to the location of the fires, elevated above the city on the mountainsides surrounding the city. The impact of fire increases with altitude above
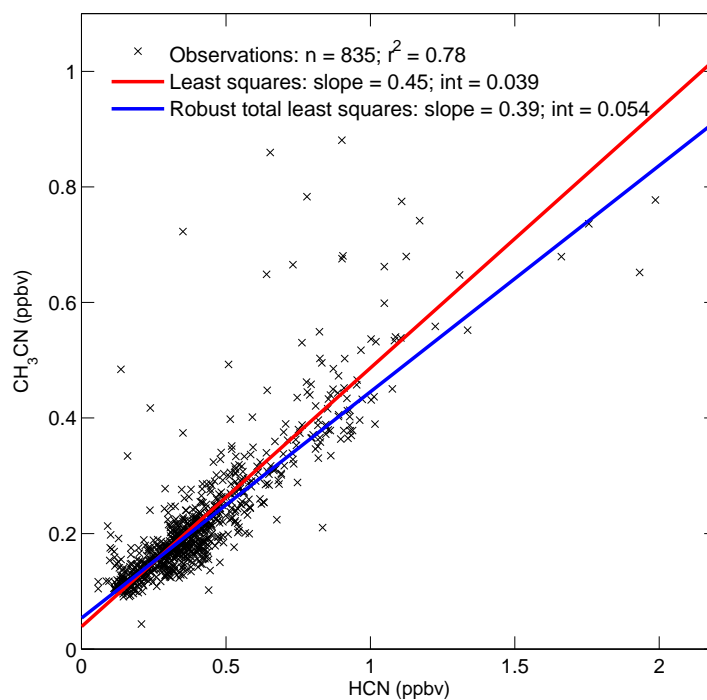
Figure 4.7 – Scatter plot of the HCN and the CH_3CN observations made aboard the C-130 during the MILAGRO experiment ($r^2 = 0.78$). The data (black x symbols) were fit using least squares (red: slope = 0.45, intercept = 0.039 ppbv), and robust total least squares (blue: slope = 0.39, intercept = 0.054 ppbv) regression techniques. Robust least squares is an iterative algorithm using reweighted least squares and a bisquare weighting function, where data that lie far from the best fit are given less weight in successive iterations. The r^2 value is calulated via the standard method.
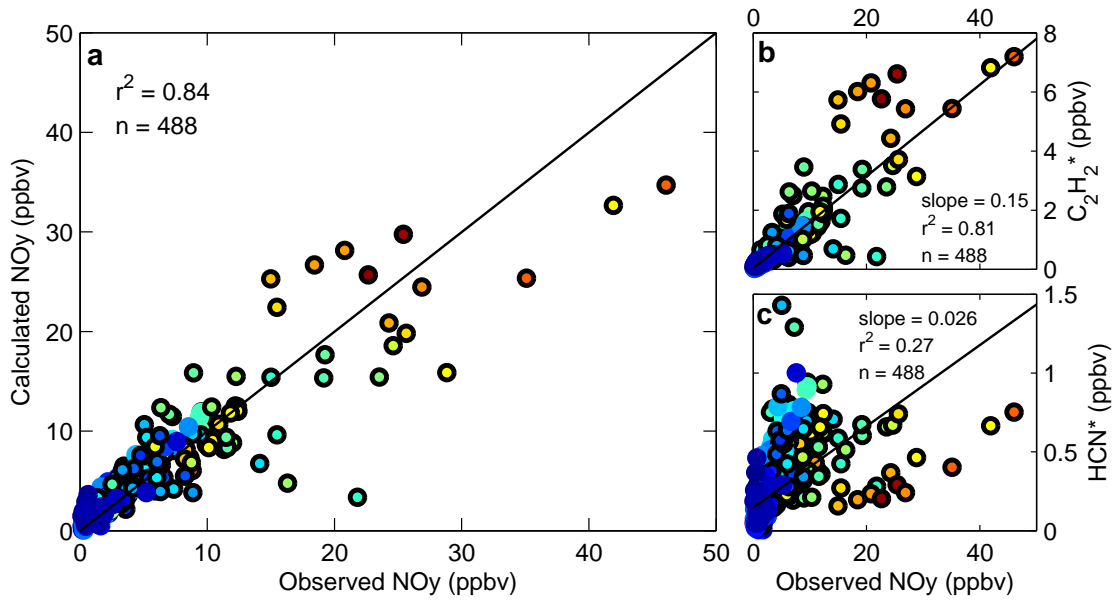
Figure 4.8 – Scatter plot for observed vs. reconstructed NO_y (a). Associated scatter plots for NO_y vs. each tracer, $[C_2H_2]^*$ (b) and $[HCN]^*$ (c). Lines are best fit to all data using total least squares (TLS) regression. Points are colored by $[toluene]/[C_2H_2]^*$, where red=1 and blue=0. Points with black border lie within the 3×3 degree study area.
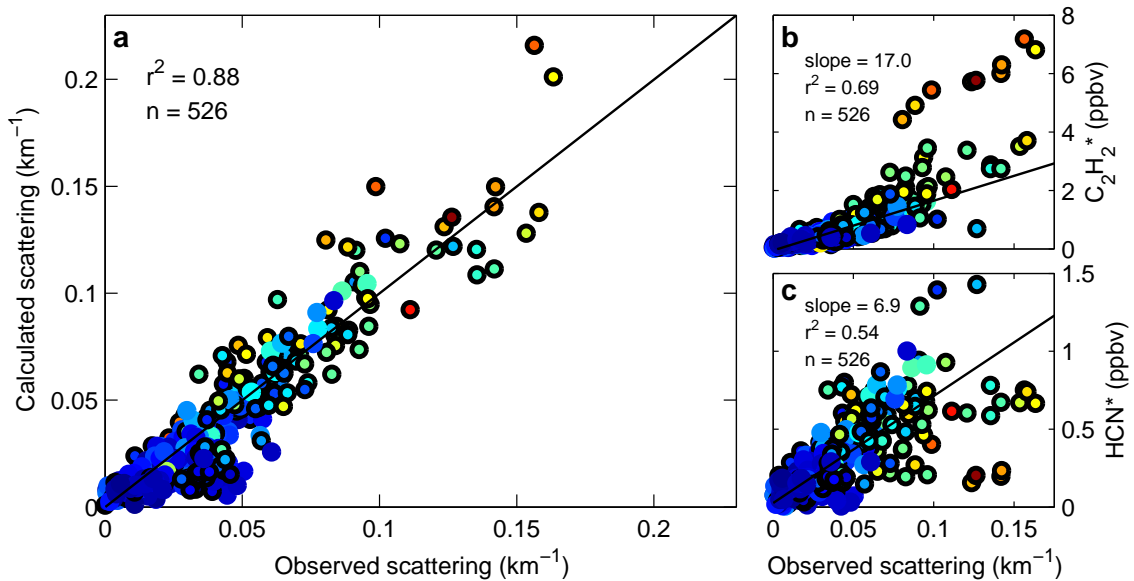
Figure 4.9 – Scatter plot for observed vs. reconstructed submicron scattering **(a)**. Associated scatter plots for submicron scattering vs. each tracer, $[C_2H_2]^*$ **(b)** and $[HCN]^*$ **(c)**. Lines are best fit to all data using total least squares (TLS) regression. Points are colored by $[toluene]/[C_2H_2]^*$, where red=1 and blue=0. Points with black border lie within the 3×3 degree study area.
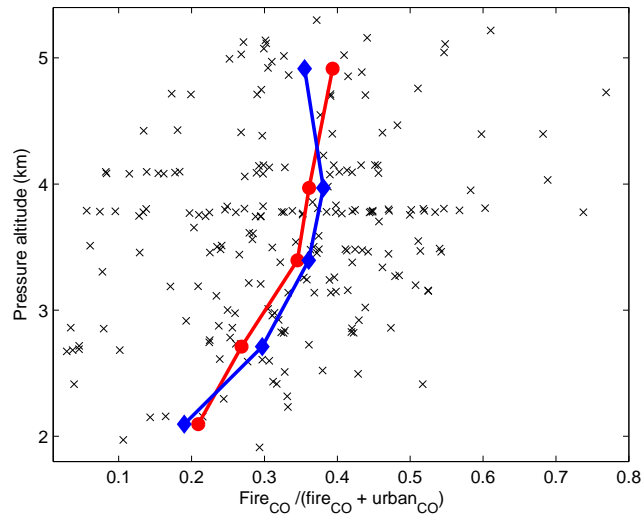
Figure 4.10 – Altitude dependence of fire CO over Mexico City region. The fraction of excess CO (CO-background), which according to the two component analysis comes from biomass burning versus pressure altitude for observations (black x symbols) made within the 3×3 degree study area around Mexico City. Note the ground level in MC is at 2.2 km pressure altitude. The mean (red circles) and median (blue diamonds) averages are shown for 750 m altitude bins.}

Mexico City (Fig. 4.10), suggesting that the smoke from the fires does not fully impact the ground.

4.6.6   Box size for study area

For the ratios of fire impact reported in the body of the main work a rectangular study area of 3×3 degrees, centered on MC, was considered. As one focuses more on MC by decreasing the box size, the urban emissions become relatively more important (Table 4.2). This makes sense considering the fires emissions originate from many diffuse sources (individual fires) scattered across the plateau, while the urban emissions are more centrally located in and around the MC basin. Table 4.2 compares the results for the two-component model using three different box sizes. Box 1 is the smallest, encompassing the populated area of Mexico City and some adjacent terrain. Box 2 is larger and includes the ring of mountains around MC. Box 3 is the largest box, equating to the 3×3 degree box used for the results presented in the main body of this work.

4.6.7   MODIS Aqua satellite image time line

A daily timeline of true color satellite images of the Mexico City area, collected from the MODIS instrument aboard the Aqua satellite, for the month of March 2006 are shown in Figs. 4.11–4.13. The images were taken at approximately 1:30 p.m. local time each day. The red boxes on each satellite

Table 4.2 – Fire impact for pollutants considering several box sizes.

Species	Box 1[a](%)	Box 2[b](%)	Box 3[c](%)
CO	21	28	31
C_6H_6	25	33	36
NO_y	24	31	34
OA	52	61	66
scattering	43	52	57

[a] Box defined by latitude: [19.269 to 19.867] and longitude: [−99.300 to −98.867].
[b] Box defined by latitude: [19.067 to 20.033] and longitude: [−99.433 to −98.667].
[c] Box defined by latitude: [17.900 to 20.900] and longitude: [−100.400 to −97.400].

image represent detected thermal anomalies. One can observe from inspection of the images that many fires are not detected due to a number of reasons, including cloud cover, smoke cover, low fire temperature, or simply lack of satellite coverage. Also, the number of detected fires does not necessarily correlate with the impact of fires on the visibility as observed from the satellite pictures. Higher resolution images are available as supplementary material for both Aqua and Terra images of the Mexico City region during March 2006.

4.7 Acknowledgments

Figure 4.11 – MODIS-Aqua images around Mexico City for 5 March through 13 March 2006. Red boxes represent detected fires. Black lines are state boundaries. Blank areas represent missing data. Images courtesy of MODIS Rapid Response Project at NASA/GSFC.
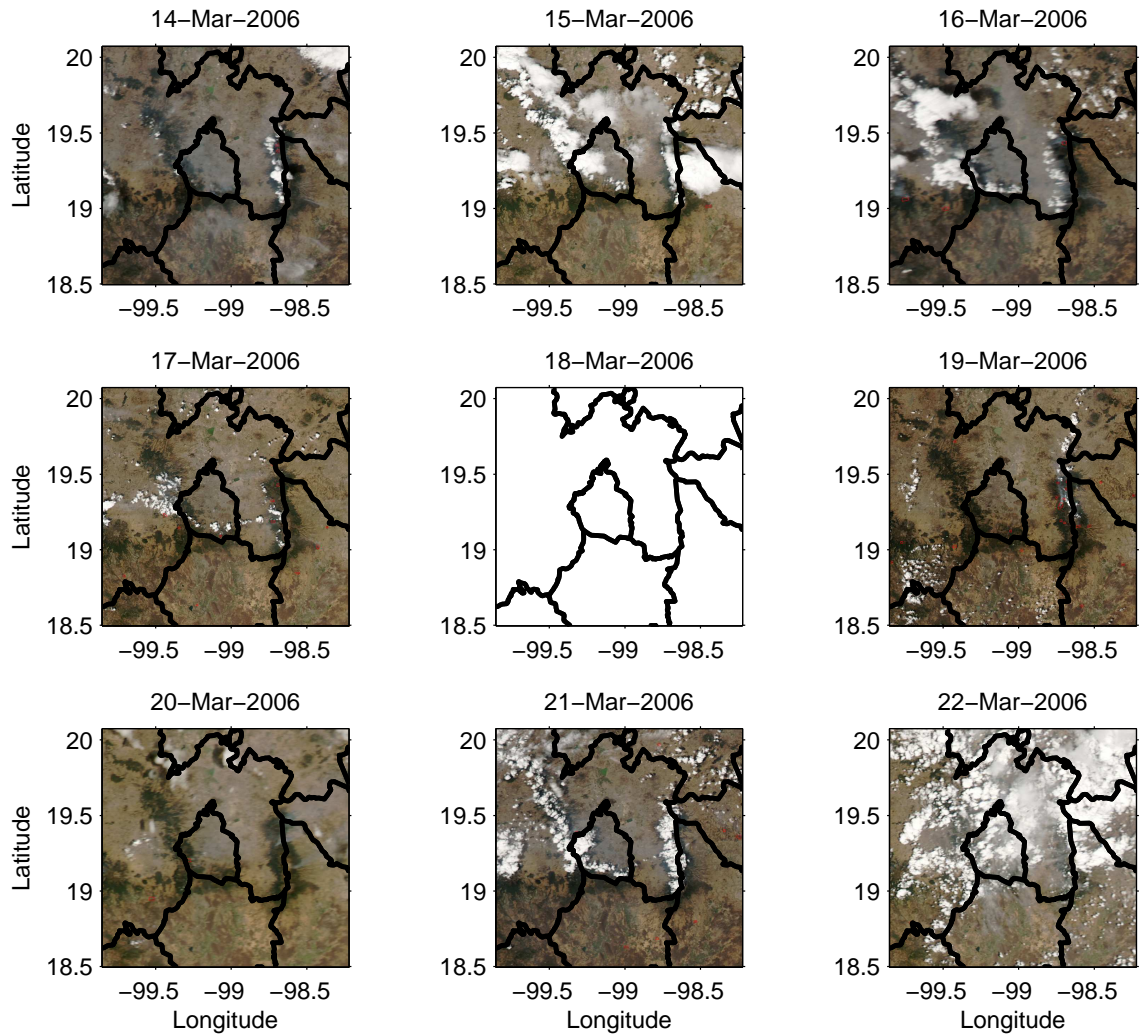
Figure 4.12 – MODIS-Aqua images around Mexico City for 14 March through 22 March 2006. Red boxes represent detected fires. Black lines are state boundaries. Blank areas represent missing data. Images courtesy of MODIS Rapid Response Project at NASA/GSFC.
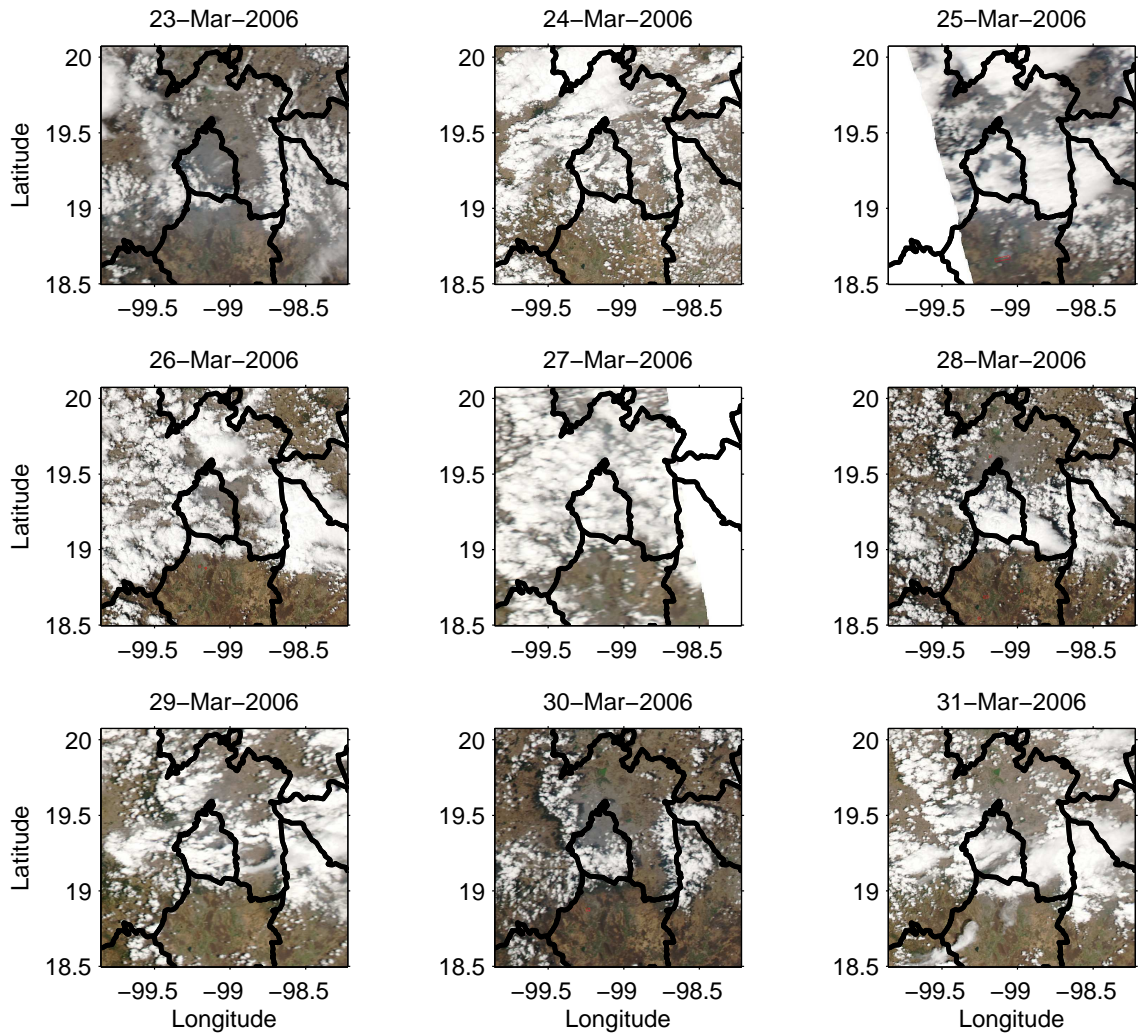
Figure 4.13 – MODIS-Aqua images around Mexico City for 23 March through 31 March 2006. Red boxes represent detected fires. Black lines are state boundaries. Blank areas represent missing data. Images courtesy of MODIS Rapid Response Project at NASA/GSFC.

views expressed in this document are solely those of the authors and the EPA does not endorse any products or commercial services mentioned in this publication.

Bibliography

Aiken, A. C., Salcedo, D., Cubison, M. J., Huffman, J. A., DeCarlo, P. F., Ulbrich, I. M., Docherty, K. S., Sueper, D., Kimmel, J. R., Worsnop, D. R., Trimborn, A., Northway, M., Stone, E. A., Schauer, J. J., Volkamer, R., Fortner, E., de Foy, B., Wang, J., Laskin, A., Shutthanandan, V., Zheng, J., Zhang, R., Gaffney, J., Marley, N. A., Paredes-Miranda, G., Arnott, W. P., Molina, L. T., Sosa, G., and Jimenez, J. L.: Mexico City aerosol analysis during MILAGRO using high resolution aerosol mass spectrometry at the urban supersite (T0) - Part 1: Fine particle composition and organic source apportionment, Atmos. Chem. Phys. Discuss., 9, 8377–8427, URL `http://www.atmos-chem-phys-discuss.net/9/8377/2009/`, 2009.

Anderson, T. L., Masonis, S. J., Covert, D. S., Ahlquist, N. C., Howell, S. G., Clarke, A. D., and McNaughton, C. S.: Variability of aerosol optical properties derived from in situ aircraft measurements during ACE-Asia, J. Geophys. Res.-Atmos., 108, doi:10.1029/2002JD003247, 2003.

Andreae, M. O. and Merlet, P.: Emission of trace gases and aerosols from biomass burning, Global Biogeochem. Cy., 15, 955–966, 2001.

Apel, E. C., Hills, A. J., Lueb, R., Zindel, S., Eisele, S., and Riemer, D. D.: A fast-GC/MS system to measure C_2 to C_4 carbonyls and methanol aboard aircraft, J. Geophys. Res.-Atmos., 108, doi:10.1029/2002JD003199, 2003.

Baum, M. M., Moss, J. A., Pastel, S. H., and Poskrebyshev, G. A.: Hydrogen cyanide exhaust emissions from in-use motor vehicles, Environ. Sci. Technol., 41, 857–862, doi:10.1021/es061402v, 2007.

Blake, N. J., Blake, D. R., Chen, T. Y., Collins, J. E., Sachse, G. W., Anderson, B. E., and Rowland, F. S.: Distribution and seasonality of selected hydrocarbons and halocarbons over the western Pacific basin during PEM-West A and PEM-West B, J. Geophys. Res.-Atmos., 102, 28 315–28 331, 1997.

Bravo, A. H., Sosa, E. R., Sanchez, A. P., Jaimes, P. M., and Saavedra, R. M. I.: Impact of wildfires on the air quality of Mexico City, 1992-1999, Environ. Pollut., 117, 243–253, 2002.

Crounse, J. D., McKinney, K. A., Kwan, A. J., and Wennberg, P. O.: Measurement of gas-phase hydroperoxides by chemical ionization mass spectrometry, Anal. Chem., 78, 6726–6732, doi:10.1021/ac0604235, 2006.

Cubison, M. J., Alfarra, M. R., Allan, J., Bower, K. N., Coe, H., McFiggans, G. B., Whitehead, J. D., Williams, P. I., Zhang, Q., Jimenez, J. L., Hopkins, J., and Lee, J.: The characterisation of pollution aerosol in a changing photochemical environment, Atmos. Chem. Phys., 6, 5573–5588, 2006.

de Gouw, J. A., Middlebrook, A. M., Warneke, C., Goldan, P. D., Kuster, W. C., Roberts, J. M., Fehsenfeld, F. C., Worsnop, D. R., Canagaratna, M. R., Pszenny, A. A. P., Keene, W. C., Marchewka, M., Bertman, S. B., and Bates, T. S.: Budget of organic carbon in a polluted atmosphere: Results from the New England Air Quality Study in 2002, J. Geophys. Res.-Atmos., 110, doi:10.1029/2004JD005623, 2005.

de Gouw, J. A., Welsh-Bon, D., Warneke, C., Kuster, W. C., Alexander, L., Baker, A. K., Beyersdorf, A. J., Blake, D. R., Canagaratna, M., Celada, A. T., Huey, L. G., Junkermann, W., Onasch, T. B., Salcido, A., Sjostedt, S. J., Sullivan, A. P., Tanner, D. J., Vargas, O., Weber, R. J., Worsnop, D. R., Yu, X. Y., and Zaveri, R.: Emission and chemistry of organic carbon in the gas and aerosol phase at a suburban site near Mexico City in March 2006 during the MILAGRO study, Atmos. Chem. Phys., 9, 3425–3442, URL http://www.atmos-chem-phys.net/9/3425/2009/, 2009.

DeCarlo, P. F., Kimmel, J. R., Trimborn, A., Northway, M. J., Jayne, J. T., Aiken, A. C., Gonin, M., Fuhrer, K., Horvath, T., Docherty, K. S., Worsnop, D. R., and Jimenez, J. L.: Field-deployable, high-resolution, time-of-flight aerosol mass spectrometer, Anal. Chem., 78, 8281–8289, doi:10.1021/ac061249n, 2006.

DeCarlo, P. F., Dunlea, E. J., Kimmel, J. R., Aiken, A. C., Sueper, D., Crounse, J., Wennberg, P. O., Emmons, L., Shinozuka, Y., Clarke, A., Zhou, J., Tomlinson, J., Collins, D. R., Knapp, D., Weinheimer, A. J., Montzka, D. D., Campos, T., and Jimenez, J. L.: Fast airborne aerosol size and chemistry measurements above Mexico City and Central Mexico during the MILAGRO campaign, Atmos. Chem. Phys., 8, 4027–4048, 2008.

Efron, B. and Tibshirani, R. J.: An Introduction to the Bootstrap, Monographs on Statistics and Applied Probability, 57, 1–177, 1993.

Fast, J. D., de Foy, B., Rosas, F. A., Caetano, E., Carmichael, G., Emmons, L., McKenna, D., Mena, M., Skamarock, W., Tie, X., Coulter, R. L., Barnard, J. C., Wiedinmyer, C., and Madronich, S.: A meteorological overview of the MILAGRO field campaigns, Atmos. Chem. Phys., 7, 2233–2257, 2007.

Fast, J. D., Aiken, A. C., Allan, J., Alexander, L., Campos, T., Canagaratna, M. R., Chapman, E., DeCarlo, P. F., de Foy, B., Gaffney, J., de Gouw, J., Doran, J. C., Emmons, L., Hodzic, A., Herndon, S. C., Huey, G., Jayne, J. T., Jimenez, J. L., Kleinman, L., Kuster, W., Marley, N., Russell, L., Ochoa, C., Onasch, T. B., Pekour, M., Song, C., Ulbrich, I. M., Warneke, C., Welsh-Bon, D., Wiedinmyer, C., Worsnop, D. R., Yu, X.-Y., and Zaveri, R.: Evaluating simulated primary anthropogenic and biomass burning organic aerosols during MILAGRO: implications for assessing treatments of secondary organic aerosols, Atmos. Chem. Phys. Discuss., 9, 4805–4871, URL `http://www.atmos-chem-phys-discuss.net/9/4805/2009/`, 2009.

Gerbig, C., Schmitgen, S., Kley, D., Volz-Thomas, A., Dewey, K., and Haaks, D.: An improved fast-response vacuum-UV resonance fluorescence CO instrument, J. Geophys. Res.-Atmos., 104, 1699–1704, 1999.

Giglio, L., Descloitres, J., Justice, C. O., and Kaufman, Y. J.: An enhanced contextual fire detection algorithm for MODIS, Remote Sens. Environ., 87, 273–282, doi:10.1016/S0034-4257(03)00184-6, 2003.

Grosjean, E., Grosjean, D., and Rasmussen, R. A.: Ambient concentrations, sources, emission rates, and photochemical reactivity of C_2-C_{10} hydrocarbons in Porto Alegre, Brazil, Environ. Sci. Technol., 32, 2061–2069, 1998.

Harvey, C. A., Garbe, R. J., Baines, T. M., Somers, J. H., Hellman, K. H., and Carey, P. M.: A study of the potential impact of some unregulated motor vehicle emissions, SAE Transactions, 92, 3–3, 1983.

Horowitz, L. W., Walters, S., Mauzerall, D. L., Emmons, L. K., Rasch, P. J., Granier, C., Tie, X. X., Lamarque, J. F., Schultz, M. G., Tyndall, G. S., Orlando, J. J., and Brasseur, G. P.: A global simulation of tropospheric ozone and related tracers: Description and evaluation of MOZART, version 2, J. Geophys. Res.-Atmos., 108, doi:10.1029/2002JD002853, 2003.

Kleinman, L. I., Springston, S. R., Daum, P. H., Lee, Y. N., Nunnermacker, L. J., Senum, G. I., Wang, J., Weinstein-Lloyd, J., Alexander, M. L., Hubbe, J., Ortega, J., Canagaratna, M. R., and Jayne, J.: The time evolution of aerosol composition over the Mexico City plateau, Atmos. Chem. Phys., 8, 1559–1575, 2008.

Kroll, J. H. and Seinfeld, J. H.: Chemistry of secondary organic aerosol: Formation and evolu-

tion of low-volatility organics in the atmosphere, Atmos. Environ., 42, 3593–3624, doi:10.1016/j. atmosenv.2008.01.003, 2008.

Leppalahti, J. and Koljonen, T.: Nitrogen evolution from coal, peat and wood during gasification - Literature-review, Fuel Process. Technol., 43, 1–45, 1995.

Li, Q., Jacob, D., Yantosca, R., Heald, C., Singh, H., Koike, M., Zhao, Y., Sachse, G., and Streets, D.: A global three-dimensional model analysis of the atmospheric budgets of HCN and CH_3CN: Constraints from aircraft and ground measurements, J. Geophys. Res.-Atmos., 108, doi:10.1029/ 2002JD003075, 2003.

Li, Q. B., Jacob, D. J., Bey, I., Yantosca, R. M., Zhao, Y. J., Kondo, Y., and Notholt, J.: Atmospheric hydrogen cyanide (HCN): Biomass burning source, ocean sink?, Geophys. Res. Lett., 27, 357–360, 2000.

Lloyd, A. C.: California clean-air initiatives - The role of fuel cells, J. Power Sources, 37, 241–253, 1992.

McKinley, G., Zuk, M., Hojer, M., Avalos, M., Gonzalez, I., Iniestra, R., Laguna, I., Martinez, M. A., Osnaya, P., Reynales, L. M., Valdes, R., and Martinez, J.: Quantification of local and global benefits from air pollution control in Mexico City, Environ. Sci. Technol., 39, 1954–1961, doi:10.1021/es035183e, 2005.

Moffet, R. C., de Foy, B., Molina, L. T., Molina, M. J., and Prather, K. A.: Measurement of ambient aerosols in northern Mexico City by single particle mass spectrometry, Atmos. Chem. Phys., 8, 4499–4516, 2008.

Molina, L. T. and Molina, M. J.: Air Quality in the Mexico Megacity: An Integrated Assessment, Kluwer Academic Publishers, 2002.

Molina, L. T., Kolb, C. E., de Foy, B., Lamb, B. K., Brune, W. H., Jimenez, J. L., Ramos-Villegas, R., Sarmiento, J., Paramo-Figueroa, V. H., Cardenas, B., Gutierrez-Avedoy, V., and Molina, M. J.: Air quality in North America's most populous city – overview of the MCMA-2003 campaign, Atmos. Chem. Phys., 7, 2447–2473, 2007.

Muhle, J., Lueker, T. J., Su, Y., Miller, B. R., Prather, K. A., and Weiss, R. F.: Trace gas and particulate emissions from the 2003 Southern California wildfires, J. Geophys. Res.-Atmos., 112, doi:10.1029/2006JD007350, 2007.

NEI: Mexico National Emissions Inventory, 1999, URL `http://www.epa.gov/ttn/chief/net/mexico/` `1999_mexico_nei_final_report.pdf`, 2008.

Ratcliff, M. A., Medley, E. E., and Simmonds, P. G.: Pyrolysis of amino-acids – Mechanistic considerations, J. Org. Chem., 39, 1481–1490, 1974.

Robinson, A. L., Donahue, N. M., Shrivastava, M. K., Weitkamp, E. A., Sage, A. M., Grieshop, A. P., Lane, T. E., Pierce, J. R., and Pandis, S. N.: Rethinking organic aerosols: Semivolatile emissions and photochemical aging, Science, 315, 1259–1262, doi:10.1126/science.1133061, 2007.

Salcedo, D., Onasch, T. B., Dzepina, K., Canagaratna, M. R., Zhang, Q., Huffman, J. A., DeCarlo, P. F., Jayne, J. T., Mortimer, P., Worsnop, D. R., Kolb, C. E., Johnson, K. S., Zuberi, B., Marr, L. C., Volkamer, R., Molina, L. T., Molina, M. J., Cardenas, B., Bernabe, R. M., Marquez, C., Gaffney, J. S., Marley, N. A., Laskin, A., Shutthanandan, V., Xie, Y., Brune, W., Lesher, R., Shirley, T., and Jimenez, J. L.: Characterization of ambient aerosols in Mexico City during the MCMA-2003 campaign with Aerosol Mass Spectrometry: Results from the CENICA Supersite, Atmos. Chem. Phys., 6, 925–946, 2006.

Sigsby, J. E., Tejada, S., Ray, W., Lang, J. M., and Duncan, J. W.: Volitile organic-compound emissions from 46 in-use passenger cars, Environ. Sci. Technol., 21, 466–475, 1987.

Singh, H. B., Salas, L., Herlth, D., Kolyer, R., Czech, E., Viezee, W., Li, Q., Jacob, D. J., Blake, D., Sachse, G., Harward, C. N., Fuelberg, H., Kiley, C. M., Zhao, Y., and Kondo, Y.: In situ measurements of HCN and CH_3CN over the Pacific Ocean: Sources, sinks, and budgets, J. Geophys. Res.-Atmos., 108, doi:10.1029/2002JD003006, 2003.

Solomon, S., Qin, D., Manning, M., Chen, Z., Marquis, M., Averyt, K., Tignor, M., and Miller, H.: IPCC, 2007: Climate Change 2007: The Physical Science Basis. Contribution of Working Group I to the Fourth Assessment Report of the Intergovernmental Panel on Climate Change, 2007.

Stone, E. A., Snyder, D. C., Sheesley, R. J., Sullivan, A. P., Weber, R. J., and Schauer, J. J.: Source apportionment of fine organic aerosol in Mexico City during the MILAGRO experiment 2006, Atmos. Chem. Phys., 8, 1249–1259, 2008.

Volkamer, R., Jimenez, J. L., San Martini, F., Dzepina, K., Zhang, Q., Salcedo, D., Molina, L. T., Worsnop, D. R., and Molina, M. J.: Secondary organic aerosol formation from anthropogenic air pollution: Rapid and higher than expected, Geophys. Res. Lett., 33, doi:10.1029/2006GL026899, 2006.

Weber, R. J., Sullivan, A. P., Peltier, R. E., Russell, A., Yan, B., Zheng, M., de Gouw, J., Warneke, C., Brock, C., Holloway, J. S., Atlas, E. L., and Edgerton, E.: A study of secondary organic aerosol formation in the anthropogenic-influenced southeastern United States, J. Geophys. Res.-Atmos., 112, doi:10.1029/2007JD008408, 2007.

WHO: Air Quality and Health, URL `http://www.who.int/mediacentre/factsheets/fs313/en/index.html`, 2008.

Wiedinmyer, C., Quayle, B., Geron, C., Belote, A., McKenzie, D., Zhang, X., O'Neill, S., and Wynne, K. K.: Estimating emissions from fires in North America for air quality modeling, Atmos. Environ., 40, 3419–3432, doi:10.1016/j.atmosenv.2006.02.010, 2006.

Xiao, Y., Jacob, D. J., and Turquety, S.: Atmospheric acetylene and its relationship with CO as an indicator of air mass age, J. Geophys. Res.-Atmos., 112, doi:10.1029/2006JD008268, 2007.

Yokelson, R. J., Karl, T., Artaxo, P., Blake, D. R., Christian, T. J., Griffith, D. W. T., Guenther, A., and Hao, W. M.: The Tropical Forest and Fire Emissions Experiment: Overview and airborne fire emission factor measurements, Atmos. Chem. Phys., 7, 5175–5196, 2007a.

Yokelson, R. J., Urbanski, S. P., Atlas, E. L., Toohey, D. W., Alvarado, E. C., Crounse, J. D., Wennberg, P. O., Fisher, M. E., Wold, C. E., Campos, T. L., Adachi, K., Buseck, P. R., and Hao, W. M.: Emissions from forest fires near Mexico City, Atmos. Chem. Phys., 7, 5569–5584, 2007b.

Chapter 5

Emissions from biomass burning in the Yucatan*

5.1 Abstract

In March 2006 two instrumented aircraft made the first detailed field measurements of biomass burning (BB) emissions in the northern hemisphere tropics as part of the MILAGRO project. The aircraft were the National Center for Atmospheric Research C-130 and a University of Montana/US Forest Service Twin Otter. The initial emissions of up to 49 trace gas or particle species were measured from 20 deforestation and crop residue fires on the Yucatan peninsula. This included two trace gases useful as indicators of BB (HCN and acetonitrile) and several rarely, or never before, measured species: OH, peroxyacetic acid, propanoic acid, hydrogen peroxide, methane sulfonic acid, and sulfuric acid. Crop residue fires emitted more organic acids and ammonia than deforestation fires, but the emissions from the main fire types were otherwise fairly similar. The Yucatan fires emitted unusually high amounts of SO_2 and particle chloride, likely due to a strong marine influence on this peninsula. As smoke from one fire aged, the ratio $\Delta O_3/\Delta CO$ increased to $\sim 15\%$ in $< \sim 1$ h similar to the fast net production of O_3 in BB plumes observed earlier in Africa. The rapid change in O_3 occurs at a finer spatial scale than is employed in global models and is also faster than predicted by micro-scale models. Fast increases in PAN, H_2O_2, and two organic acids were also observed. The amount of secondary organic acid is larger than the amount of known precursors. Rapid secondary formation of organic and inorganic aerosol was observed with the ratio $\Delta PM_{2.5}/\Delta CO$ more than doubling in $\sim 1.4 \pm 0.7$ h. The OH measurements revealed high initial levels ($>1 \times 10^7$ molecules cm^{-3}) that were likely caused in part by high initial HONO ($\sim 10\%$ of NO_y). Thus, more research is needed to understand critical post-emission processes for the second-largest trace gas source on Earth. It is estimated that ~ 44 Tg of biomass burned in the Yucatan in the spring of 2006. Mexican BB (including Yucatan BB) and urban emissions from the Mexico City area can both influence the March–May air quality in much of Mexico and the US.

5.2 Introduction

The MILAGRO (Megacity Initiative Local and Global Research Observations) project was designed to study the local to global atmospheric affects of pollution from megacities (`http://www.eol.ucar.edu/projects/milagro`). Megacities have a population > 10 million and are rapidly increasing in number on the five most populated continents. The first MILAGRO field campaigns occurred in March 2006 and studied the impact of trace gases and particles generated in Mexico City (MC, North America's largest metropolitan area) on regional atmospheric chemistry (Fast et al., 2007;

Molina et al., 2007). Regional biomass burning (BB) was also studied because it is a major emission source in Mexico that peaks during the February–May dry season. Earlier papers estimated that BB located adjacent to MC accounted for ∼20–30% of the CO (and several other important trace gases) and about one-half of the particle mass in the March 2006 MC outflow (Yokelson et al., 2007b; Crounse et al., 2009). Another very important source of BB emissions in the MILAGRO study region is the Yucatan, which accounts for 7% of Mexico's land area, but almost 30% of the total biomass burned in Mexico annually (2002–2006 average) and almost 40% of the biomass burned in Mexico in 2006. (Section 5.5 describes the model used to generate these estimates.) From the perspective of the MILAGRO campaign, Yucatan BB emissions are important because MC and the Yucatan impact nearly the same regional environment and Yucatan emissions can be transported to MC or interact with the MC plume downwind of the city. For example, in 1998 intense BB in the Yucatan impacted air quality in much of Mexico and the US (Kreidenweis et al., 2001). Yucatan BB is also of interest beyond the scope of the MILAGRO campaign. On a global basis, BB is the largest source of primary fine carbonaceous particles, the second largest source of trace gases, and it occurs mostly in the tropics, which play a critical role in global atmospheric chemistry (Andreae and Merlet, 2001; Kreidenweis et al., 2001). However, both the initial emissions from BB and the post-emission chemistry in smoke are poorly characterized and MILAGRO offered an opportunity to study these topics with well-equipped research aircraft. Further, most of the research on BB has been done in the southern hemisphere (SH) tropics during the SH dry season June–October (Andreae and Merlet, 2001). However, significant amounts of BB also occur in the northern hemisphere (NH) tropics, which experience a dry season and a peak in BB in February–May. Major fire theatres in the NH tropics include the Indochina peninsula, the Indian subcontinent, the Sahel region of Africa, northern South America, Central America, and the Yucatan (Lacaux et al., 1996, http://maps.geog.umd.edu). Finally, the tropical dry forests of the Yucatan are an example of the ecosystem that accounts for the most biomass burned globally (Desanker et al., 1997). Emissions measurements have been made in the tropical dry, "Miombo" forests of Africa (Sinha et al., 2004). However, the Miombo region is minimally developed with mostly understory burning and only limited, primitive slash and burn agriculture (Desanker et al., 1997). In contrast, the Yucatan has high rates of forest clearing (using fire) for conversion to mechanized agriculture and also burning of residues from existing crops. This paper presents the first detailed measurements of the initial trace gas and particle emissions from fires in the NH tropics (up to 49 species on 20 fires). It includes the first *in situ* measurement of OH in a BB plume and measurements of numerous post-emission changes in trace gas and particle

species in one plume. Only a few observations of the chemical evolution of individual BB plumes have been made (Goode et al., 2000; Yokelson et al., 2003; Jost et al., 2003; Hobbs et al., 2003; Abel et al., 2003) and the observed evolution is only partially reproduced by models (Tabazadeh et al., 2004; Trentmann et al., 2005; Mason et al., 2006; Alvarado and Prinn, 2009). Thus, these measurements of smoke evolution add substantially to our limited knowledge of this topic. We estimate the monthly to annual production of fire emissions from the Yucatan and summarize their regional transport to show the impact of these fires on the region. Finally, some general comments on global NH tropical biomass burning are offered.

5.3   Experimental details

Due to the large number of instruments deployed on the two research aircraft we can only present a list of the species measured and a few basic details here. More detail is found on all the instruments on the Twin Otter in Yokelson et al. (2007b) and in various other papers cited for each C-130 measurement.

5.3.1   Measurements on the Twin Otter

The University of Montana airborne Fourier transform infrared spectrometer (AFTIR) measured samples temporarily detained in the flow-through gas cell to quantify water vapor (H_2O), carbon dioxide (CO_2), carbon monoxide (CO), methane (CH_4), nitric oxide (NO), nitrogen dioxide (NO_2), ammonia (NH_3), hydrogen cyanide (HCN), ethene (C_2H_4), acetylene (C_2H_2), formaldehyde (HCHO), methanol (CH_3OH), acetic acid ($CH_3C(O)OH$), formic acid (HC(O)OH), and ozone (O_3). Ram air was grab-sampled into stainless steel canisters (whole air sampling (WAS)) that were later analyzed at the University of Miami by gas chromatography (GC) with a flame ionization detector (FID) for CH_4, and the following non-methane hydrocarbons (NMHC): ethane, C_2H_4, C_2H_2, propane, propene, isobutane, n-butane, t-2-butene, 1-butene, isobutene, c-2-butene, 1,3-butadiene, cyclopentane, isopentane, and n-pentane. CO was measured in parallel with the CH_4 measurement, but utilized GC with a Trace Analytical Reduction Gas Detector (RGD). Canisters were also collected for later analysis at the United States Forest Service (USFS) Fire Sciences Laboratory by GC/FID/RGD for CO_2, CO, CH_4, H_2, and several C_2-C_3 hydrocarbons. The canister-filling inlet (large diameter, fast flow) also supplied sample air for a Radiance Research Model 903 integrating nephelometer that measured "dry" (inlet RH < 20%) b_{scat} at 530 nm at 0.5 Hz. The b_{scat} measured

at the inlet temperature and pressure was converted to b_{scat} at standard temperature and pressure (STP, 273 K, 1 atm) and then multiplied by 208800±11900 to yield the mass of particles with aerodynamic diameter < 2.5 microns ($PM_{2.5}$) in $\mu g\ sm^{-3}$ of air, based on a gravimetric "calibration" similar to that described in Trent et al. (2000). An isokinetic particle inlet sampled fine particles with a diameter cut-off of a few microns. Particles of diameter < 1 micron account for nearly all the fine particle ($PM_{2.5}$) mass emitted by biomass fires (Radke et al., 1991). This inlet supplied sample air to two particle samplers (MPS-3, California Measurements, Inc.) that were used to collect aerosol particles onto transmission electron microscope (TEM) grids in three size ranges over time intervals of ∼l to 10 minutes for subsequent TEM analyses. Details of the analyses are described in Adachi and Buseck (2008). The same inlet also supplied a LiCor (Model #7000) measuring CO_2 and H_2O at 5 Hz and a UHSAS (Ultra High Sensitivity Aerosol Spectrometer, Particle Metrics, Inc.) deployed by the University of Colorado (CU). The UHSAS provided the number of particles in each of 99 user-selectable bins for diameters between 55 and 1000 nm at 1 Hz. All three Twin Otter inlets were located within 30 cm of each other. The nephelometer was not available on the 12 March flight so we used the UHSAS particle counting/size data to indirectly determine particle mass. We assumed spherical particles and integrated over the dry size distribution measured by the UHSAS, to obtain an estimate of the volume of particles (PV_1, $\mu m^3\ cm^{-3}$) of air at 1 Hz. We then noted that on 22 and 29 of March the PV_1 (for $PV_1 < \sim30$) was related to b_{scat} as follows:

$$b_{scat} = PV_1 \times 1.25(\pm0.25) \times 10^{-5} \qquad (5.1)$$

On March 12, the PV_1 did not exceed 30 $\mu m^3\ cm^{-3}$ in the plume of Fire #3. We used equation 1 to convert PV_1 to b_{scat} and then converted b_{scat} to $PM_{2.5}$ as described above.

5.3.2 Measurements on the C-130

5.3.2.1 Continuous measurements

The continuous measurements are listed in order of their sampling frequency starting with nominal 1 s resolution. A CO vacuum ultraviolet (VUV) resonance fluorescence instrument, similar to that of Gerbig et al. (1999), was operated on the C-130 through the National Center for Atmospheric Research (NCAR) and NSF. Sulfur dioxide (SO_2) was measured by the NOAA UV pulsed fluorescence instrument (Thermo Electron model 43C-TL modified for aircraft use). O_3, NO, NO_2, and NO_y (the sum of all N-containing species minus HCN, NH_3, and N_2) were measured by the NCAR

chemiluminescence instrument (Ridley et al., 2004). Formaldehyde was measured by the NCAR difference frequency generation (DFG) airborne spectrometer (Weibring et al., 2007). The absorption (530 nm), scattering (550 nm), number, and size distribution of dry particles was measured at 1–10 s resolution by a particle soot absorption photometer (PSAP), nephelometer (TSI 3563), and optical particle counter (OPC) all deployed by the University of Hawaii (Clarke et al., 2004). The total 550 nm scattering was converted to STP scattering and then $PM_{2.5}$ (μg sm^{-3}) using a dry mass scattering efficiency (MSE) of 4.8$\pm$1.0 obtained for a USFS TSI model 3563 during the gravimetric calibration carried out for the Twin Otter nephelometer. The absorption was used directly with the scattering to calculate single scattering albedo (SSA) or converted to an estimated black carbon in μg sm^{-3} using a mass absorption efficiency (MAE) of 12$\pm$4 (Martins et al., 1998). The NCAR Scanning Actinic Flux Spectroradiometers measured 25 J-values at 10 s resolution (Shetter and Muller, 1999). An NCAR selected ion chemical ionization mass spectrometer (SICIMS) measured the hydroxyl radical (OH), sulfuric acid (H_2SO_4), and methane sulfonic acid (MSA) at 30 s time resolution (Mauldin et al., 2003).

5.3.2.2 Discrete measurements

The PAN-CIGARette (PAN-CIMS Instrument by Georgia Tech and NCAR, small version, Slusher et al., 2004) measured compounds collectively referred to as PANs (PAN, peroxyacetyl nitrate; PPN, peroxypropionyl nitrate; PBN, peroxybutyryl nitrates = sum of peroxy-n-butyryl- and peroxyisobutyryl nitrates; MoPAN, Methoxyperoxyacetyl nitrate; APAN, peroxyacryloyl nitrate; MPAN, peroxymethacryloyl nitrate) in turn on a 2 s cycle. A California Institute of Technology (Caltech) CIMS measured a suite of organic acids (acetic, peroxyacetic, formic, and propanoic acid); and SO_2, HCN, hydrogen peroxide (H_2O_2), nitrous acid (HONO), and nitric acid (HNO_3). The mixing ratio of each species was measured for 0.5 s, in turn during a multispecies scan, with a period ranging from 4–20 s for each analyte (Crounse et al., 2006). An Aerodyne high-resolution time-of-flight aerosol mass spectrometer (HR-ToF-AMS) operated by CU (DeCarlo et al., 2006, 2008; Aiken et al., 2008) measured the organic aerosol mass (OA); the OA to organic carbon (OC) mass ratio; and non-refractory (NR) sulfate, nitrate, ammonium, and chloride (μg sm^{-3} 1 atm, 273 K) for the last 6 seconds of each 12 s measurement cycle. (The first 6 s of each cycle measured size distributions.) At times continuous 4 s particle chemistry averages were recorded instead. A proton transfer mass spectrometer (PTR-MS) measured CH_3OH, acetonitrile (CH_3CN), acetaldehyde, acetone, methyl ethyl ketone, methyl propanal, hydroxyacetone plus methyl acetate, benzene, and 13 other species

in a 35 s cycle (Karl et al., 2007, 2009).

5.3.3 Generalized airborne sampling protocol

The Twin Otter and C-130 were based in Veracruz with other MILAGRO research aircraft. The main goal of the Twin Otter flights was to sample fires and the C-130 also sampled a few fires. On both aircraft, background air (i.e., ambient boundary layer (BL) air not in plumes) was characterized when not sampling BB plumes. The continuous instruments operated in real time in background air. The discrete instruments acquired numerous spot measurements in background air. These spot measurements should be representative since the continuous instruments showed that the background air was well-mixed on the spatial scale corresponding to the discrete sampling intervals.

To measure the initial emissions from the fires, the aircraft usually sampled smoke less than several minutes old by penetrating the column of smoke 150–600 m above the active flame front. A few "fresh" smoke samples up to 10–30 minutes old were acquired at elevations up to 1700 m. The continuous instruments monitored their species while penetrating the plume up to five times per fire. On the Twin Otter, the AFTIR, MPS-3, and WAS were used for spot measurements in the smoke plumes. To allow calculation of excess concentrations in the smoke plume; paired background spot measurements were made just outside the plume. The discrete instruments on the C-130 always acquired at least one sample, and usually several, that were within the fresh smoke plumes. The background for those samples was taken as the average of the discrete measurements in the background air near the plume.

More than a few kilometers downwind from the source, smoke samples are already "photochemically aged" and better for probing post-emission chemistry than estimating initial emissions (Goode et al., 2000; Hobbs et al., 2003). Both aircraft acquired some samples in aged plumes up to ∼14 km downwind and ∼1.5 h old (see Section 5.4.4).

5.3.4 Data processing and synthesis

Grab, or discrete, samples of both a plume and the adjacent background can be used to calculate excess mixing ratios (ΔX, the mixing ratio of species "X" in the plume minus the mixing ratio of "X" in the background air). ΔX reflects the degree of dilution of the plume and the instrument response time. Thus, a useful, derived quantity is the normalized excess mixing ratio (NEMR) where ΔX is divided by the "simultaneously" measured excess mixing ratio of another species (ΔY); usually a fairly long-lived plume "tracer" such as ΔCO or ΔCO_2. The uncertainty in the NEMR includes a

contribution due to differences in response times if two instruments are involved. A measurement of $\Delta X / \Delta Y$ in a plume up to a few minutes old is a molar emission ratio (ER). We computed fire-average molar ER for each individual fire from grab or discrete samples as follows. First, if there is only one sample of a fire then the calculation is trivial and equivalent to the definition of $\Delta X / \Delta Y$ given above. For multiple grab (or discrete) samples of a fire, the fire-average, ER was obtained from the slope of the least squares line (with the intercept forced to zero) in a plot of one set of excess mixing ratios versus another. This method is justified in detail by Yokelson et al. (1999). When the AFTIR and the USFS WAS measured the same pair of compounds on the same fire, their data were combined in the plots as shown in Figure 5.1a.

Emission ratios can also be obtained from the continuous instruments by comparing the integrals of ΔX and ΔY as the aircraft passes through a nascent smoke plume. Comparing the integrals helps compensate for the different instrument response times (Karl et al., 2007). When only one pass is made through the plume of a fire (as on the C-130), the ratio of those integrals gives the ER. When more than one pass is made through the plume of a single fire with continuous instruments (e.g. PM and CO_2 on the Twin Otter), we plot the integrals versus each other and obtain the ER from the slope, analogous to grab sample plots. For the C-130 we usually compared integrals for various species to the integrals for CO. The exception was the PTR-MS. For the PTR-MS we obtained ER to methanol averaged over the three C-130 fires by comparing the integrated excess for all three fires to the integrated excess amount for methanol. Finally, it is sometimes possible to use a "proxy" to generate continuous data from discrete samples. For example, the ratio of HCN to NO_y should not vary much throughout an individual plume. Thus, an estimate of the real-time variation in HCN can be obtained by multiplying the continuous NO_y data by the HCN/NO_y ratio measured intermittently in the plume. Subsequently, the "continuous" HCN trace can be integrated and compared to integrals from other continuous instruments such as CO. For two species measured discretely by the Caltech CIMS (SO_2 and HCN) it was meaningful to compare the "integral-based" ER to CO to the "plot-based" ER to CO. In comparison to the integral-based ER, the plot-based approach returned individual fire ER that were less than 10% different when 2–3 minutes were spent in plume and up to 19% different for brief sample periods. The ER obtained from the plot-based method did not show significant bias when averaged over all five comparable samples (the plot-based ER was 0.998±0.14 of the integral based ER).We take this as a rough estimate of the additional uncertainty affecting the study-average ER calculated from discrete samples. The lack of bias makes sense since, e.g., a slower-responding CO instrument could read a little low when entering the plume,
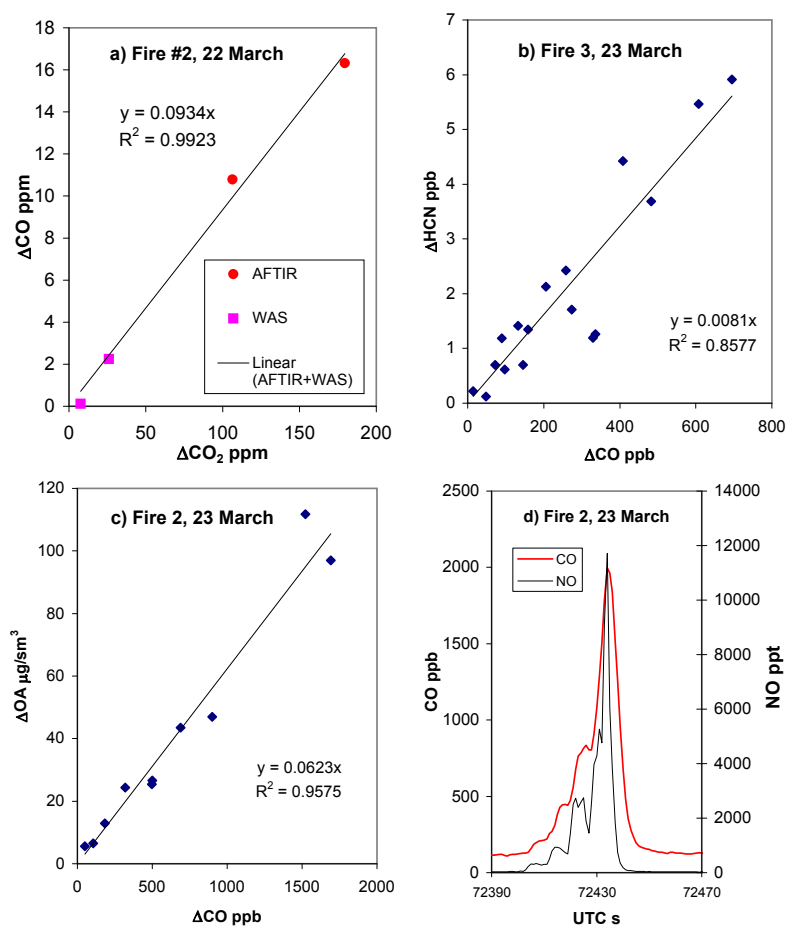
Figure 5.1 – a) WAS and AFTIR spot measurements were coupled to determine the ER $\Delta CO/\Delta CO_2$ on the Twin Otter and they agreed well with each other. This is a key quantity used to synthesize data from the two aircraft. b) The $\Delta HCN/\Delta CO$ ER from plotting discrete CIMS samples vs. the CO measured at the same time for all data in the fresh and aging plume of Fire #3. The slope of the plot gives the same ER as the proxy method (Section 5.3.4). $\Delta HCN/\Delta CO$ does not vary greatly in the downwind samples. c) Four-second averages for ΔOA from the AMS plotted versus the 4-s averages of ΔCO. d) Continuous NO and CO for same fire as in c). Comparison of the integrated amounts above background yields the ER.

but a little high when leaving the plume. Figure 5.1 illustrates typical analyte levels encountered and gives examples of ER derivations.

It is also possible to estimate ER from measurements that were not made simultaneously, or that were made on different aircraft. For example, the molar ER to CO_2 for the NMHC measured by U-Miami WAS on the Twin Otter was derived for each fire as follows. The molar ER to CO measured by WAS from a fire was multiplied by the molar $\Delta CO/\Delta CO_2$ ER measured on that same fire by AFTIR. The study-average molar ER to CO_2 for species measured on the C-130 (no CO_2 data on C-130) was estimated by multiplying the C-130 molar emission ratio to CO or CH_3OH by the study-average molar emission ratio of these latter species to CO_2 measured by AFTIR/WAS on board the Twin Otter (on different fires). CO was measured with high accuracy by AFTIR, the VUV instrument, and WAS. Methanol was measured with high accuracy by the AFTIR and PTR-MS. This facilitated coupling data from various platforms and instruments or for different fires. As a plume ages, the downwind NEMR ($\Delta X/\Delta Y$) can vary from the ER that was measured at the source. The accuracy of downwind $\Delta X/\Delta Y$ may be reduced by differences in the time response of instruments, but in the dilute plume, the excess mixing ratios tend to vary slower in time and space making timing differences less critical. Section 5.4.4 discusses uncertainty in the aging plume in detail.

5.3.4.1 Estimation of fire-average initial emission factors

For any carbonaceous fuel, a set of ER to CO_2 for the other major carbon emissions (i.e., CO, CH_4, a suite of non-methane organic compounds (NMOC), particle carbon, etc) can be used to calculate emission factors (EF, g compound emitted/kg dry fuel burned) for all the emissions quantified from the source using the carbon mass-balance method (Yokelson et al., 1996). In this project, EF were calculated for all the individual fires sampled by the Twin Otter from AFTIR measurements of CO_2, CO, CH_4, and NMOC and WAS measurements of CO_2, CO, CH_4, and non-methane hydrocarbons (NMHC, a subset of NMOC consisting of compounds containing only C and H and no O or N). The nephelometer $PM_{2.5}$ and the AMS/PSAP measurements of the mass fraction of C in the Yucatan BB aerosol (0.48±0.08) were used to estimate the particulate carbon. We also calculated study-average EF for the species measured on the C-130 by using the study average ER for those species to CO_2 calculated using the overlap species with the AFTIR as described above. The carbon mass-balance method assumes that all the volatilized carbon is detected. By ignoring unmeasured gases, we may overestimate the emission factors by 1–2% (Andreae and Merlet, 2001). We also assumed all the

fires burned in fuels that were 50% C by mass on a dry weight basis (Susott et al., 1996), but the actual fuel carbon percentage could vary by $\pm 10\%$ (2σ) of our nominal value. EF scale linearly with the assumed fuel carbon fraction. Because much of the NO is quickly converted to NO_2 after emission, we also report an EF for "NO_x as NO." For any species "X" we abbreviate the EF as EFX.

5.3.5   Details of flights

5.3.5.1   Twin Otter flight of 12 March

Figure 5.2a shows the Twin Otter flight path over the Yucatan peninsula on 12 March along with the location of the fires that we sampled and the hotspots detected by MODIS. (The MODIS hotspots were obtained from the Mexican Comisión Nacional para el Conocimiento y Uso de la Biodiversidad (CONABIO) website at:

   `http://www.conabio.gob.mx/conocimiento/puntos_calor/doctos/puntos_calor.html`

hereinafter cited as "CONABIO"). The fire locations and characteristics and any matches with hotspot locations are also shown in Table 5.1. Widespread cloud cover over the Yucatan could have obscured some fires during both of the satellite overpasses that covered the Yucatan: 10:34 LT (Terra 1, usually before most burning) and 13:38 LT (Aqua 2) (CONABIO). All three fires were sampled between 14:00 and 16:00 LT and all the fires were located near the coast S of Campeche. The fuel for all these fires was crop residue (CR) with a minor fraction in adjoining woodlands on Fire #5. The fire numbers begin with #3 because two fires were sampled en route to the Yucatan that will be described elsewhere.

5.3.5.2   Twin Otter flight of 22 March

Figure 5.2b shows the Twin Otter flight path over the Yucatan peninsula on 22 March along with the locations of the fires sampled and the MODIS hotspots. The fire locations, characteristics, and hotspot matches are also shown in Table 5.1. Eight fires were sampled between 13:14 and 15:29 LT of which five were deforestation fires (DF, burning forest slash) and three were "mixed" (CR fires that escaped and burned adjacent forest, or CR/DF). (Section 5.5 gives more detail on the fires.) The sampling was all after the last satellite overpass with coverage of the Yucatan (Aqua 1 12:40 LT). At the time we sampled Fire #3 it was burning slash in a small clearing surrounded by intact forest. The fire evidently began burning the adjacent forest by 23 March and was then sampled by the C-130 (see next section). Our Fire #8 was located near the coast in a patchwork of small fields and different-aged forests suggesting intensive use by small holders. The fire started as
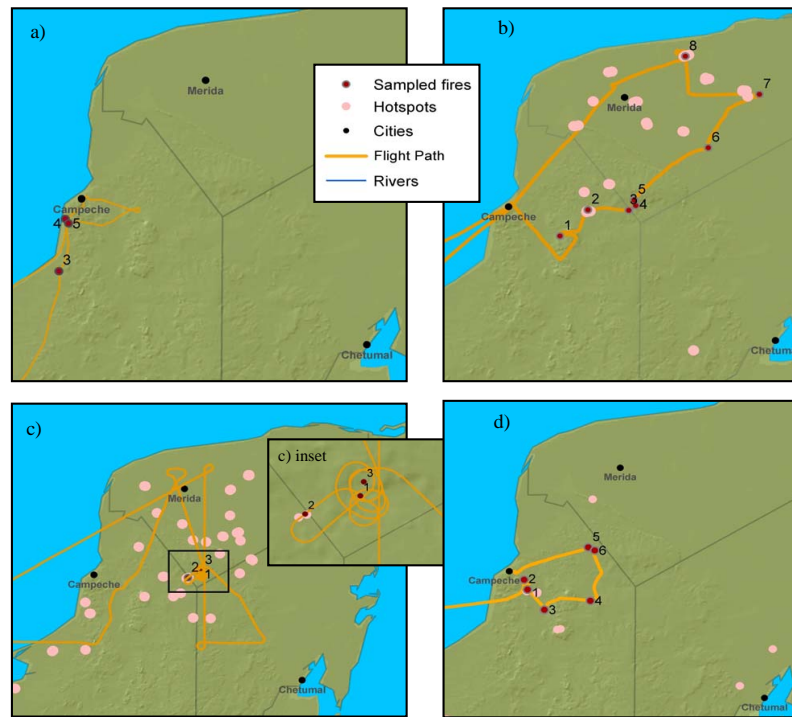
Figure 5.2 – Fires sampled, hotspots, and flight tracks for: a) 12 March 2006. b) 22 March 2006 c) 23 March 2006. d) 29 March 2006. Scale varies from plot to plot. For comparison the distance from Campeche to Merida is 155 km.

Table 5.1 – Details of the fires sampled in the Yucatan by the Twin Otter and C-130 during MILAGRO (March 2006).

Date	Fire	Lat	Long	Time	Coverage by cloud-free MODIS OP		Hotspot	Fuels
dd/mm/yy	#	dd.dddd	dd.dddd	LT	Terra hhmm LT	Aqua hhmm LT	Y/n	observed from aircraft
12/03/06	3	19.1834	-90.7269	1405-1409	1034	1338	n	crop residue (CR) some small-holdings
12/03/06	4	19.6330	-90.6758	1420-1424	1034	1338	n	CR larger holdings
12/03/06	5	19.5947	-90.6497	1555	1034	1338	n	nearly all CR, one spot in forest
22/03/06	1	19.5306	-90.1063	1314-1317	1110	1240	n	CR/deforestation (DF) for mechanized agriculture (MA)
22/03/06	2	19.7748	-89.8675	1329-1333	1110	1240	Y	CR/DF mixed (MA)
22/03/06	3	19.7703	-89.5177	1344-1348	1110	1240	n	deforestation (DF) adjacent to MA
22/03/06	4	19.8158	-89.4578	1353-1356	1110	1240	n	DF adj. MA
22/03/06	5	19.8649	-89.4717	1358-1401	1110	1240	n	DF adj. MA
22/03/06	6	20.3532	-88.8383	1424-1427	1110	1240	n	DF adj. MA
22/03/06	7	20.8525	-88.4018	1447-1450	1110	1240	n	DF adj. MA
22/03/06	8	21.2085	-89.0345	1512-1529	1110	1240	Y	CR/DF many small fields; also burned brush, scrub, and grass
23/03/06	1	19.8266	-89.3825	1410	1016	1321	n	unknown
23/03/06	2	19.7648	-89.5220	1412	1016	1321	Y	unknown
23/03/06	3	19.8201	-89.3681	1417	1016	1321	n	unknown
29/03/06	1	19.6235	-90.3815	1337-1353	1116	1246	Y	CR/DF clearing scrub/brush for MA
29/03/06	2	19.7208	-90.4108	1346	1116	1246	n	DF adjacent to mid-sized fields
29/03/06	3	19.4230	-90.2315	1400	1116	1246	n	CR/DF many small fields; also burned brush, scrub, and grass
29/03/06	4	19.5128	-89.8192	1412-1416	1116	1246	n	CR MA
29/03/06	5	20.0371	-89.8395	1435-1448	1116	1246	n	CR MA
29/03/06	6	20.0055	-89.7808	1438-1441	1116	1246	n	CR MA

a crop residue fire, but spread to adjoining fields and forest. Strong surface winds pushed this fire aggressively towards the southeast. At 600–700 m altitude, the plume "curled back" and dispersed northwest at higher elevations. Three samples of this fire's plume were obtained below 669 m (msl) and then 2 more were acquired at ∼1700 m where the plume had probably aged ∼10–30 min. Fire #8 was one of several sampled fires that were detected by MODIS and in the case of Fire #8 this indicates that it had burned for at least ∼3 hours.

5.3.5.3 C-130 flight of 23 March: Yucatan portion

On 23 March, from 14:05:35–14:06:39 LT, the C-130 descended through three closely spaced "stacked" smoke layers (with embedded fair-weather cumulus) near the top of the boundary layer (2200–2500 m) over the Yucatan (Figure 5.2c, Table 5.1). The three high smoke layers had aged up to several hours and probably experienced some cloud processing (based on the proximity of the clouds and the fact that the RH exceeded 100% as the C-130 passed through the middle layer). Next, at lower altitude, nascent smoke was sampled from three fires in the area; once per fire (14:09:31-14:16:47 LT). The sample of Fire #2 acquired by the C-130 on 23 March was located ∼750 meters from the sample acquired by the Twin Otter on 22 March of their "Fire #3." A photograph of the C-130 Fire

#2 shows a large area of burned forest. Thus, this fire was likely a continuation of the one sampled from the Twin Otter a day earlier. This fire was also the only fire sampled by the C-130 that was detected by MODIS (CONABIO, Table 5.1).

The last C-130 sample of nascent smoke (from Fire #3 on 23 March) was at 1700 m and thus about 10–30 minutes old. Immediately after this sample, the aircraft stayed in the plume and followed the smoke in a curving path for about 14 km down wind probing smoke that had presumably aged an additional ~1.5±0.7 hours relative to the sample of nascent smoke (14:16:48–14:18:31 LT) (Section 5.4.4). During the nominal aging interval from 1.27–1.47 hours the RH exceeded 100% indicating possible cloud processing. By 14:19:41 LT, the C-130 had climbed back above the boundary layer and set course for Veracruz.

5.3.5.4 Twin Otter flight of 29 March

Figure 5.2d shows the Twin Otter flight path over the Yucatan peninsula on 29 March, the fires sampled (from 13:37–14:41 LT), and the hotspot locations (from Terra 1 at 11:16 LT and Aqua 1 at 12:46 LT). The fire, fire type, and hotspot matches are also in Table 5.1. In contrast to the 22 March flight when most of the fires found were DF, on 29 March all but one of the fires found were originally CR. Thus, of the six fires found, there was one DF, three CR, and two mixed (CR that escaped and also burned some woodland).

5.4 Results and discussion

5.4.1 Fire-average initial emission factors measured on the Twin Otter

The fire-average emission factors (EF g/kg) measured on the Twin Otter are shown in Table 5.2 along with the study-average EF for DF and CR fires. If molar ER are preferred for an application, they can be obtained from the EF in Table 5.2 with consideration of the difference in molecular mass. The modified combustion efficiency (MCE, $\Delta CO_2/(\Delta CO_2+\Delta CO)$) for each fire is also shown in Table 5.2. The MCE indicates the relative amount of flaming and smoldering combustion for biomass burning. Lower MCE indicates more smoldering (Yokelson et al., 2003). Figure 5.3 shows EFCH$_3$OH vs MCE and demonstrates that much of the large variation in EFCH$_3$OH (factor of ~4.5) is correlated with the different MCE that occur naturally on biomass fires. In principle, it would be advantageous to incorporate this variability into emissions estimates. Unfortunately, at this time, MCE cannot be measured from satellites nor can seasonal trends in MCE be confidently
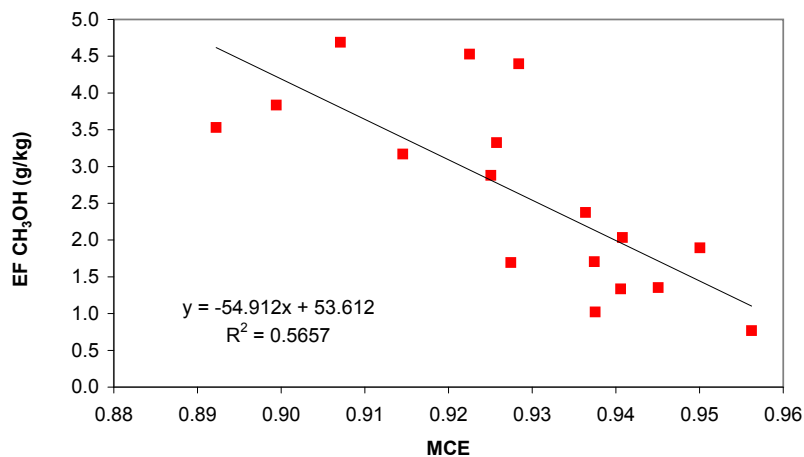
Figure 5.3 – The variation in the fire-average initial EF for NMOC is typically high and it is usually well correlated with the modified combustion efficiency (MCE). High MCE indicates relatively more flaming combustion and low MCE indicates more smoldering.

assigned (Yokelson et al., 2008). For N and S species EF variability also arises from the variable N and S components of the fuel (Yokelson et al., 1996, 2003, 2008). We note that the sum of the EF for gas-phase non-methane organic compounds (NMOC) in Table 5.2 is 12.8 and 12.0 g/kg for CR and DF fires, respectively. However, oxygenated volatile organic compounds (OVOC) normally dominate the gas-phase NMOC emitted by biomass fires and in this study many OVOC common in biomass smoke were not measured on the Twin Otter. In an earlier study of fire emissions with enhanced detection of gas-phase OVOC, the combined instrumentation could not identify about 50% of the gas-phase NMOC by mass (Yokelson et al., 2008). Therefore, we speculate that 30 g/kg is a conservative estimate of the real sum of gas-phase NMOC from these Yucatan fire types (see also Section 5.4.2).

5.4.1.1   Comparison to previous work on Yucatan and other deforestation fires

Coffer et al. (1993) made the only other fire emissions measurements in the Yucatan. They measured CO_2, CO, H_2, CH_4, and total NMHC (TNMHC) on two deforestation fires in February of 1990 and 1991. Utilizing all 23 WAS smoke samples and 11 backgrounds that they collected, yielded an average CO/CO_2 ratio of 0.071 – equivalent to an MCE of 0.934. Their MCE is a little higher than our DF average (0.927), but well within our range for DF (0.907-0.945). We can not derive EF from their data because the average molecular mass and carbon fraction of their TNMHC is unknown. We can directly compare to their molar ratios to CO for H_2 (0.35±0.13; 0.44±0.21 (Twin Otter)) and CH_4 (0.096±0.03; 0.125±0.056 (Twin Otter)). Thus, while there is no statistically significant

Table 5.2 – The date, fire number, fire type (see text), and emission factors (g/kg) sorted by primary technique for fires sampled by the Twin Otter in the Yucatan during March 2006. Blank indicates no data.

Species	12/3 3 CR	12/3 4 CR	12/3 5 CR	22/3 1 MIX	22/3 2 MIX	22/3 3 DF	22/3 4 DF	22/3 5 DF	22/3 6 DF	22/3 7 DF	22/3 8 MIX	29/3 1 MIX	29/3 2 DF	29/3 3 MIX	29/3 4 CR	29/3 5 CR	29/3 6 CR	CR Avg	CR Stdev	DF Avg	DF Stdev
AFTIR																					
CO_2	1631	1722	1729	1607	1627	1644	1651	1711	1600	1651	1671	1656	1682	1695	1603	1679	1689	1676	50	1656	38
CO	80.04	57.63	50.38	114.4	96.76	84.71	88.22	63.27	104.3	84.26	72.25	82.44	71.35	68.13	123.2	67.25	71.74	75.04	25.81	82.68	14.21
MCE	0.928	0.950	0.956	0.899	0.915	0.925	0.923	0.945	0.907	0.926	0.936	0.927	0.938	0.941	0.892	0.941	0.937	0.934	0.023	0.927	0.013
NO				4.780	1.620	2.688	3.866	1.275	1.496	0.877	5.386	2.412	3.909	6.345	3.206	1.960	1.322	2.163	0.958	2.352	1.334
NO_2	4.457	7.077	4.550	11.51	2.360	2.049	3.559	1.248	4.598	3.858	12.43	4.818	6.253	9.669	4.753	1.253	1.275	3.894	2.256	3.594	1.791
NO_x as NO	2.907	4.615	2.968	12.29	3.159	4.025	6.187	2.089	4.495	3.394	13.49	4.568	7.987	12.65	5.673	2.777	2.154	3.516	1.337	4.696	2.099
CH_4	9.648	1.471	2.067	7.349	6.302	6.055	7.326	2.557	9.213	6.595	4.151	3.517	3.718	4.883	5.131	4.402	2.709	4.238	2.993	5.911	2.427
HCHO						3.136	6.661	0.886	0.879	2.613										2.760	2.726
CH_3OH	4.397	1.892	0.766	3.834	3.168	2.879	4.527	1.354	4.689	3.325	2.376	1.694	1.021	1.336	3.530	2.034	1.704	2.387	1.327	2.966	1.544
$CH_3C(O)OH$	4.643	6.476	7.070			3.544	2.534	2.412	1.431	4.678	3.416	6.359				3.250	2.388	4.765	2.013	2.894	1.220
HC(O)OH	3.859	0.618	3.739															2.738	1.838		
ceNH3	0.910	3.902	1.393	0.626	0.080	1.869		0.539	0.309	0.366	1.675					0.350	0.339	1.379	1.477	0.771	0.739
HCN					0.102	0.302		0.225		0.172	0.449			0.250		0.277		0.277		0.233	0.065
WAS																					
ethane	1.476	0.153	0.190			1.187		0.490	1.611	1.065	0.668	0.866	0.992			0.897	0.662	0.676	0.548	1.069	0.403
ethene	1.465	0.526	0.594			0.992		0.742	1.452	1.127	1.065	0.813	0.925	0.433	0.962	0.761	0.746	0.842	0.341	1.048	0.265
propane	0.436	0.040	0.054													0.256	0.184	0.194	0.163		
propene	0.942	0.173	0.205			0.521		0.423	1.215	0.669	0.845	1.386	3.924			0.630	0.634	0.517	0.325	1.350	1.471
isobutane	0.032	0.003	0.004													0.020	0.012	0.014	0.012		
n-butane	0.097	0.009	0.014													0.045	0.048	0.042	0.035		
ethyne	0.292	0.144	0.139									0.295				0.234	0.202	0.202	0.064		
t-2-butene	0.089	0.011	0.012													0.057	0.034	0.041	0.033		
1-butene	0.195	0.041	0.044													0.127	0.080	0.097	0.065		
isobutene	0.176	0.022	0.031													0.117	0.064	0.082	0.064		
c-2-butene	0.067	0.008	0.009													0.043	0.025	0.031	0.025		
cyclopentane	3×10^{-3}	1×10^{-4}	4×10^{-4}													2×10^{-3}	1×10^{-3}	1×10^{-3}	1×10^{-3}		
isopentane	0.014	0.001	0.000													0.010	0.010	0.007	0.006		
n-pentane	0.030	0.003	0.005													0.020	0.014	0.014	0.011		
1,3-butadiene	0.214	0.033	0.057													0.130	0.072	0.101	0.073		
H_2						3.00		2.16	4.32	2.27	2.37	1.44	1.29		4.76	1.66	1.68	2.70	1.79	2.61	1.13
Neph/UHSAS																					
$PM_{2.5}$	6.52			8.29	8.83	5.48	5.49	2.12	6.59	3.73	10.06	6.21	3.56	5.69	5.78	7.06	3.87	5.81	1.39	4.50	1.64

difference, our measurements imply moderately higher emissions of these smoldering compounds. The response of TNMHC instruments to OVOC is poorly characterized, but their large molar ratio of TNMHC/CO (24%) agrees with our statement above (and Section 5.4.2) that the Twin Otter total NMOC is too low. The present study does, however, greatly expand the extent of speciation of Yucatan fire emissions.

We compare our DF data to the most recent and extensive measurements of DF in the Amazon, a study that included both airborne measurements of nascent emissions and ground-based measurements of the smoldering emissions that cannot be sampled from an aircraft (Yokelson et al., 2008). A few main features stand out. The largest difference occurs for initial emissions of particles. The $EFPM_{2.5}$ for the Twin Otter Yucatan DF is only 4.5 ± 1.6 g/kg compared to 14.8 ± 3.4 g/kg for the Amazon. Both of these values are significantly different from the recommendation of Andreae and Merlet (2001) of 9.1 ± 1.5 g/kg, although their recommendation agrees remarkably well with the average of the Yucatan and Amazon values (9.7 g/kg). A main factor contributing to the observed difference in $EFPM_{2.5}$ is probably that the March 2006 early dry season fires that we were able to sample in the Yucatan were much smaller and less "intense" than the late dry season fires sampled in Brazil. As discussed in detail by Yokelson et al. (2007a) and references therein, it is likely that larger more intense fires have much larger particle emission factors. Since a large fraction of annual biomass burning occurs late in the dry season, the late dry season EFPM may better represent the annual particle production. Also, we show in Section 5.4.4 that the $\Delta PM_{2.5}/\Delta CO$ ratio could increase by a factor of ~2.6 in ~1.4 h after emission. This factor times our initial $EFPM_{2.5}$ of 4.5 g/kg suggests that shortly after emission, about 12 g/kg of $PM_{2.5}$ have been produced even by the small Yucatan fires considered here.

The Yucatan fires had higher mean $EFCO_2$ (1656 ± 38 (1601 Amazon)) and lower mean EFCO (83 ± 14 (108 Amazon)). This is indicative of relatively more flaming combustion, which is also reflected in the higher MCE (0.927 (0.904 Amazon)). The higher MCE and a possible tendency for the biomass to be higher in nitrogen content may explain the higher mean $EFNO_x$ (4.7 (1.7 Amazon). Propene was also emitted in higher amounts from Yucatan fires (1.36 (0.5 Amazon)).

Most of the compounds that were measured in both studies had average EF that were not statistically different between the two forest environments. The means (in g/kg) for these compounds are: CH_4 (5.9 Yucatan, 6.3 Amazon); HCHO (2.6 Yucatan, 1.7 Amazon); CH_3OH (2.98 Yucatan, 2.95 Amazon); NH_3 (.78 Yucatan, 1.1 Amazon); ethane (1.08 Yucatan, 1.01 Amazon); ethene (1.05 Yucatan, 0.98 Amazon) and HCN (0.23 Yucatan, 0.66 ± 0.56 Amazon). Two compounds had signifi-

cantly lower emissions from the Yucatan deforestation fires: $CH_3C(O)OH$ (2.9 Yucatan, 4.3 Amazon) and $HC(O)OH$ (below detection limit in Yucatan, 0.57 Amazon).

The EF measured for a single understory fire in a tropical dry forest in Africa were all within the range of EF we measured for the Yucatan DF, except that the EF for total PM for the African understory fire was 13 g/kg (Sinha et al., 2004). There are not enough measurements of understory fires to determine if their EF are significantly different from the EF for DF. For species not measured in this study, the EF measured for deforestation fires in Brazil are probably the best estimate for these, and global tropical forest fires (Yokelson et al., 2008). By extension, the EF values measured in this work, but not in Brazil (Section 5.4.2) are likely the best estimate for global tropical forest fires.

5.4.1.2   Comparison of Yucatan deforestation and crop residue fires

We also compare the EF from the two main types of fires we observed in the Yucatan. Despite the fuel differences, the EF overlap within 1 standard deviation for most species. However, the tendency towards higher emissions of organic acids and ammonia from crop residue fires is clear ($CH_3C(O)OH$ (4.8 CR, 2.9 DF); $HC(O)OH$ (2.7 CR, below detection limit DF); and NH_3 (1.38 CR, 0.775 DF)). "Higher than normal" emissions of these species were also observed from burning rice straw by Christian et al. (2003) in a lab study. The Yucatan DF emitted more HCHO than the CR fires we sampled (below detection limit CR, 2.6 DF). However, the rice straw fire sampled by Christian et al. (2003) had very high HCHO emissions. Thus, low HCHO emissions are not likely a universal feature of CR fires. In summary, since the EF were about equal for most species, this suggests that the overall average trace gas speciation of the emissions from the region may not be very sensitive to a shift in the relative amount of these two main fire types for most species.

5.4.2   Fire initial emissions measured on the C-130

No CO_2 data was collected on the C-130 so we present ER to CO in Table 5.3. Also the fuels were not positively identified so the C-130 data was not included in the "fire-type specific" comparison above. However, the extensive instrumentation on the C-130, and the well-designed flight path, provided a large amount of valuable data.

The initial fire emissions of several species were measured for the first time in the field by the Caltech CIMS. These include H_2O_2, peroxyacetic acid, and propanoic acid. All these reactive compounds were present in significant amounts in the youngest smoke samples. The presence of

Table 5.3 – Initial emission ratios to CO[a] measured in nascent smoke and normalized excess mixing ratios (to CO) measured in aged smoke layers on the C-130 on 23 March 2006

Species	Instrument	Fire number and averages					Altitude of aged smoke layers			
		1	2	3	Avg	Stdev	2476 m	2292 m	2166 m	Avg 3 layers[b]
SO_2	NOAA UV	0.0243		0.0264	0.0254	0.0015	0.009	0.0186	0.0188	0.0155
SO_2	Caltech CIMS slope	0.0257	0.0048	0.0213	0.0173	0.011				
SO_2	Ratio 2 methods	1.06		0.81	0.93	0.18				
NO	NCAR Chemiluminescence	0.008	0.0032	0.0085	0.0066	0.0029	0.0069	0.0011	0.0008	0.003
NO_2	NCAR Chemiluminescence	0.027	0.0147	0.0377	0.0265	0.0115	0.0088	0.0012	0.0017	0.0039
NO_x/CO	NCAR Chemiluminescence	0.035	0.0179	0.0462	0.033	0.0142	0.0157	0.0023	0.0025	0.0068
NO_y/CO	NCAR Chemiluminescence	0.0471	0.0282	0.0607	0.0453	0.0163	0.0424	0.0108	0.007	0.0201
NO_x/NO_y	NCAR Chemiluminescence	0.7423	0.6369	0.7606	0.7133	0.0668	0.3708	0.2103	0.3625	0.3145
O_3	NCAR Chemiluminescence						0.17	0.0458	0.0189	0.0782
$\sum PANs/NO_y$	NCAR spectrometer						0.113	0.135	0.303	0.1837
HCHO	NCAR diode laser			0.0252	0.0252		0.0344		0.0164	0.0254
HCN	CIMS NO_y proxy	0.0148	0.0063	0.0088	0.01	0.0044				
HCN	CIMS slope	0.0152	0.0074	0.0081	0.0102	0.0043				0.0022
HCN	Ratio 2 methods	1.03	1.17	0.92	1.04	0.13				
HONO	CIMS NO_y proxy	0.0023	0.0031	0.0029	0.00277	0.00042				
HONO	CIMS slope	0.0022	0.0075	0.0028	0.00417	0.0029	0.00033		0.00008	
$CH_3C(O)OH$	CIMS slope	0.0093	0.0466	0.0158	0.0239	0.0199				0.024
$HC(O)OH$	CIMS slope	0.0023	0.0034	0.0025	0.0027	0.0006				0.0055
H_2O_2	CIMS slope	0.0018	0.0013	0.0013	0.00147	0.0003				
Peroxyacetic Acid	CIMS slope	0.00013	0.00026	0.00017	0.00019	0.0001				0.0011
Propanoic Acid	CIMS slope	0.00098	0.0028	0.00086	0.00155	0.0011				0.0007
Acetonitrile	NCAR PTR-MS				0.0043					
Acetaldehyde	NCAR PTR-MS				0.0187					
Acetone	NCAR PTR-MS				0.0066					
Methanol	NCAR PTR-MS				0.0254					
Methylethylketone	NCAR PTR-MS				0.003					
Methylpropanal	NCAR PTR-MS				0.0011					
$\sum$Hydroxyacetone, Methylacetate	NCAR PTR-MS				0.007					
Benzene	NCAR PTR-MS				0.0034					
Ammonium (PM_1)	CU HR-ToF-AMS	0.0034	0.0005	0.0033	0.0024	0.0017	0.0141			0.0062
Chloride (PM_1)	CU HR-ToF-AMS	0.009	0.0009	0.0092	0.0063	0.0047	0.0122			0.0025
Nitrate (PM_1)	CU HR-ToF-AMS	0.0031	0.0022	0.0034	0.0029	0.0007	0.0257			0.0057
Sulfate (PM_1)	CU HR-ToF-AMS	0.0004	0.0004	0.001	0.0006	0.0003	0.0196			0.0022
Organic Aerosol (PM_1)	CU HR-ToF-AMS	0.033	0.0498	0.039	0.0406	0.0086	0.1714			0.0751
Organic Carbon (PM_1)	CU HR-ToF-AMS	0.0203	0.0342	0.0248	0.0264	0.0071	nm			
$\sum PM_1$ Species	CU HR-ToF-AMS	0.0489	0.0538	0.0558	0.0528	0.0036	0.2429			0.0917
Black Carbon ($PM_{2.5}$)	UH PSAP	0.0066	0.0043	0.0081	0.0063	0.0019	nm			0.0039
Total $PM_{2.5}$	UH Nephelometer	0.0698	0.073	0.0624	0.0684	0.0054	0.2185			0.1151
% $PM_{2.5}$ speciated	AMS, PSAP, Nephelometer	79	80	102	87.1	13.3	111			83
Particle surface area[c]	UH OPC and FMPS	50.7	52.3	41.1	48	6.1	29.5			34.6

[a] Trace gas ratios to CO are molar ratios and particle species ratios to CO are mass ratios (273 K, 1 atm).
[b] Computed as average of individual layers when available or as single value for all layers.
[c] Dry $PM_{3.0}$ surface area in $m^2/gPM_{2.5}$.

the peroxide species in the nascent smoke may partially reflect fast initial photochemistry (e.g., recombination of peroxy radicals (RO_2, HO_2)). There was no increase with altitude in the ratio of peroxide species to CO when comparing the freshest sample of each fire, but we cannot rule out a photochemical contribution to our reported initial emissions since even the freshest smoke (from Fire #2) could have been ~3–10 minutes old and photochemical production of H_2O_2 was observed in the aging plume from Fire #3 (Section 5.4.4). They are important as a HO_x reservoir and the H_2O_2 plays an important role (along with HCHO) in the oxidation of sulfur in clouds (Finlayson-Pitts and Pitts Jr, 2000).

The NCAR SICIMS detected traces of H_2SO_4 ($\Delta H_2SO_4/\Delta CO$, $5.4 \times 10^{-7} \pm 5.2 \times 10^{-7}$) and MSA ($\Delta MSA/\Delta CO$ ~$8.4 \times 10^{-8} \pm 1.3 \times 10^{-7}$) in the young fire emissions also for the first time. The initial amount of these species varies greatly potentially due to differences in fuel S and plume reactivity. To "normalize" for fuel S variation and highlight any altitude dependence, which could indicate fast initial chemistry, we computed the initial ratios of H_2SO_4 or MSA to SO_2. No trend was observed with altitude in these ratios, but due to the high variability and uncertain formation process we do not report initial emissions for these species in the Tables.

The combination of PTR-MS and the Caltech CIMS made it possible to detect many gas-phase NMOC that have been measured from fires before, but not on the Twin Otter in this study. In Table 5.4 where the results from the two aircraft are combined (as detailed in Section 5.4.3) the sum of identified gas-phase NMOC is 22 g/kg. This value is close to the sum of identified gas-phase NMOC for Brazilian deforestation fires (25.8 g/kg) reported byYokelson et al. (2008). However, both of these values are only ~50% of the true sum of gas-phase NMOC, which includes detected, but unidentified, species that are mostly high molecular weight OVOC (Yokelson et al., 2008). The sum of the molar ratios to CO (Table 5.4 data) for the OVOC that could be measured was 0.1295. The sum of the molar ER to CO for measurable NMHC was 0.0393. Thus, the OVOC/NMHC ratio in the initial gas-phase emissions was about 3.3 — or OVOC accounted for 77% of measured, emitted NMOC on a molar basis. The dominance of NMOC by OVOC in BB plumes causes significant photochemistry differences compared to fossil fuel burning plumes, where NMOC are dominated by NMHC (Singh et al., 1995; Mason et al., 2001).

An important species detected by PTR-MS was acetonitrile, which is thought to be produced almost exclusively by biomass burning (de Gouw et al., 2003) and thus has value as a BB tracer with relatively long (few months) atmospheric lifetime. The ER to CO for this species averaged over the three C-130 fires was 0.0043. The recommended acetonitrile to CO ER for 18 Brazilian

Table 5.4 – Initial ER[a] to CO and EF (g/kg) for Yucatan Fires as measured by both Twin Otter (seventeen fires) and C-130 (three fires).

Compound	Twin Otter ER to CO avg	Twin Otter ER to CO stdev	C-130 ER to CO avg	C-130 ER to CO stdev	Yucatan Average Initial[b] ER to CO avg	Yucatan Average Initial[b] EF g/kg	Yucatan Average Initial[b] EF Stdev
CO_2	13.024	0.321			13.024	1641	40
CO	1	0.242			1	80.18	19.4
NO	0.0338	0.0196	0.0066	0.0029	0.0202	1.733	1.264
NO_2	0.0378	0.0256	0.0265	0.0115	0.0321	4.235	3. 406
NO_x as NO	0.0645	0.0431	0.033	0.0142	0.0488	4.188	3.328
NO_y			0.0453	0.0163	0.0453		
HONO[c]			0.0028	0.0004	0.0063	0.853	0.636
SO_2 (Caltech CIMS three fires)			0.0173	0.011	0.0173	3.164	2.016
CH_4	0.1104	0.0517			0.1104	5.059	2.369
HCHO	0.0326	0.0275	0.0252		0.0289	2.482	2.095
CH_3OH	0.0282	0.0138	0.0254		0.0282	2.586	1.264
$CH_3C(O)OH$	0.0231	0.0105	0.0239	0.0199	0.0235	4.036	3.829
$HC(O)OH$	0.0205	0.0141	0.0027	0.0006	0.0116	1.532	1.105
NH_3	0.0209	0.0219			0.0209	1.017	1.066
HCN	0.0032	0.0014	0.01	0.0044	0.0066	0.512	0.316
Acetonitrile			0.0043		0.0043	0.5	
Acetaldehyde			0.0187		0.0187	2.355	
Acetone			0.0066		0.0066	1.103	
Methylethylketone			0.003		0.003	0.624	
Methylpropanal			0.0011		0.0011	0.219	
∑Hydroxyacetone, Methylacetate			0.007		0.007	1.475	
Benzene			0.0034		0.0034	0.759	
H_2O_2			0.0015	0.0003	0.0015	0.143	0.029
Peroxyacetic Acid			0.0002	0.0001	0.0002	0.04	0.022
Propanoic Acid			0.0015	0.0011	0.0015	0.328	0.233
Ethane	0.0098	0.0052			0.0098	0.844	0.449
Ethene	0.0111	0.0038			0.0111	0.889	0.305
Propane	0.0015	0.0013			0.0015	0.192	0.161
Propene	0.0079	0.0082			0.0079	0.952	0.988
Isobutane	0.00009	0.00007			8.60E-05	0.014	0.012
n-Butane	0.00025	0.00021			2.50E-04	0.042	0.035
Ethyne	0.00289	0.00091			0.0029	0.215	0.068
t-2-Butene	0.00025	0.0002			2.50E-04	0.04	0.033
1-Butene	0.0006	0.0004			6.00E-04	0.096	0.064
Isobutene	0.00051	0.0004			5.10E-04	0.081	0.064
c-2-Butene	0.00019	0.00015			1.90E-04	0.03	0.025
Cyclopentane	5.80E-06	4.80E-06			5.80E-06	0.0012	0.001
Isopentane	3.40E-05	3.00E-05			3.40E-05	0.007	0.006
n-Pentane	6.90E-05	5.40E-05			6.90E-05	0.014	0.011
1,3-Butadiene	0.00065	0.00046			6.50E-04	0.1	0.072
H_2	0.4301	0.206			0.4301	2.463	1.18
$PM_{2.5}$	0.0733	0.0261	0.0684	0.0054	0.0709	5.877	2.142
Ammonium (PM_1)			0.0024	0.0017	0.0024	0.192	0.136
Chloride (PM_1)			0.0063	0.0047	0.0063	0.509	0.377
Nitrate (PM_1)			0.0029	0.0007	0.0029	0.233	0.056
Sulfate (PM_1)			0.0006	0.0003	0.0006	0.047	0.024
Organic aerosol mass (OA) (PM_1)			0.0406	0.0086	0.0406	3.254	0.69
Organic carbon (OC) (PM_1)			0.0264	0.0071	0.0264	2.117	0.569
Black carbon (BC) ($PM_{2.5}$)			0.0063	0.0019	0.0063	0.541	0.163

[a] Molar ratio to CO for gases and mass ratio to CO (273 K, 1 atm) for particle species.
[b] Straight average of Twin Otter and C-130 data when species measured from both aircraft.
[c] Yucatan initial values calculated assuming that initial HONO is about 10% of NO_y. Uncertainty from Keene et al. (2006) (see text).

DF was 0.0026±0.0007 (Yokelson et al., 2008). Without better information on the variability of this ratio in the Yucatan we cannot say it is different from the ER for Brazilian DF. HCN is another compound produced mainly by biomass burning and used as a tracer (Li et al., 2000). The ΔHCN/ΔCO ER measured on the C-130 was 0.0100±0.0044 ($n = 3$) and the Twin Otter ΔHCN/ΔCO ER for all fires was 0.0032±0.0014 ($n = 7$). The combined average for both aircraft is about 0.0066±0.0041, which is not significantly higher than the ΔHCN/ΔCO ER obtained for Brazilian DF (0.0063±0.0054). The ΔCH3CN/ΔHCN molar ER is fairly consistent for several recent field studies: 0.39 MC-area (Crounse et al., 2009), 0.41 Brazil DF (Yokelson et al., 2008) and ~0.43 in the Yucatan if we only consider the fires where both species were measured. The ΔCH$_3$CN/ΔHCN molar ER for laboratory fires in six different tropical fuels was 0.56±0.31 (Christian et al., 2003).

As noted in Section 5.4.1.1, the Yucatan DF emitted more NOx than Brazilian DF, which could suggest a higher fuel N content in the Yucatan and the hypothesis that NOx is produced by oxidation of most of the N-containing compounds in the fuel. The fact that HCN and acetonitrile emissions are highly variable in both locations, but not larger (on average) from the Yucatan fires suggests that these species may arise from the pyrolysis of only specific, N-containing precursor compounds in the fuel that vary in concentration, but on average are about the same in Brazil as in the Yucatan. In any case, potential, total fuel N differences do not provide a simple rationale for all our observations (Yokelson et al., 2008).

Nitrous acid (HONO) is known to be a direct initial emission from fossil fuel combustion (Finlayson-Pitts and Pitts Jr, 2000, pp 274) and Keene et al. (2006) and Yokelson et al. (2007a) observed direct emission of HONO from biomass burning in the lab and field, respectively. Photolysis with unit quantum yield to OH and NO is the only important daytime loss for HONO and occurs within 10–20 minutes (Finlayson-Pitts and Pitts Jr, 2000). Thus we expect the lower altitude samples of the Yucatan BB plumes to have higher ΔHONO/ΔNO$_y$ values (where this ratio should normalize for fuel N differences to some extent). This trend is evidenced in our samples since ΔHONO/ΔNO$_y$ was the highest for Fire #2 (~0.11, sampled at 390 m) and decreased for Fires 1 (~0.05, 1110 m) and 3 (~0.044, 1730 m). Since NO$_y$ is about 75% NO$_x$ (Table 5.3), a comparable value for ΔHONO/ΔNO$_x$ of 0.14 was measured at lower altitudes (predominantly ~580 m) in Brazil by Yokelson et al. (2007a). The lab BB study of Keene et al. (2006) reported a ΔHONO/ΔNO$_x$ molar ratio of 0.13±0.097. In the aging Fire #3 plume (Sect. 3.4) the ΔHONO/ΔCO dropped to about one-tenth of the initially observed value within ~20 minutes and ΔHONO/ΔCO was even lower in the aged haze layers (Table 5.3, Section 5.4.5). Thus, we conclude that HONO accounts for

about 10% of initial BB NO_y and that it makes a major contribution to both OH and NO in fresh BB plumes.

Both the Caltech CIMS and NOAA UV instruments confirmed higher than average emission of SO_2 from these fires. The average SO_2/CO ER from the CIMS instrument reflects one more fire than sampled by the NOAA UV instrument. The CIMS average molar ER of 0.0173 is approximately 7 times larger than the average for tropical forest fires (0.0024) quoted by Andreae and Merlet (2001). The reason for this could involve the fuel S content, which could be high in the Yucatan because of soil S; manure used as fertilizer; or deposition of marine sulfur. There are some very large SO_2 sources in central Mexico including volcanoes and petrochemical refineries (de Foy et al., 2007; Grutter et al., 2008). These sources are normally downwind of the Yucatan, but there may be occasional meteorological circumstances where they contribute to sulfate deposition in the Yucatan.

The mean $PM_{2.5}$ mass ratio to CO (0.0684±0.0054, Table 5.3) obtained by coupling the UH nephelometer with the NCAR CO for the three C-130 fires was very similar to the average ratio obtained for all 17 fires on the Twin Otter (0.073±0.026). This suggests that the two aircraft sampled a similar mix of biomass burning and confirms that the PM emissions were below the literature average for tropical forest fires. The UH PSAP allowed a rough measurement of black carbon (BC) based on light absorption. Martins et al. (1998) compared BC measurements by light absorption to those made by thermal evolution techniques. They found significant variation in the MAE with mixing state, size distribution etc, and obtained an average MAE for fresh-aged Brazilian BB smoke of 12±4 m^2 g^{-1}. Using this MAE we obtained an average initial mass fraction of BC to $PM_{2.5}$ of 0.095±0.036, which is a little higher than the average initial mass fraction obtained for Brazilian fires by Ferek et al. (1998)(0.071±0.012). Black carbon is the main component of smoke that lowers the single scattering albedo (SSA). Christian et al. (2003) showed that EFBC increase with MCE (BC is a flaming combustion product) while CO correlates with smoldering combustion, which also tends to emit a "white" reflective smoke high in organic mass (Yokelson et al., 1997). Fires 1 and 3 sampled by the C-130 had updraft cores that directly rose to high altitudes in the boundary layer due to vigorous flaming, while Fire #2 had a lower buoyancy plume (C-130 flight video, http://data.eol.ucar.edu/). The plume dynamics are consistent with the BC and SSA data as Fires 1 and 3 had low SSA (0.67 and 0.73) and high BC/CO mass ratios (0.066 and 0.081) compared to Fire 2 (SSA 0.84, BC/CO 0.043).

From the OPC data, assuming spherical particles, we calculated the dry surface area of particles 0.15–3 microns in diameter, which should account for most of the particle surface emitted (Table

5.3). The average value was 48 ± 6.1 m^2/gPM$_{2.5}$. The lowest individual value was obtained for Fire #3 (41.1 m^2/gPM$_{2.5}$), which was sampled at the highest altitude (1700 m) and likely reflected fast initial coagulation. The more aged upper haze layers had values near 30 m^2/gPM$_{2.5}$, and this is likely a good estimate of the dry surface area after most of the coagulation is complete. Ambient RH in the upper boundary layer ranged from 70–100% so the ambient particles would have been significantly larger due to addition of water. Measurements of the growth of BB particles as they hydrate typically show an exponential increase in total scattering to about a factor of 2 near 80% RH, which is usually the cut-off for the measurement (Magi and Hobbs, 2003). Thus, the particle surface area could certainly double as "dry smoke" becomes "wet smoke." Assuming an aged smoke layer dry PM$_{2.5}$ of 100 μg sm^{-3} we obtain a dry particle surface area concentration of $\sim$3$\times$10^{-3} m^2 sm^{-3}. Multiplying by a typical number of active sites per m^2 (1019, Bertram et al., 2001) suggests a "few ppbv" of active surface sites are available for heterogeneous chemistry in a typical wet or dry smoke plume. This is a significant available surface area, but much smaller than the droplet surface area within clouds (up to 0.5 m^2 sm^{-3}). The tendency of smoke-impacted clouds to have more, but smaller droplets (Kaufman and Nakajima, 1993) can cause the surface area in smoky clouds to be 2-7 times larger than in clean clouds. Depending on the extent of smoke-cloud interaction this could be the most important influence of BB on available surface area.

The AMS coupled with the VUV-CO provided the mass ratio to CO for a suite of particle constituents: NR sulfate, nitrate, ammonium, chloride, and organic mass (Tables 5.3 and 5.4). Coupling the AMS with the UH nephelometer allowed an estimate of the mass fraction of each AMS species to the total PM$_{2.5}$ (Tables 5.3-5.5). These ratios can be compared to measurements in plume penetrations of nascent smoke from Brazilian fires by Ferek et al. (1998). (Since these ratios change rapidly after emission, it is best to compare initial ratios from similarly aged, very fresh samples.) Since Ferek et al., report a higher average ratio of PM$_4$ to CO (0.10) this could bias a comparison of ratios to CO between the two studies. Thus we compare our mass fractions of total PM$_{2.5}$ to the mass fractions of total PM$_4$ that they obtained for the average of four fire types shown in their Table 3. The average MCE for their data treated in this manner is 0.924; close to the average MCE (0.929) measured on the Twin Otter for all Yucatan biomass burning.

Fire #2, which may have been a forest fire (based on the video and photos) had the highest OA and lowest BC and is the C-130 fire that is most like the Brazil fires (Table 5.5). Fires 1 and 3 have much higher initial NR chloride, nitrate, and ammonium than Fire 2 or the Brazilian fires. This could indicate that these fires were burning crop residue and that the emissions were impacted

Table 5.5 – Estimated speciation of the total PM$_{2.5}$ as a percentage of the mass for fires 1-3 on 23 March 2006 (sampled by C-130).

Species	Yucatan This Work					Amazon[a]		Yucatan/Amazon
	Fire-1	Fire-2	Fire-3	Avg	Stdev	Avg	Stdev	
Sulfate (PM$_1$)	0.57	0.55	1.54	0.89	0.56	1.95	0.83	0.45
Nitrate (PM$_1$)	4.47	2.96	5.51	4.31	1.28	0.96	0.33	4.49
Organic Aerosol Mass (PM$_1$)	47.19	68.26	62.42	59.29	10.88			
Organic Carbon (PM$_1$)	29.09	46.8	39.82	38.57	8.92	61.8	6.4	0.62
Ammonium (PM$_1$)	4.93	0.66	5.26	3.61	2.56	0.09	0.08	40.14
Chloride (PM$_1$)	12.83	1.21	14.74	9.59	7.33	1.8	1.1	5.33
$\sum$AMS-PM$_1$ Species	69.99	73.63	89.46	77.7	10.35			
BC (PM$_{2.5}$)	9.45	5.87	13.02	9.45	3.58	7.1	1.2	
K						3.7	2.7	
PM$_4$ % speciated (Amazon)						77.4	4.4	
PM$_{2.5}$ % speciated (Yucatan)	79.44	79.5	102.48	87.14	13.29			

[a] Source: mass percent of PM$_4$ from Ferek et al., (1998).

by fertilizers. However, the high average EFCl$^-$ in the Yucatan could also reflect wet deposition of marine aerosol on the fuels (McKenzie et al., 1996). The lower EFCl$^-$ for Fire #2 might indicate that it was not burning hot enough to volatilize the fuel chlorine efficiently. Despite the high SO$_2$ emissions from the Yucatan fires the initial PM$_{2.5}$ is not elevated in sulfate, which makes sense since the atmospheric oxidation of SO$_2$ to sulfate typically requires about a week. The sum of species characterized by Ferek et al. on their filters was about 77 % of their PM$_4$. The main species they did not measure is non-carbon organic mass since they analyzed for organic carbon (OC) only. Adding their residue to their OC suggests a ΔOA/ΔOC ratio of $\sim$1.34$\pm$0.11, which is a little lower than the ΔOA/ΔOC of 1.55$\pm$0.08 measured by the AMS for the Yucatan fires. The average Yucatan OC was 39$\pm$9% of the PM$_{2.5}$ on a mass basis, which is below the average of $\sim$62$\pm$6% obtained by Ferek et al. in Brazil. However, the OA for Yucatan fires may be a little higher. Clarke et al. (2007) and Hoffer et al. (2006) suggested that a small fraction of BBOA (up to $\sim$20%) is refractory. The classification as "refractory" depends on the technique so some BBOA defined as "refractory" in other studies may be detected by the AMS. Finally, one African tropical dry forest fire emitted "total" PM that was only 23% OC (Sinha et al., 2004). The sum of the species analyzed on the C-130 accounted for 87$\pm$13% of the total PM$_{2.5}$ as calculated from our MSE-based approach. Other methods of computing total PM$_{2.5}$ on the C-130 could be used such as the size distribution coupled with the particle number and an assumed density. But the agreement obtained from the MSE-based

approach is adequate as each technique only claims accuracy of $\sim$25%. The main aerosol species not quantified on the C-130 is potassium (K). The K^+ signal in the AMS can reflect both surface and electron impact ionization making it difficult to quantify the amount of K in ambient particles. K was about 3.7% of particle mass in Ferek et al., but its incorporation into particles depends strongly on the amount of flaming combustion (Ward and Hardy, 1991) as may also be the case for chloride.

5.4.3 Overall combined initial emissions from Yucatan biomass burning

In this study we simply take the average of all the Twin Otter data and weight it equally to the average of all the C-130 data. As discussed in Section 5.5, this approach may weight the emissions from CR fires too heavily to be a true regional average, but it allows us to use the valid measurements from mixed or unknown fire types. Since, we have also presented the emissions data in the original stratified form (Tables 5.2 and 5.3), this allows alternate coupling schemes for future applications. In any case, as noted above, the fire type may not affect the smoke chemistry dramatically except for organic acids, NH_3, and some PM species. In addition, the smoke transported away from the Yucatan will not have the same composition as the initial emissions due to rapid photochemistry detailed in Section 5.4.4.

To couple data from both aircraft in our estimate we proceed as follows. Both molar ER to CO and EF are useful for regional estimates and only the former was measured on the C-130. Thus, in Table 5.4, Column 2, we have converted the average EF for all the species and all the fires measured from the Twin Otter (DF, CR, and mixed) to molar ER to CO. Column 4 shows the average ER to CO measured for all the species for all fires sampled by the C-130. In Column 6 the combined average ER to CO is shown for all species. When a species was measured on both aircraft or by two instruments we took the straight average of the two values as our preliminary estimate of the study average regional value (except for SO_2 as detailed above). Finally, in Column 7, the study-average initial ER from Column 6 have been converted to EF using the Twin Otter average CO/CO_2 and the carbon mass-balance method (Section 5.3.4.1).

It is worth noting briefly that, on average, similar fires were sampled by each aircraft. The $PM_{2.5}/CO$ ratios are close as noted above. A best calculation of the methanol to CO ratio measured on the C-130 (allowing for sampling rate differences) gives an average value for the three C-130 fires of 0.0254, which is within 10% of the average measured by AFTIR for the 17 fires sampled on the Twin Otter (0.0282). The $\Delta CH_3C(O)OH/\Delta CO$ and $\Delta HCHO/\Delta CO$ ER measured on the two different aircraft were also very similar (Table 5.4). The means were not as close for NO_x and HCN,

but the standard deviation about the mean was large for both species on both aircraft. We do note that, the $\Delta HCN/\Delta CO$ ER measured on Fire #3 by the AFTIR on 22 March was 0.0037, which is not far from the value measured by the Caltech CIMS (0.0047) on the continuation of that fire the next day, though perhaps burning partly different fuels.

5.4.4 Photochemical aging of smoke (first 1.5 hours)

Post-emission chemistry determines much of the atmospheric impact of smoke from fires. In this study, the C-130 first sampled Fire #3 at 1700 m where the smoke would have been $\sim$10–30 minutes old and then immediately followed the plume downwind. About 14 km downwind, ΔCO in the plume suddenly decreased from values that were $\geq$ 10–20 times the variation in the background ($\sim$5 ppbv CO) to only 2–3 times the background variation. The measurements continued beyond this point, but we do not discuss them since the excess values are highly uncertain. The average windspeed measured in the aging plume was 9.6$\pm$4.2 km h$_{-1}$. Assuming the average winds were the same when the downwind smoke was originally emitted implies that the downwind smoke had aged up to an additional $\sim$1.5$\pm$0.7 h.

In Figure 5.4a, $\Delta O_3/\Delta CO$ is plotted versus the estimated change in smoke age. A rapid increase in this ratio to $\sim$15% occurs in < 1 h. Figure 5.4a also shows $\Delta O_x/\Delta CO$ versus time where "O_x" approximates the total odd oxygen. In this work the sum of O_3, NO_2, and PANs account for nearly all the odd oxygen. The rise in $\Delta O_x/\Delta CO$ is very similar to that in $\Delta O_3/\Delta CO$ confirming that O_3 is being produced through photochemical oxidation of NMOC (Crutzen et al., 1999). Yokelson et al. (2003) measured a rise in $\Delta O_3/\Delta CO$ to $\sim$9% in $\sim$0.7 h on three isolated BB plumes in Africa and the $\Delta O_3/\Delta CO$ observed in this work after $\sim$0.7 h of smoke aging ($\sim$8%) is close to the value observed in the African plumes. The chemical evolution of one of the above-mentioned African plumes was measured in great detail (Hobbs et al., 2003) and Trentmann et al. (2005) constructed a comprehensive photochemical model for comparison with those measurements. The model agreed with the measured rate of increase in $\Delta O_3/\Delta CO$ only if plausible, but unconfirmed, heterogeneous reactions were added; or if the measured initial emissions of NMOC were increased by 30% (on a molar basis) as a surrogate for unmeasured NMOC. The latter assumption is consistent with our earlier statement that $\sim$50% of the NMOC emitted by BB are unidentified on a mass basis and this should perhaps be a standard assumption in the modeling of BB plumes. The rate of increase in $\Delta O_3/\Delta CO$ seen in the Yucatan and Africa is faster than observed in some BB plumes; especially at high latitudes (Goode et al., 2000; de Gouw et al., 2006), but most BB occurs in the tropics. In

any case, from southern Africa to Alaska it has been shown that large-scale chemical changes can occur in BB plumes in an initial photochemical regime that is different from the ambient boundary layer and at a spatial scale that could challenge regional-global models.

In Figure 5.4a, and some of the Figures that follow, there is some non-monotonic structure and/or "scatter" in the downwind normalized excess mixing ratios (NEMR). This is expected due to several factors including: (1) Different parts of the plume can age at different rates. An aircraft cannot fly exactly down the plume center-line and instead goes in and out of regions where the smoke is more concentrated and there is less light. Also, the combustion rate at the source can fluctuate leading to a non-monotonic decay in total smoke concentration downwind. (2) The fuels and initial emissions can vary over the course of a fire. When a fire burns freely into homogeneous fuels, the flaming/smoldering ratio and the initial emission ratios may be fairly constant (Hobbs et al., 2003), but this is not always the case. (3) Mixing with fresh or aging plumes from other fires is possible. $\Delta HCN/\Delta CO$ is one of the ER that varies the most from fire to fire and this NEMR was fairly constant for the 1.5 h of Fire #3 data we show. (Figure 5.1b shows all the HCN and CO values in the aging Fire #3 plume.) However, some degree of mixing with other plumes cannot be completely ruled out.

A rigorous error estimate is not possible for each of the above terms or the assumption of a similar windspeed before our sampling. Thus we point out obvious trends in the data and, in some cases, we fit a line to the data and compare the slope to the standard error in the slope to determine if there is a statistically significant trend. The plume chemistry is not expected to be linear: the linear fit is employed as a simple test of whether the values at the beginning and end of the aging sequence are significantly different from each other. Below, we show that the initial emissions were likely very similar for the samples probed at the beginning and the end of the sequence and so significant differences between these points are then evidence for a net change due mostly to photochemistry. The fractional uncertainty in the effective "rate" of any process that might be derived from the fit would be larger than the standard error divided by the slope due to the additional uncertainty in the sample ages. Probably all the samples have experienced more aging, or all the samples have experienced less aging, than estimated. The real uncertainty in the rate is probably about a factor of two.

Figure 5.4b suggests that there were likely some gradual changes in the initial emissions of Fire #3 and the post-emission processing environment that help interpret our data in the aging plume. Figure 5.4b shows $\Delta BC/\Delta CO$ at the 5 s time resolution of the PSAP. BC is a flaming product
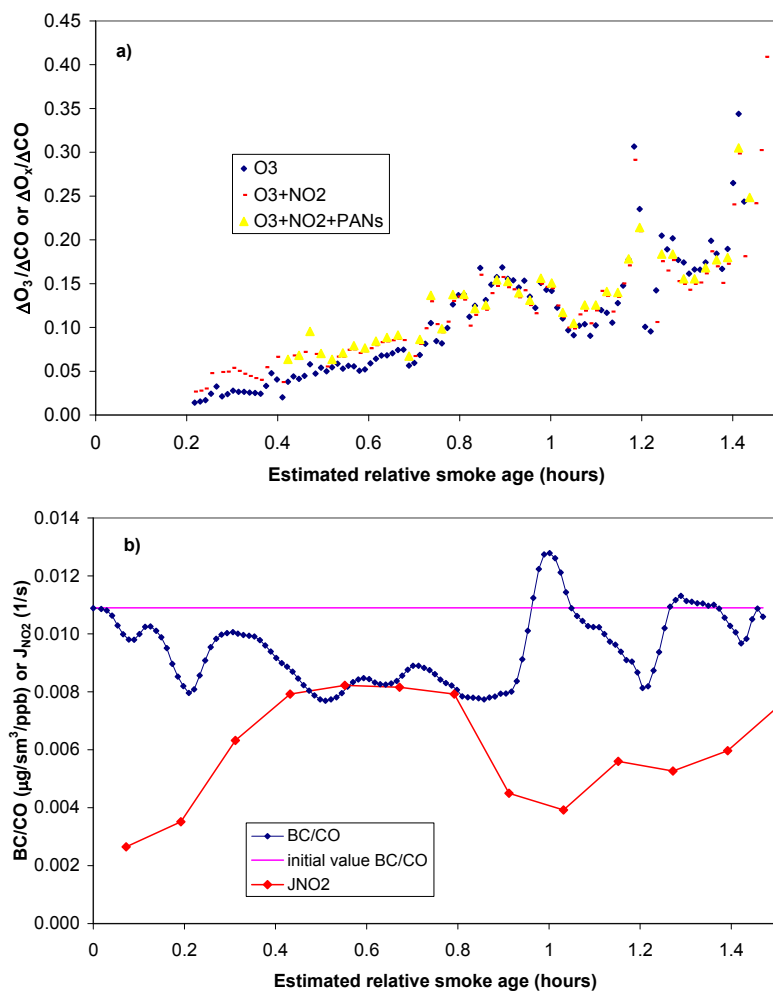
Figure 5.4 – a) Rapid increase in $\Delta O_3/\Delta CO$ and $\Delta O_x/\Delta CO$ in the aging plume of the C-130 Fire #3 discussed in Section 5.4.4. b) The plot of $\Delta BC/\Delta CO$ in the same plume shows that the flaming to smoldering ratio at the source, and the initial emissions, were probably similar for the beginning and end of the aging sequence shown. The J_{NO_2} trace shows that the rate of photochemistry can vary within the same plume (Section 5.4.4).

and CO is a smoldering product. As the C-130 flew downwind in the plume, the gradual 20% decrease in $\Delta BC/\Delta CO$ until about 0.9 h suggests the instruments were sampling smoke originally produced at a gradually decreasing flaming/smoldering (F/S) ratio. The peak in BC/CO at ~1 h could reflect a temporary increase in the F/S ratio at the source about an hour before the sampling started. For the older samples, the F/S ratio was again close to the F/S ratio at the time of the first C-130 sample. Thus a comparison of the beginning and end NEMRs may best reflect post-emission chemistry. The variation in J_{NO_2} is also shown in Figure 5.4b. J_{NO_2} first increases by about a factor of 3 as the smoke dilutes. Near the one-hour aging mark J_{NO_2} decreases by ~2, $\Delta O_3/\Delta CO$ decreases slightly, and CO increases. The aircraft is evidently entering a region of the plume with greater total smoke concentration. After one hour, both $\Delta O_3/\Delta CO$ and J_{NO_2} increase, the smoke concentration decreases, and minimal cloud-processing may occur.

A key driver for photochemistry besides UV is OH. In Hobbs et al. (2003) the rate of decrease of numerous NMHC in one African biomass burning plume was used to estimate an average plume OH over the first 40 minutes of aging of $\sim 1.7 \times 10^7$ molecules cm^{-3}. On our Fire #3, no NMHC were measured within the aging plume, but an OH instrument was on board. The first OH value in the aging plume (averaged over 29 s of flight time and a calculated range of smoke aging of 22–43 minutes) is 1.14×10^7 molecules cm^{-3}. This is 5–20 times larger than the OH values in nearby background air. The plume OH levels thereafter decreased to about twice the average OH in the boundary layer. To our knowledge this is the first *in situ* measurement of OH in a BB plume and it confirms the potential for very high initial OH in BB plumes. The measurements imply a major shortening of reactive species "lifetimes" in comparison to ambient air as predicted earlier (Mason et al., 2001). HO_2 and RO_2 would likely be elevated along with OH (Mason et al., 2001). However, the one minute time resolution of the HO_2 instrument and some missing data make it difficult to determine the levels of this species in the three BB plumes sampled on the C-130.

Trace gases other than O_3 also increased. The initial $\Delta HCHO/\Delta CO$ from the NCAR DFG spectrometer was 0.025 ± 0.01 and it increased to 0.038 ± 0.01 at 0.8 ± 0.1 hours. Similar increases in this NEMR were also seen in an African plume in samples acquired near the top of the plume (Hobbs et al., 2003). The $\Delta HCHO/\Delta CO$ increased dramatically when smoke entered a cloud in Africa (Tabazadeh et al., 2004) and may have also increased strongly in the Fire 3 plume for the points that may be cloud impacted ($\sim 0.065 \pm 0.025$).

The ratio $\Delta H_2O_2/\Delta CO$ was 0.0013 in the nascent smoke from Fire #3 and then increased by ~4 to 0.0054 after ~1.3 hours of aging (Figure 5.5). In Figure 5.5, the intercept is forced to the

$$y = 0.0031 \ (\pm 0.0012) \ x + 0.0013$$
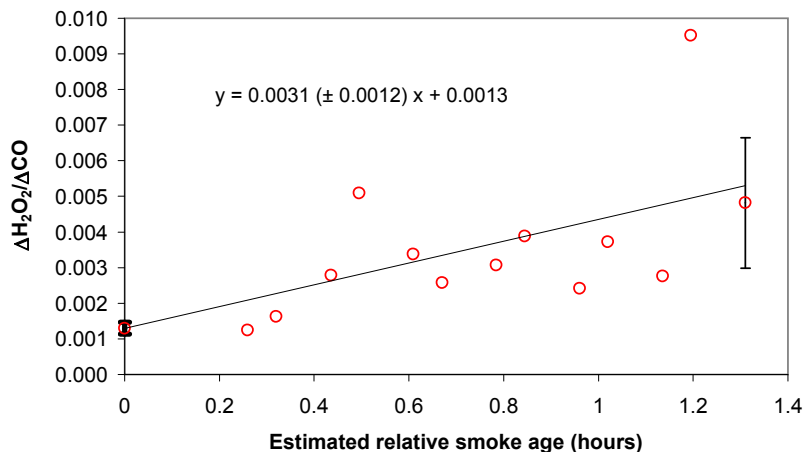
Figure 5.5 – The plot and comparison of the standard error in the slope to the slope indicates that there is a statistically significant increase in $\Delta H_2O_2/\Delta CO$ with aging. The uncertainty in the rate of increase is probably about a factor of two when uncertainty in the age of the samples is considered (Section 5.4.4).

initial $\Delta H_2O_2/\Delta CO$ value that was determined by plotting ΔH_2O_2 versus ΔCO for all the samples in the nascent smoke of Fire #3. We force the intercept because it is based on more samples (with higher S:N) and it has lower uncertainty than the individual downwind NEMRS. With additional aging, the $\Delta H_2O_2/\Delta CO$ ratio would likely increase significantly beyond the ratio measured at 1.3 h due to lower NO_x and entrainment of the BL air which had an absolute H_2O_2/CO ratio of 0.0125. Lee et al. (1997) observed $\Delta H_2O_2/\Delta CO$ ratios of 0.01–0.046 in BB-impacted SH BL air.

Figure 5.6 shows post-emission growth in peroxyacyl nitrates both as $\Delta PAN/\Delta CO$ and $\Delta \sum PAN/\Delta NO_y$. An initial value for ΔPAN or $\Delta \sum PAN$ may not be meaningful (as for O_3) and was not measured due to interference in the nascent smoke. However, Figure 5.6a shows that the $\Delta PAN/\Delta CO$ ratio increases rapidly from $\sim$0.0025 (at $\sim$0.4 h) to $\sim$0.006 (at $\sim$1.4 h). The NEMR reached in $\sim$1.4 hours is as large as the NEMR observed in smoke from Canada that was $\sim$8 days old during NEAQS (F. Flocke private communication). This demonstrates that large variability in initial emissions and/or photochemical processing can be associated with BB plumes. Figure 5.6b shows the $\Delta \sum PAN/\Delta NO_y$ with aging in the Fire #3 plume. In the $\sim$1.2–1.4 h aging interval, $\Delta PAN/\Delta NO_y$ alone has increased to about 13%. The other PAN-like species showed similar trends, but were present in smaller amounts. The sum of the most abundant other PAN-like species (APAN and PPN) was about 20% of PAN in the 1.2–1.4 h interval and the $\Delta \sum PAN/\Delta NO_y$ had increased to 0.167$\pm$0.036 in this interval. In the initial Fire #3 plume $\Delta NO_x/\Delta NO_y$ was 0.76 (based on comparing integrals) and in the 1.2–1.4 h aging interval $\Delta NO_x/\Delta NO_y$ was 0.41$\pm$0.1. This implies a NO_x loss of 46$\pm$11%. A second estimate of the percentage of NO_x loss based on the decrease
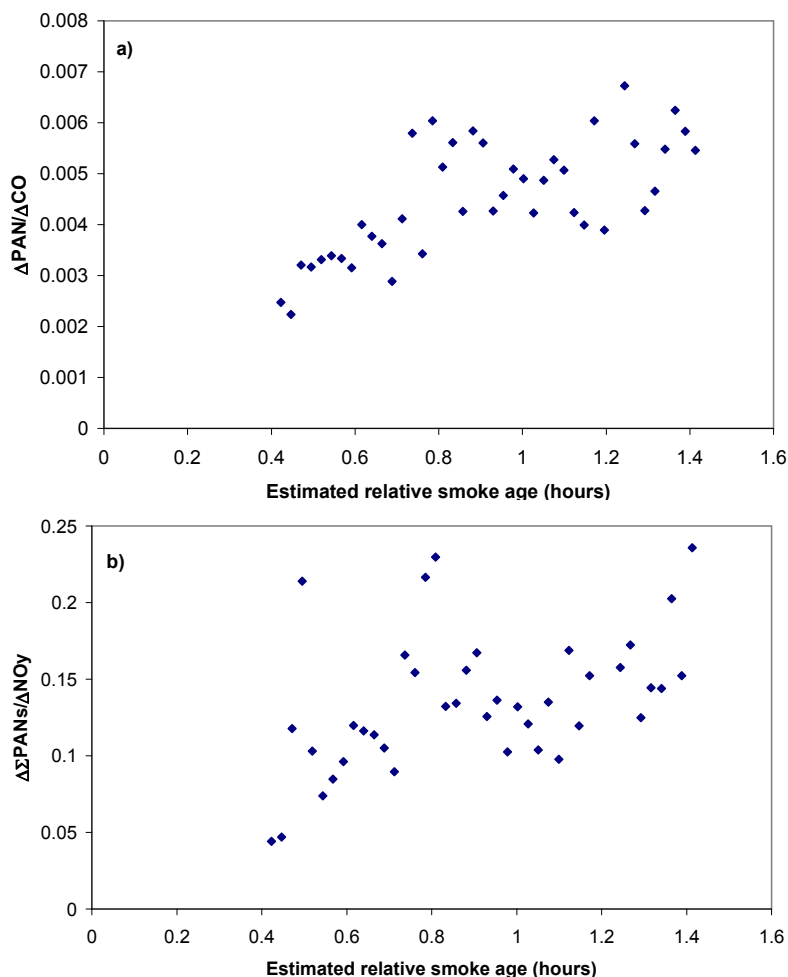
Figure 5.6 – (a) ΔPAN/ΔCO increases quickly. (b) The increase in PANs accounts for $\sim$31% of the loss in NO_x (Section 5.4.4).

in $\Delta NO_x/\Delta CO$ is 62±16%. Averaging these estimates of the NO_x loss gives 54±19% implying that PANs accounted for 31±13% of the loss of NO_x. Similar trends were not observed for HNO_3. Modestly elevated mixing ratios of HNO_3 occurred in some parts of the BL, but were not correlated with the obvious presence of fresh or aged smoke (i.e. elevated CO). The NH_3/NO_x molar ER measured by AFTIR on Yucatan fires was as high as 1.5 and averaged 0.46±0.42. Thus, much of the HNO_3 formed may have reacted quickly with NH_3 to form particle nitrate as also discussed later.

The post-emission fate of organic acids in BB plumes is variable. Goode et al. (2000) observed secondary increases in both excess formic acid (ΔFAc) and excess acetic acid (ΔHAc) ratioed to ΔCO for one Alaskan fire, but only in ΔFAc/ΔCO for another Alaskan fire. In three different African BB plumes, Yokelson et al. (2003) observed ΔHAc/ΔCO increase to 6–9% in < 1 h, but saw no

post-emission increase in $\Delta FAc/\Delta CO$. A huge regional plume emanating from the Brazilian Amazon had much higher $\Delta FAc/\Delta CO$ ($\sim 1.6\%$) and $\Delta HAc/\Delta CO$ ($\sim 5\%$) than the initial values measured for Amazonian fires (Yokelson et al., 2007a). Within the aged Fire #3 plume, we measured more organic acids than previously possible. The excess mixing ratios of FAc and peroxyacetic acid normalized to ΔCO both increased (Figure 5.7) while the excess mixing ratios of HAc and propanoic acid normalized to ΔCO did not show significant trends. In general, the ratio of excess carbon contained in organic acids to excess carbon contained in CO is large in fresh smoke and very large in slightly aged smoke (4–18% in the Yucatan, Brazil, and Africa). Thus, in many BB plumes organic acids are the third most important carbon reservoir behind CO_2 and CO and ahead of CH_4. The observed growth in organic acids is often much larger than the amount of known precursors. There may be currently unidentified high molecular weight precursors that are emitted in quite variable amounts.

The total NO_x loss for the 1.2–1.4 h aging interval was $54\pm 19\%$ with the formation of PANs accounting for a NO_x loss of $\sim 17\%$ as shown earlier. The measured OH (starting at 1.1×10^7 and dropping to 4.1×10^6) coupled with the pseudo-second-order rate constant for $OH + NO_2$ (1.02×10^{-11} cm^3 molecule^{-1} s^{-1}) at the temperature and pressure of the plume (288 K, 815 hPa) predicts an additional 30% loss (Sander et al., 2006). The additive loss from these two channels (47%) is close to the total loss considering the uncertainty in the sample ages (a factor of 2) and the rate constant ($\sim 30\%$), but other loss processes are not excluded. For the 22 March Twin Otter Fire #8, $\Delta NO_x/\Delta CO$ decreased $\sim 75\%$ between the young and aged samples. This larger decrease could be partly due to changes in this ratio at the source, but may also reflect the fact that the Twin Otter sampled initial smoke at lower altitude (300-600 m) than the C-130 (~ 1700 m). OH may be higher in the fresher smoke (Hobbs et al., 2003).

Figure 5.8 shows $\Delta SO_2/\Delta CO$ from both the NOAA UV and the Caltech CIMS in the C-130 Fire #3 plume. The ratio drops from the initial average of 0.0239 to ~ 0.015 by ~ 0.7 h. A decrease this fast is not likely to be due only to gas-phase or heterogeneous processes in the aging plume. The fact that SO_2 is produced by flaming combustion and CO is mainly from smoldering combustion probably explains much of the observed drop. As shown in Figure 5.4b, the samples with nominal aging times up to almost 1 h reflected relatively more smoldering at the source. For the 1.2–1.4 h aging interval, the F/S was about the same as the initial value and $\Delta SO_2/\Delta CO$ was 0.0186 ± 0.006 on the continuous instrument (no CIMS samples). This could imply an SO_2 loss of $23\pm 8\%$ due mainly to plume processes. The expected loss by OH oxidation is only $\sim 3\%$ at 1.3 ± 0.1 h. According to Seinfeld and Pandis (2006), SO_2 loss is very fast in cloud droplets and also significant on particles
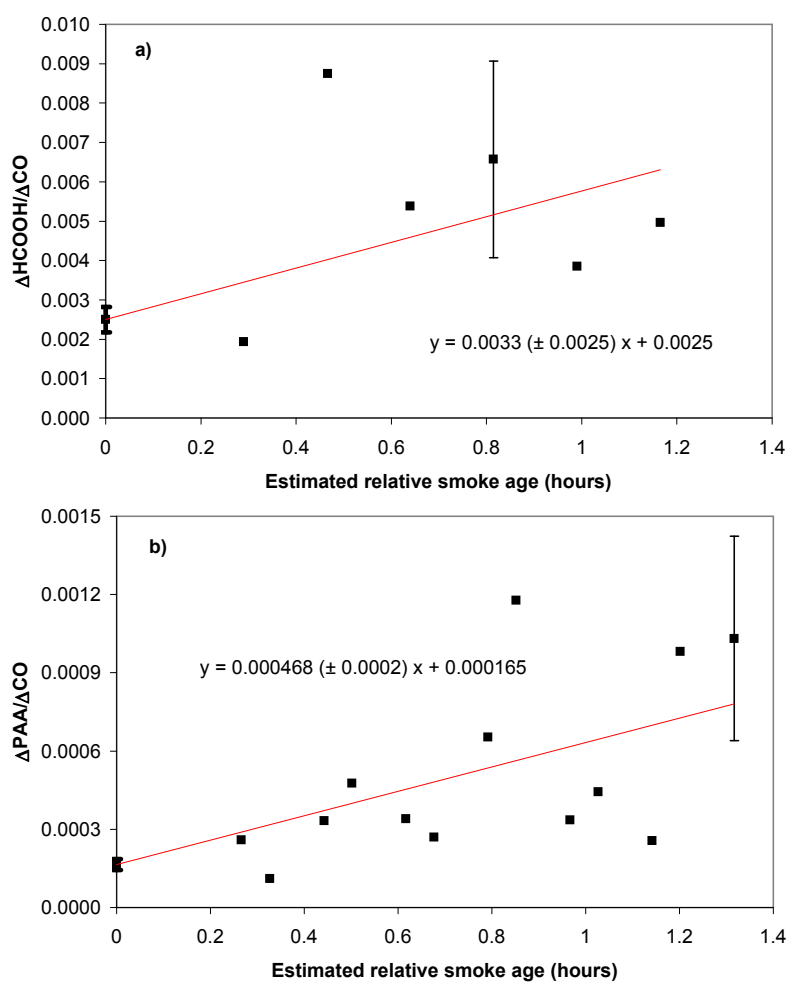
Figure 5.7 – Net production of both formic acid (a) and peroxyacetic acid (PAA) (b) in the aging smoke from the C-130 Fire #3 (Section 5.4.4).
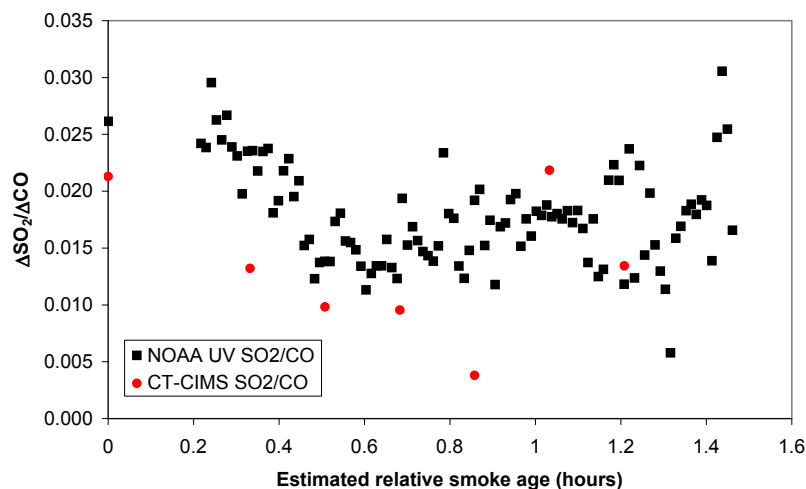
Figure 5.8 – Continuous and discrete measurements of $\Delta SO_2/\Delta CO$ in the aging C-130 Fire #3 plume. Much of the initial drop in $\Delta SO_2/\Delta CO$ is likely due to the gradually decreasing ratio of flaming to smoldering combustion (F/S) at the source (Section 5.4.4). The F/S for the beginning and end of the aging sequence shown is about the same and the average $\Delta SO_2/\Delta CO$ value in the 1.2–1.4 h aging interval is ~23% lower than the initial ratio.

at RH $> 90\%$ or near NH_3 sources, conditions which are met for much of the Fire #3 plume. The expected and observed changes in sulfur species over the relatively short time monitored in the Fire #3 plume are small and uncertain, but heterogeneous processes may well have contributed.

A large increase in $\Delta PM_{2.5}/\Delta CO$ was observed in the aging Fire 3 plume. Figure 5.9a shows a rapid initial rise in $\Delta PM_{2.5}/\Delta CO$, which may partly reflect decreased F/S at the source combined with the higher EFPM normally observed for smoldering Yokelson et al. (2007a). At ~1.4 h of aging the $\Delta PM_{2.5}/\Delta CO$ had increased by a factor of 2.6±1.5, which is independent of the choice of a fixed MSE. Figure 5.9b shows the mass fraction $\Delta BC/\Delta PM_{2.5}$, which decreased by 2.6 over the same aging period. This decrease is independent of the choice of fixed MAE. Since BC is made only by flaming combustion at the source and $\Delta BC/\Delta CO$ is similar at the source and the end of the aging period, the complementary change in the above ratios confirms that the overall change in $\Delta PM_{2.5}/\Delta CO$ is due to secondary aerosol formation. Also shown in Figure 5.9b is the increase in SSA from ~0.75 to ~0.93 as the mass fraction of BC decreases in the $PM_{2.5}$. This is analogous to the increase in SSA from 0.84 to 0.885 measured by Abel et al. (2003) over ~2.4 hours of aging in an African BB plume. In this work, we also quantified the secondary formation of the individual non-absorbing constituents using the AMS as described next.

Figure 5.10 shows the Fire #3 aging results for all the particle species measured by the AMS except for NR chloride. The excess amounts of all the particle species shown are normalized to excess
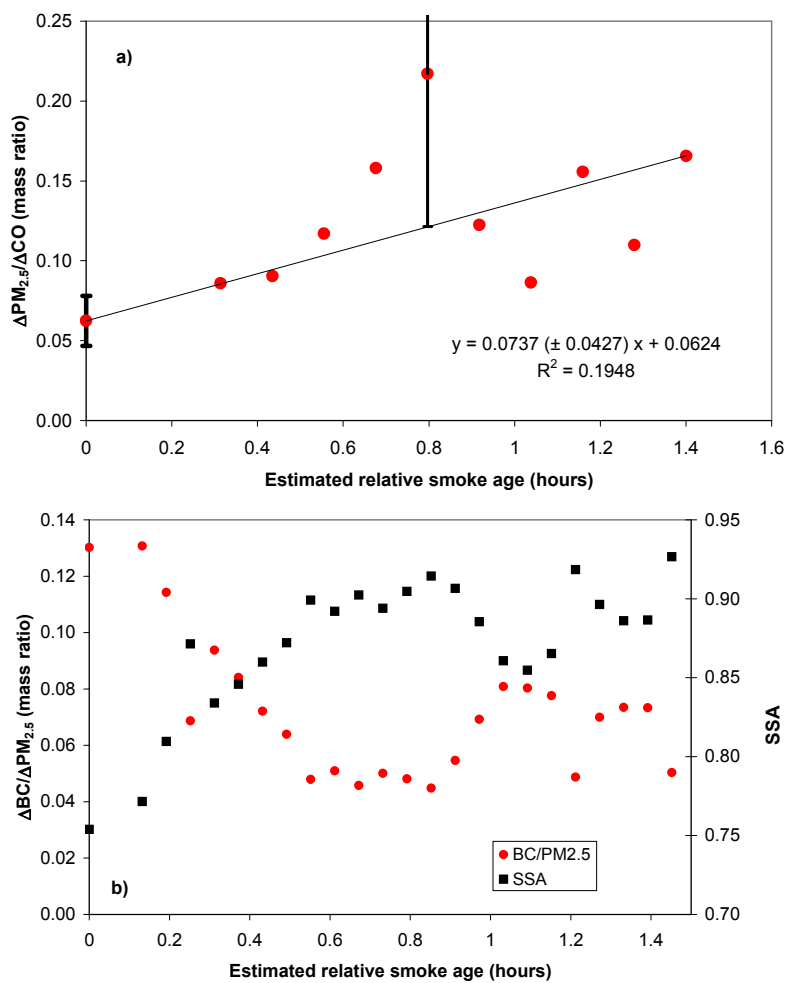
Figure 5.9 – a) The mass ratio of $\Delta PM_{2.5}/\Delta CO$ increases by 2.6 as the smoke from the C-130 Fire #3 ages 1.4 h using the endpoint of the fit line. (The apparent faster initial increase may reflect the higher particle emissions for smoldering combustion.) b) As the particles age, BC is conserved ($\Delta BC/PM_{2.5}$ decreases by 2.6), non-absorbing components are added, and SSA increases.
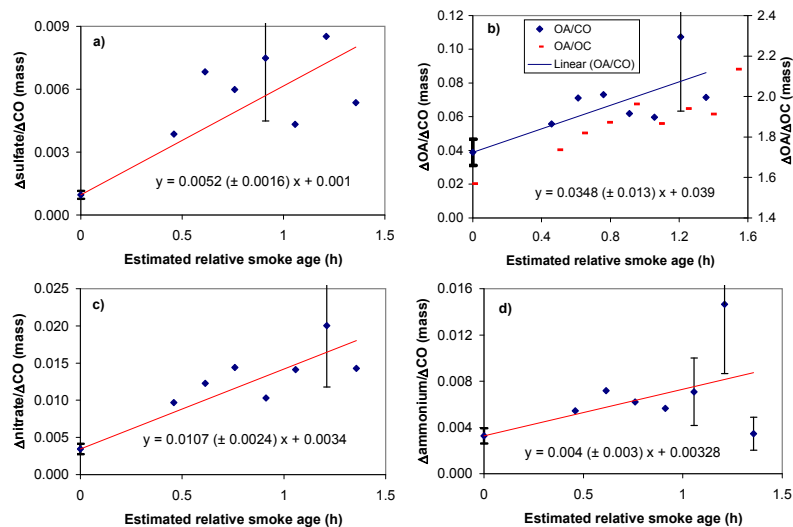
Figure 5.10 – Secondary formation of organic and inorganic aerosol in the aging plume of C-130 Fire #3 (see Section 5.4.4).

CO and all these ratios increased significantly. (Δchloride/ΔCO remained constant over $\sim$1.4 h). Summing the ER to CO (on a mass basis) in the fresh smoke of Fire #3 gives a total of 5.6%. We derived a "final" mass ER to CO from the fit shown at 1.4 hours and then summed these ratios to obtain 13.3%. Thus, the excess mass of all AMS species ratioed to excess CO increases by a factor of 2.4 over this time period – in good agreement with the factor of 2.6 implied by the light scattering.

The changes in the mass percentage of the ΔPM$_{2.5}$ were also computed for each species yielding complementary results since the particles were adding mass. For instance, the Δsulfate/ΔCO ratio increased by a factor of 8.6$\pm$2.7 (95% CI) from its initial value to its value at 1.4 h. This was larger than the overall PM$_{2.5}$ growth factor of $\sim$2.6 so the mass percentage of the particles accounted for by sulfate increased from $\sim$1.5 to $\sim$5%. The growth factor measured for ΔOA/ΔCO was 2.3$\pm$0.85, which is slightly smaller than the overall PM$_{2.5}$ growth of $\sim$2.6 so the calculated mass fraction of OA in the PM$_{2.5}$ decreased slightly from 62 to 53%. Disregarding uncertainty, the calculation suggests that the particles could be adding organic mass, but adding inorganic mass at an even higher rate. The growth factor for ΔNO$_3^-$/ΔCO was 5.4$\pm$1.2 and the mass percentage of nitrate increased from 5.5 to 11%. The ratio ΔNH$_4^+$/ΔCO increased by 2.7$\pm$2.0 and so the computed mass percentage of ammonium was nearly unchanged (5.3% initial to 5.4% final). Since ΔCl$^-$/ΔCO (final) divided by ΔCl$^-$/ΔCO (initial) was 1.02, the calculated mass percentage of Cl$^-$ decreased by 2.6 (from 14.7% to 5.7%); the inverse of the overall particle growth. Note in this case Cl$^-$ was not lost from the particles; it simply represented a decreasing fraction of the PM. The AMS spectra showed

that the ΔOA/ΔOC ratio increased with aging (Figure 5.10). This is consistent with an increasing contribution of oxygenated secondary OA (Zhang et al., 2005) since heterogeneous chemistry with OH is too slow to add so much oxygen on this timescale (DeCarlo et al., 2008).

On a molar basis, as the plume from Fire #3 ages, the increase in ΔNO$_3^-$/ΔCO accounts for 49$\pm$16% of the decrease in ΔNO$_x$/ΔCO expected due to OH reaction. The molar increase in Δsulfate/ΔCO accounts for 39$\pm$16% of the total observed ΔSO$_2$/ΔCO decrease. Similar calculations for ammonium are not possible since NH$_3$ was not measured on the C-130. However, on a molar basis, the ammonium formation is nearly equal to the sum of the sulfate and nitrate formation. A balance between the loss of gas-phase organic precursors emitted by BB and the secondary formation of BBOA is complex for several reasons. The condensed phase species comprising BBOA are mostly unknown and they likely added mass during gas-phase oxidation. In addition, only $\sim$50% of the total gas-phase NMOC emitted by BB have been identified. Grieshop et al. (2009) recently found that the loss of known secondary OA (SOA) precursors in wood stove smoke only accounted for $\sim$20% of the measured SOA formation in a smog chamber experiment. They also developed a model that accounted for all the observed SOA formation by assuming that unspecified low volatility organic compounds were present in significant amounts; an assumption that is not included in other current SOA models. Finally, in real BB plumes some of the secondary aerosol formation can occur due to condensation of trace gases from other sources. However, we get a rough idea of the magnitude of the conversion process as follows. We estimate the growth for each AMS particle species by applying the measured growth factor from Fire #3 to the average initial EF for that species shown in Table 5.4. We then divide by the average initial EF in Table 5.4 for the trace gas precursor to get an upper limit for the fractional precursor conversion. With these assumptions, the mass of the PM species formed in $\sim$1.4 h divided by the mass of the co-emitted gas-phase precursor is: sulfate/SO$_2$ (0.11), OA/ΔNMOC (0.19), NO$_3^-$/NO$_x$ (0.25), and NH$_4^+$/NH$_3$ (0.32). The OA/NMOC fraction is overestimated as explained above: i.e., the projected mass yield of OA at 1.4 h is 0.10 compared to estimated total NMOC (including unmeasured species). However, the growth factors observed in this work, coupled with the TEM results presented next may be the most comprehensive evidence available for rapid secondary formation of both organic and inorganic aerosol in a BB plume. The large amount of secondary formation observed in this work has important implications for air quality, radiative transfer, and visibility. This is especially true because biomass burning is the second-largest global source of NMOC ($\sim$500 Tg yr^{-1}) after biogenic emissions ($\sim$1000 Tg yr^{-1}) (Yokelson et al., 2008). Finally, large formation of SOA may not always occur in BB plumes (Capes et al., 2008) so

this subject deserves significant further research.

TEM analysis of individual aerosol particles shows that their composition and structure in the smoke changed within 30 minutes of emission, presumably through condensation, heterogeneous reactions, or both (Figure 5.11). We compared TEM samples that were collected at two altitudes ($\sim$600 m and $\sim$1700 m) on the Twin Otter from the 22 March Fire #8.

The younger sample was collected within a few minutes of emission. The older sample had aged between 10 and 30 minutes since emission. The younger sample contains many particles with a large fraction of KCl, whereas the older one has particles that contain K, S, and Na and that presumably consist of K_2SO_4, Na_2SO_4, and their mixtures. The older sample also includes spherical organic aerosol particles (tar balls; indicated with a "T" in Figure 5.11c) like those reported by Posfai et al. (2003) and Hand et al. (2005).

The increases in S and organic C with aging measured by using the TEM are consistent with the increases for the same species measured using the AMS on the C-130 Fire #3. One possible difference between the two fires is that the TEM data show that there is almost no Cl in the 10–30 minute old sample whereas measurements with the AMS revealed a decrease in the mass percentage of chlorine, but a constant chlorine/CO ratio with aging. Chlorine could decrease with age as the result of reactions in the atmosphere. Similar Cl loss was also observed in African biomass burning plumes (Posfai et al., 2003; Li et al., 2003). KCl reacts with sulfuric acid and forms K_2SO_4, releasing Cl as HCl. A possible reason for the difference in the results for the two fires could be that Cl loss is a fast initial process and the youngest AMS sample was at the same altitude as the oldest TEM sample. If most of the KCl particles reacted within 10 to 30 minutes of emission, no further Cl decrease would have been detected with AMS in their biomass burning plume. Another possibility is that as the sulfate is replacing the chloride in KCl, the chloride is recondensing as NH_4Cl, which is detectable with the AMS but is likely lost in the vacuum of the TEM (Johnson et al., 2008). In any case, to our knowledge, Cl^- has been observed to decrease or be conserved as BB plumes age, but not to increase.

5.4.5   Chemistry of aged smoke layers at top of boundary layer

Unlike the case for C-130 Fire #3, we do not know the initial ER for the fires that contributed to the aged, and potentially cloud-processed, smoke layers that were penetrated at the top of the BL on 23 March. However, we can compare the normalized excess mixing ratios in these high-altitude, aged smoke layers to our study-average initial ER measured in nascent smoke and the trends observed in
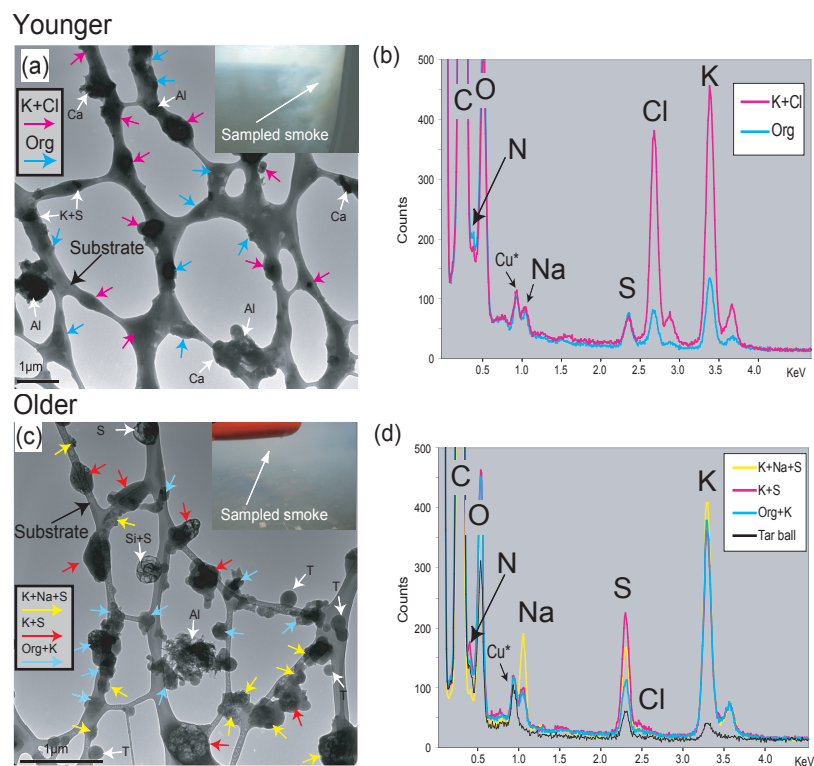
Figure 5.11 – Morphologies and compositions of individual particles from young (a few minutes old) and older (∼10 to 30 minutes) biomass-burning samples collected on 22 March from fire #8. (a) TEM image of the younger aerosol particles. The thin black linear features are the lacy-carbon substrate on which the samples were collected. The white arrows plus chemical symbols indicate particles that are rich in Ca, Al, or K+S. (b) Energy-dispersive X-ray spectrometer (EDS) spectra of typical particles in image (a). (c) TEM image of the older aerosol particles. The white arrows plus chemical symbols indicate particles that are rich in S, Si+S, or Al. T indicates tar ball particles. (d) EDS spectra of typical particles in image (c). We used an electron beam ∼0.2 μm in diameter and 30 second counting times for the EDS analyses. The spectra were averaged across the particles indicated by arrows in the images. Almost all particles included strong C and O signals from organic material and the lacey-carbon filter. N-bearing species such as nitrates and ammonium were not well measured using EDS because N signals are generally weak plus these species decompose rapidly in the TEM beam. The Cu peak is marked with an asterisk because it is from the TEM grid. Sample collection times were less than a minute for both samples. Scale bars in both images indicate 1 μm. Org indicates organic material.

the aging of the Fire #3 plume to gain some additional insight into the likely nature of smoke aging. The general observation is that these layers tend to have normalized excess mixing ratios similar to those in the aged Fire #3 plume or exhibit a continuation of the aging trends noted in the plume downwind of Fire #3. But some caveats are noted.

The $\Delta O_3/\Delta CO$ ratio in these layers increases with altitude from ~ 0.02 to ~ 0.05 to 0.17 (Table 5.3) suggesting that the highest layer is the oldest and ~ 1.5 hours old. On the other hand the $\Delta OA \Delta CO$ (~ 0.17) and Δsulfate$/\Delta CO$ (~ 0.02) ratios in the highest layer are about twice the value in the Fire 3 plume at ~ 1.4 h. This would suggest an age of about 3 hours if a linear aging rate and similar initial emissions are assumed. The largest gas-phase H_2O_2 mixing ratios occurred just above the highest smoke layer. Thus the aqueous H_2O_2 in clouds is likely also largest for the highest smoke layer, which may contribute to the high degree of sulfate formation and the low $\Delta SO_2/\Delta CO$ ratio of this layer. On the other hand, the $\Delta NO_y/\Delta CO$ ratio varies greatly between the three high smoke layers and it is much larger in the highest layer, which strongly suggests that the initial emissions are not identical for each layer. This complicates the comparison of layers. Also illustrating variability, the $\Delta HCN/\Delta CO$ average over all three layers (0.0022) is closer to the Twin Otter average (0.0032±0.0014) than the C-130 average (0.0108±0.008).

In the smoke layers at the top of the BL $\Delta NO_x/\Delta NO_y$ ranged from 0.21 to 0.37, which are all values lower than the average (0.46) in the Fire #3 plume at ~ 1.4 h. This suggests that the smoke had aged for more than ~ 2 hours. However, the lowest value (indicating the oldest layer) was in the middle layer rather than the top layer, which $\Delta O_3/\Delta CO$ indicated was the oldest. $\Delta \sum PANs/\Delta NO_y$ was the highest in the bottom layer (~ 0.3) and < 0.15 in the other layers. This would imply that the bottom layer is the oldest. Thus, several normalized excess mixing ratios that can be used as "photochemical clocks" do not all indicate the same average age or relative ages – possibly due to varying initial emissions, mixing of different aged plumes, and different processing environments. An important point of this discussion is that given fire to fire variability (Figure 5.3) and the high uncertainty in mean EF (Table 5.2) it could be misleading to compare aged and fresh smoke from different fires even when they occur or originate in the same region (Capes et al., 2008). Conversely, a non-representative characterization of the average initial BB emissions from a region, even if coupled with adequate knowledge of the post-emission transformations (which is unlikely), could cause erroneous calculations of the speciation of the BB emissions exported from a region. We discuss the representativeness of our initial emissions measurements and the topic of scaling to regional emissions next.

5.5   Implications and impact on the regional environment

5.5.1   Fire characteristics and estimates of regional emissions

It is important to characterize the fires we sampled, consider how well they represented the regional biomass burning, and help guide reasonable estimates of regional emissions from our spot measurements. In this effort, we rely on notes and photographs from the sampling aircraft, the literature, and remote-sensing data. Based on visual observations from the Twin Otter, nearly all the fires fit into a simple classification scheme: (1) Deforestation fires (DF) – enclaves in the forest where heavy slash was burning to initiate or expand agricultural areas. (2) Burning of crop residue (CR) or "agricultural waste" in fields. (3) DF or CR fires which had "escaped" into nearby unslashed forest where they consumed mostly understory fuels. If the unintended burned area was $< \sim 10\%$ of the planned burn, the fire was classified as DF or CR in Tables 5.1 and 5.2. If the planned and unplanned areas were comparable the fire was classified as "mixed." Surface windspeeds were high throughout southern Mexico in March of 2006 and at least one-third of the fires we observed from the Twin Otter had escaped their apparent intended boundaries. The fact that much of the Yucatan forest canopy is leafless in the dry season also promotes large amounts of unintended burning; in contrast to evergreen forests where the intact canopy maintains a moist micro-climate during the shorter "dry"/fire season.

During our flights a total of 6 DF, 6 CR, 5 mixed, and three fires of unknown type were observed. This suggested that the clearing of new areas and the disposal of crop waste were responsible for a roughly equal number of fires. In addition, we estimated the area burned and fuel consumption for the whole Yucatan region using a model developed at NCAR by Wiedinmyer et al. (2006). Briefly, MODIS thermal anomalies were used to identify the daily time and location of fires. The area burned at each fire was assumed to be 1 km^2 (100 ha), scaled to the amount of vegetated area at the same location (determined by the MODIS Vegetation Continuous Fields product, Hansen et al., 2003). The fuel loading at each site was dependent on the ecosystem at each fire location (based on the GLC200 dataset; Latifovic et al., 2003). Finally, the fuel consumption was assumed to be a function of both the fuel loading and the vegetation coverage at each site. On average the model fuel consumption per unit area for the two main fires types was 4.5 Mg/ha (CR) and 52 Mg/ha (DF).

The average modeled fuel consumption values are in reasonable agreement with field measurements of fuel consumption in tropical dry forest and crop waste fires. Kauffman et al. (2003) measured late dry season fuel consumption on five fires in slashed dry forest in western Mexico and

northeastern Brazil ranging from 57-108 Mg/ha. Fuel consumption values near 10 Mg/ha were measured when only understory fuels were burning in tropical dry forests in Brazil and Africa (Ward et al., 1992; Shea et al., 1996; Hoffa et al., 1999). For crop waste fires total biomass and the percentage that constitutes residue varies considerably by crop. Further, the percentage of residue that decomposes before burning varies with climate and drying time and use of residue as fertilizer, animal feed, or household fuel also varies (Yevich and Logan, 2003). We could not identify the plant material that was burned in this study. However, cereals are the most common crop worldwide and data from de Zarate et al. (2005) suggests a range of fuel consumption of 0.36–4.2 Mg/ha for cereal crop residue burning. Higher values have been measured for other crops that are important in Mexico with the largest values typically being reported for sugar cane (20 Mg/ha, Lara et al., 2005). Thus, the NCAR model averages lie well within the rather large range of values that occur for these fire types.

The uncertainty in the MODIS-based area burned has two chief components: detection efficiency and the estimation of burned area from counts of fire pixels. The MODIS hotspots show daily trends in fire frequency and the spatial distribution of biomass burning, but not all fires are detected. The timing of the Terra and Aqua MODIS overpasses (at 20°N) results in close spacing ($\sim$100 minutes) of the midday observations and leads to omission errors for short-lived fires or fire activity initiated following the last daytime pass. There are also times when clouds preclude fire detection or overpasses do not cover an area of interest. Additionally, the detection rate decreases with burn size, Hawbaker et al. (2008) found the MODIS detection rate crossed the 50% mark at a fire size of $\sim$100 ha. In fact, only a small fraction (4/20) of the fires we sampled were detected by MODIS (Table 5.1). Most of the "missed fires" were sampled after the last MODIS overpass and all of the fires we photographed were $<$ 100 ha. Missing fires would cause the model to underestimate burned area. On the other hand, all the fires that we could roughly size were significantly smaller than the $\sim$100 ha size assumed in the model. In addition, Giglio et al. (2006) estimated that, on average, a MODIS fire pixel represented $\sim$0.4 km^2 (40 ha) of burned area in southern Mexico and Central America. Thus, it's likely that the area burned is overestimated for some of the individual Yucatan fires. The two main sources of error in area burned tend to offset. In light of the above-discussed challenges, the overall model uncertainty in the total amount of emissions is estimated at a factor of 2 (Wiedinmyer et al., 2006).

The results of applying the NCAR model to the Yucatan peninsula ($\sim$18–22N by 87–91W) for March through May of 2006 are shown in Table 5.6. The ratio of area burned in forest to croplands is about 6:1 for March 2006 and 7.5:1 for the entire March–May 2006 biomass burning season. This

contrasts with our airborne observation that the two fire types occurred in roughly equal numbers. Because of the higher fuel consumption per unit area for forest burning, forest fires account for nearly all the modeled fuel consumption on a mass basis. We compared the NCAR model result for March 2006 with a separate analysis using a different vegetation map (CONABIO, 1999) and the ratio of MODIS active fire detections in forested areas to agricultural areas was in rough agreement at 4:1. The predominance of fire in forested areas in the MODIS based analyses compared to the airborne sampling may reflect several factors. 1) The airborne sampling was concentrated nearer the coast (Figure 5.2) while the fraction of forested area (and probably the relative amount of deforestation) increases inland (CONABIO, 1999). 2) The vegetation maps (1 km^2 resolution) may classify smaller fields surrounded by forest, which appeared common in the Twin Otter photographs, as forest and neither vegetation map accounts for the deforestation since 2001. 3) The heavier fuel loads of deforestation fires support longer duration fires compared to croplands – increasing the likelihood of detection as a thermal anomaly by one of the four daily MODIS overpasses. 4) If DF fires tended to be initiated earlier in the day this would favor their detection by MODIS and enhance the forest to crop fire ratio relative to the airborne observations due to the different sampling periods (1300–1600 LT for airborne sampling vs. 1000–1330 LT for MODIS overpasses). Giglio (2007) observed that Brazilian fire activity associated with deforestation occurred earlier in the day compared with cropland burning, while Smith et al. (2007) attributed the low MODIS detection rate (13%) for crop residue fires in Australia to the tendency of farmers to burn later in the day after MODIS overpasses. In reality a 1:1 burned area ratio for DF/CR may be an upper limit as it represents approximately doubling the area under agriculture annually. This upper limit would imply an approximately 11:1 ratio in fuel consumption, which suggests our simple average of all ER presented in Table 5.4 might ultimately be improved upon.

5.5.2   Regional transport and estimated total production of emissions

As discussed above, the fuels and the mix of flaming and smoldering impact the initial emissions from fires, which can then evolve rapidly. The post-emission transport dictates what areas of the atmosphere are impacted by the emissions and the photochemical processing environment. Figure 5.12 shows 5-day HYSPLIT forward trajectories from three starting altitudes from each fire we sampled (Draxler and Rolph, 2003). Similar forward trajectories were confirmed for multiple days in April and May of 2006, which are the peak biomass burning months. About one-half of the emissions tend to disperse northwesterly and remain at altitudes that are likely within the boundary layer.

Table 5.6 – Estimation of area burned and biomass burned in the Yucatan in 2006 and comparison with MCMAEI[a].

Land cover	March	Area Burned (ha) April	May	March	Biomass Burned (Metric Tons) April	May	March-May Area Ha	March-May Mass Tg	Percent of March-May Mass
Forest	53395	401073	383286	2587590	20652195	20133816	837755	43	98.8
Grasslands	100	1180	1200	992	15288	11746	2480	0.03	0.1
Croplands	8599	57197	45298	38513	255178	202126	111094	0.5	1.1
sum	62094	459450	429784	2627096	20922660	20347688	951329	44	100

Species[b]	Fire EF g/kg	2006 Speciated Emissions (Metric Tons) Yucatan March	MCMA March	Yucatan April	Yucatan May	Yucatan annual[c]	MCMA annual	Yucatan/MCMA annual	Yucatan/MCMA Mar-06
PM_{10}	7.42	19489	1724	155213	150947	339021	20686	16.4	11.3
$PM_{2.5}$	6.18	16241	552	129344	125789	282517	6622	42.7	29.4
CO	80.47	211402	149340	1683646	1637378	3677479	1792081	2.1	1.4
VOC	22.08	58006	44347	461972	449277	1009056	532168	1.9	1.3
CH_4	5.08	13343	19589	106266	103346	232110	235065	1	0.7
SO_2	3.18	8344	554	66450	64624	145143	6646	21.8	15.1
NO_x	3.68	9673	15000	77037	74920	168267	179996	0.9	0.6
NH_3	1.02	2677	1460	21320	20734	46568	17514	2.7	1.8

[a] MCMAEI = Mexico City metropolitan area emissions inventory (2004), March 2006 estimated as annual/12.
[b] Primary PM only, fire PM_{10} approximated as $1.2 \times PM_{2.5}$, fire EF from Table 5.4 this work, VOC are identified VOC only.
[c] Yucatan speciated emissions for 2006 based on 45.7 Tg biomass burned in 2006.

These trajectories tend to cross under NE trending trajectories from MC over the Gulf of Mexico. There is potential for the Yucatan and MC plumes to eventually mix (after some evolution of each plume) over the US. Forward trajectories that start in the early evening (not shown) can disperse directly to the west towards Mexico City. Much of that transport will happen at night. In any case, it is possible for Yucatan emissions to reach Mexico City, other areas in Mexico, or a large area of the Midwestern and eastern US as has been documented in detail elsewhere (Lyons et al., 1998; Kreidenweis et al., 2001; Rogers and Bowman, 2001; Bravo et al., 2002; Lee et al., 2006; Massie et al., 2006). Because a large area is impacted by Yucatan BB emissions we next discuss the amount of these emissions as calculated by the NCAR model described above (Table 5.6). To help place the estimated amount of Yucatan emissions in perspective we compare to the emissions from the Mexico City Metropolitan Area (MCMA). Specifically, we start by comparing the annual and March 2006 Yucatan BB emissions directly to speciated data from the 2004 MCMA Emissions Inventory (EI) in the bottom half of Table 5.6 (`http://www.sma.df.gob.mx/sma/index.php?opcion=26&id=392`). Based on this simple first step, the Yucatan fires appear to emit 20–40 times more SO_2 and primary $PM_{2.5}$ on an annual basis than the MCMA. Since biomass burning peaks in April–May, our initial comparison for the March 2006 MILAGRO performance period indicates that the Yucatan fires emitted 15–30 times more SO_2 and primary $PM_{2.5}$ and about equal amounts of other trace gases as the MCMA. However, the $PM_{2.5}$ in the MCMAEI could be more than a factor of 2 low (calculated from Salcedo
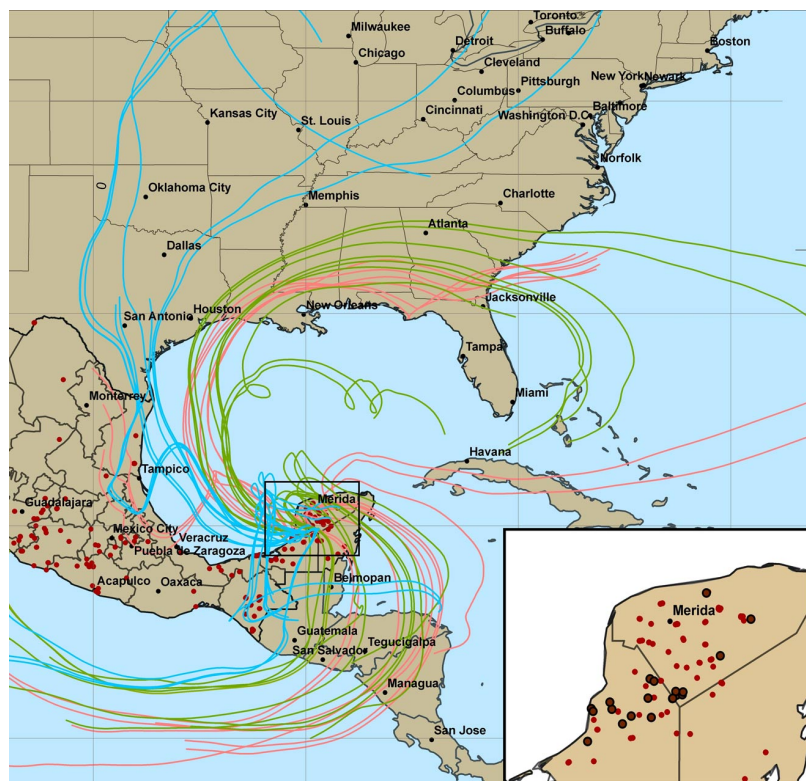
Figure 5.12 – Three 5-day forward trajectories starting from each fire sampled (red dots with black border). The starting time is the sampling time shown in Table 5.1. The starting altitudes above ground level are blue (250 m), green (1000 m), and red (2500 m). The projected altitudes stay mainly within the boundary layer. The hotspots (red dots, no border) due to biomass burning throughout Mexico are shown for the dates sampling was conducted in this work.

et al., 2006). In addition, the simple comparison in Table 5.6 does not include secondary aerosol formation, which could increase the amount of $PM_{2.5}$ 10-fold in the MCMA emissions (Kleinman et al., 2008) and a factor of 2 or more in the BB emissions (Section 5.4.4). Adjusting for the above factors implies that the Yucatan SO_2 and $PM_{2.5}$ sources are likely about 2 and 4 times larger, respectively, than MCMA on an annual basis. Additional important pollution sources are located in the region including fires in other parts of Mexico and Central America and large SO_2 emissions from the Popocatépetl volcano (894000 t yr^{-1}, Grutter et al., 2008), the Tula refinery (158000 t yr^{-1}, de Foy et al., 2007), and other volcanoes and refinery complexes. Notably, both the Popocatépetl and Tula SO_2 sources are estimated to be larger than the Yucatan BB or MCMA SO_2 source. Clearly though, our BB estimates for the Yucatan establish it as one of the major regional sources of trace gases and particles.

5.5.3 Distribution of biomass burning in the global northern hemisphere

Inspection of the TOMS ozone monitoring instrument global aerosol index (AI) images for March-May 2006 is instructive (`http://jwocky.gsfc.nasa.gov/aerosols/aerosols_v8.html`). Even though we know significant biomass burning is occurring in the Yucatan during this time, no enhancements of the AI are depicted in the global images. However, other areas of the NH tropics show frequent, very strong AI enhancements during the same time period. This suggests that these other areas (Indochina, India, Sahel, etc.) experience a much larger amount of biomass burning. Most of these areas are also heavily populated and suffer from severe air quality problems (Ramanathan et al., 2001).

5.6 Conclusions

This study increased both the total number of fires sampled (from 2 to 22) and the total number of plume species quantified (from 4 to 51) for biomass burning (BB) in the Yucatan. These are the first detailed measurements of NH tropical BB and they include some species measured for the first time in young plumes (OH, peroxyacetic acid, propanoic acid, hydrogen peroxide, etc). The OH measurement in an aging BB plume confirmed the possibility of very high early OH (1.14 ± 10^7 molecules cm^{-3}) likely caused in part by high initial HONO ($\sim10\%$ of NO$_y$). Rapid net production of O$_3$ was observed with ΔO$_3$/ΔCO reaching 15% in about one hour of aging in one plume. Significant post-emission increases in HCHO, H$_2$O$_2$, HC(O)OH, PANs, and other gases were also observed. The most detailed observations to date of secondary aerosol formation in a BB plume showed that the ΔPM$_{2.5}$/ΔCO can more than double in less than several hours. Growth in nitrate, ammonium, sulfate and organic mass accounted for nearly all of the secondary formation. Currently unidentified high molecular weight NMOC may contribute significantly to the above observed changes. It was shown that comparing aged and fresh smoke from different fires can be misleading due to high fire-fire variability. The two main types of BB were deforestation and crop residue fires, but determining the regional average mix of these types is difficult. BB in the Yucatan is a major source of trace gases and particles in the region.

5.7 Acknowledgements

Bibliography

Abel, S. J., Haywood, J. M., Highwood, E. J., Li, J., and Buseck, P. R.: Evolution of biomass burning aerosol properties from an agricultural fire in southern Africa, Geophys. Res. Lett., 30, doi:10.1029/2003GL017342, 2003.

Adachi, K. and Buseck, P. R.: Internally mixed soot, sulfates, and organic matter in aerosol particles from Mexico City, Atmos. Chem. Phys., 8, 6469–6481, 2008.

Aiken, A. C., Decarlo, P. F., Kroll, J. H., Worsnop, D. R., Huffman, J. A., Docherty, K. S., Ulbrich, I. M., Mohr, C., Kimmel, J. R., Sueper, D., Sun, Y., Zhang, Q., Trimborn, A., Northway, M., Ziemann, P. J., Canagaratna, M. R., Onasch, T. B., Alfarra, M. R., Prevot, A. S. H., Dommen, J., Duplissy, J., Metzger, A., Baltensperger, U., and Jimenez, J. L.: O/C and OM/OC ratios of primary, secondary, and ambient organic aerosols with high-resolution time-of-flight aerosol mass spectrometry, Environ. Sci. Technol., 42, 4478–4485, doi:10.1021/es703009q, 2008.

Alvarado, M. J. and Prinn, R. G.: Formation of ozone and growth of aerosols in young smoke plumes from biomass burning: 1. Lagrangian parcel studies, J. Geophys. Res.-Atmos., 114, doi: 10.1029/2008JD011144, 2009.

Andreae, M. O. and Merlet, P.: Emission of trace gases and aerosols from biomass burning, Global Biogeochem. Cy., 15, 955–966, 2001.

Bertram, A. K., Ivanov, A. V., Hunter, M., Molina, L. T., and Molina, M. J.: The reaction probability of OH on organic surfaces of tropospheric interest, J. Phys. Chem. A, 105, 9415–9421, doi:10.1021/jp0114034, 2001.

Bravo, A. H., Sosa, E. R., Sanchez, A. P., Jaimes, P. M., and Saavedra, R. M. I.: Impact of wildfires on the air quality of Mexico City, 1992-1999, Environ. Pollut., 117, 243–253, 2002.

Capes, G., Johnson, B., McFiggans, G., Williams, P. I., Haywood, J., and Coe, H.: Aging of biomass burning aerosols over West Africa: Aircraft measurements of chemical composition, microphysical properties, and emission ratios, J. Geophys. Res.-Atmos., 113, doi:10.1029/2008JD009845, 2008.

Christian, T. J., Kleiss, B., Yokelson, R. J., Holzinger, R., Crutzen, P. J., Hao, W. M., Saharjo, B. H., and Ward, D. E.: Comprehensive laboratory measurements of biomass-burning emissions: 1. Emissions from Indonesian, African, and other fuels, J. Geophys. Res.-Atmos., 108, doi:10. 1029/2003JD003704, 2003.

Clarke, A., McNaughton, C., Kapustin, V., Shinozuka, Y., Howell, S., Dibb, J., Zhou, J., Anderson, B., Brekhovskikh, V., Turner, H., and Pinkerton, M.: Biomass burning and pollution aerosol over North America: Organic components and their influence on spectral optical properties and humidification response, J. Geophys. Res.-Atmos., 112, doi:10.1029/2006JD007777, 2007.

Clarke, A. D., Shinozuka, Y., Kapustin, V. N., Howell, S., Huebert, B., Doherty, S., Anderson, T., Covert, D., Anderson, J., Hua, X., Moore, K. G., McNaughton, C., Carmichael, G., and Weber, R.: Size distributions and mixtures of dust and black carbon aerosol in Asian outflow: Physiochemistry and optical properties, J. Geophys. Res.-Atmos., 109, doi:10.1029/2003JD004378, 2004.

Coffer, W. R., Levine, J. S., Winstead, E. L., Stocks, B. J., Cahoon, D. R., and Pinto, J. P.: Trace gas emissions from tropical biomass fires – Yucatan Peninsula, Mexico, Atmos. Environ. A-Gen., 27, 1903–1907, 1993.

Crounse, J. D., McKinney, K. A., Kwan, A. J., and Wennberg, P. O.: Measurement of gas-phase hydroperoxides by chemical ionization mass spectrometry, Anal. Chem., 78, 6726–6732, doi:10.1021/ac0604235, 2006.

Crounse, J. D., DeCarlo, P. F., Blake, D. R., Emmons, L. K., Campos, T. L., Apel, E. C., Clarke, A. D., Weinheimer, A. J., McCabe, D. C., Yokelson, R. J., Jimenez, J. L., and Wennberg, P. O.: Biomass burning and urban air pollution over the Central Mexican Plateau, Atmos. Chem. Phys., 9, 4929–4944, 2009.

Crutzen, P. J., Lawrence, M. G., and Poschl, U.: On the background photochemistry of tropospheric ozone, Tellus A, 51, 123–146, international Symposium to Commemorate the 100th Anniversary of the Birth of Carl Gustaf Rossby (Rossby-100), Stockholm, Sweden, Jun 08-12, 1998, 1999.

de Foy, B., Lei, W., Zavala, M., Volkamer, R., Samuelsson, J., Mellqvist, J., Galle, B., Martinez, A. P., Grutter, M., Retama, A., and Molina, L. T.: Modelling constraints on the emission inventory and on vertical dispersion for CO and SO_2 in the Mexico City metropolitan area using solar FTIR and zenith sky UV spectroscopy, Atmos. Chem. Phys., 7, 781–801, 2007.

de Gouw, J. A., Warneke, C., Parrish, D. D., Holloway, J. S., Trainer, M., and Fehsenfeld, F. C.: Emission sources and ocean uptake of acetonitrile (ceCH3CN) in the atmosphere, J. Geophys. Res.-Atmos., 108, doi:10.1029/2002JD002897, 2003.

de Gouw, J. A., Warneke, C., Stohl, A., Wollny, A. G., Brock, C. A., Cooper, O. R., Holloway, J. S., Trainer, M., Fehsenfeld, F. C., Atlas, E. L., Donnelly, S. G., Stroud, V., and Lueb, A.: Volatile

organic compounds composition of merged and aged forest fire plumes from Alaska and western Canada, J. Geophys. Res.-Atmos., 111, doi:10.1029/2005JD006175, 2006.

de Zarate, I. O., Ezcurra, A., Lacaux, J. P., Van Dinh, P., and de Argandona, J. D.: Pollution by cereal waste burning in Spain, Atmos. Res., 73, 161–170, doi:10.1016/j.atmosres.2004.07.006, 2005.

DeCarlo, P. F., Kimmel, J. R., Trimborn, A., Northway, M. J., Jayne, J. T., Aiken, A. C., Gonin, M., Fuhrer, K., Horvath, T., Docherty, K. S., Worsnop, D. R., and Jimenez, J. L.: Field-deployable, high-resolution, time-of-flight aerosol mass spectrometer, Anal. Chem., 78, 8281–8289, doi:10.1021/ac061249n, 2006.

DeCarlo, P. F., Dunlea, E. J., Kimmel, J. R., Aiken, A. C., Sueper, D., Crounse, J., Wennberg, P. O., Emmons, L., Shinozuka, Y., Clarke, A., Zhou, J., Tomlinson, J., Collins, D. R., Knapp, D., Weinheimer, A. J., Montzka, D. D., Campos, T., and Jimenez, J. L.: Fast airborne aerosol size and chemistry measurements above Mexico City and Central Mexico during the MILAGRO campaign, Atmos. Chem. Phys., 8, 4027–4048, 2008.

Desanker, P. V., Frost, P. G. H., Justice, C. O., and Scholes, R. J., eds.: The miombo network: Framework for a terrestrial transect study of land-use and landcover change in the miombo ecosystems of central Africa, IGBP Rep. 41, International Geosphere-Biosphere Programme, Stockholm (Sweden), Stockholm, Sweden, 1997.

Draxler, R. R. and Rolph, G. D.: HYSPLIT (HYbrid Single-Particle Lagrangian Integrated Trajectory) Model access via NOAA ARL READY Website, URL `http://www.arl.noaa.gov/ready/hysplit4.html`, 2003.

Fast, J. D., de Foy, B., Rosas, F. A., Caetano, E., Carmichael, G., Emmons, L., McKenna, D., Mena, M., Skamarock, W., Tie, X., Coulter, R. L., Barnard, J. C., Wiedinmyer, C., and Madronich, S.: A meteorological overview of the MILAGRO field campaigns, Atmos. Chem. Phys., 7, 2233–2257, 2007.

Ferek, R. J., Reid, J. S., Hobbs, P. V., Blake, D. R., and Liousse, C.: Emission factors of hydrocarbons, halocarbons, trace gases and particles from biomass burning in Brazil, J. Geophys. Res.-Atmos., 103, 32 107–32 118, 1998.

Finlayson-Pitts, B. J. and Pitts Jr, J. N.: Chemistry of the Upper and Lower Atmosphere: Theory, Experiments and Applications, Academic Press, San Diego, CA, USA, 2000.

Gerbig, C., Schmitgen, S., Kley, D., Volz-Thomas, A., Dewey, K., and Haaks, D.: An improved fast-response vacuum-UV resonance fluorescence CO instrument, J. Geophys. Res.-Atmos., 104, 1699–1704, 1999.

Giglio, L.: Characterization of the tropical diurnal fire cycle using VIRS and MODIS observations, Remote Sens. Environ., 108, 407–421, doi:10.1016/j.rse.2006.11.018, 2007.

Giglio, L., Descloitres, J., Justice, C. O., and Kaufman, Y. J.: An enhanced contextual fire detection algorithm for MODIS, Remote Sens. Environ., 87, 273–282, doi:10.1016/S0034-4257(03)00184-6, 2003.

Giglio, L., van der Werf, G. R., Randerson, J. T., Collatz, G. J., and Kasibhatla, P.: Global estimation of burned area using MODIS active fire observations, Atmos. Chem. Phys., 6, 957–974, 2006.

Goode, J. G., Yokelson, R. J., Ward, D. E., Susott, R. A., Babbitt, R. E., Davies, M. A., and Hao, W. M.: Measurements of excess O_3, CO_2, CO, CH_4, C_2H_4, C_2H_2, HCN, NO, NH_3, HCOOH, CH_3COOH, HCHO, and CH_3OH in 1997 Alaskan biomass burning plumes by airborne fourier transform infrared spectroscopy (AFTIR), J. Geophys. Res.-Atmos., 105, 22 147–22 166, 2000.

Grieshop, A. P., Logue, J. M., Donahue, N. M., and Robinson, A. L.: Laboratory investigation of photochemical oxidation of organic aerosol from wood fires 1: measurement and simulation of organic aerosol evolution, Atmos. Chem. Phys., 9, 1263–1277, 2009.

Grutter, M., Basaldud, R., Rivera, C., Harig, R., Junkerman, W., Caetano, E., and Delgado-Granados, H.: SO_2 emissions from Popocatepetl volcano: emission rates and plume imaging using optical remote sensing techniques, Atmos. Chem. Phys., 8, 6655–6663, 2008.

Hand, J. L., Malm, W. C., Laskin, A., Day, D., Lee, T., Wang, C., Carrico, C., Carrillo, J., Cowin, J. P., Collett, J., and Iedema, M. J.: Optical, physical, and chemical properties of tar balls observed during the Yosemite Aerosol Characterization Study, J. Geophys. Res.-Atmos., 110, doi:10.1029/2004JD005728, 2005.

Hansen, M. C., DeFries, R. S., Townshend, J. R. G., Carroll, M., Dimiceli, C., and Sohlberg, R. A.: Global Percent Tree Cover at a Spatial Resolution of 500 Meters: First Results of the MODIS Vegetation Continuous Fields Algorithm, Earth Interactions, 7, 2003.

Hawbaker, T. J., Radeloff, V. C., Syphard, A. D., Zhu, Z., and Stewart, S. I.: Detection rates of the MODIS active fire product in the United States, Remote Sens. Environ., 112, 2656–2664, doi:10.1016/j.rse.2007.12.008, 2008.

Hobbs, P. V., Sinha, P., Yokelson, R. J., Christian, T. J., Blake, D. R., Gao, S., Kirchstetter, T. W., Novakov, T., and Pilewskie, P.: Evolution of gases and particles from a savanna fire in South Africa, J. Geophys. Res.-Atmos., 108, doi:10.1029/2002JD002352, 2003.

Hoffa, E. A., Ward, D. E., Hao, W. M., Susott, R. A., and Wakimoto, R. H.: Seasonality of carbon emissions from biomass burning in a Zambian savanna, J. Geophys. Res.-Atmos., 104, 13 841–13 853, 1999.

Hoffer, A., Gelencser, A., Blazso, M., Guyon, P., Artaxo, P., and Andreae, M. O.: Diel and seasonal variations in the chemical composition of biomass burning aerosol, Atmos. Chem. Phys., 6, 3505–3515, 2006.

Johnson, K. S., Laskin, A., Jimenez, J. L., Shutthanandan, V., Molina, L. T., Salcedo, D., Dzepina, K., and Molina, M. J.: Comparative analysis of urban atmospheric aerosol by particle-induced X-ray emission (PIXE), proton elastic scattering analysis (PESA), and aerosol mass spectrometry (AMS), Environ. Sci. Technol., 42, 6619–6624, doi:10.1021/es800393e, 2008.

Jost, C., Trentmann, J., Sprung, D., Andreae, M., McQuaid, J., and Barjat, H.: Trace gas chemistry in a young biomass burning plume over Namibia: Observations and model simulations, J. Geophys. Res.-Atmos., 108, doi:10.1029/2002JD002431, 2003.

Karl, T., Apel, E., Hodzic, A., Riemer, D. D., Blake, D. R., and Wiedinmyer, C.: Emissions of volatile organic compounds inferred from airborne flux measurements over a megacity, Atmos. Chem. Phys., 9, 271–285, 2009.

Karl, T. G., Christian, T. J., Yokelson, R. J., Artaxo, P., Hao, W. M., and Guenther, A.: The Tropical Forest and Fire Emissions Experiment: method evaluation of volatile organic compound emissions measured by PTR-MS, FTIR, and GC from tropical biomass burning, Atmos. Chem. Phys., 7, 5883–5897, 2007.

Kauffman, J. B., Steele, M. D., Cummings, D. L., and Jaramillo, V. J.: Biomass dynamics associated with deforestation, fire, and, conversion to cattle pasture in a Mexican tropical dry forest, Forest Ecol. Manag., 176, 1–12, 2003.

Kaufman, Y. J. and Nakajima, T.: Effect of Amazon smoke on cloud microphysics and albedo - Analysis from satellite imagery, J. Appl. Meteorol., 32, 729–744, 1993.

Keene, W. C., Lobert, R. M., Crutzen, P. J., Maben, J. R., Scharffe, D. H., Landmann, T., Hely, C., and Brain, C.: Emissions of major gaseous and particulate species during experimental burns of southern African biomass, J. Geophys. Res.-Atmos., 111, doi:10.1029/2005JD006319, 2006.

Kleinman, L. I., Springston, S. R., Daum, P. H., Lee, Y. N., Nunnermacker, L. J., Senum, G. I., Wang, J., Weinstein-Lloyd, J., Alexander, M. L., Hubbe, J., Ortega, J., Canagaratna, M. R., and Jayne, J.: The time evolution of aerosol composition over the Mexico City plateau, Atmos. Chem. Phys., 8, 1559–1575, 2008.

Kreidenweis, S. M., Remer, L. A., Bruintjes, R., and Dubovik, O.: Smoke aerosol from biomass burning in Mexico: Hygroscopic smoke optical model, J. Geophys. Res.-Atmos., 106, 4831–4844, 2001.

Lacaux, J. P., Delmas, R., Jambert, C., and Kuhlbusch, T. A. J.: NOx emissions from African savanna fires, J. Geophys. Res.-Atmos., 101, 23 585–23 595, 1996.

Lara, L. L., Artaxo, P., Martinelli, L. A., Camargo, P. B., Victoria, R. L., and Ferraz, E. S. B.: Properties of aerosols from sugar-cane burning emissions in Southeastern Brazil, Atmos. Environ., 39, 4627–4637, doi:10.1016/j.atmosenv.2005.04.026, 2005.

Latifovic, R., Zhu, Z., Cihlar, J., Beaubien, J, and R, F.: The Land Cover Map for North America in the Year 2000, GLC2000 database, URL http://www-tem.jrc.it/glc2000, 2003.

Lee, M., Heikes, B. G., Jacob, D. J., Sachse, G., and Anderson, B.: Hydrogen peroxide, organic hydroperoxide, and formaldehyde as primary pollutants from biomass burning, J. Geophys. Res.-Atmos., 102, 1301–1309, 1997.

Lee, Y. S., Collins, D. R., Li, R., Bowman, K. P., and Feingold, G.: Expected impact of an aged biomass burning aerosol on cloud condensation nuclei and cloud droplet concentrations, J. Geophys. Res.-Atmos., 111, doi:10.1029/2005JD006464, 2006.

Li, J., Posfai, M., Hobbs, P. V., and Buseck, P. R.: Individual aerosol particles from biomass burning in southern Africa: 2, Compositions and aging of inorganic particles, J. Geophys. Res.-Atmos., 108, doi:10.1029/2002JD002310, 2003.

Li, Q. B., Jacob, D. J., Bey, I., Yantosca, R. M., Zhao, Y. J., Kondo, Y., and Notholt, J.: Atmospheric hydrogen cyanide (HCN): Biomass burning source, ocean sink?, Geophys. Res. Lett., 27, 357–360, 2000.

Lyons, W. A., Nelson, T. E., Williams, E. R., Cramer, J. A., and Turner, T. R.: Enhanced positive cloud-to-ground lightning in thunderstorms ingesting smoke from fires, Science, 282, 77–80, 1998.

Magi, B. I. and Hobbs, P. V.: Effects of humidity on aerosols in southern Africa during the biomass burning season, J. Geophys. Res.-Atmos., 108, doi:10.1029/2002JD002144, 2003.

Martins, J. V., Artaxo, P., Liousse, C., Reid, J. S., Hobbs, P. V., and Kaufman, Y. J.: Effects of black carbon content, particle size, and mixing on light absorption by aerosols from biomass burning in Brazil, J. Geophys. Res.-Atmos., 103, 32 041–32 050, 1998.

Mason, S. A., Field, R. J., Yokelson, R. J., Kochivar, M. A., Tinsley, M. R., Ward, D. E., and Hao, W. M.: Complex effects arising in smoke plume simulations due to inclusion of direct emissions of oxygenated organic species from biomass combustion, J. Geophys. Res.-Atmos., 106, 12 527–12 539, 2001.

Mason, S. A., Trentmann, J., Winterrath, T., Yokelson, R. J., Christian, T. J., Carlson, L. J., Warner, T. R., Wolfe, L. C., and Andreae, M. O.: Intercomparison of two box models of the chemical evolution in biomass-burning smoke plumes, J. Atmos. Chem., 55, 273–297, doi:10.1007/s10874-006-9039-5, 2006.

Massie, S. T., Gille, J. C., Edwards, D. P., and Nandi, S.: Satellite observations of aerosol and CO over Mexico city, Atmos. Environ., 40, 6019–6031, doi:10.1016/j.atmosenv.2005.11.065, 13th International Symposium on Transport and Air Pollution, Boulder, CO, SEP 13-15, 2004, 2006.

Mauldin, R. L., Cantrell, C. A., Zondlo, M. A., Kosciuch, E., Ridley, B. A., Weber, R., and Eisele, F. E.: Measurements of OH, H_2SO_4, and MSA during Tropospheric Ozone Production About the Spring Equinox (TOPSE), J. Geophys. Res.-Atmos., 108, doi:10.1029/2002JD002295, 2003.

McKenzie, L. M., Ward, D. E., and Hao, W. M.: Chlorine and Bromine in the biomass of tropical and temperate ecosystems, in Biomass Burning and Global Change, MIT Press, Cambridge, Mass., USA, 1996.

Molina, L. T., Kolb, C. E., de Foy, B., Lamb, B. K., Brune, W. H., Jimenez, J. L., Ramos-Villegas, R., Sarmiento, J., Paramo-Figueroa, V. H., Cardenas, B., Gutierrez-Avedoy, V., and Molina, M. J.:

Air quality in North America's most populous city – overview of the MCMA-2003 campaign, Atmos. Chem. Phys., 7, 2447–2473, 2007.

Posfai, M., Simonics, R., Li, J., Hobbs, P. V., and Buseck, P. R.: Individual aerosol particles from biomass burning in southern Africa: 1. Compositions and size distributions of carbonaceous particles, J. Geophys. Res.-Atmos., 108, doi:10.1029/2002JD002291, 2003.

Radke, L. F., Hegg, D. A., Hobbs, P. V., Nance, J. D., Lyons, J. H., Laursen, K. K., Weiss, R. E., Riggan, P. J., and Ward, D. E.: Particulate and trace gas emissions from large biomass fires in North-America, in: Global Biomass Burning – Atmospheric, Climatic, and Biospheric Implications, edited by Levine, J. S., pp. 209–224, NASA; NSF; US EPA; USDA, Forest Serv.; Int. Geosphere Biosphere Program; Int. Global Atmos. Chem. Project, MIT Press, chapman conf. on global biomass burning: Atmospheric, climatic, and biospheric implications, Williamsburg, VA, Mar 19-23, 1990, 1991.

Ramanathan, V., Crutzen, P. J., Lelieveld, J., Mitra, A. P., Althausen, D., Anderson, J., Andreae, M. O., Cantrell, W., Cass, G. R., Chung, C. E., Clarke, A. D., Coakley, J. A., Collins, W. D., Conant, W. C., Dulac, F., Heintzenberg, J., Heymsfield, A. J., Holben, B., Howell, S., Hudson, J., Jayaraman, A., Kiehl, J. T., Krishnamurti, T. N., Lubin, D., McFarquhar, G., Novakov, T., Ogren, J. A., Podgorny, I. A., Prather, K., Priestley, K., Prospero, J. M., Quinn, P. K., Rajeev, K., Rasch, P., Rupert, S., Sadourny, R., Satheesh, S. K., Shaw, G. E., Sheridan, P., and Valero, F. P. J.: Indian Ocean Experiment: An integrated analysis of the climate forcing and effects of the great Indo-Asian haze, J. Geophys. Res.-Atmos., 106, 28 371–28 398, 2001.

Ridley, B., Ott, L., Pickering, K., Emmons, L., Montzka, D., Weinheimer, A., Knapp, D., Grahek, F., Li, L., Heymsfield, G., McGill, M., Kucera, P., Mahoney, M., Baumgardner, D., Schultz, M., and Brasseur, G.: Florida thunderstorms: A faucet of reactive nitrogen to the upper troposphere, J. Geophys. Res.-Atmos., 109, doi:10.1029/2004JD004769, 2004.

Rogers, C. M. and Bowman, K. P.: Transport of smoke from the Central American fires of 1998, J. Geophys. Res.-Atmos., 106, 28 357–28 368, 2001.

Salcedo, D., Onasch, T. B., Dzepina, K., Canagaratna, M. R., Zhang, Q., Huffman, J. A., DeCarlo, P. F., Jayne, J. T., Mortimer, P., Worsnop, D. R., Kolb, C. E., Johnson, K. S., Zuberi, B., Marr, L. C., Volkamer, R., Molina, L. T., Molina, M. J., Cardenas, B., Bernabe, R. M., Marquez, C., Gaffney, J. S., Marley, N. A., Laskin, A., Shutthanandan, V., Xie, Y., Brune, W., Lesher, R.,

Shirley, T., and Jimenez, J. L.: Characterization of ambient aerosols in Mexico City during the MCMA-2003 campaign with Aerosol Mass Spectrometry: results from the CENICA Supersite, Atmos. Chem. Phys., 6, 925–946, 2006.

Sander, S. P., Finlayson-Pitts, B. J., Friedl, R. R., and et al.: Chemical kinetics and photochemical data for use in atmospheric studies, evaluation number 15, JPL Publication 06-2, 2006.

Seinfeld, J. H. and Pandis, S. N.: Atmospheric chemistry and physics: From air pollution to climate change, Wiley, Hoboken, NJ, 2006.

Shea, R. W., Shea, B. W., Kauffman, J. B., Ward, D. E., Haskins, C. I., and Scholes, M. C.: Fuel biomass and combustion factors associated with fires in savanna ecosystems of South Africa and Zambia, J. Geophys. Res.-Atmos., 101, 23 551–23 568, 1996.

Shetter, R. E. and Muller, M.: Photolysis frequency measurements using actinic flux spectroradiometry during the PEM-Tropics mission: Instrumentation description and some results, J. Geophys. Res.-Atmos., 104, 5647–5661, 1999.

Singh, H. B., Kanakidou, M., Crutzen, P. J., and Jacob, D. J.: High-concentrations and photochemical fate of oxygented hydrocarbons in the global troposphere, Nature, 378, 50–54, 1995.

Sinha, P., Hobbs, P. V., Yokelson, R. J., Blake, D. R., Gao, S., and Kirchstetter, T. W.: Emissions from miombo woodland and dambo grassland savanna fires, J. Geophys. Res.-Atmos., 109, doi:10.1029/2004JD004521, 2004.

Slusher, D. L., Huey, L. G., Tanner, D. J., Flocke, F. M., and Roberts, J. M.: A thermal dissociation-chemical ionization mass spectrometry (TD-CIMS) technique for the simultaneous measurement of peroxyacyl nitrates and dinitrogen pentoxide, J. Geophys. Res.-Atmos., 109, doi:10.1029/2004JD004670, 2004.

Smith, R., Adams, M., Maier, S., Craig, R., Kristina, A., and Maling, I.: Estimating the area of stubble burning from the number of active fires detected by satellite, Remote Sens. Environ., 109, 95–106, doi:10.1016/j.rse.2006.12.011, 2007.

Susott, R. A., Olbu, G. J., Baker, S. P., Ward, D. E., Kauffman, J. B., and Shea, R.: Carbon, hydrogen, nitrogen, and thermogravimetric analysis of tropical ecosystem biomass, in Biomass Burning and Global Change, edited by, MIT Press, Cambridge, Mass., 1996.

Tabazadeh, A., Yokelson, R. J., Singh, H. B., Hobbs, P. V., Crawford, J. H., and Iraci, L. T.: Heterogeneous chemistry involving methanol in tropospheric clouds, Geophys. Res. Lett., 31, doi: 10.1029/2003GL018775, 2004.

Trent, A., Davies, M. A., Fisher, R., Thistle, H., and Babbitt, R.: Evaluation of optical instruments for real-time, continuous monitoring of smoke particulates, Tech. Rep. Tech. Rep. 0025 2860 MTDC, USDA Forest Service, Missoula Technology and Development Center, Missoula, MT, USA, 2000.

Trentmann, J., Yokelson, R. J., Hobbs, P. V., Winterrath, T., Christian, T. J., Andreae, M. O., and Mason, S. A.: An analysis of the chemical processes in the smoke plume from a savanna fire, J. Geophys. Res.-Atmos., 110, doi:10.1029/2004JD005628, 2005.

Ward, D. E. and Hardy, C. C.: Smoke emissions from wildland fires, Environ. Int., 17, 117–134, 1991.

Ward, D. E., Susott, R. A., Kauffman, J. B., Babbitt, R. E., Cummings, D. L., Dias, B., Holben, B. N., Kauffman, Y. J., Rasmussen, R. A., and Setzer, A. W.: Smoke and fire characteristics for cerrado and deforestation burns in Brazil – Base-B experiment:, J. Geophys. Res.-Atmos., 97, 14 601–14 619, 1992.

Weibring, P., Richter, D., Walega, J. G., and Fried, A.: First demonstration of a high performance difference frequency spectrometer on airborne, Opt. Express, 15, 13 476–13 495, 2007.

Wiedinmyer, C., Quayle, B., Geron, C., Belote, A., McKenzie, D., Zhang, X., O'Neill, S., and Wynne, K. K.: Estimating emissions from fires in North America for air quality modeling, Atmos. Environ., 40, 3419–3432, doi:10.1016/j.atmosenv.2006.02.010, 2006.

Yevich, R. and Logan, J. A.: An assessment of biofuel use and burning of agricultural waste in the developing world, Global Biogeochem. Cy., 17, doi:10.1029/2002GB001952, 2003.

Yokelson, R. J., Griffith, D. W. T., and Ward, D. E.: Open-path Fourier transform infrared studies of large-scale laboratory biomass fires, J. Geophys. Res.-Atmos., 101, 21 067–21 080, 1996.

Yokelson, R. J., Susott, R., Ward, D. E., Reardon, J., and Griffith, D. W. T.: Emissions from smoldering combustion of biomass measured by open-path Fourier transform infrared spectroscopy, J. Geophys. Res.-Atmos., 102, 18 865–18 877, 1997.

142

Yokelson, R. J., Goode, J. G., Ward, D. E., Susott, R. A., Babbitt, R. E., Wade, D. D., Bertschi, I., Griffith, D. W. T., and Hao, W. M.: Emissions of formaldehyde, acetic acid, methanol, and other trace gases from biomass fires in North Carolina measured by airborne Fourier transform infrared spectroscopy, J. Geophys. Res.-Atmos., 104, 30 109–30 125, 1999.

Yokelson, R. J., Bertschi, I. T., Christian, T. J., Hobbs, P. V., Ward, D. E., and Hao, W. M.: Trace gas measurements in nascent, aged, and cloud-processed smoke from African savanna fires by airborne Fourier transform infrared spectroscopy (AFTIR), J. Geophys. Res.-Atmos., 108, doi:10.1029/2002JD002322, 2003.

Yokelson, R. J., Karl, T., Artaxo, P., Blake, D. R., Christian, T. J., Griffith, D. W. T., Guenther, A., and Hao, W. M.: The Tropical Forest and Fire Emissions Experiment: overview and airborne fire emission factor measurements, Atmos. Chem. Phys., 7, 5175–5196, 2007a.

Yokelson, R. J., Urbanski, S. P., Atlas, E. L., Toohey, D. W., Alvarado, E. C., Crounse, J. D., Wennberg, P. O., Fisher, M. E., Wold, C. E., Campos, T. L., Adachi, K., Buseck, P. R., and Hao, W. M.: Emissions from forest fires near Mexico City, Atmos. Chem. Phys., 7, 5569–5584, 2007b.

Yokelson, R. J., Christian, T. J., Karl, T. G., and Guenther, A.: The tropical forest and fire emissions experiment: laboratory fire measurements and synthesis of campaign data, Atmos. Chem. Phys., 8, 3509–3527, 2008.

Zhang, Q., Worsnop, D. R., Canagaratna, M. R., and Jimenez, J. L.: Hydrocarbon-like and oxygenated organic aerosols in Pittsburgh: insights into sources and processes of organic aerosols, Atmos. Chem. Phys., 5, 3289–3311, 2005.

Chapter 6

Isoprene photooxidation: new insights into the production of acids and organic nitrates*

6.1 Abstract

We describe a nearly explicit chemical mechanism for isoprene photooxidation guided by chamber studies that include time-resolved observation of an extensive suite of volatile compounds. We provide new constraints on the chemistry of the poorly-understood isoprene δ-hydroxy channels, which account for more than one third of the total isoprene carbon flux and a larger fraction of the nitrate yields. We show that the *cis* branch dominates the chemistry of the δ-hydroxy channel with less than 5% of the carbon following the *trans* branch. The modelled yield of isoprene nitrates is $12 \pm 3\%$ with a large difference between the δ and β branches. The oxidation of these nitrates releases about 50% of the NO_x. Methacrolein nitrates (modelled yield $\simeq 15\pm3\%$ from methacrolein) and methylvinylketone nitrates (modelled yield $\simeq 11\pm3\%$ yield from methylvinylketone) are also observed. Propanone nitrate, produced with a yield of 1% from isoprene, appears to be the longest-lived nitrate formed in the total oxidation of isoprene. We find a large molar yield of formic acid and suggest a novel mechanism leading to its formation from the organic nitrates. Finally, the most important features of this mechanism are summarized in a condensed scheme appropriate for use in global chemical transport models.

6.2 Introduction

Isoprene (2-methyl-1,3-butadiene, C_5H_8) is a short-lived compound ($\tau_{1/2} = 1$–2 hours) emitted by many deciduous trees during daylight hours. Between 0.5% and 2% of the carbon fixed by isoprene emitting plants is released to the atmosphere as isoprene (Harley et al., 1999), a flux accounting for about one third of the total anthropogenic and natural volatile organic compounds (VOC) emissions (Guenther et al., 2006). Isoprene plays a crucial role in determining the oxidative chemistry of the troposphere. Ozone levels in urban as well as in rural sites are impacted by the sequestration and transport of NO_x via formation of isoprene nitrates (Horowitz et al., 1998) and various isoprene-derived peroxyacylnitrates. Moreover, field (Claeys et al., 2004) and chamber studies (Kroll et al., 2006; Surratt et al., 2006) have recently shown that compounds formed in isoprene photooxidation, such as methylglyceric acid or methylerythritol, are ubiquitous in aerosol particles and may contribute significantly to the aerosol global burden (Henze and Seinfeld, 2006; van Donkelaar et al., 2007). In the light of the potential for significant change in isoprene emissions due to climate and land use changes (Shallcross and Monks, 2000), studies have been made to predict the impact of altered isoprene emissions on tropospheric ozone (Sanderson et al., 2003;

Wiedinmyer et al., 2006). von Kuhlmann et al. (2004) and Fiore et al. (2005) note, however, that quantifying this impact is difficult due to uncertainties regarding: 1) the dependence of isoprene emissions on temperature (Harley et al., 2004) and CO_2 concentration (Rosenstiel et al., 2003); and 2) the isoprene photooxidation scheme, especially the yields and fates of isoprene nitrates. In this study, we use anion chemical ionization mass spectrometry (CIMS) to monitor the photooxidation of isoprene. This technique greatly expands the range of compounds that can be observed during the photooxidation of isoprene and other hydrocarbons (Ng et al., 2008). Quantitative interpretation is challenging, however, because 1) calibration standards are not available for many of the compounds identified and 2) mass analogs (compounds having the same mass) are not differentiated. Therefore the iterative development of a detailed mechanism is used to analyze the different signals and derive branching ratios and yields for the compounds identified. First, we briefly describe the experiment emphasizing the calibration of CIMS measurements. Next, we report and identify the largest signals monitored by CIMS. We then discuss how these signals help constrain the development of the model emphasizing the δ-hydroxy channels, the organic nitrate yield and fate, as well as some routes to organic acids. Finally we discuss the potential implications of our findings for tropospheric chemistry and present a reduced mechanism suitable for inclusion in chemical transport model.

6.3 Experiment

6.3.1 Experimental setting

The data of the present study were collected in the 28 m^3 Caltech atmospheric chamber, in an experiment similar to those described by Kroll et al. (2006). Initial concentrations of isoprene, NO, and H_2O_2 were 94 ppbv, 500 ppbv and 2.1 ppmv. The photolysis of H_2O_2 constitutes the primary OH source in the experiment. NO was added prior to isoprene so that the chamber was initially ozone free. The initial relative humidity was less than 6% and is assumed to be constant in this study. The temperature increased by about 5 degrees in the first 100 minutes and remained constant thereafter at 296.5 K. To simplify modelling, we consider this temperature to hold during the whole experiment. Isoprene decay was monitored using GC-FID. Ozone was measured by UV absorption (Horiba) and NO and NO_2 (after conversion to NO) by chemiluminescence. The size distribution and the volume concentration of secondary organic aerosol (SOA) were measured using a differential mobility analyzer (DMA, TSI 3760). Further details are available in Kroll et al. (2006).

6.3.2 CIMS

Gas-phase products were monitored using a novel CIMS technique (Crounse et al., 2006) with CF_3O^- as the reagent anion. Non-reactive with ozone, carbon dioxide and dioxygen (Huey et al., 1996), CF_3O^- is a versatile reagent ion suitable for the study of many oxygenated compounds. In general, two primary ionization pathways are observed:

$$VOC + CF_3O^- \rightarrow VOC^-_{-H} \cdot HF + CF_2O \tag{R6.1}$$

$$VOC + CF_3O^- \rightleftarrows VOC \cdot CF_3O^- \tag{R6.2}$$

A minor ionization pathway is observed for certain compounds:

$$CF_3O^- + HOOX(O)R \rightarrow HF + CF_2O \cdot OOX(O)R^- \tag{R6.3}$$
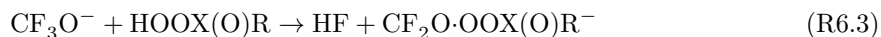
In Reaction R6.3, CF_2O is incorporated into the original neutral molecule. Reaction R6.3 has been observed for peroxynitric acid (PNA) and for peroxy acetic acid (PAA). While Reaction R6.3 is not the major ionization pathway, in several cases it is useful for distinguishing certain mass analogs. The dominant ionization pathway for an analyte depends mostly on the acidity (or fluoride affinity) of the neutral species (Amelynck et al., 2000b; Crounse et al., 2006). Highly acidic compounds, such as nitric acid, only form the transfer product ion through Reaction R6.1 while hydrogen peroxide and methylhydrogen peroxide (MHP) form only the cluster product ions through Reaction R6.2. Species with intermediate acidity (e.g., formic and acetic acids) form both the transfer and cluster products. Most of the VOC measured in this study follow Reaction R6.2. In this study, air was drawn from the chamber through a perfluoroalkoxy Teflon line of 1.2 m length and 0.635 cm outer diameter (OD), at a rate of 10 standard liters per minute (slm), and then sub-sampled into the CIMS flow tube using a critical orifice made of glass. The orifice constrained the flow from the chamber into the CIMS to be 145 standard cubic centimeters per minute (sccm). Upon introduction to the CIMS flow tube, the chamber gas was diluted with 1760 sccm of UHP N_2 (99.999%) to a total pressure of 35 hPa, primarily to reduce the concentration of H_2O_2 to manageable levels. The gas is expanded in a flow tube (17.8 cm, 2.54 cm OD Pyrex glass coated with a thin layer of Teflon (Fluoropel 801A, from Cytonix Corp.)) before reacted with a transverse ion beam of the reagent anion (Crounse et al. 2006, Fig. 1). Mass scans were conducted using a quadrupole mass spectrometer from $m/z = 18$ to $m/z = 275$ dwelling on each mass for 1 s (giving a scan cycle of about $4\frac{1}{2}$ min). The mass scans were

repeated throughout the duration of the experiment (17 h). Zero scans were conducted periodically throughout the experiment by overfilling the critical orifice on the high pressure (chamber) side with UHP N_2. In addition to providing instrumental backgrounds, the temporal response of the zero scans give insight into the strength of the interaction of the measured compounds with the equipment walls. The instrumental background signals for most of the large molecular weight products produced in isoprene oxidation are very small (after the instrument has been sampling clean zero air for an extended period of time), which suggests that variations in instrumental background over the course of the experiment are not important for these signals. Compounds with a smaller molecular weight (e.g., formic and acetic acids) do have instrumental backgrounds, but the level of the instrumental background is small relative to the signal generated in the isoprene oxidation experiment (more than 10 times smaller), so ignoring instrumental background changes over the course of the experiment for these species does not introduce a substantial error.

6.3.3   Calibration

The concentration of a compound X, whose product ion is detected at $m/z = p$, is calculated through:

$$[X]_{\text{ppbv}} = \frac{\widehat{\text{Signal}(m/z\text{=p})}}{c_X} \tag{6.1}$$

where Signal(m/z = p) is the normalized signal associated with X (cf. Appendix 6.7.2.1) and c_X is the calibration constant for the compound X in ppbv^{-1}. In many cases, no standard is readily available and no experimental determination of c_X can be made. In such cases, we assume that c_X is related to the thermal capture rate (k_X) and the binding energy of the cluster. k_X is estimated from the Langevin-Gioumousis-Stevenson-based collision rate. We use the empirical approach developed by Su and Chesnavich (1982) to calculate k_X from the dipole moment (μ_X) and the polarizability (α_X) of X. In the absence of experimental determinations of μ_X and α_X, we use quantum chemical calculations to estimate them. The lowest energy conformers of the molecules are found with the conformer searches method within the Spartan06 quantum package (Wavefunction, 2006) at the B3LYP/6-31G(d) level of theory. The dipole moments and static polarizabilities are then calculated for the optimized geometries at the same level of theory. When a molecule has several low energy conformers, a thermally-weighted average of their reaction rate coefficients is used for k_X (cf. Appendix 6.7.2.2 for details). The sensitivity of the instrument to X also depends on the binding energy between X and the reagent anion as well as the nature of the reagent anion. In the

presence of abundant ligands (L) such as water or hydrogen peroxide, the sensitivity of the CIMS to some VOC is modified through two different processes: 1) $CF_3O^- \cdot L$ may react faster with X than the bare CF_3O^- anion because ligand exchange reactions can stabilize the product ion to a greater extent; 2) the cluster $CF_3O^- \cdot L$ may be sufficiently stable leading to a lower sensitivity at higher L mixing ratio due to ligand exchange:

$$VOC \cdot CF_3O^- + L \rightleftarrows VOC + CF_3O^- \cdot L, \tag{R6.4}$$

$$L = H_2O, H_2O_2.$$
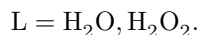
For example, Crounse et al. (2006) reported that the sensitivity to methylhydroperoxide (MHP) decreases with the water vapor mixing ratio due to Reaction R6.4. In general large molecules featuring several functional groups (peroxide, nitrooxy, alcohol, carbonyl) exhibit only a weak dependence on the amount of water. Therefore, we neglect the binding energy effect in this study and take:

$$c_X = \frac{k_X}{k_{HNO_3}} c_{HNO_3} \tag{6.3}$$

where $k_{HNO_3} = 1.93 \times 10^{-9}\,\mathrm{cm^3\,molecule^{-1}\,s^{-1}}$ is calculated using the experimental dipole and polarizability of nitric acid and c_{HNO_3} is the sensitivity to nitric acid for typical conditions where the flow tube was operated (water vapor mixing ratio=150 ppmv). HNO_3 is used as the calibration reference because of the weak dependence of the sensitivity with water and its thorough laboratory study (Huey et al., 1996; Amelynck et al., 2000b; Crounse et al., 2006). When several compounds are observed at the same m/z, we report the signal calibrated with a reference calibration c_{ref} and the modeled concentrations of each compound X_i multiplied by $s_{X_i} = c_{X_i}/c_{ref}$, so that one can compare measured signal with the prediction of the mechanism. The predicted concentration of a specific compound is therefore $[X_i]_{calibrated\ model}/s_{X_i}$. Finally, molecules such as isoprene, methacrolein (MACR), methylvinylketone (MVK) or peroxyacylnitrate (PAN) are not observed with our measurement technique despite their relatively large dipole moment. More generally, the method is not sensitive to simple aldehydes, alcohols, and ketones, presumably due to the low binding energy of these compounds with CF_3O^-.

6.4 Results

After the photolysis lights are turned on, isoprene decays with a half life of 20 min (Fig. 6.3). Several inorganic markers of the chemical evolution of the system can be monitored by CIMS (Table 6.1 and Fig. 6.19). Nitrous acid (transfer at $m/z = 66$, cluster at $m/z = 132$, Fig. 6.19), peaks after 50 min and has mostly disappeared after 150 min. HONO is associated with a very large concentration of NO that defines our first chemical regime ($0 \leq t \leq 150$ min). Given the high concentration of NO, little ozone is formed and isoprene photooxidation proceeds almost entirely through OH addition. Pernitric acid (PNA, transfer at $m/z = 98$, cluster at $m/z = 164$, Fig. 6.19) grows steadily peaking at 600 min. Given the sensitivity of PNA to the ratio $HO_2:NO_2$, the time when PNA reaches its maximum indicates the transition from a NO_x (Regime 2: $150 \leq t \leq 600$ min) to a HOx-dominated chemistry (Regime 3: $t \geq 600$ min). In this study, we focus on the NO_x-dominated chemistry, limiting our discussion to the first and second regimes. Studies of low NO_x chemistry will follow in a separate manuscript. Nitric acid (transfer at $m/z = 82$) grows steadily during the experiment to reach 430 ppb at the end of the experiment. We estimate dinitrogen pentoxide profile by removing the nitric acid contribution to the NO_3^- ($m/z = 62$) temporal signal (Huey et al., 1996). The corrected signal exhibits a shape similar to PNA, peaking after 500 min at 3 ppb. In Table 6.1 and Figs. 6.1 to 6.15, we report the main signals measured by CIMS, the chemical formula of the associated compounds as well as their most likely identification using mechanistic considerations. To our knowledge, this is the first time that the temporal evolutions of isoprene nitrates (cluster at $m/z = 232$, Fig. 6.9) and methacrolein/methylvinylketone nitrates (cluster at $m/z = 234$, Fig. 6.13) have been monitored. We also observe the formation of small carboxilic acids such as formic and acetic acid, which can be clearly identified given that they undergo both Reactions R6.1 and R6.2. This specificity helps identify larger acidic compounds such as (Z)-2/3-methyl-4-oxobut-2-enoic acid (MOBA): the signal recorded at $m/z = 199$ (cluster) correlates with the associated transfer at $m/z = 133$ ($\rho = 0.93$ for the first 400 min). This also allows differentiation of certain mass analogs, e.g., the contribution of acetic acid cluster to $m/z = 145$ can be removed using its experimental ratio between transfer and cluster. The residual is the cluster of glycolaldehyde ($m/z = 145$). Unfortunately most mass analogs, such as isoprene nitrates ($m/z = 232$) are positional isomers, and thus cannot be specifically identified using this approach, thus precluding the derivation of their concentrations. To overcome this difficulty, a detailed mechanism has been developed iteratively using the constraints of organic and inorganic signals in association with previously identified mechanisms (Appendix 6.7.1).

Table 6.1 – Signals monitored by Chemical Ionization Mass Spectrometry. C denotes a cluster (Reaction R6.1) and T a transfer (Reaction R6.2). Uncertain identifications (cf. text) are highlighted by a *.

m/z	Nature	Attribution	Formula	CAS
Organic				
65	T	Formic Acid	CH_2O_2	64-18-6
79	T	Acetic Acid	$C_2H_4O_2$	64-19-7
107	T	Pyruvic Acid*	$C_3H_4O_3$	127-17-3
131	C	Formic Acid	CH_2O_2	64-18-6
133	C	MHP	CH_4O_2	3031-73-0
133	T	MOBA Z(1,4)	$C_5H_6O_3$	63170-47-8
133	T	MOBA Z(4,1)	$C_5H_6O_3$	70143-04-3
145	C	Acetic Acid	$C_2H_4O_2$	64-19-7
145	C	GLYC	$C_2H_6O_2$	141-46-8
159	C	HACET	$C_3H_6O_2$	116-09-6
161	C	PAA	$C_2H_4O_3$	116-09-6
169	C	HMHP	CH_4O_3	15932-89-5
173	C	HOPL*	$C_3H_4O_3$	997-10-4
173	C	Pyruvic Acid*	$C_3H_4O_3$	127-17-3
175	C	DHPN	$C_3H_6O_3$	96-26-4
185	C	HC5 E(4,1)	$C_5H_8O_2$	
185	C	HC5 Z(1,4)	$C_5H_8O_2$	519148-47-1
185	C	HC5 Z(4,1)	$C_5H_8O_2$	519148-44-8
189	C	DHB	$C_4H_8O_3$	57011-15-1
190	C	ETHLN	$C_2H_3NO_4$	72673-15-5
199	C	MOBA Z(1,4)	$C_5H_6O_3$	63170-47-8
199	C	MOBA Z(4,1)	$C_5H_6O_3$	70143-04-3
201	C	MHBL*	$C_5H_8O_3$	
204	C	PROPNN	$C_3H_5NO_4$	6745-71-7
217	C	DHMOB(1,4)	$C_5H_8O_4$	
217	C	DHMOB(4,1)	$C_5H_8O_4$	
232	C	ISOPN(1,2)	$C_5H_9NO_4$	227607-01-4
232	C	ISOPN(1,4) Z	$C_5H_9NO_4$	227606-97-5
232	C	ISOPN(1,4) E	$C_5H_9NO_4$	227606-98-6
232	C	ISOPN(2,1)	$C_5H_9NO_4$	227607-02-5
232	C	ISOPN (3,4)	$C_5H_9NO_4$	601487-80-3
232	C	ISOPN(4,1) Z	$C_5H_9NO_4$	227606-99-7
232	C	ISOPN(4,1) E	$C_5H_9NO_4$	227607-00-3
232	C	ISOPN(4,3)	$C_5H_9NO_4$	227606-96-4
234	C	MACRN	$C_4H_7NO_5$	
234	C	MACRN(m)	$C_4H_7NO_5$	
234	C	MVKN	$C_4H_7NO_5$	
234	C	MVKN(m)	$C_4H_7NO_5$	
Inorganic				
62		NO_3^- (proxy for N_2O_5)		14797-55-8
66	T	HONO		7782-77-6
82	T	HNO_3		7697-37-2
98	T	HO_2NO_2		26404-66-0
119	C	H_2O_2		7722-84-1
132	C	HONO		7782-77-6
148	C	HNO_3		7697-37-2
164	C	HO_2NO_2		26404-66-0

6.5   Discussion

6.5.1 δ-hydroxy channels

Under chamber experimental conditions, isoprene photooxidation proceeds primarily through the addition of OH to the two double bonds (position 1, 2, 3, and 4, in Fig. 6.1). In the following we will denote the different channels by the couple (i, j), where i and j refer, respectively, to the carbon on which the OH and O_2 addition occurs. Besides β-hydroxy peroxy radicals (1,2) and (4,3), additions to positions 1 and 4 can lead, after addition of O_2, to four δ-hydroxy peroxy radicals (Sprengnether et al., 2002), referred to as $Z_{1,4}$, $E_{1,4}$, $Z_{4,1}$, $E_{4,1}$. The branching ratio between these different channels remain uncertain (cf. Sect. 6.7.3.1). Here we use a combination of theoretical (Lei et al., 2000) and experimental results (Sprengnether et al. (2002) and this study) as constraints: $Y_{1,2}{\simeq}41\%$, $Y_{1,4}{\simeq}15\%$, $Y_{2,1}{\simeq}2\%$, $Y_{4,3}{\simeq}23\%$, $Y_{4,1}{\simeq}14\%$, $Y_{3,4}{\simeq}5\%$. As most studies of isoprene photooxidation have focused on the main decomposition channels (1,2 and 4,3) yielding MACR and MVK (Paulson et al., 1992; Sprengnether et al., 2002; Karl et al., 2006), the δ-hydroxy channels, which account for about 30% of the carbon and a large fraction of the organic nitrates, remain poorly constrained. A large number of products originating from the δ-hydroxy channels can be monitored by CIMS which motivates our emphasis on their chemistry.

6.5.1.1   Chemistry of the δ-hydroxy channels

$Z_{1,4}$. The reaction of the peroxy radical with NO yields an alkoxy radical which undergoes a δ_1^5 isomerization (Atkinson, 1997; Park et al., 2004). The resulting β-hydroxy allyl radical can then react with O_2 and form a 1,4-hydroxycarbonyl, (2Z)-4-hydroxy-2-methylbut-2-enal (HC5 Z(1,4)) detected as a cluster at $m/z = 185$ (Fig. 6.2). The detection of its ^{13}C isotope at $m/z = 186$ supports the attribution of the signal to HC5. Formation of glycolaldehyde (GLYC cluster at $m/z = 145$, Fig. 6.3) and methylglyoxal (MGLYX) at this stage of the photooxidation have also been described by (Dibble, 2004a,b). This reaction is based on the stabilization of the alkoxy radical, reproduced below, through a double hydrogen bond, which prevents its decomposition while enhancing a double hydrogen shift involving the hydrogen of the alcohol groups.
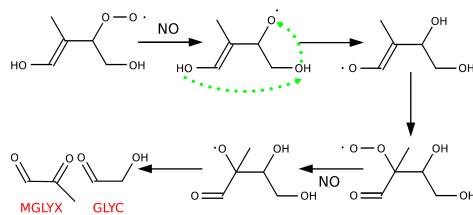
OH can add to the HC5 Z(1, 4) double bond (channels ② and ③ in Fig. 6.1), abstract the aldehydic hydrogen (channel ④) or the hydrogen to the alcohol (channel ①). Addition on position ② is expected to yield GLYC and MGLYX. The signal detected at $m/z = 217$ (Fig. 6.4) suggests the existence of channel ③. In this pathway the alkoxy radical formed after addition of OH on position 3 is stabilized enough by a double hydrogen bond, so that reaction of O_2 becomes competitive with unimolecular decomposition. This mechanism yields 2,4-dihydroxy-2-methyl-3-oxobutanal (DHMOB (1, 4)).

The signal recorded at $m/z = 199$ correlates well ($\rho = 0.93$ for the first 400 min) with the one at $m/z = 133$. This correlation between a cluster and a transfer is usually associated with an acid functional group (cf. Sect. 6.3.2), which supports the formation of (Z)-2-methyl-4-oxobut-2-enoic acid (MOBA Z(1, 4)), a five carbon acid, from HC5 through channel ④ (Fig. 6.5).

$E_{1,4}$. The isomerization of the initial alkoxy radical can yield 2-(hydroxymethyl)prop-2-enal (HMPL) after reaction with O_2. A second isomerization would yield 4-hydroxy-3-oxobutanal (HOBL) or 4-hydroxy-3-(hydroxymethyl)but-2-enal (MHBL). The further photooxidation of HMPL and MHBL is expected to yield mainly dihydroxypropanone (DHPN), whose CF_3O^- cluster is observed at $m/z = 175$ (Fig. 6.6), and hydroxyoxopropanal (HOPL, cluster at $m/z = 173$ with pyruvic acid).

The reaction of OH with HOPL is expected to yield an acylperoxy radical which can further react with NO_2 yielding a PAN-like compound, 3-hydroxy-oxo-peroxyacylnitrate (PAN 250). This compound may be associated with the signal monitored at $m/z = 250$, although the identification is not certain.

Signals originating from the E branch are much smaller than those originating from its Z counterpart. This suggests a large asymmetry between the E and Z δ-hydroxy channels.

Due to the similarity between the (4,1) and (1,4) branch, we only address the major differences.

$Z_{4,1}$. Hydroxyacetone (HACET, cluster at $m/z = 159$, Fig. 6.7) and glyoxal (GLYX) can be formed from the decomposition of HC5 Z(4,1) and HC5 E(4,1). Similar to the formation mechanism of DHMOB(1,4), the addition of OH to the less preferred position of HC5 Z(4,1) (and E(4,1)) is expected to yield 3,4-dihydroxy-3-methyl-2-oxobutanal referred to as DHMOB(4,1) (Fig. 6.4).

Figure 6.1 – Summary of the most prevalent first steps of isoprene photooxidation under high NO_x conditions. Abbreviations: i: δ_1^5 isomerization–Reaction R6.16, h: OH + VOC (abstraction or addition) denotes the location of the reaction, o: $R+O_2 \rightarrow RO_2$, O: Reaction R6.15, D: Dibble mechanism (cf. Section 6.5.1.1), n: $RO_2 + NO$–Reaction R6.7, d: decomposition–Reaction R6.14, k: keto-enol tautomerism (possibly due to heterogeneous enol/ketone conversion). Blue circles: detected and correctly captured by the model. Red square: Insufficient data/model discrepancy.

Figure 6.2 – Signal recorded at m/z=185 (black circles) and modeled HC5=HC5 Z(1,4) + HC5 Z(4,1) + HC5 E(4,1) (monitored as a cluster).
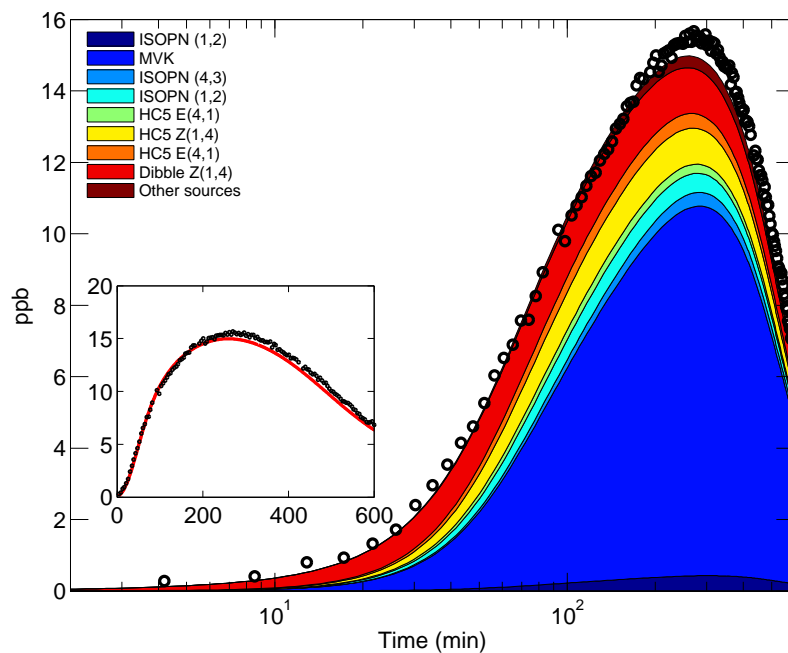
Figure 6.3 – Signal recorded at m/z=145 (black circles) compared with modeled GLYC profile. The contribution of acetic acid cluster has been removed using acetic acid transfer at m/z=79. Colored bars indicate the instantaneous modeled contributions of the different sources of GLYC.
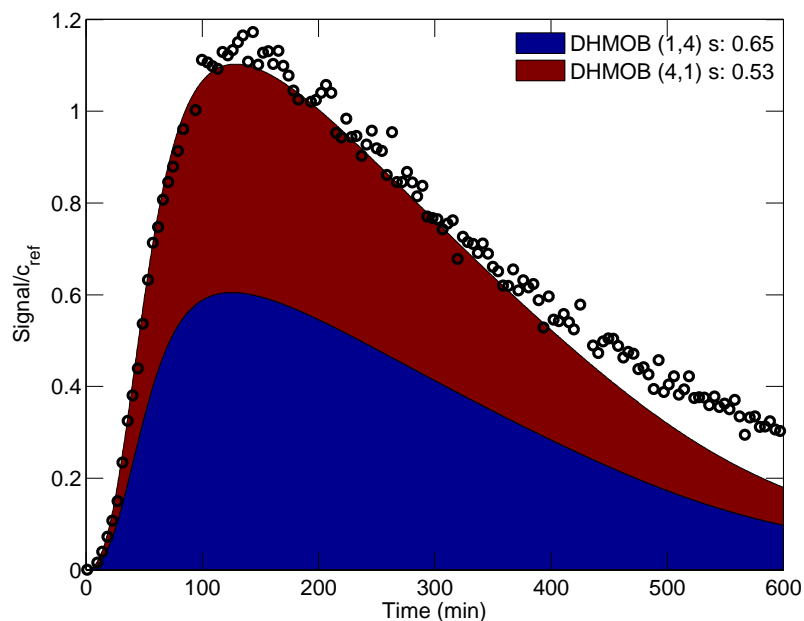
Figure 6.4 – Signal recorded at m/z=217 (black circles) and modeled DHMOB = DHMOB(1,4) + DHMOB(4,1) (monitored as a cluster).
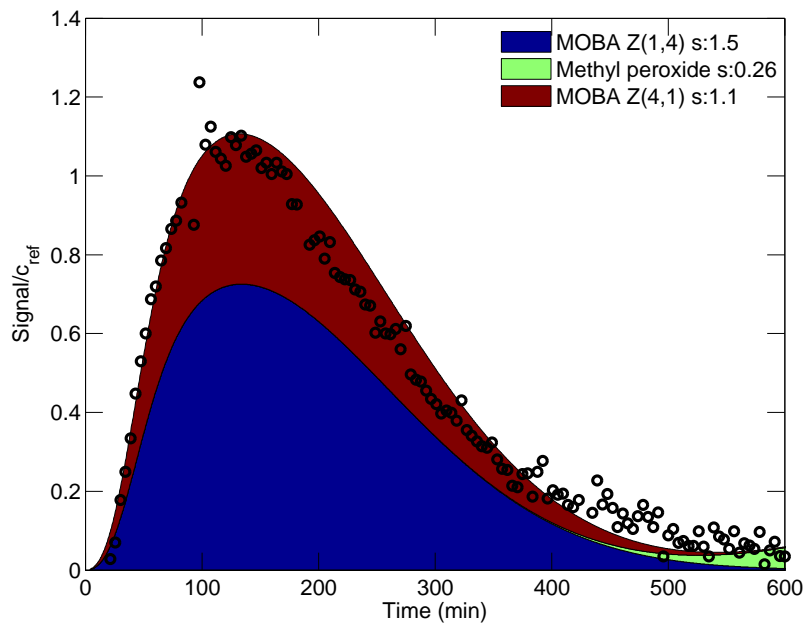
Figure 6.5 – Sum of the signals recorded at m/z=133 and m/z=199 (black circles) compared with MOBA = MOBA Z(1,4) + MOBA Z(4,1) (m/z=133 (transfer) + 199 (cluster)) and MHP (cluster at m/z=133).
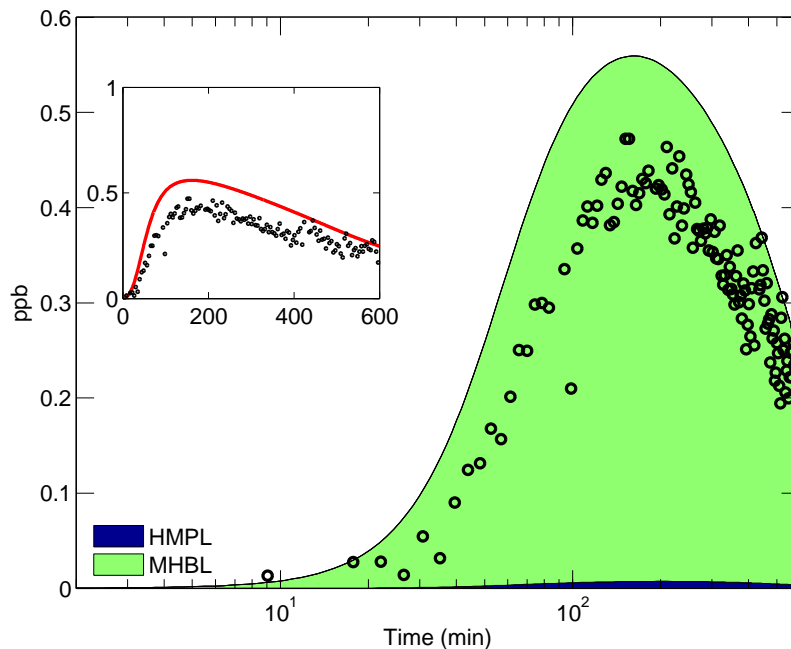
Figure 6.6 – Signal recorded at m/z=175 (black circles) compared to modeled DHPN (measured as a cluster).

$E_{4,1}$. The alkoxy radical configuration prevents δ_1^5 isomerization (Reaction R6.16) and slows down its decomposition (Reaction R6.14). Therefore it is expected to react entirely with O_2 (Reaction R6.15) to yield a HC5 isomer (HC5 E(4,1)).

6.5.1.2   Consequences

The observations of numerous compounds formed at different stages of δ-hydroxy pathways lead to several inferences about the general mechanism:

Channel asymmetry. If an equal partitioning of the carbon is assumed between $E_{1,4}$ and $Z_{1,4}$ as suggested by the theoretical work of Dibble (2002), the concentrations of both HOPL and DHPN are greatly overestimated while the concentrations of HC5 = HC5 Z(1,4) + HC5 E(4,1) + HC5 Z(4,1) and its products (DHMOB, MOBA) are underestimated. Good agreement with the observations is obtained when

$$\frac{Y_{E_{1,4}}}{Y_{Z_{1,4}}} = \frac{15}{85} \tag{6.4}$$

An additional piece of evidence suggesting that little flux of carbon occurs through $E_{1,4}$ is the low signal recorded at $m/z = 201$, which should include 3-methylhydroxy-4-hydroxybutenal (MHBL) based on its structural similarity with HC5. We use $k_{OH} = 6.13{\times}10^{-12}\,\mathrm{cm^3\,molecule^{-1}\,s^{-1}}$ for
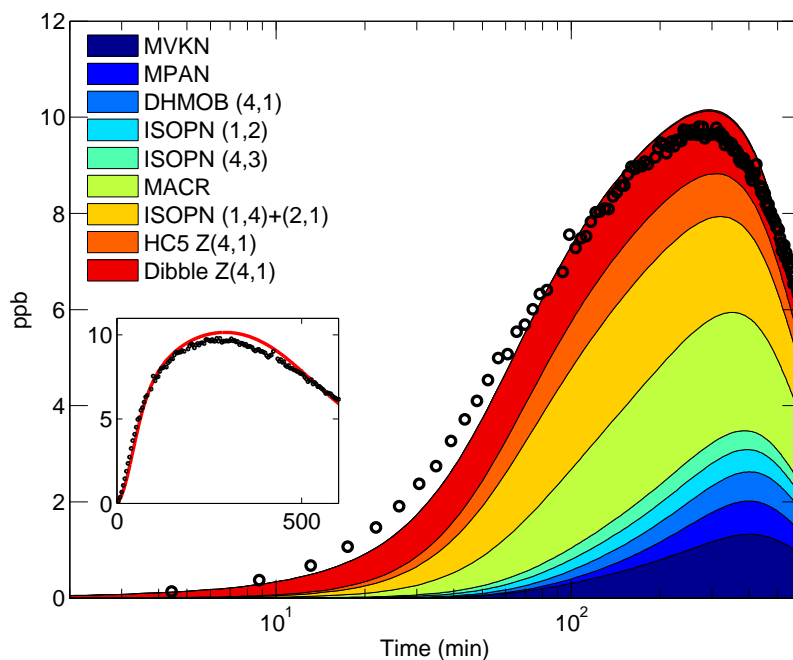
Figure 6.7 – Signal recorded at $m/z=159$ (black circles) compared with modeled HACET profile. Colored bars indicate the instantaneous modeled contributions of the different sources of HACET. MPAN source has been described by Orlando et al. (2002).

DHPN (25% more than the SAR estimate) and $k_{OH} = 2.23 \times 10^{-11}\,\text{cm}^3\,\text{molecule}^{-1}\,\text{s}^{-1}$ for HOPL in order to properly capture their measured temporal profiles (Fig. 6.6). The asymmetry between Z/E isomers contradicts the conclusions drawn from quantum mechanical calculations (Dibble, 2002) as well as the assumption made by most kinetic models of isoprene photooxidation (Paulson and Seinfeld, 1992; Fan and Zhang, 2004).

The discrepancy with quantum mechanical calculations may be related to a difference in the reaction of the *cis/trans* radical with O_2. The radicals are formed with approximately 40 kcal/mol excess energy. The minimum isomerization barrier is estimated to be about 15 kcal/mol (Dibble, 2002). Therefore, assuming a collision stabilization of 100 cm^{-1} collision$_{-1}$, the radicals undergo nearly 100 collisions (20 with O_2) before they are cooled below the isomerization barrier. If, based on reported rate coefficients for $R \cdot + O_2$ (Atkinson et al., 2006), one reaction among ten is assumed to be reactive, peroxyradicals are likely to be formed before the isomers are cooled below the isomerization barrier. Therefore, the equilibrium may be shifted if the reaction of the *trans* radical with O_2 is faster than the reaction of the *cis* radical. Measurements made with reduced partial pressure of O_2 could test this hypothesis. The *cis* and *trans* forms can also be interconverted later in the photooxidation by the δ_1^5 isomerization. Therefore the observed discrepancy may also be attributed

to the additional stability of the *cis*-hydroxy allyl radical provided by the interaction between the alcohol groups.

Evidence for Dibble's mechanism. Both HACET (Fig. 6.7) and GLYC (Fig. 6.3) exhibit a very prompt source. To our knowledge, the mechanism proposed by Dibble (2004a,b) and reproduced in Sect. 6.5.1.1 is the only mechanism able to yield both compounds after a single OH reaction. For GLYC, we set the branching ratio quenching:thermalization to 7:3 in good agreement with the theoretical estimate (Dibble, 2004b). The same branching ratio was applied to capture the prompt formation of HACET from the $Z_{4,1}$ branch. Theoretical considerations do not support such a large hydroxyacetone formation (Dibble, 2004b). The hydroxyacetone rate constant with OH is set to $k_{OH} = 5.98 \times 10^{-12}\,\mathrm{cm^3\,molecule^{-1}\,s^{-1}}$ (Dillon et al., 2006) and the rate constant of glycolaldehyde with OH is set to $k_{OH} = 8 \times 10^{-12}\,\mathrm{cm^3\,molecule^{-1}\,s^{-1}}$ (Karunanandan et al., 2007).

HC5 chemistry. HC5 (Fig. 6.2) exhibits a very fast decay consistent with a reaction rate coefficient with OH similar to isoprene (1.0–$1.2 \times 10^{-10}\,\mathrm{cm^3\,molecule^{-1}\,s^{-1}}$). This estimate is consistent with the fastest rate recently derived by Baker et al. (2005) and 80% greater than the SAR estimate ($k_{OH}^{SAR} = 6.82 \times 10^{-11}\,\mathrm{cm^3\,molecule^{-1}\,s^{-1}}$ or $7.9 \times 10^{-11}\,\mathrm{cm^3\,molecule^{-1}\,s^{-1}}$ with the correction from Bethel et al. (2001); Papagni et al. (2001)). This discrepancy can be partly explained by the effect of the alcohol group of the double bond, which enhances the addition of OH (Papagni et al., 2001). The large measured yield of MOBA=MOBA Z(1,4)+MOBA Z(4,1) (Fig. 6.5) also suggests that the abstraction of the aldehydic hydrogen (channel ④) is faster than predicted, possibly related to a long distance interaction between the alcohol group and the carbonyl group (Neeb, 2000).

Experimental evidence for the formation of 3-methylfuran (3-MF) from the $Z_{1,4}$ and $Z_{4,1}$ branches have been reported (Tuazon and Atkinson, 1990). However the mechanism remains unclear with evidence for both heterogeneous formation (Baker et al., 2005; Dibble, 2007; Atkinson et al., 2008) from HC5 and homogeneous formation from its parent alkoxy (Francisco-Marquez et al., 2005).

In our model, 3-MF yield is set to 4.5% based on experimental results (Atkinson et al., 1989; Paulson et al., 1992) and formed from the parent alkoxy of HC5. As a result, 37% of the alkoxyradical formed in the $Z_{1,4}$ and $Z_{4,1}$ branches must decompose to 3-MF in order to match the experimental yield. We cannot rule out 3-MF heterogeneous formation. We note, however, that if heterogeneous processes yield 3-MF, the calculated HC5 yield would be 20% higher. Moreover, the decay rate required to match HC5 profile would likely be faster than observed. 3-MF formation mechanism has little impact on the conclusions of this paper but has significant consequences for atmospheric chemistry. Indeed if formed through heterogeneous processes, 3-MF yield is likely to be smaller than
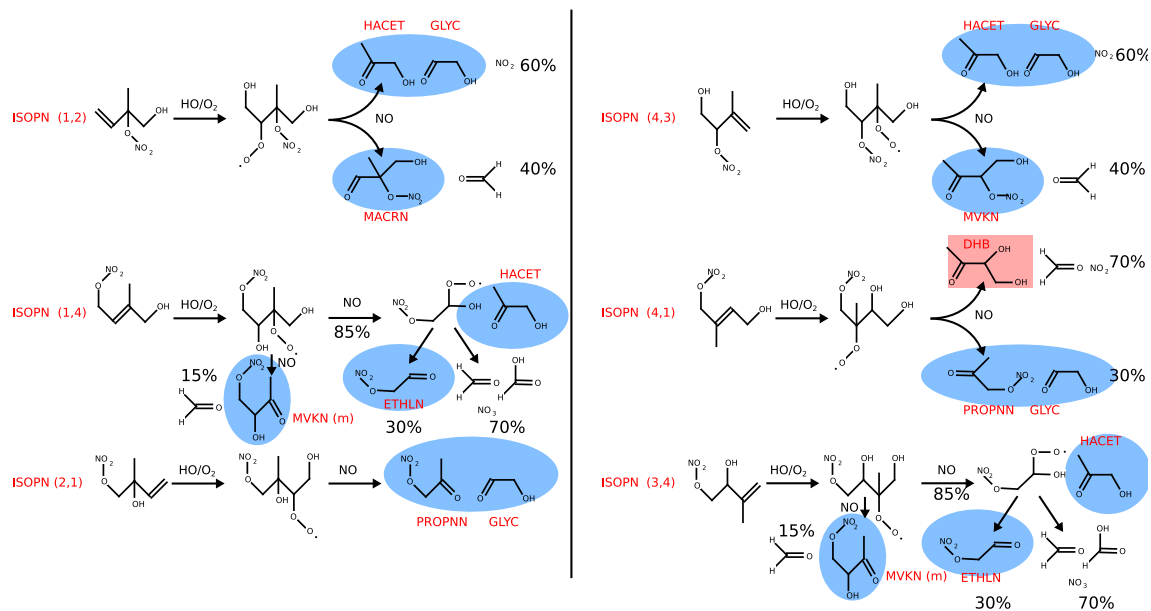
Figure 6.8 – Decomposition pathway of the different isoprene nitrates after their reaction with OH. Reaction of ISOPN with OH, O_2, and NO, also yields dihydroxy-dinitrates through Reaction R6.7. Color code is identical to Fig. 6.1.

determined in atmospheric chambers. Further work is clearly required to quantify this issue and determine the products of 3-MF photooxidation.

We note, finally, that the observation of large yields for HC5 and 3-MF are consistent with an asymmetry between the E and Z branches. If the branching ratio E:Z were close to 1:1, the fraction of peroxy radical $Z_{1,4}$ and $Z_{4,1}$ required to decompose to 3-MF would be 62% and the yield of HC5 only 6.1% This is inconsistent with the yields previously reported (Baker et al., 2005).

6.5.2 Organic nitrates

The observation of the organic nitrates of isoprene and MVK/MACR as well as some of the products of their photooxidation (Figs. 6.8 to 6.13), provides constraints on the isoprene nitrate yields, their lifetimes and the amount of NO_x recycled through the first stage of their photooxidation as well as their lifetimes.

6.5.2.1 δ-hydroxy isoprene nitrates

The fate of the δ-hydroxy isoprene nitrates (1,4) and (4,1), respectively ISOPN (1,4) and ISOPN (4,1), can be followed through their degradation products (Fig. 6.8): ethanal nitrate (ETHLN) monitored at $m/z = 190$ (Fig. 6.10) and propanone nitrate (PROPNN) at $m/z = 204$ (Fig. 6.11).
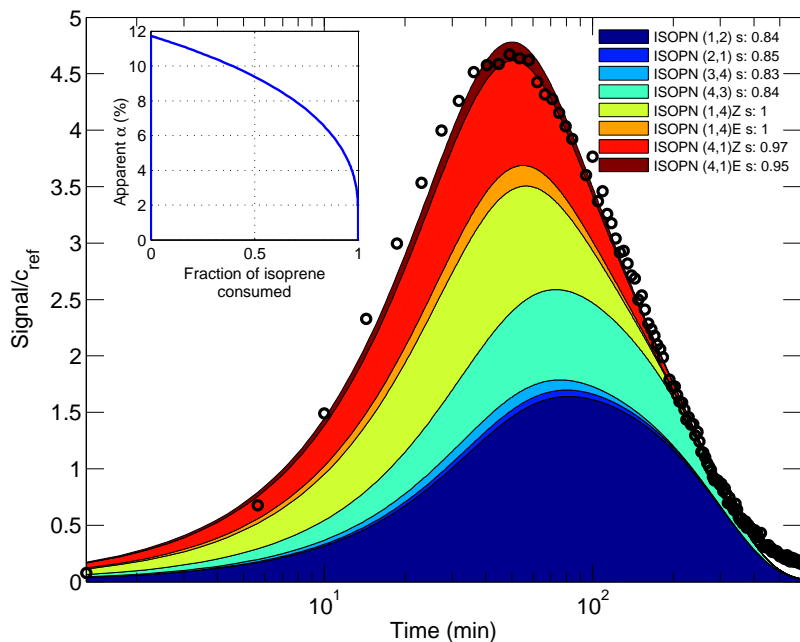
Figure 6.9 – Signal recorded at $m/z{=}232$ (black circles) compared to modeled isoprene nitrates (ISOPN(1,2), (1,4)E/Z, (2,1), (4,3), (3 4), (4,1)E/Z (measured as clusters)) corrected for calibration changes.

PROPNN features a very prompt source, which requires a fast reaction rate coefficient of ISOPN(4,1) with OH: $k_{OH}^{ISOPN(4,1)} = 9.5{\times}10^{-11}\,\mathrm{cm^3\,molecule^{-1}\,s^{-1}}$. This is 45% faster than SAR and suggests an inadequate parameterization of the effects of nitroxy groups on the reactivity of the double bond (Neeb, 2000). No significant signal is observed at $m/z = 230$, confirming that the abstraction of the hydrogen in of the alcohol of ISOPN is negligible compared to addition on the double bond.

SAR suggests that ISOPN(1,4) and ISOPN(4,1) are similarly short-lived with respect to OH. This is consistent with the prompt source of ETHLN (Fig. 6.10), a product of the oxidation of ISOPN (1,4) (Fig. 6.8). The use of the primary nitrate photolysis rate (cf. 6.7.1.3) and SAR rate estimate for the reaction ETHLN + OH underpredicts its decay. To match the measured profile (Fig. 6.10), we take $k_{OH} = 1{\times}10^{-11}\,\mathrm{cm^3\,molecule^{-1}\,s^{-1}}$, three times faster than the SAR estimate. If the ETHNL photolysis rate is larger than estimated ($J{\sim}4{\times}10^{-7}\mathrm{s}^{-1}$ using $1{-}C_4H_9ONO_2$, ETHLN reaction rate coefficient with OH would be commensurately slower.

NO_x recycling from the (4,1) branch is 70% based on the measured ratio PROPNN: dihydroxybutanone (DHB, cluster at $m/z = 189$). The reaction rate coefficient of DHB with OH is estimated to be $1.3{\times}10^{-11}\,\mathrm{cm^3\,molecule^{-1}\,s^{-1}}$ or 60% of SAR (Fig. 6.12).
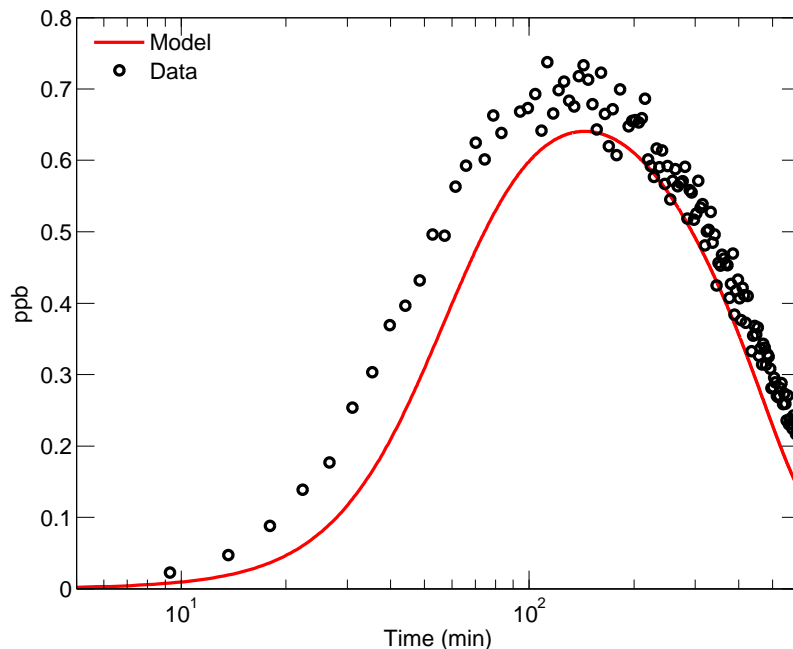
Figure 6.10 – Signal recorded at m/z=190 (black circles) compared to modeled ETHLN (measured as a cluster).

The yield of ETHLN is substantially overestimated if the yield of the reaction $RC^\cdot OH + O_2 \rightarrow RC(O) + HO_2$ is 100%. As will be discussed further in Sect. 6.5.3, we suggest that unimolecular decomposition of the δ-hydroxyperoxy radical from ISOPN(1,4) yields formic acid, resolving this discrepancy.

6.5.2.2 β-hydroxy isoprene nitrates

To capture the decay of the $m/z = 232$ signal requires that β-hydroxy isoprene nitrates (ISOPN (1,2), (2,1), (4,3) and (3,4)) be much longer-lived than δ-hydroxy isoprene nitrates (ISOPN (1,4) and (4,1)). Unfortunately, the products of their photooxidation have multiple other sources, precluding a direct derivation of their lifetime. For instance methylvinylketone nitrate (MVKN) and methacrolein nitrate (MACRN) are also formed from MVK and MACR with similar rates. The evolution of the $m/z = 232$ signal can be captured when the SAR chemical rates for these nitrates are reduced by 20%.

The reaction of the isoprene nitrate with ozone is included for ISOPN (1,2) and ISOPN (4,3), because their long lifetimes allow them to encounter high concentrations of ozone in the chamber (Fig. 6.17). We do not observe the formation of 3-hydroxy-2-nitrooxy-2-methyl propanoic acid (no correlation between $m/z = 184$ and $m/z = 250$). Therefore, we use a simplified version of
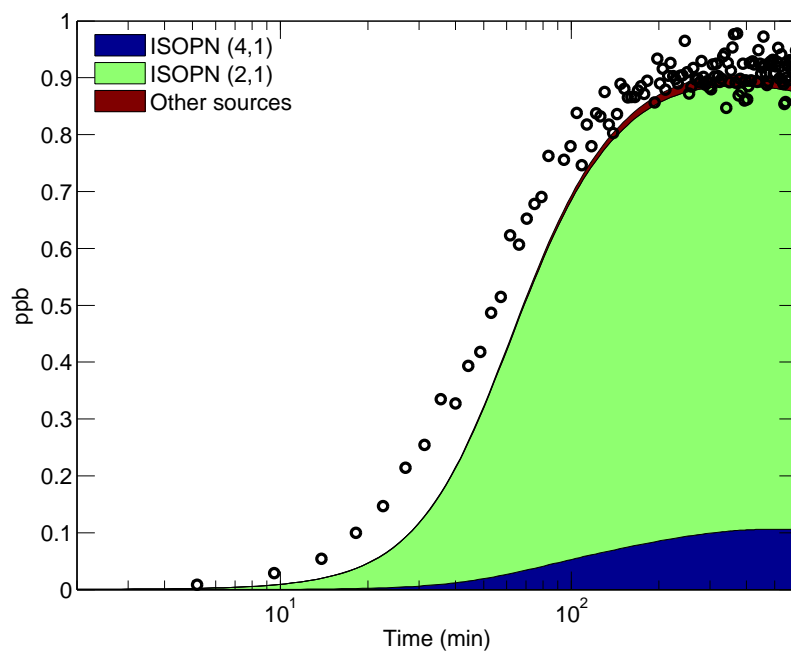
Figure 6.11 – Signal recorded at m/z=204 (black circles) compared to modeled PROPNN (measured as a cluster). Colored bars indicate the instantaneous modeled contributions of the different sources of PROPNN.
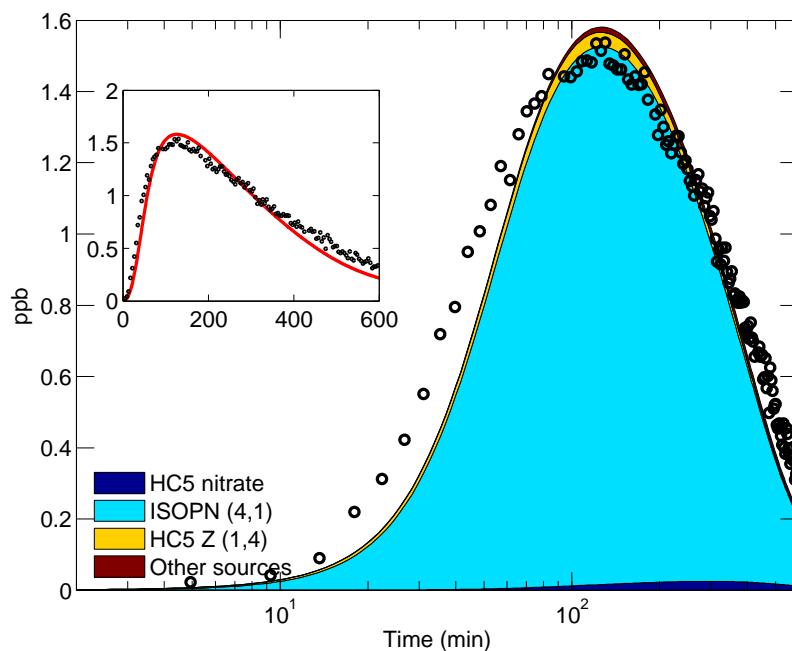
Figure 6.12 – Signal recorded at m/z=189 (black circles) compared to modeled DHB (measured as a cluster). Colored bars indicate the instantaneous modeled contributions of the different sources of DHB.
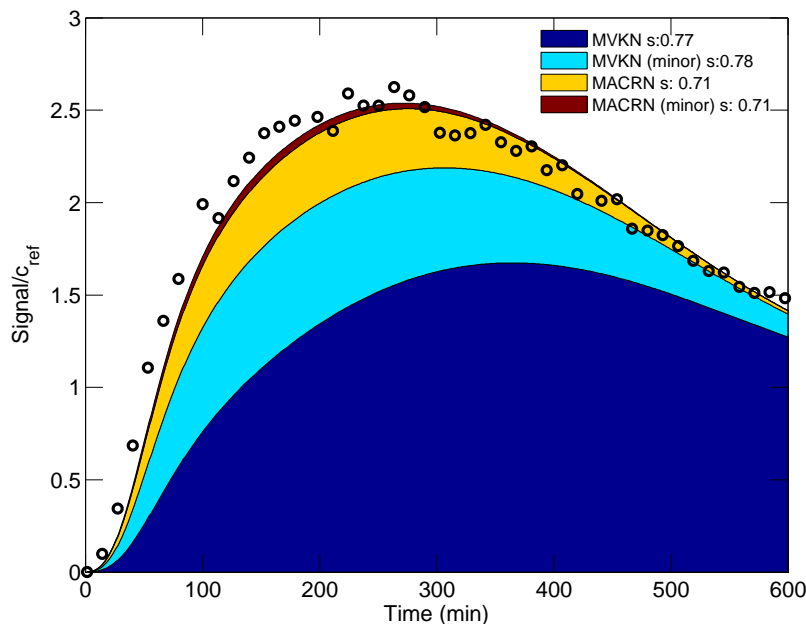
Figure 6.13 – Signal recorded at m/z=234 (black circles) compared to the modeled profile of MVKN + MVKN(m) + MACRN + MACRN(m) (measured as clusters) corrected for changing calibrations.

the ozonolysis products proposed by Giacopelli et al. (2005) assuming that this reaction yields only MACRN and MVKN. These reactions contribute significantly to the total yield of MVKN and MACRN in this experiment.

6.5.2.3 Methacrolein and methylvinylketone hydroxynitrates

MVKN and MACRN are monitored through their clusters with CF_3O^- at $m/z = 234$ (Fig. 6.13). MACRN features an aldehyde group, which suggests a much faster decomposition than MVKN. This is confirmed by the profile of hydroxyacetone which does not exhibit any significant late source. As a result, the third regime of the experiment is dominated by MVKN and its reaction rate coefficient with OH can be estimated: $k_{OH}^{MVKN} = 2.8 \times 10^{-12}\,\mathrm{cm^3\,molecule^{-1}\,s^{-1}}$. The yield of MVKN can be constrained using GLYC profile since MVK is its major source: $\alpha_{MVK} = (11\pm3)\%$. Applying the same approach to MACR/MACRN/HACET is more complicated since hydroxyacetone has many more sources than glycolaldehyde (Fig. 6.7). We find that a yield of MACRN of $(15\pm3)\%$ and a reaction rate coefficient with OH of $5\times10^{-11}\,\mathrm{cm^3\,molecule^{-1}\,s^{-1}}$ best match the peak time of $m/z = 234$. These values are consistent with the study of Chuong and Stevens (2004).

The abstraction of the hydrogen to the alcohol in MACRN, MVKN and MVKN(m) is expected to yield dicarbonyl nitrates. We expect CIMS to be sensitive to this class of compounds since we are able

to measure compounds featuring a carbonyl in of the nitrate group, such as PROPNN or ETHLN. Since $m/z = 232$ only features early stages compounds, isoprene nitrates, there is no evidence for the formation of dicarbonyl nitrates. Recent theoretical studies (Peeters et al., 2001; Hermans et al., 2005) show that primary α-hydroxy-alkylperoxy radicals can be sufficiently stabilized to undergo reactions with NO and yield formic acid. Nevertheless the photooxidation of MVKN occurs in a mostly low-NO$_\mathrm{x}$ environment, which suggests that α-hydroxy-alkylperoxy radicals may undergo an intramolecular decomposition to yield a carboxilic acid and the nitrate radical. Such a reaction may involve a four or six-e$^-$ mechanism.
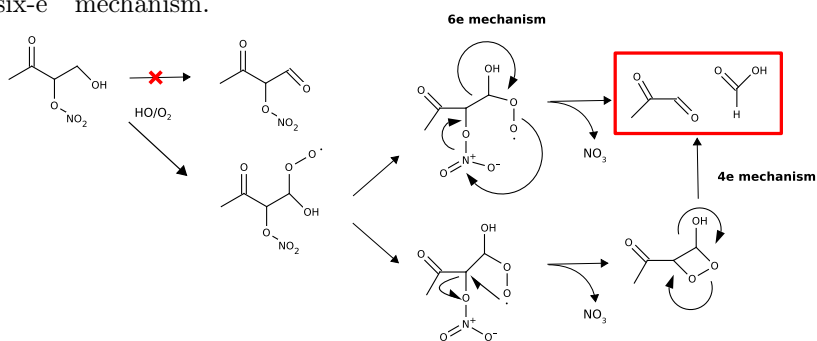
Finally, $m/z = 234$ signal features a prompt source which can not be accounted for by MVK or MACR nor by the β-hydroxy isoprene nitrates, which have a similar lifetime with respect to OH. Conversely ISOPN(1,4) is very short-lived and a MVKN(m) yield of 10–15% enables to capture this feature (Fig. 6.13).

6.5.3 Acids

6.5.3.1 Formic acid

Formic acid is detected as a cluster ($m/z = 131$) and a transfer ($m/z = 65$) with about equal sensitivity. At the NO$_\mathrm{x}$ titration (600 min), a molar yield of about (10±3)% is obtained (Fig. 6.14). The measured profile of formic acid (Fig. 6.14) features the three characteristic chemical regimes of this experiment as described (cf. Sect. 6.4).

First regime. A very early source of formic acid is noticeable (Fig. 6.14). Several observations suggest that formic acid may be formed from an intramolecular decomposition of ISOPN(1,4) similar to the one described for MVKN earlier: 1) This source is absent from the experiments performed in the absence of NO$_\mathrm{x}$ 2) the early formic acid profile correlates very well with the propanone nitrate, which originates from ISOPN(4,1) decomposition 3) ETHNL would be largely overevaluated in the absence of other decomposition channel for ISOPN(1,4). Matching the ETHLN profile (Fig. 6.10) results in a branching ratio for formic acid to ETHLN of 3:1. ISOPN(2,1) may yield acetic acid, but

is not included since its contribution would be negligible.

Bierback et al. (1995) report 4-oxo-pentenal as the major product of the photooxidation of 2-methylfuran in the absence of NO_x, while formic acid accounts for about 6%. We are unaware of any study of the photooxidation of 3-MF in the presence of NO_x. Since the reaction rate coefficient of methylfuran with OH is similar to that derived for ISOPN(1,4) and (4,1), its photooxidation may contribute to the early sources of formic acid:
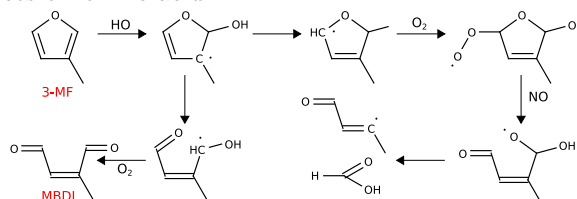
Second regime. Butkovskaya et al. (2006a,b) report a formic acid yield from the photooxidation of GLYC (HAC) of 18% (respectively 7%). The formation of formic acid from the decomposition of MVKN described in Sect. 6.5.2.3 also plays a minor role in this regime.

Third regime (not shown). As NO_x becomes limiting, hydroxymethyl hydroperoxide (HMHP) formation from the reaction of CH_2OO with water is enhanced. HMHP can account for most of the late formation of formic acid through its reaction with OH and its photolysis. A large additional source is missing, however, in the mechanism. Heterogeneous decomposition of HMHP (Neeb et al., 1997) and aerosol processes (Walser et al., 2007) are likely to account for this missing source. An upper limit for the strength of the aerosol source can be estimated from the decrease of the aerosol volume -2.5 $\mu m^3/cm^3$ which would represent a release of 2.6 ppbv C=O in the chamber assuming a density of 1.25 g/cm^3 (Kroll et al., 2006). Since the same phenomenon is observed for acetic acid (Fig. 6.15), most likely both HO_x-dominated VOC oxidation as well as organic aerosol oxidation are needed to explain the observed increase in formic and acetic acid in the third regime.

6.5.3.2 Acetic acid

The production of acetic acid (Fig. 6.15) occurs primarily through the oxidation of hydroxyacetone as described by (Butkovskaya et al., 2006a). Additional routes include direct formation from $CH_3CHO + OH$ (Cameron et al., 2002) as well as $CH_3C(O)OO + HO_2$ following Reaction R6.11.

Two additional minor routes are hypothesized: 1) decomposition of MACRN(m), 2) decomposition of DHMOB(1,4) ($m/z = 217$), inspired by the mechanism proposed by Butkovskaya et al. (2006b). Following their analysis, we assume a 37% acetic molar yield, the remaining falling apart as CO_2 and hydroxybutane-2,3-dione ($m/z = 187$).
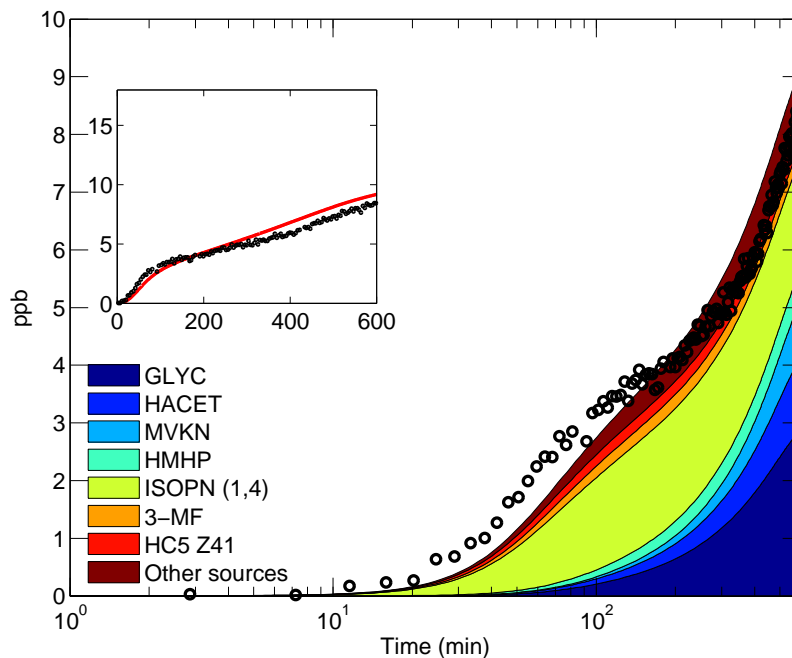
Figure 6.14 – Signal recorded at m/z=65 (black circles) compared to modeled formic acid. Colored bars indicate the instantaneous modeled contributions of the different sources of formic acid.
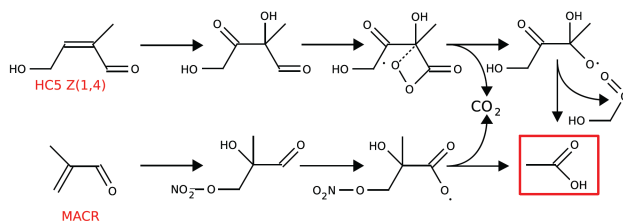
6.5.3.3 MOBA

MOBA, the class of five-carbon acids identified at $m/z = 133$ and 199 in Sect 6.5.1 can react with OH and ozone under the chamber conditions. The slow decay of the signal suggests that its reactivity is dominated by ozone in the chamber and that the acid group significantly hinders the addition of OH onto the double bond. A good match is obtained by setting $k_{OH} = 3 \times 10^{-12}$ cm^3 molecule^{-1} s^{-1} (FC(O)OH=0.1 in terms of SAR) and $k_{O_3} = 2 \times 10^{-17}$ cm^3 molecule^{-1} s^{-1}.

Little signal is observed at $m/z = 93$, which suggests no or minor formation of oxoacetic acid. This suggests that the reaction with OH does not conserve the acid group, which is likely lost as CO_2. Pyruvic acid can be expected to be a major product of MOBA ozonolysis.
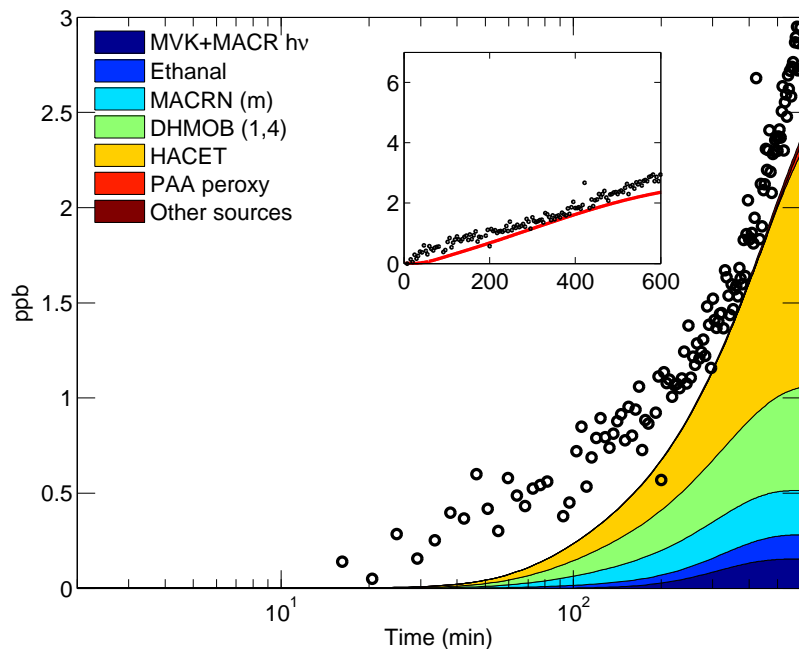
Figure 6.15 – Signal recorded at m/z=79 (black circles) compared to modeled acetic acid (observed as a transfer at this mass). Colored bars indicate the instantaneous modeled contributions of the different sources of acetic acid.

6.5.3.4 Pyruvic acid

Pyruvic acid is a precursor for glyoxylic and oxalic acids, two carboxylic acids detected in the aerosol phase (Carlton et al., 2006). It is observed as a cluster at $m/z = 173$ in association with HOPL, a product of DHPL photooxidation. Due to its stickiness to the walls of the flow tube, the theoretical calibration is expected to largely overestimate our sensitivity to this compound. The yield of pyruvic acid after 600 min is $2\pm1\%$.

Qualitatively, the major sources of pyruvic acid are expected to include (heterogeneous) hydrolysis of the Criegee intermediate produced in the ozonolysis of MVK and MOBA as well as the decomposition of MVKN(m) following the scheme presented in Sect. 6.5.2.3.

6.5.4 Atmospheric relevance

6.5.4.1 Fate of organic nitrogen

The formation of organic nitrates, and more specifically isoprene nitrates, plays an important role in determining the amount of NOx and thus ozone production in many environments.

The observation of isoprene nitrate clusters with CF_3O^- as well as some of the products of their

photooxidation, provides constraints on the isoprene nitrate yields, the amount of NO_x recycled through the first stage of their photooxidation, and their lifetimes (Table 6.2). These three parameters are necessary to accurately assess the influence of isoprene photooxidation on atmospheric chemistry.

Yield. Previous estimates for the isoprene nitrate yield span a very large range. Chen et al. (1998) reported an overall yield of 4.4%; Chuong and Stevens (2002), 15% using an indirect method; Sprengnether et al. (2002), 12%; Patchen et al. (2007), 7% at 130 hPa. Using experimental yields collected for compounds similar to isoprene, Giacopelli et al. (2005) estimated the nitrate yield of the β and δ-hydroxy isoprene nitrates to be respectively 5.5% for the former and 15% for the latter, for an overall yield of 8.6%. Since organic nitrates sequester NO_x, such a large variation in the estimated yields has profound implications for the assessment of ozone production caused by isoprene photooxidation (von Kuhlmann et al., 2004; Fiore et al., 2005; Horowitz et al., 2007).

We report a yield of $(11.7\pm3)\%$ with a large discrepancy between the yields of the nitrates originating from $\delta(\simeq24\%)$ and β-hydroxy channels ($\simeq6.7\%$). We emphasize, however, that we derived a total yield rather than specific branching ratios so that the specific organic nitrate yields are affected by the choice of the initial $\beta{:}\delta$-hydroxy channel ratio (cf. Sect. 6.7.3.1). Nevertheless, the discrepancy between δ-hydroxy channels and β-hydroxy channels is a reliable feature, with the δ-hydroxy isoprene nitrates accounting for about 60% of the total isoprene nitrate yield. Giacopelli et al. (2005) suggested this behavior previously using measurement collected for similar compounds.

Lifetime. The efficiency of both NO_x transport and removal through organic nitrates is related to their lifetimes. The transport of isoprene-nitrates and their alkylnitrate degradation products is of special importance since it is thought to be a major source of NO_x in rural areas (Horowitz et al., 1998). In this NO_x-limited environment, the release of NO_x through their decomposition would greatly influence O_3 production. In the absence of experimental data, Giacopelli et al. (2005) estimated using Kwok's SAR that the δ-hydroxy isoprene nitrates should be significantly shorter-lived than the β-hydroxy isoprene nitrates. With the help of the propanone nitrate profile, we can experimentally confirm this discrepancy (Table 6.2). With $[OH] = 10^6$ molecule^{-1} cm^{-3}, the photochemical lifetime with OH of the δ-hydroxy isoprene nitrates (respectively the β-hydroxy isoprene nitrate) is $\tau_{OH}^{\delta} = 3$ h ($\tau_{OH}^{\beta} = 18$ h). Horowitz et al. (2007) show that the deposition of isoprene nitrates is likely to be dominated by dry processes and that $\tau_d^{HNO_3}\simeq7\,h\leq\tau_d^{ISOPN}\leq\tau_d^{PAN}\simeq100\,h$. As a result, the fate of the δ-hydroxy isoprene nitrates is likely to be dominated by their reactivity with OH and possibly O_3 similar to isoprene while other processes such as dry deposition and reac-

Table 6.2 – Isoprene nitrate kinetic data. The uncertainty is smaller than 30%.

	Molar yield (%)	α (%)	k_{OH} ($\times 10^{-11}$)	k_{O_3} ($\times 10^{-17}$)	Recycling (cf. text)
ISOPN(1,2)	2.7	6.7	1	1	45
ISOPN(1,4) Z	3.1	24	9.5		52
ISOPN(1,4) E	0.54	24	9.5		52
ISOPN(2,1)	0.13	6.7	3.4		-10
ISOPN(3,4)	0.33	6.7	6.6		52
ISOPN(4,3)	1.5	6.7	1.9	1	56
ISOPN(4,1) Z	2.9	24	9.5		68
ISOPN(4,1) E	0.51	24	9.5		68
Weighted Average	11.7	55			

tion with NO_3 must be taken into account for proper modeling of the β-hydroxy isoprene nitrates. Therefore, the latter are likely to have greater influence on tropospheric chemistry.

The large difference in the lifetime of the organic nitrates formed in the δ-hydroxy and β-hydroxy channels may explain some of the spread in the reported yields and NO_x recyclings. Studies focusing on the very first step of isoprene photooxidation (e.g., Sprengnether et al. 2002) tend to report the highest nitrate yield, suggesting that the short-lived δ-hydroxy isoprene nitrates may have been underestimated in some previous experiments (see inset of Fig. 6.9). The same argument may also explain the observations of a greater variety of isoprene nitrates in laboratory experiments than in the field (Giacopelli et al., 2005).

Recycling. The efficiency of the NO_x sequestration depends on the fate of the isoprene nitrates and more specifically on how much NO_x is released in their subsequent photooxidation. NO_x-recycling is defined as the difference between the NO_x released by the reaction and the NO consumed. As a result, since ISOPN(2,1) oxidation does not yield any NO_2, its recycling is negative due to the formation of dinitrates (Fig. 6.8 and Table 6.2), which we have observed at $m/z = 311$ in another experiment. Horowitz et al. (2007) obtain the best agreement with the boundary layer data when 40% of the NO_x is recycled with a low nitrate yield (4%). We find a NOx recycling of $(55\pm10)\%$ by the isoprene peroxy radicals consistent with Horowitz et al. (2007) conclusion despite our very different yields. As highlighted in the inset of (Fig. 6.9), this may be related to the wrong estimation of isoprene nitrate yield due to the short lifetime of the δ-hydroxy channels.

The photooxidation of isoprene leads to the formation of other significant organic nitrates MVKN, MACRN, PROPNN ($\simeq$1%) and ETHLN ($\simeq$1%). All these compounds are substantially longer-

lived than isoprene nitrates and therefore are more likely to influence the NO_x-balance on a larger scale (assuming a similar deposition velocity). The formation of PROPNN and MVKN appear especially important as their photochemical sinks are very slow: $\tau_{OH}^{MVKN} \simeq 100\,h$ and $\tau_{OH}^{PROPNN} > 200\,h$. Therefore, they may constitute important pathways for NO_x transport as well as significant NO_x sinks through deposition. They also can contribute to the growing source of atmospheric nitrogen to the open ocean (Duce et al., 2008).

In contrast to ISOPN, MACRN and MVKN release most of their NO_x in the course of their decomposition, possibly through the formation of formic and pyruvic acids. These organic nitrate channels may contribute significantly to the missing source of small carboxylic acid in the free troposphere.

6.5.4.2 Acids

Small carboxylic acids are ubiquitous in the atmosphere both in the gas-phase and in the aqueous phase, playing an important role in rain acidity and cloud reactions (Chebbi and Carlier, 1996).

The photooxidation of isoprene under high NO_x produces substantial amounts of formic (yield $\simeq (10\pm3)\%$ after 600 min) and acetic acids (yield $\simeq (3\pm1)\%$ after 600 min). Acetic and formic acids are highly correlated after the first 150 minutes ($\rho = 0.988$), since their main source, hydroxyacetone for acetic acid and glycolaldehyde for formic acid, share a similar origin and lifetimes (Figs. 6.14 and 6.15). We find [Acetic Acid] $= 0.46\pm0.02\times$[Formic Acid] $- (0.02\pm0.01)\times$[Isoprene]$_0$.

A strong correlation between formic and acetic acids has been observed previously over Amazonia (Andreae et al., 1988) and Virginia (Talbot et al., 1995). In most large scale chemical models, these compounds originate primarily from biomass burning and to a lesser extent from ozonolysis of alkenes. Since the main source of both acids in the chamber is unlikely to result from the ozonolysis of the alkenes, our study shows that additional channels for their formation should be included. The main identified sources (hydroxyacetone, glycolaldehyde, organic nitrates) are much longer-lived than the ones currently included in global model which may help resolve part of the discrepancy between models (Jacob and Wofsy, 1988) and atmospheric observations (Andreae et al., 1988; Talbot et al., 1990).

Finally the identification of MOBA, a five-carbon acid, could be important for aerosols as its vapor pressure and the vapor pressures of the products of its photooxidation are expected to be low.

171

6.5.4.3 Development of a reduced mechanism

The new constraints derived in this study primarily originate from our observation of the chemistry of the δ-hydroxy channels. In particular, we have shown that these channels account for a large fraction of the isoprene nitrates and small carboxylic acids, whose role is important on a global scale. Most of the reduced isoprene photooxidation mechanism implemented in chemical transport models, e.g., MOZART (Pfister et al., 2008), do not adequately account for the chemistry of the δ-hydroxy channels, thus impeding proper modeling of the consequences of isoprene photooxidation on troposheric chemistry.

The detailed chemical mechanism described in this study is too complex to be included in large-scale atmospheric chemistry simulations. To aid in such investigations, we propose that a few modifications of these simplified mechanisms be implemented (Table 6.3). While adding little complexity and maintaining carbon balance, these few changes describe more accurately the formation and fate of nitrates as well as the yield of carboxylic acid. In particular, the long lifetime of PROPNN and MVKN enables transport of organic nitrates over long distances.

In our reduced mechanism, we neglect the E δ-hydroxy channel branch (≃5% of the carbon) as well as the non-Dibble branch yielding MPDL and OBL (Fig. 6.1). We have only included the formation of organic nitrates which were directly constrained in this study (ISOPN, PROPNN, ETHNL). The yield of minor organic nitrates can be derived using the number of carbons of the parent peroxy radical, a common approach in most chemical transport models. We introduce a generic four-carbon hydrocarbon, HC4, to account for the decomposition of MOBA. This study does not constrain the fate of 3-methylfuran and the reaction of isoprene nitrates with ozone; more theoretical and experimental work is required.

6.6 Conclusions

A substantial fraction of the terrestrial Northern Hemisphere is characterized by conditions in which the fate of isoprene peroxy radicals is dominated by reactions with NO. Chameides et al. (1988) demonstrated that they play a major role in the formation of ozone in urban areas. This study complements previous investigations of isoprene photooxidation mechanism by focusing on the δ-hydroxy channels, whose chemistry is not adequately represented in chemical transport models. We focus on the large yields of small carboxylic acids and propose new constraints for the yield and the fate of organic nitrates. Both constitute outstanding uncertainties in the photooxidation of isoprene,

Table 6.3 – Suggested modifications of isoprene condensed photooxidation mechanism under high NO_x conditions. (2,1), (3,4), E(1,4) and E(4,1) branches are not treated. Formation of organic nitrates is limited to isoprene, MVK, and MACR peroxy radicals. The reaction of the isoprene nitrates with respect to O_3 as well as the fate of 3-MF are not tackled by this mechanism (cf. text). MGLYX denotes methylglyoxal and HC4, a generic four-carbon VOC.

Reaction			k(T = 298) $10^{-11}\,\mathrm{cm^3\,molecule^{-1}\,s^{-1}}$
ISOP + OH	→	$ISOPO_2$	10
$ISOPO_2$ + NO	→	0.40 MVK + 0.26 MACR + 0.883 NO_2 + 0.07 $ISOPN_\delta$ + 0.047 $ISOPN_\beta$ + 0.66 HCHO + 0.10 HC5 + 0.043 (3–MF) + 0.08 DIBOO + 0.803 HO_2	0.81
HC5 + OH	→	HC5OO	11
HC5OO + NO	→	NO_2 + 0.234 (GLYC + MGLYX) + 0.216 (GLYX + HACET) + 0.29 DHMOB + 0.17 MOBA + 0.09 HC4 + 0.09 CO + HO_2	0.81
$ISOPN_\delta$ + OH	→	$ISOPNOO_\delta$	9.5
$ISOPNOO_\delta$ + NO	→	0.34 DHBN + 0.15 PROPNN + 0.44 HACET + 0.07 MVKN + 0.13 ETHLN + 0.31 HC(O)OH + 0.31 NO_3 + 0.72 HCHO + 0.15 GLYC + 1.34 NO_2 + 0.35 HO_2	0.81
$ISOPN_\beta$ + OH	→	$ISOPNOO_\delta$	1.3
$ISOPNOO_\beta$ + NO	→	0.6 (GLYC + HACET) + 0.4 (HCHO + HO_2) + 0.26 MACRN + 0.14 MVKN + 1.6 NO_2	0.81
DIBOO + NO	→	NO_2 + HO_2 + 0.52 (GLYC + MGLYX) + 0.48 (GLYX + HACET)	0.81
MVK + OH	→	MVKOO	1.75
MVKOO + NO	→	0.625 (GLYC + $CH_3C(O)OO$) + 0.265 (MGLYX + HCHO + HO_2) + 0.11 MVKN + 0.89 NO_2	0.81 / 0.81
MVKN + OH	→	0.65 (HC(O)OH + MGLYX) + 0.35 (HCHO + $CH_3C(O)C(O)OH$) + NO_3	0.56
MACR + OH	→	0.47 MACROO + 0.53 MCO_3	2.95
MACROO + NO	→	0.85 (NO_2 + HO_2) + 0.425 (HACET + CO) + 0.425 (HCHO + MGLYX) + 0.15 MACRN	0.81
MACRN + OH	→	0.08 ($CH_3C(O)OH$ + HCHO + NO_3) + 0.07 (HC(O)OH + NO_3 + MGLYX) + 0.85 (HACET + NO_2) + 0.93 CO_2	5
MC(O)OO + NO	→	NO_2 + CO + CO_2 + HCHO + CH_3OO	2.1
GLYC + OH	→	0.75 HO_2 + 0.25 OH + 0.13 GLYX + 0.52 CO + 0.35 CO_2 + 0.16 HC(O)OH + 0.71 HCHO	0.8
HACET + OH	→	0.75 MGLYX + 0.825 HO_2 + 0.125 HC(O)OH + 0.1 OH + 0.125 CH_3OO + 0.20 CO_2 + 0.05 CO + 0.125 $CH_3C(O)OH$	0.6
ETHLN + OH	→	HCHO + CO_2 + NO_2	1
DHMOB + OH	→	1.5 CO + 0.5 HO_2 + 0.5 HACET + 0.5 HC4	1
MOBA + HO	→	MOBAOO	0.3
MOBAOO + NO	→	HC4 + CO_2 + HO_2 + NO_2	0.8

impeding proper modeling of tropospheric chemistry on a global scale. To aid in the development of improved simulations of this chemistry, we propose simple modifications of current condensed mechanism, which maintains carbon balance and accounts for the new constraints and mechanisms identified in this study (Table 6.3).

6.7 Appendices

6.7.1 Appendix A: Photooxidation mechanism

6.7.1.1 VOC chemistry

Except as noted below, we use the known rate coefficients of bimolecular and termolecular reactions as tabulated in IUPAC (Atkinson et al., 2004, 2006) and JPL (Sander, 2006) reports.

   OH. Reactions of OH with VOC are limited to its addition on a double bond and the abstraction of the aldehydic hydrogen and the hydrogen α to an alcohol, i.e., the abstraction of hydrogens from alcohols is neglected. For the addition of OH onto double bonds, in the absence of data or previous information enabling differentiation between the two carbons, we assume that the reaction occurs only on the most favorable location based on steric considerations. A structure-activity relationship (SAR) method is used to determine unknown reaction rate coefficients (Kwok and Atkinson, 1995). Following the studies of Orlando and Tyndall (2001) and Mereau et al. (2001), acylradicals are assumed to decompose promptly when the alkyl group features a carbonyl or an alcohol (with R secondary or tertiary) in β to the carbonyl:

$$R_1R_2R_3CCHO + OH \rightarrow R_1R_2R_3CCO + H_2O \tag{R6.5}$$

$$R_1R_2R_3CCO \rightarrow R_1R_2R_3C + CO \tag{R6.6}$$

We also assume that acylradicals featuring a nitrooxy group in β to the carbonyl undergo unimolecular decomposition. In all other cases, the acyl radical is assumed to add O_2 to yield the associated peroxy radical. In case of resonance, the branching between the addition of O_2 on the carbon in α of alcohol (denoted ⓐ in Fig. 6.1) or in γ (ⓑ) is unknown. Addition on ⓐ features a more stable double bond as well as a kinetically favored radical. In the mechanism, we set the branching ⓐ:ⓑ to 65%:35%. Furthermore we note that HOPL does not exhibit any early source, suggesting that the yield of HMPL is negligible. Indeed, its formation appears unfavorable on both a thermodynamic (the double bond is less substituted) and a kinetic (formation of a secondary radical) basis. Thus,

the branching ratio is set to $Y_a^{E_{1,4}} = 95\%$ and $Y_b^{E_{1,4}} = 5\%$.

Ozone. Ozone reacts with alkenes via the formation of a molozonide, quickly followed by its decomposition into a carbonyl and a Criegee intermediate. Assuming a generic rate constant for the reaction of alkenes with ozone, $10^{-17}\,\mathrm{cm^3\,molecule^{-1}\,s^{-1}}$, the reaction of an alkene with ozone is included if $\tau_{\mathrm{OH}} > \frac{\tau_{\mathrm{O_3}}}{10}$, where τ_{OH} and $\tau_{\mathrm{O_3}}$ are the lifetimes of the alkenes with respect to OH and $\mathrm{O_3}$, respectively. Ozone reactions are included for isoprene, MACR, and MVK, following IUPAC recommendations.

NO$_3$. Reactions of NO$_3$ with alkenes and aldehydes have been neglected, since $\frac{k_{\mathrm{alkenes/aldehydes}}^{\mathrm{NO_3}}[\mathrm{NO_3}]}{k_{\mathrm{alkenes/aldehydes}}^{\mathrm{OH}}[\mathrm{OH}]} \ll 1$ throughout the experiment.

6.7.1.2 Peroxyradical chemistry

NO. NO reacts with peroxy radicals with a rate coefficient of $2.43 \times 10^{-12} \exp(360/\mathrm{T})\,\mathrm{cm^3}$ molecule^{-1}

s^{-1} (Atkinson et al., 2006) through

$$\mathrm{RO_2 + NO} \rightarrow (1-\alpha)(\mathrm{RO + NO_2}) + \alpha\mathrm{RONO_2} \tag{R6.7}$$
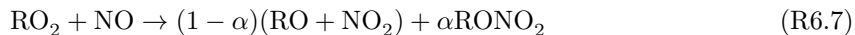
The reaction rate coefficient of acyl peroxy radical with NO is set to $6.7 \times 10^{-12} \exp(340/\mathrm{T})\,\mathrm{cm^3}$ molecule^{-1} s^{-1} based on $\mathrm{CH_3CH_2C(O)OO}$. Carter's parameterization is used to compute the alkyl nitrate yield (Carter and Atkinson, 1989; Arey et al., 2001):

$$\frac{\alpha}{1-\alpha} = \frac{Y_0^{298}[\mathrm{M}](\mathrm{T}/298)^{-m_0}}{1+\Theta} \times F^z \times m \tag{6.5}$$

with $z = (1+[\log(\frac{Y_0^{298}[\mathrm{M}](\mathrm{T}/298)^{-m_0}}{Y_\infty^{298}[\mathrm{M}](\mathrm{T}/298)^{-m_\infty}})]^2)^{-1}$, $F = 0.41$, $m_0 = 0$, $m_\infty = 8.0$, $\beta{=}1$, $\Theta = \frac{Y_0^{298}[\mathrm{M}](\mathrm{T}/298)^{-m_0}}{Y_\infty^{298}(\mathrm{T}/298)^{-m_\infty}}$, $\gamma = 2 \times 10^{-22}\,\mathrm{cm^3\,molecule^{-1}}$, $Y_\infty^{298} = 0.43$, $Y_0^{298} = \gamma e^{\beta n}$, where n is the number of carbons in the molecule. The parameter m is set to 0.4, 1.0 and 0.3 for primary, secondary, and tertiary nitrates, respectively (Arey et al., 2001).

For β-hydroxy peroxy radicals, α is divided by two to account for the effect of the hydroxy group as highlighted by O'Brien et al. (1998). For acylnitrates, the yield is set to the alkyl tertiary nitrate yield, providing it does not exceed 4%.

NO$_2$. NO$_2$ reacts with peroxy acyl radicals to yield peroxyacylnitrate-like compounds, which

decompose thermally or photolytically:

$$RC(O)OO + NO_2 \rightleftarrows RC(O)OONO_2 \tag{R6.8}$$

The rates of formation and decomposition of methacryloyl peroxy nitrate (MPAN) are used for all PAN-like compounds except PAN itself. Most PAN-like compounds except PAN itself have other reactive groups (aldehyde, primary or a secondary alcohol, double bond) causing their major sink to be reaction with OH.

NO_3. NO_3 reacts with peroxy radicals through

$$NO_3 + RO_2 \rightarrow NO_2 + RO + O_2 \tag{R6.9}$$
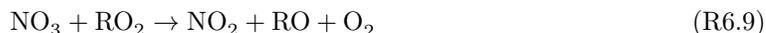
The rate coefficient is set to $2.3 \times 10^{-12} \, \text{cm}^3 \, \text{molecule}^{-1} \, \text{s}^{-1}$ independent of both the temperature and the peroxyradical.

HO_2 and peroxy radicals. HO_2 reacts with peroxy radicals through four different channels:

$$HO_2 + RO_2 \rightarrow ROOH + O_2 \tag{R6.10}$$

$$HO_2 + RO_2 \rightarrow ROH + O_3 \tag{R6.11}$$

$$HO_2 + RO_2 \rightarrow RO + O_2 + OH \tag{R6.12}$$

$$HO_2 + RO_2 \rightarrow R_{-H}(O) + H_2O + O_2 \tag{R6.13}$$
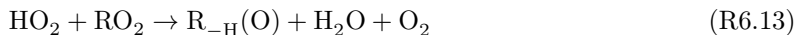
Reaction R6.13 has only been observed for compounds such as RCH_2OCH_2OO and is not considered in this study. Acyl peroxides are assumed to react through Reaction R6.10, Reaction R6.11, and Reaction R6.12 with a branching ratio 0.4:0.2:0.4 (Hasson et al., 2004; Jenkin et al., 2007). Acetonylperoxy radicals have also been shown to react through channels Reaction R6.10 and Reaction R6.12 with a branching ratio 1:2 (Hasson et al., 2004). The other alkylperoxy are assumed to react through Reaction R6.10 only. The reaction rate coefficient for the reaction of alkylperoxy with HO_2 is set to $2.91 \times 10^{-13} \exp(1300/\text{T}) \times (1 - \exp(-0.245 n_c)) \, \text{cm}^3 \, \text{molecule}^{-1} \, \text{s}^{-1}$ where n_c is the number of carbon atoms (Saunders et al., 2003). For the acyl peroxy radicals, the reaction rate coefficient is set to $5.2 \times 10^{-13} \exp(983/\text{T}) \, \text{cm}^3 \, \text{molecule}^{-1} \, \text{s}^{-1}$ based on the reaction of the methylacylperoxy radical.

$RO_2 + RO_2$ reactions are neglected in this study. In the early stages of isoprene photooxidation

the chemistry of peroxyradicals is entirely dominated by NO. At the end of the experiment, peroxy radical chemistry is dominated by HO_2, which concentration is high enough so that $RO_2 + RO_2$ reactions can be safely neglected.

6.7.1.3 Photolysis

The photolysis rate of a compound i is computed via:

$$J_i = \int_{\lambda_1}^{\lambda_2} I_e(\lambda)\sigma_i(\lambda)\phi_i(\lambda)\,d\lambda \tag{6.6}$$

The effective light flux I_e is computed using an experimental determination of J_{HONO} and a spectrum of the lamp output made every nanometer (LI-COR LI1800 $\lambda_1 = 300$ nm, $\lambda_2 = 600$ nm). HONO is scaled using the oscillator strength recently reported by Wall et al. (2006). This gives $J_{\mathrm{HOOH}} = 3.1 \times 10^{-6}\,s^{-1}$. The photolysis of compounds with unknown absorption cross sections is estimated from the known photolysis rate constants of similar compounds. The photolysis of organic nitrates is assumed to yield only $RO + NO_2$. For primary organic nitrate, the photolysis rate is taken from $1-C_4H_9ONO_2$, for secondary organic nitrates from $2-C_4H_9ONO_2$ and for tertiary nitrates from tertbutylnitrate (Roberts and Fajer, 1989; Atkinson et al., 2006).

6.7.1.4 Fate of the alkoxy radicals

Alkoxy radicals can react following three different pathways:

$$R_1R_2R_3CO\cdot \rightarrow R_1R_2CO + R_3\cdot \tag{R6.14}$$

$$R_1R_2R_3CO\cdot + O_2 \rightarrow R_1R_2CO + HO_2, \text{ if } R_3 = H \tag{R6.15}$$

$$R_1R_2R_3CO\cdot \rightarrow R_1R_2COHCCCC\,\dot{R}_{3'}, \text{ with } R_3 = CCCCR_{3'} \tag{R6.16}$$
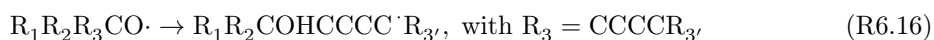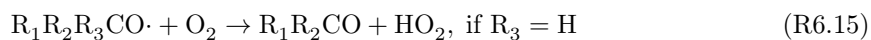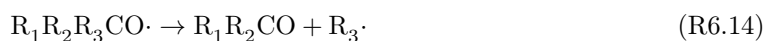
Since the isomerization reaction, Reaction R6.16, requires at least four carbons (Atkinson, 1997), it occurs only in the first stages of isoprene photooxidation, when major products retain five carbons. In the case of isoprene, isomerization (Reaction R6.16) is faster than decomposition (Reaction R6.14) and reaction with O_2 (Reaction R6.15). Alkoxy radicals which cannot undergo Reaction R6.16 are assumed to decompose through Reaction R6.14, i.e., their reaction with O_2 (Reaction R6.15) is generally neglected except for a few cases detailed in the discussion section.

Generally the decomposition of an alkoxy radical can occur through different channels, whose

branching ratios (Y_i) are estimated using their respective activation energies, E_{bi}.

$$R_1R_2R_3CO\cdot \rightarrow R_2R_3CO + R_1\cdot \; Y_1 \qquad\qquad (R6.17)$$

$$R_1R_2R_3CO\cdot \rightarrow R_1R_3CO + R_2\cdot \; Y_2 \qquad\qquad (R6.18)$$

$$R_1R_2R_3CO\cdot \rightarrow R_1R_2CO + R_3\cdot \; Y_3 \qquad\qquad (R6.19)$$
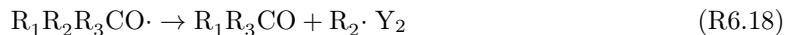
with

$$\forall i \in (1,2,3), Y_i = \exp\left(\frac{E_{b1} + E_{b1} + E_{b1} - E_{bi}}{RT}\right) \qquad\qquad (6.7)$$

E_b is calculated using the generalized structure-activity relationship developed by Peeters et al. (2004).

6.7.1.5 Skill of the model

The evolution of the modelled chemical system can be examined through its instantaneous speciation (Fig. 6.16). Furthermore, given that the oxidation of CO by OH is negligible in the time scale of experiment, we define the chemical speed of the system, V, as $\frac{d[CO+CO_2]}{dt}$ (Fig. 6.17). Both proxies indicate that the system undergoes three different regimes:

First regime (0<t<150 min). This regime is characterized by a large supply of NO, as well as very reactive compounds featuring a double bond. V reaches a maximum after a few minutes at 0.7 ppbv(C)/min. O_3 and PNA are very low in this regime, underlying a chemistry dominated by NO. The organic nitrate concentration reaches its maximum at the end of this regime. The reduction in [OH] corresponds to an increase of [NO_2] leading to the formation of nitric acid.

Second regime (150<t<550 min). This regime is characterized by a very stable V (0.5 ppbv(C)/min) with a chemistry dominated by aldehydes. OH recycling though HO_2 + NO is less efficient than in the first regime due to the abundance of O_3, which favors the formation of PAN. Nevertheless, the reduction in the chemical speed due to the transition from "double-bond-dominated" to "aldehyde-dominated" reduces OH sinks which ultimately leads to a slow increase in OH, leveling off when PNA peaks, i.e., when the NO_x is titrated.

Third regime (550<t<1000 min). After the PNA peak, the chemistry is dominated by HO_2, as evidenced by the formation of peracetic acid (PAA cluster at $m/z = 161$) and methylhydroperoxide (MHP cluster $m/z = 133$). Low-reactivity compounds such as ketones or long-lived nitrates dominate the chamber composition. Despite the almost constant OH, the chemical speed drops significantly
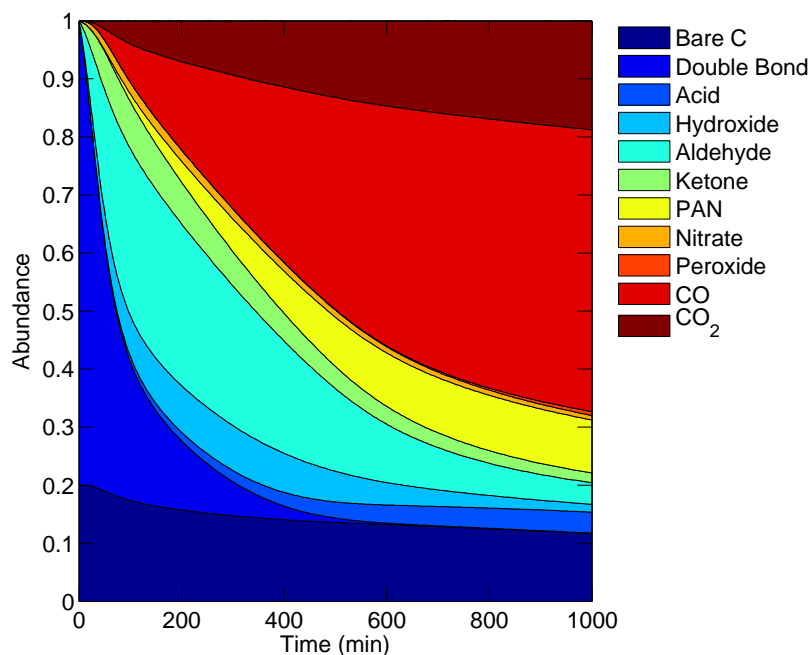
Figure 6.16 – Evolution of the speciation during isoprene photooxidation. The abundance of a functional group Π is defined as the sum of the carbons bearing Π normalized by the total amount of carbon in the chamber, i.e., 5 times the initial amount of isoprene.
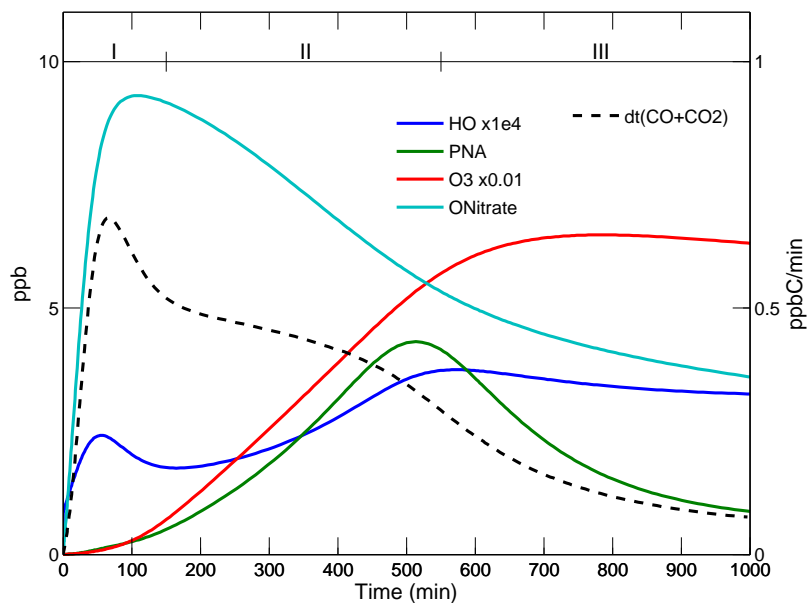
Figure 6.17 – Different stages of the reaction. Regime I: alkene chemistry, NO_x-dominated. Regime II: aldehyde chemistry, NO_x-dominated. Regime III: ketone and peroxide chemistry, HO_x-dominated.
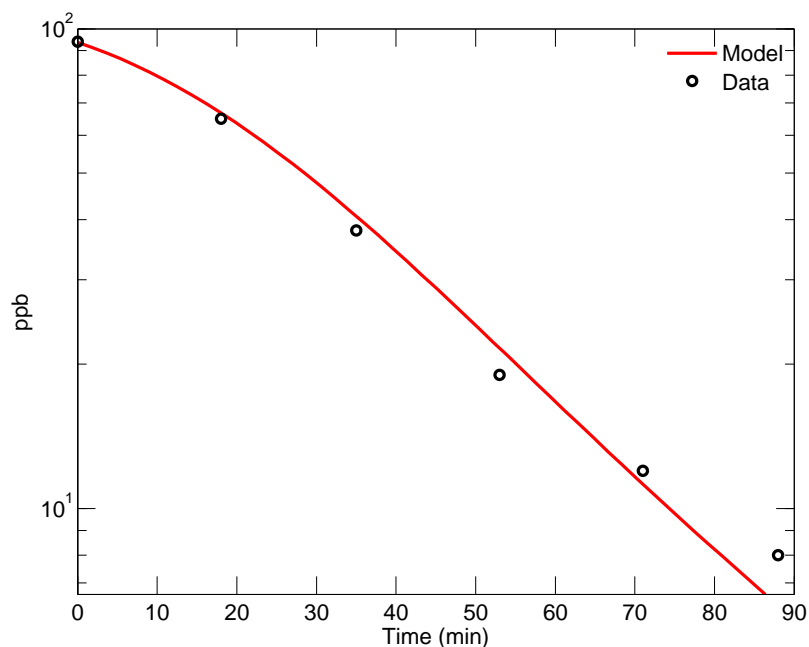
Figure 6.18 – Isoprene profile monitored by GC-FID compared to modeled isoprene.

to 0.1 ppbv(C)/min.

These three distinct chemical regimes are consistent with the ones derived using the experimental profiles of HONO and PNA, i.e., the mechanism accurately represents the average evolution of the chemical system (Figs. 6.16 and 6.17). The skill of the mechanism can be evaluated in greater details by comparing the times when various species peak as well as their maxima between mechanism and experiment (Table 6.4). The mechanism generally captures correctly the peak times indicating that the chemical speed is properly modeled in the first and second regime. The error regarding the maximum intensity falls within the uncertainty of this study ($\pm$20–30%). The sensitivity of the CIMS to PNA is probably overevaluated due to ligand exchange with H_2O_2. Satisfactory representation for the background chemistry species is also reached (Figs. 6.18 and 6.19). In particular, HO_2NO_2, a very sensitive marker for the ratio of NO_x and HO_x, is well captured during the first and second regimes.

Figure 6.19 – Comparison of CIMS measurements of inorganic species with their modeled concentrations using experimental calibrations. Calibrations for HO_2NO_2 and N_2O_5 are uncertain.

Table 6.4 – Skill of the model. $\Delta t = t_{max}^{model}/t_{max}^{data} - 1$ and $\Delta c = c_{max}^{model}/c_{max}^{data} - 1$.

	HACET	GLYC	ISOPN	MVKN +MACRN	HC5
$\Delta t(\%)$	4.8	-1.4	<1	<1	<1
$\Delta c_{max}(\%)$	3.6	-4.4	2.4	-3.1	38
	ETHN	DHB	DHPN	HONO	PNA
$\Delta t(\%)$	<1	<1	2.1	16	-11
$\Delta c_{max}(\%)$	-11	3.5	22	2.2	-37

6.7.2 Appendix B: Calibration

6.7.2.1 Definitions

We define the normalized signal, $\widehat{\mathrm{Signal}(m/z)}$, as the absolute number of counts recorded at m/z divided by the number of counts associated with the reagent anion, $\mathrm{CF_3O^-}$:

$$\widehat{\mathrm{Signal}(m/z)} = \frac{\mathrm{Signal}(m/z)}{\mathrm{Signal}(\mathrm{CF_3O^-})} \tag{6.8}$$

For the chamber experimental conditions, the reagent ion was found in several forms: $\mathrm{CF_3O^-}$, $\mathrm{CF_3O^-\cdot H_2O}$ and $\mathrm{CF_3O^-\cdot H_2O_2}$. Due to the high count rates for the primary isotopes of the reagent ions (sum ~ 14 MHz), the ^{13}C isotopes were monitored instead:

$$\widehat{\mathrm{Signal}(\mathrm{CF_3O^-})} = \sum_{m/z=86,104,120} \mathrm{Signal}(m/z) \tag{6.9}$$

As stated in Sect. 6.3.3, in order to get the concentration for an analyte, X, detected as a product ion with $m/z = p$, we divide the normalized signal for m/z by the sensitivity (c_X) for that analyte under chamber conditions Eq. 6.1. The above method fails when mass analog ions, i.e., different ions with the same mass-to-charge ratio, exist at the m/z of interest. The mass analog ions correspond to different analytes in the chamber, which have different reaction rate coefficients with the reagent ion. While the CIMS instrument cannot separate mass analogs, the explicit model can. To compare the model results with a measured signal composed of mass analogs, we use the following:

$$\left[\mathrm{X}_{\mathrm{measured}\ m/z=a}\right]_\mathrm{ppbv} = \frac{\widehat{\mathrm{Signal}(m/z)}}{c_\mathrm{ref}} \tag{6.10}$$

$$\left[\mathrm{X}_{\mathrm{model}\ m/z=a}\right]_\mathrm{ppbv} = \sum_{i\in A}[\mathrm{X}_i]\frac{c_{\mathrm{X}_i}}{c_\mathrm{ref}} \tag{6.11}$$

where a is a m/z featuring mass analog ions, A the subset of compounds yielding product ions with $m/z = a$ and $c_\mathrm{ref} = 3.85 \times 10^{-4}\,\mathrm{pptv^{-1}}$ is taken as an approximate general calibration. Nominally, $\widehat{\mathrm{Signal}(\mathrm{CF_3O^-})} = 120$ kcounts s^{-1}, this gives $c_\mathrm{ref} = 46\,\mathrm{counts\,s^{-1}\,pptv^{-1}}$, in the CIMS flow tube. Including the dilution factor (13.2), the sensitivity is $3.5\,\mathrm{counts\,s^{-1}\,pptv^{-1}}$ in the chamber air.

6.7.2.2 Dipoles and polarizabilities computed by quantum mechanics

The dipole moment and polarizability of a molecule depend on its charge distribution. Thus, different conformers of a molecule can have very different dipole moments. The polarizability is essentially

determined by the number of electrons and so is not significantly altered by conformers. We have calculated the dipole moment and polarizability using density functional theory. Many of the molecules of interest have a large number of structural conformers and we have calculated a conformer distribution for all molecules. To generate the initial set of conformers, we have allowed 3-fold rotation about all CC, CO, CN single bonds. This leads to, for example, 34 guess structures in the case of ISOPN Z(1,4). For each guess conformer, geometry optimization is conducted at the B3LYP/6-31G(d) level. The optimized conformers are ranked by energy and relative population for a temperature of 298 K is determined. We have only calculated the polarizability of the lowest energy structure for each of the molecules as we found this to be relatively insensitive to structure. All calculations were performed with Spartan'06, with the default convergence criteria (Wavefunction Inc., 2006). Test calculations on a few small molecules for which the dipole moment has been measured show that the B3LYP/6-31G(d) calculated dipole moments are in good agreement with experiment (Table 6.5).

6.7.3 Appendix C: Uncertainty

6.7.3.1 Initial branching ratio uncertainty

The addition of OH onto isoprene yields eight different peroxyradicals (Fig. 6.1). The reported branching ratios vary significantly (Lei et al., 2001; Greenwald et al., 2007).

MACR and MVK are only produced through the reaction of the β-hydroxy alkoxy radicals with NO and by ozonolysis of isoprene (Fig. 6.1). Since the latter accounts for less than 0.5% of the total isoprene consumption in the chamber, we can use the direct determination of the yield of these products (Sprengnether et al., 2002) as a constraint.

$$(1 - \alpha_\beta)(Y_{1,2} + Y_{2,1}) = 0.44 \pm 0.06 \tag{6.12}$$

$$(1 - \alpha_\beta)(Y_{4,3} + Y_{3,4}) = 0.28 \pm 0.04 \tag{6.13}$$

We consider that all β-hydroxy peroxy radical have the same nitrate branching ratio, as suggested by Giacopelli et al. (2005). In this study, we assume that channels (2,1) (respectively (3,4)) yield MVK and MACR. Park et al. (2003) proposed that the radicals formed in these channels undergo a cyclization, thus reducing the yield of MVK and MACR. The yield of the nitrates that should originate from the hydrocarbons proposed by Park et al. (2003) is too small to provide conclusive experimental evidence in favor or against this mechanism. Given the small combined yield of these channels, this uncertainty remains small compared to the ones affecting the major channels.

Table 6.5 – Weighted average dipoles ($\bar{\mu}$) and polarizabilities (α). Experimental determinations are indicated in parenthesis when available. k_X, is the weighted average of the collision rates calculated for conformers with an abundance greater than 5%. $k_{HNO_3} = 1.92{\times}10^{-9}\,cm^3\,molecule^{-1}\,s^{-1}$. σ is the weighted standard deviation of the distribution of thermal collision rate constants, i.e., it indicates the sensitivity of the calibration to the calculated distribution of conformers.

Molecule (X)	$\bar{\mu}$(D)	$\alpha(text)$	k_X/k_{HNO_3}	σ
Acetic Acid	1.6 (1.7$^\diamond$)	3.9 (5.1*)	0.80 (0.84)	$\emptyset$
DHB	2.3	7.5	1.0	0.027
DHMOB(1,4)	1.5	9.3	0.79	0.26
DHMOB(4,1)	1.1	9.1	0.66	0.12
DHPN	1.5	6.0	0.74	$\emptyset$
ETHLN	2.7	6.2	1.1	0.4
Formic Acid	1.4 (1.4$^\diamond$)	2.4 (3.3$^\diamond$)	0.76 (0.78)	$\emptyset$
GLYC	2.3 (2.34§)	4.5	1.1 (1.1)	$\emptyset$
HACET	3.1 (3.1†)	5.5	1.4 (1.4)	$0.72{\times}10^{-3}$
HC5 E(4,1)	2.8	8.9	1.2	0.22
HC5 Z(1,4)	3.5	8.7	1.5	0.14
HC5 Z(4,1)	3.7	8.9	1.5	$\emptyset$
HOPL	1.2	5.7	0.65	$1.6{\times}10^{-3}$
ISOPN(1,2)	2.5	11	1.0	0.032
ISOPN(2,1)	2.5	11	1.0	0.17
ISOPN(3,4)	2.4	11	1.0	0.11
ISOPN(4,3)	2.5	11	1.0	0.068
ISOPN(1,4)E	3.2	11	1.3	0.17
ISOPN(4,1)E	2.9	12	1.2	0.085
ISOPN(1,4)Z	3.2	11	1.3	0.028
ISOPN(4,1)Z	3.0	11	1.2	0.041
MACRN(m)	2.4	9.9	1.0	0.38
MACRN	2.0	9.8	0.87	0.045
MNBL Z(1,4)	3.6	11	1.4	0.089
MNBL Z(4,1)	3.9	12	1.5	0.12
MNBOL Z(1,4)	4.3	12	1.6	0.073
MNBOL Z(4,1)	4.2	12	1.6	0.083
MOBA Z(1,4)	4.6	9.1	1.8	0.22
MOBA Z(4,1)	3.2	9.2	1.3	$\emptyset$
MVKN(m)	2.2	9.7	0.95	0.39
MVKN	2.3	9.9	0.95	0.078
PROPNN	3.0	7.7	1.3	0.46
Propanoic Acid	1.5	5.4	0.76	0.034
Pyruvic Acid	2.4	5.5	1.0	$\emptyset$

$\diamond$: Johnson III (2006), $\dagger$: Apponi et al. (2006), $\star$: Cox et al. (1971)

$\star$: Maryott and Buckley (1953), $\S$: Marstokk and Mollendal (1973)

Theoretical determinations of the branching ratio have also been made (Lei et al., 2000; Greenwald et al., 2007):

$$Y_{1,2} + Y_{1,4} = 0.56; \ 0.67 \tag{6.14}$$

$$Y_{4,3} + Y_{4,1} = 0.29; \ 0.37 \tag{6.15}$$

$$Y_{2,1} = 0.02 \tag{6.16}$$

$$Y_{3,4} = 0.02; \ 0.05 \tag{6.17}$$

The product of the decomposition of the isoprene nitrates formed in the (4,1) branch, dihydroxybutanone (DHB) and propanone nitrate (PROPNN), provide an additional constraint (Fig. 6.8):

$$0.01 \pm 0.002 < (1 - \alpha_{2,1}^{dn}) \gamma \alpha_\beta Y_{2,1} + (1 - \alpha_{4,1}^{dn}) \alpha_\delta Y_{4,1} < 0.034 \pm 0.007 \tag{6.18}$$

where α_δ is the nitrate yield from the δ-hydroxy peroxy radicals, γ is the branching ratio of the pathway yielding propanone nitrate from ISOPN(2,1), computed using Eq. 6.7, $\alpha_{2,1}^{dn}$ and $\alpha_{4,1}^{dn}$, the respective organic dinitrate branching ratios from ISOPN(2,1) and ISOPN(4,1).

The upper and lower bounds reflect the uncertainty on the identification of the $m/z{=}189$ signal. The upper bound is derived assuming all $m/z{=}189$ signal originates from the DHB yielded by ISOPN(4,1). The lower limit assumes that no DHB is formed from ISOPN but rather that the signal measured at $m/z{=}189$ results from the photooxidation of HC5 Z(1,4) (negligible based on Peeters' SAR) and ISOPN (1,4) (formation of dihydroxymethylpropanal (DHMPL) from addition of OH on the less sterically favored carbon).

In the mechanism, we use the constraints implied by the study of Lei et al. (2000), $Y_{MACR} = 0.26$ and $Y_{MVK} = 0.40$ and the upper bound of Eq. 6.18. Since the use of the non-linear system formed by Eqs. 6.12 to 6.18 in order to solve for α_β, α_γ and $Y_{i,j}$ does not yield a single solution, we use the branching ratios derived by Lei et al. (2001) to initialize the numerical solution of this non-linear system and obtain: $Y_{1,2} \simeq 41\%$, $Y_{1,4} \simeq 15\%$, $Y_{2,1} \simeq 2\%$, $Y_{4,3} \simeq 23\%$, $Y_{4,1} \simeq 14\%$, $Y_{3,4} \simeq 5\%$, $\alpha_\delta \simeq 24\%$, $\alpha_\beta \simeq 6.7\%$ This set of parameters yields a self-consistent mechanism that captures correctly most of our observations.

The constraints implied by the theoretical study of Greenwald et al. (2007) and the experimental work of Sprengnether et al. (2002) cannot be reconciled with our observations in a consistent fashion. Consider the extreme case where $Y_{MACR} = 24\%$, $Y_{4,3} + Y_{4,1} = 29\%$ and $Y_{2,1} = 2\%$ and assume a nitrate yield of 10% for the β-hydroxy channels gives $Y_{4,1} \simeq 4.7\%$. A direct consequence of the

small branching ratio for (4,1) branch is to preclude DHBN from being an important product of ISOPN(4,1). The signal measured at m/z=189 would therefore mostly correspond to DHMPL formed from the photooxidation of ISOPN(1,4). There are two major inconsistencies with this hypothesis. First, due to the small carbon flux through the (4,1) branch, we are not able to capture the prompt source of hydroxyacetone attributed to Dibble mechanism. Second, DHMPL features an aldehydic group so that its lifetime with respect of OH is expected to be much shorter than DHB, which is inconsistent with the signal recorded at m/z=189 (Fig. 6.12).

While the derivation of the specific branching ratio is affected by this major uncertainty, the determination of the overall yield of the different products identified is, on the other hand, strongly constrained by observations and thus relatively insensitive to our choice. The asymmetry of the nitrate yields between the β and δ-hydroxy channels is therefore a reliable feature. Indeed this conclusion bears a striking similarity with the estimate derived by Giacopelli et al. (2005) using a corrected Carter's parameterization. It is also consistent with the suggestion of O'Brien et al. (1998) that hydrogen bonding in β-hydroxy-substituted ROONO intermediate weakens the RO$-$ONO bond, enhancing RO + NO$_2$ production.

6.7.3.2 Quantum mechanics

In this study, we have assumed that ligand exchange has a negligible impact on CIMS sensitivity. Therefore to assess the accuracy of our calibration, we compare the calculated collision rate with the fastest experimental collision rate:

$$k_{\mathrm{X}}^r = \frac{c_{\mathrm{X}}^e}{c_{\mathrm{HNO}_3}} k_{\mathrm{HNO3}}^r \tag{6.19}$$

where $k_{\mathrm{HNO3}}^r = 2.2 \times 10^{-9} \, \mathrm{cm^3 \, molecule^{-1} \, s^{-1}}$ (Huey et al., 1996; Amelynck et al., 2000b) and c_{X}^e is the maximum sensitivity of this technique determined experimentally by changing the water vapor mixing ratio (often found at zero water vapor mixing ratio). The sensitivity of the CIMS to strong acids (nitric acid ($r = \frac{k_{\mathrm{X}} \cdot k_{\mathrm{HNO}_3}^r}{k_{\mathrm{HNO}_3} k_{\mathrm{X}}^r} = 0.9$)) or representative VOC (glycolaldehyde, r=0.85) appears to be correctly captured using the thermal collision rate. Furthermore in a recent study, Ng et al. (2008) monitored the oxidation of isoprene by NO$_3$ using CIMS. Using the dipoles and the polarizabilities of MNBOL(1,4)/(4,1) ((2Z)-2/3-methyl-4-(nitrooxy)but-2-ene-1-peroxol) and MNBL(1,4)/(4,1) ((2Z)-3/2-methyl-4-(nitrooxy)but-2-enal) and ISOPN(4,1) (Table 6.5), we infer that they account for 100% of the carbon flux, consistent with previous determination. Conversely, the sensitivity to smaller molecules such as formic (r=1.5) or acetic acid (r=2) is largely overpredicted. If the experimental

rates of Amelynck et al. (2000b) are used, the agreement is much better with r=1.0 for formic acid and r=1.1 for acetic acid. The discrepancy may be explained by the smaller collisional energy used in the Amelynck et al. (2000b)'s experiment, which would result in fewer $A^-\cdot HF$ complexes being broken during the expansion into the high vacuum.

6.7.3.3 Inorganic chemistry uncertainties

In addition to uncertainties associated with the VOC chemistry, proper modeling of the background chemistry must be achieved to derive conclusions regarding the VOC chemistry. The model is especially sensitive to the following parameters:

Nitric acid. The rate of $OH + NO_2 + M \rightarrow HNO_3 + M$ is an important uncertainty regarding the background chemistry. We use the recently reported rate coefficient of $9.16 \times 10^{-12}\ cm^3\ molecule^{-1}\ s^{-1}$ (Okumura and Sander, 2005), which tends to reduce the rate of formation of nitric acid and conversely increases the formation rate of ozone in comparison with the previous estimates (Atkinson et al., 2006).

Dinitrogen Pentoxide. N_2O_5 is known to react with water on surfaces (aerosol, walls) to yield nitric acid:

$$N_2O_5 + H_2O \xrightarrow{S} 2HNO_3 \tag{R6.20}$$

The DMA measurements can be used to obtain the aerosol surface area S and the collision rate, $k_{coll} = \frac{1}{4}\sqrt{\frac{8RT}{\pi M}} S = 2 \times 10^{-3}\ cm^3\ molecule^{-1}\ s^{-1}$. The accommodation coefficient is set to 0.05.

Initial concentration of H_2O_2. Due to the technique used in this experiment to introduce H_2O_2 into the chamber, its concentration is not known accurately. No calibration is available at such a high hydrogen peroxide level, so that its estimate based on CIMS measurement is uncertain: 1.9–2.3 ppmv. A new injection method has been developed to reduce this uncertainty in future studies.

Acknowledgements

Bibliography

Amelynck, C., Schoon, N., and Arijs, E.: Gas phase reactions of CF_3O^- and $CF_3O^- \cdot H_2O$ with nitric, formic, and acetic acid, Int. J. Mass. Spectrom., 203, 165–175, 2000.

Andreae, M. O., Talbot, R. W., Andreae, T. W., and Harriss, R. C.: Formic and acetic-acid over the central Amazon region, Brazil. I - Dry season, J. Geophys. Res.-Atmos., 93, 1616–1624, 1988.

Apponi, A. J., Hoy, J. J., Halfen, D. T., Ziurys, L. M., and Brewster, M. A.: Hydroxyacetone (CH_3COCH_2OH): A combined microwave and millimeter-wave laboratory study and associated astronomical search, Astrophys. J., 652, 1787–1795, 2006.

Arey, J., Aschmann, S. M., Kwok, E. S. C., and Atkinson, R.: Alkyl nitrate, hydroxyalkyl nitrate, and hydroxycarbonyl formation from the NO_x-air photooxidations of C_5-C_8 n-alkanes, J. Phys. Chem. A, 105, 1020–1027, 2001.

Atkinson, R.: Gas-phase tropospheric chemistry of volatile organic compounds .1. Alkanes and alkenes, J. Phys. Chem. Ref. Data, 26, 215–290, 1997.

Atkinson, R., Aschmann, S. M., Tuazon, E. C., Arey, J., and Zielinska, B.: Formation of 3-methylfuran from the gas-phase reaction of OH radicals with isoprene and the rate-constant for its reaction with OH radical, Int. J. Chem. Kinet., 21, 593–604, 1989.

Atkinson, R., Baulch, D. L., Cox, R. A., Crowley, J. N., Hampson, R. F., Hynes, R. G., Jenkin, M. E., Rossi, M. J., and Troe, J.: Evaluated kinetic and photochemical data for atmospheric chemistry: Volume I – gas phase reactions of O_x, HO_x, NO_x and SO_x species, Atmos. Chem. Phys., 4, 1461–1738, 2004.

Atkinson, R., Baulch, D. L., Cox, R. A., Crowley, J. N., Hampson, R. F., Hynes, R. G., Jenkin, M. E., Rossi, M. J., and Troe, J.: Evaluated kinetic and photochemical data for atmospheric chemistry: Volume II – gas phase reactions of organic species, Atmos. Chem. Phys., 6, 3625–4055, 2006.

Atkinson, R., Arey, J., and Aschmann, S. M.: Atmospheric chemistry of alkanes: Review and recent developments, Atmos. Environ., 42, 5859–5871, doi:10.1016/j.atmosenv.2007.08.040, 1st International Conference on Atmospheric Chemical Mechanisms, Davis, CA, Dec 06-08, 2006, 2008.

Baker, J., Arey, J., and Atkinson, R.: Formation and reaction of hydroxycarbonyls from the reaction of OH radicals with 1,3-butadiene and isoprene, Environ. Sci. Technol., 39, 4091–4099, doi:10.1021/es047930t, 2005.

Bethel, H. L., Atkinson, R., and Arey, J.: Kinetics and products of the reactions of selected diols with the OH radical, Int. J. Chem. Kinet., 33, 310–316, 2001.

Bierback, A., Barnes, I., and Becker, K. H.: Product and kinetic-study of the OH-initiated gas-phase oxidation of furan, 2-methylfuran and furanaldehydes at approximate-to-300 K, Atmos. Environ., 29, 2651–2660, 1995.

Butkovskaya, N. I., Pouvesle, N., Kukui, A., and Le Bra, G.: Mechanism of the OH-initiated oxidation of glycolaldehyde over the temperature range 233–296 K, J. Phys. Chem. A, 110, 13 492–13 499, doi:10.1021/jp064993k, 2006a.

Butkovskaya, N. I., Pouvesle, N., Kukui, A., Mu, Y. J., and Le Bras, G.: Mechanism of the OH-initiated oxidation of hydroxyacetone over the temperature range 236–298 K, J. Phys. Chem. A, 110, 6833–6843, doi:10.1021/jp056345r, 2006b.

Cameron, M., Sivakumaran, V., Dillon, T. J., and Crowley, J. N.: Reaction between OH and CH_3CHO – Part 1. Primary product yields of CH_3 (296 K), CH_3CO (296 K), and H (237–296 K), Phys. Chem. Chem. Phys., 4, 3628–3638, doi:10.1039/b202586h, 2002.

Carlton, A. G., Turpin, B. J., Lim, H. J., Altieri, K. E., and Seitzinger, S.: Link between isoprene and secondary organic aerosol (SOA): Pyruvic acid oxidation yields low volatility organic acids in clouds, Geophys. Res. Lett., 33, doi:10.1029/2005GL025374, 2006.

Carter, W. P. L. and Atkinson, R.: Alkyl nitrate formation from the atmospheric photooxidation of alkanes – A revised estimation method, J. Atmos. Chem., 8, 165–173, 1989.

Chameides, W. L., Lindsay, R. W., Richardson, J., and Kiang, C. S.: The role of biogenic hydrocarbons in urban photochemical smog – Atlanta as a case-study, Science, 241, 1473–1475, 1988.

Chebbi, A. and Carlier, P.: Carboxylic acids in the troposphere, occurrence, sources, and sinks: a review, Atmos. Environ., 30, 4233–4249, 1996.

Chen, X. H., Hulbert, D., and Shepson, P. B.: Measurement of the organic nitrate yield from OH reaction with isoprene, J. Geophys. Res.-Atmos., 103, 25 563–25 568, 1998.

Chuong, B. and Stevens, P.: Measurements of the kinetics of the OH-initiated oxidation of methyl vinyl ketone and methacrolein, Int. J. Chem. Kinet., 36, 12–25, doi:10.1002/kin.10167, 2004.

Chuong, B. and Stevens, P. S.: Measurements of the kinetics of the OH-initiated oxidation of isoprene, J. Geophys. Res.-Atmos., 107, doi:10.1029/2001JD000865, 2002.

Claeys, M., Graham, B., Vas, G., Wang, W., Vermeylen, R., Pashynska, V., Cafmeyer, J., Guyon, P., Andreae, M. O., Artaxo, P., and Maenhaut, W.: Formation of secondary organic aerosols through photooxidation of isoprene, Science, 303, 1173–1176, 2004.

Cox, A. P., Brittain, A. H., and Finnigan, D. J.: Microwave spectrum, structure, dipole moment and quadrupole coupling constants of cis and trans nitrous acids, T. Faraday Soc., 67, 2179, 1971.

Crounse, J. D., McKinney, K. A., Kwan, A. J., and Wennberg, P. O.: Measurement of gas-phase hydroperoxides by chemical ionization mass spectrometry, Anal. Chem., 78, 6726–6732, doi:10.1021/ac0604235, 2006.

Dibble, T. S.: Isomerization of OH-isoprene adducts and hydroxyalkoxy isoprene radicals, J. Phys. Chem. A, 106, 6643–6650, doi:10.1021/jp025682m, 2002.

Dibble, T. S.: Prompt chemistry of alkenoxy radical products of the double H-atom transfer of alkoxy radicals from isoprene, J. Phys. Chem. A, 108, 2208–2215, doi:10.1021/jp0312161, 2004a.

Dibble, T. S.: Intramolecular hydrogen bonding and double H-atom transfer in peroxy and alkoxy radicals from isoprene, J. Phys. Chem. A, 108, 2199–2207, doi:10.1021/jp0306702, 2004b.

Dibble, T. S.: Cyclization of 1,4-hydroxycarbonyls is not a homogenous gas phase process, Chem. Phys. Lett., 447, 5–9, doi:10.1016/j.cplett.2007.08.088, 2007.

Dillon, T. J., Horowitz, A., Holscher, D., Crowley, J. N., Vereecken, L., and Peeters, J.: Reaction of HO with hydroxyacetone ($HOCH_2C(O)CH_3$): rate coefficients (233-363 K) and mechanism, Phys. Chem. Chem. Phys., 8, 236–246, doi:10.1039/b513056e, 2006.

Duce, R. A., LaRoche, J., Altieri, K., Arrigo, K. R., Baker, A. R., Capone, D. G., Cornell, S., Dentener, F., Galloway, J., Ganeshram, R. S., Geider, R. J., Jickells, T., Kuypers, M. M., Langlois, R., Liss, P. S., Liu, S. M., Middelburg, J. J., Moore, C. M., Nickovic, S., Oschlies, A., Pedersen, T., Prospero, J., Schlitzer, R., Seitzinger, S., Sorensen, L. L., Uematsu, M., Ulloa, O., Voss, M., Ward, B., and Zamora, L.: Impacts of atmospheric anthropogenic nitrogen on the open ocean, Science, 320, 893–897, doi:10.1126/science.1150369, 2008.

Fan, J. and Zhang, R.: Atmospheric Oxidation Mechanism of Isoprene, Environ. Chem., 1, 140–149, doi:10.1071/EN04045, 2004.

Fiore, A. M., Horowitz, L. W., Purves, D. W., Levy, H., Evans, M. J., Wang, Y. X., Li, Q. B., and Yantosca, R. M.: Evaluating the contribution of changes in isoprene emissions to surface ozone trends over the eastern United States, J. Geophys. Res.-Atmos., 110, doi:10.1029/2004JD005485, 2005.

Francisco-Marquez, M., Alvarez-Idaboy, J. R., Galano, A., and Vivier-Bunge, A.: A possible mechanism for furan formation in the tropospheric oxidation of dienes, Environ. Sci. Technol., 39, 8797–8802, doi:10.1021/es0500714, 2005.

Giacopelli, P., Ford, K., Espada, C., and Shepson, P. B.: Comparison of the measured and simulated isoprene nitrate distributions above a forest canopy, J. Geophys. Res.-Atmos., 110, doi:10.1029/2004JD005123, 2005.

Greenwald, E. E., North, S. W., Georgievskii, Y., and Klippenstein, S. J.: A two transition state model for radical-molecule reactions: Applications to isomeric branching in the OH-Isoprene reaction, J. Phys. Chem. A, 111, 5582–5592, doi:10.1021/jp071412y, 2007.

Guenther, A., Karl, T., Harley, P., Wiedinmyer, C., Palmer, P. I., and Geron, C.: Estimates of global terrestrial isoprene emissions using MEGAN (Model of Emissions of Gases and Aerosols from Nature), Atmos. Chem. Phys., 6, 3181–3210, 2006.

Harley, P., Vasconcellos, P., Vierling, L., Pinheiro, C. C. D., Greenberg, J., Guenther, A., Klinger, L., De Almeida, S. S., Neill, D., Baker, T., Phillips, O., and Malhi, Y.: Variation in potential for isoprene emissions among Neotropical forest sites, Glob. Change Biol., 10, 630–650, doi:10.1111/j.1529-8817.2003.00760.x, 2004.

Harley, P. C., Monson, R. K., and Lerdau, M. T.: Ecological and evolutionary aspects of isoprene emission from plants, Oecologia, 118, 109–123, 1999.

Hasson, A. S., Tyndall, G. S., and Orlando, J. J.: A product yield study of the reaction of HO_2 radicals with ethyl peroxy ($C_2H_5O_2$), acetyl peroxy ($CH_3C(O)O_2$), and acetonyl peroxy ($CH_3C(O)CH_2O_2$) radicals, J. Phys. Chem. A, 108, 5979–5989, doi:10.1021/jp048873t, 2004.

Henze, D. K. and Seinfeld, J. H.: Global secondary organic aerosol from isoprene oxidation, Geophys. Res. Lett., 33, doi:10.1029/2006GL025976, 2006.

Hermans, I., Muller, J. F., Nguyen, T. L., Jacobs, P. A., and Peeters, J.: Kinetics of alpha-hydroxy-alkylperoxyl radicals in oxidation processes. HO_2-initiated oxidation of ketones/aldehydes near the tropopause, J. Phys. Chem. A, 109, 4303–4311, doi:10.1021/jp044080v, 2005.

Horowitz, L. W., Liang, J. Y., Gardner, G. M., and Jacob, D. J.: Export of reactive nitrogen from North America during summertime: Sensitivity to hydrocarbon chemistry, J. Geophys. Res.-Atmos., 103, 13 451–13 476, 1998.

Horowitz, L. W., Fiore, A. M., Milly, G. P., Cohen, R. C., Perring, A., Wooldridge, P. J., Hess, P. G., Emmons, L. K., and Lamarque, J.-F.: Observational constraints on the chemistry of isoprene nitrates over the eastern United States, J. Geophys. Res.-Atmos., 112, doi:10.1029/2006JD007747, 2007.

Huey, L. G., Villalta, P. W., Dunlea, E. J., Hanson, D. R., and Howard, C. J.: Reactions of CF_3O^- with atmospheric trace gases, J. Phys. Chem., 100, 190–194, 1996.

Jacob, D. J. and Wofsy, S. C.: Photochemistry of biogenic emissions of the Amazon forest, J. Geophys. Res.-Atmos., 93, 1477–1486, 1988.

Jenkin, M. E., Hurley, M. D., and Wallington, T. J.: Investigation of the radical product channel of the $CH_3C(O)O_2+HO_2$ reaction in the gas phase, Phys. Chem. Chem. Phys., 9, 3149–3162, doi:10.1039/b702757e, 2007.

Johnson III, R. D.: NIST Computational Chemistry Comparison and Benchmark Database NIST Standard Reference Database Number 101 Release 14, URL `http://srdata.nist.gov/cccbdb`, 2006.

Karl, M., Dorn, H. P., Holland, F., Koppmann, R., Poppe, D., Rupp, L., Schaub, A., and Wahner, A.: Product study of the reaction of OH radicals with isoprene in the atmosphere simulation chamber SAPHIR, J. Atmos. Chem., 55, 167–187, doi:10.1007/s10874-006-9034-x, 2006.

Karunanandan, R., Hoelscher, D., Dillon, T. J., Horowitz, A., Crowley, J. N., Vereecken, L., and Peeters, J.: Reaction of HO with glycolaldehyde, $HOCH_2CHO$: Rate coefficients (240-362 k) and mechanism, J. Phys. Chem. A, 111, 897–908, doi:10.1021/jp0649504, 2007.

Kroll, J. H., Ng, N. L., Murphy, S. M., Flagan, R. C., and Seinfeld, J. H.: Secondary organic aerosol formation from isoprene photooxidation, Environ. Sci. Technol., 40, 1869–1877, doi:10.1021/es0524301, 2006.

Kwok, E. S. C. and Atkinson, R.: Estimation of hydroxyl radical reaction-rate constants for gas-phase organic-compounds using a structure-reactivity relationship - An update, Atmos. Environ., 29, 1685–1695, 1995.

Lei, W. F., Zhang, R. Y., McGivern, W. S., Derecskei-Kovacs, A., and North, S. W.: Theoretical study of isomeric branching in the isoprene-OH reaction: implications to final product yields in isoprene oxidation, Chem. Phys. Lett., 326, 109–114, 2000.

Lei, W. F., Zhang, R. Y., McGivern, W. S., Derecskei-Kovacs, A., and North, S. W.: Theoretical study of OH-O$_2$-isoprene peroxy radicals, J. Phys. Chem. A, 105, 471–477, 2001.

Marstokk, K. M. and Mollendal, H.: Microwave-spectra of isotopic glycolaldehydes, substitution structure, intermolecular hydrogen-bond and dipole moment, J. Mol. Struct., 16, 259–270, 1973.

Maryott, A. A. and Buckley, F.: US National Bureau of Standards Circular No. 537, Tech. rep., National Bureau of Standards, Washington, DC, 1953.

Mereau, R., Rayez, M. T., Rayez, J. C., Caralp, F., and Lesclaux, R.: Theoretical study on the atmospheric fate of carbonyl radicals: kinetics of decomposition reactions, Phys. Chem. Chem. Phys., 3, 4712–4717, 2001.

Neeb, P.: Structure-reactivity based estimation of the rate constants for hydroxyl radical reactions with hydrocarbons, J. Atmos. Chem., 35, 295–315, 2000.

Neeb, P., Sauer, F., Horie, O., and Moortgat, G. K.: Formation of hydroxymethyl hydroperoxide and formic acid in alkene ozonolysis in the presence of water vapour, Atmos. Environ., 31, 1417–1423, 1997.

Ng, N. L., Kwan, A. J., Surratt, J. D., Chan, A. W. H., Chhabra, P. S., Sorooshian, A., Pye, H. O. T., Crounse, J. D., Wennberg, P. O., Flagan, R. C., and Seinfeld, J. H.: Secondary organic aerosol (SOA) formation from reaction of isoprene with nitrate radicals (NO$_3$), Atmos. Chem. Phys., 8, 4117–4140, 2008.

O'Brien, J. M., Czuba, E., Hastie, D. R., Francisco, J. S., and Shepson, P. B.: Determination of the hydroxy nitrate yields from the reaction of C$_2$-C$_6$ alkenes with OH in the presence of NO, J. Phys. Chem. A, 102, 8903–8908, 1998.

Okumura, M. and Sander, S. P.: Gas phase formation of nitric acid and its isomers under urban conditions, Tech. rep., California Enivonmental Protection Agency, Air Resources Board, 2005.

Orlando, J. J. and Tyndall, G. S.: The atmospheric chemistry of the HC(O)CO radical, Int. J. Chem. Kinet., 33, 149–156, 2001.

Orlando, J. J., Tyndall, G. S., Bertman, S. B., Chen, W. C., and Burkholder, J. B.: Rate coefficient for the reaction of OH with $CH_2=C(CH_3)C(O)OONO_2$ (MPAN), Atmos. Environ., 36, 1895–1900, 2002.

Papagni, C., Arey, J., and Atkinson, R.: Rate constants for the gas-phase reactions of OH radicals with a series of unsaturated alcohols, Int. J. Chem. Kinet., 33, 142–147, 2001.

Park, J., Stephens, J. C., Zhang, R. Y., and North, S. W.: Theoretical study of the alkoxy radicals derived from isoprene: pressure- and temperature-dependent decomposition rates, J. Phys. Chem. A, 107, 6408–6414, doi:10.1021/jp0303321, 2003.

Park, J., Jongsma, C. G., Zhang, R. Y., and North, S. W.: OH/OD initiated oxidation of isoprene in the presence of O_2 and NO, J. Phys. Chem. A, 108, 10 688–10 697, doi:10.1021/jp040421t, 2004.

Patchen, A. K., Pennino, M. J., Kiep, A. C., and Elrod, M. J.: Direct kinetics study of the product-forming channels of the reaction of isoprene-derived hydroxyperoxy radicals with NO, Int. J. Chem. Kinet., 39, 353–361, doi:10.1002/kin.20248, 2007.

Paulson, S. E. and Seinfeld, J. H.: Development and evaluation of a photooxidation mechanism for isoprene, J. Geophys. Res.-Atmos., 97, 20 703–20 715, 1992.

Paulson, S. E., Flagan, R. C., and Seinfeld, J. H.: Atmospheric Photooxidation of isoprene. I – the hydroxyl radical and ground-state atomic oxygen reactions, Int. J. Chem. Kinet., 24, 79–101, 1992.

Peeters, J., Vereecken, L., and Fantechi, G.: The detailed mechanism of the OH-initiated atmospheric oxidation of alpha-pinene: a theoretical study, Phys. Chem. Chem. Phys., 3, 5489–5504, 2001.

Peeters, J., Fantechi, G., and Vereecken, L.: A generalized structure-activity relationship for the decomposition of (substituted) alkoxy radicals, J. Atmos. Chem., 48, 59–80, 2004.

Pfister, G. G., Emmons, L. K., Hess, P. G., Lamarque, J. F., Orlando, J. J., Walters, S., Guenther, A., Palmer, P. I., and Lawrence, P. J.: Contribution of isoprene to chemical budgets: A model tracer study with the NCAR CTM MOZART-4, J. Geophys. Res.-Atmos., 113, doi: 10.1029/2007JD008948, 2008.

Roberts, J. M. and Fajer, R. W.: UV absorption cross-sections of organic nitrates of potential atmospheric importance and estimation of atmospheric lifetimes, Environ. Sci. Technol., 23, 945–951, 1989.

Rosenstiel, T. N., Potosnak, M. J., Griffin, K. L., Fall, R., and Monson, R. K.: Increased CO_2 uncouples growth from isoprene emission in an agriforest ecosystem, Nature, 421, 256–259, doi: 10.1038/nature01312, 2003.

Sander, S.: Chemical kinetics and photochemical data for use in atmospheric studies evaluation number 15, 2006.

Sanderson, M. G., Jones, C. D., Collins, W. J., Johnson, C. E., and Derwent, R. G.: Effect of climate change on isoprene emissions and surface ozone levels, Geophys. Res. Lett., 30, doi:10.1029/2003GL017642, 2003.

Saunders, S. M., Jenkin, M. E., Derwent, R. G., and Pilling, M. J.: Protocol for the development of the Master Chemical Mechanism, MCM v3 (Part A): tropospheric degradation of non-aromatic volatile organic compounds, Atmos. Chem. Phys., 3, 161–180, 2003.

Shallcross, D. E. and Monks, P. S.: New Directions: A role for isoprene in biosphere-climate-chemistry feedbacks, Atmos. Environ., 34, 1659–1660, 2000.

Sprengnether, M., Demerjian, K. L., Donahue, N. M., and Anderson, J. G.: Product analysis of the OH oxidation of isoprene and 1,3-butadiene in the presence of NO, J. Geophys. Res.-Atmos., 107, doi:10.1029/2001JD000716, 2002.

Su, T. and Chesnavich, W. J.: Parametrization of the ion-polar molecule collision rate-constant by trajectory calculations, J. Chem. Phys., 76, 5183–5185, 1982.

Surratt, J. D., Murphy, S. M., Kroll, J. H., Ng, a. L. N., Hildebrandt, L., Sorooshian, A., Szmigielski, R., Vermeylen, R., Maenhaut, W., Claeys, M., Flagan, R. C., and Seinfeld, J. H.: Chemical composition of secondary organic aerosol formed from the photooxidation of isoprene, J. Phys. Chem. A, 110, 9665–9690, doi:10.1021/jp061734m, 2006.

Talbot, R. W., Andreae, M. O., Berresheim, H., Jacob, D. J., and Beecher, K. M.: Sources and sinks of formic, acetic, and pyruvic acids over central Amazonia: 2-Wet season, J. Geophys. Res.-Atmos., 95, 16 799–16 811, 1990.

Talbot, R. W., Mosher, B. W., Heikes, B. G., Jacob, D. J., Munger, J. W., Daube, B. C., Keene, W. C., Maben, J. R., and Artz, R. S.: Carboxylic-acids in the rural continental atmosphere over the eastern United States during the Shenandoah cloud and photochemistry experiment, J. Geophys. Res.-Atmos., 100, 9335–9343, 1995.

Tuazon, E. C. and Atkinson, R.: A product study of the gas-phase reaction of isoprene with the OH radical in the presence of NOx, Int. J. Chem. Kinet., 22, 1221–1236, 1990.

van Donkelaar, A., Martin, R. V., Park, R. J., Heald, C. L., Fu, T.-M., Liao, H., and Guenther, A.: Model evidence for a significant source of secondary organic aerosol from isoprene, Atmos. Environ., 41, 1267–1274, doi:10.1016/j.atmosenv.2006.09.051, 2007.

von Kuhlmann, R., Lawrence, M. G., Poschl, U., and Crutzen, P. J.: Sensitivities in global scale modeling of isoprene, Atmos. Chem. Phys., 4, 1–17, 2004.

Wall, K. J., Schiller, C. L., and Harris, G. W.: Measurements of the HONO photodissociation constant, J. Atmos. Chem., 55, 31–54, doi:10.1007/s10874-006-9021-2, 2006.

Walser, M. L., Park, J., Gomez, A. L., Russell, A. R., and Nizkorodov, S. A.: Photochemical aging of secondary organic aerosol particles generated from the oxidation of d-limonene, J. Phys. Chem. A, 111, 1907–1913, doi:10.1021/jp066293l, 2007.

Wavefunction: Spartan '06, 2006.

Wiedinmyer, C., Tie, X., Guenther, A., Neilson, R., and Granier, C.: Future changes in biogenic isoprene emissions: How might they affect regional and global atmospheric chemistry?, Earth Interactions, 10, international Young Scientists Global Change Conference 2003, Trieste, Italy, Nov 16-19, 2003, 2006.

Chapter 7

Unexpected epoxide formation in the gas-phase photooxidation of isoprene*

7.1   Abstract

Emissions of non-methane hydrocarbon compounds to the atmosphere from the biosphere exceed those from anthropogenic activity. Isoprene, a five-carbon diene, contributes more than 40% of these emissions. Once emitted to the atmosphere, isoprene is rapidly oxidized by the hydroxyl radical OH. We report here that under pristine conditions isoprene is oxidized primarily to hydroxyhydroperoxides. Further oxidation of these hydroxyhydroperoxides by OH leads efficiently to the formation of dihydroxyepoxides and OH reformation. Global simulations show an enormous flux – nearly 100 teragrams of carbon per year – of these epoxides to the atmosphere. The discovery of these highly soluble epoxides provides a missing link tying the gas-phase degradation of isoprene to the observed formation of organic aerosols.

7.2   Introduction

Isoprene is the largest source of non-methane hydrocarbons to the atmosphere ($\sim$500 Tg C/year) (Guenther et al., 2006). It is produced by deciduous plants (Harley et al., 1999) and plays a critical role in tropospheric chemistry over large regions of the globe (Fuentes et al., 2000). In many forested regions, isoprene oxidation by OH occurs far from combustion of biomass and fossil fuel, so nitric oxide (NO) concentrations are very low. Many of the details of the chemical oxidation mechanism under these conditions remain to be elucidated, hindering assessment of the consequences of changes in isoprene emissions from land use and climate variation (Guenther et al., 2006; Rosenstiel et al., 2003; Wiedinmyer et al., 2006; von Kuhlmann et al., 2004) or changes in NO emissions. In addition to the uncertainty in the gas-phase chemistry, there is no agreement on the mechanism involved in the formation of secondary organic aerosol (SOA) from isoprene oxidation (Claeys et al., 2004).

Where NO is low, isoprene photooxidation is expected to yield the hydroxyhydroperoxides, ISOPOOH = β-ISOPOOH + δ-ISOPOOH (Scheme 7.1, A and B) (Crutzen et al., 2000; Reeves and Penkett, 2003). These series of reactions are expected to strongly depress the concentrations of OH and HO_2 (together known as HO_x) in regions with high isoprene emissions. Observed HO_x levels remain, however, almost unchanged over a wide range of isoprene concentrations, inconsistent with the simulated influence of Scheme 7.1, A and B (Thornton et al., 2002; Lelieveld et al., 2008; Ren et al., 2008). Simulations and measurements of HO_x have been partly reconciled with substitution of the speculative Scheme 7.1C, where formation of methacrolein (MACR) and formaldehyde is accompanied by OH formation, thus reducing the impact of isoprene on HO_x levels (Lelieveld et al.,

Scheme 7.1 First step in isoprene + OH under low NO$_x$ conditions.
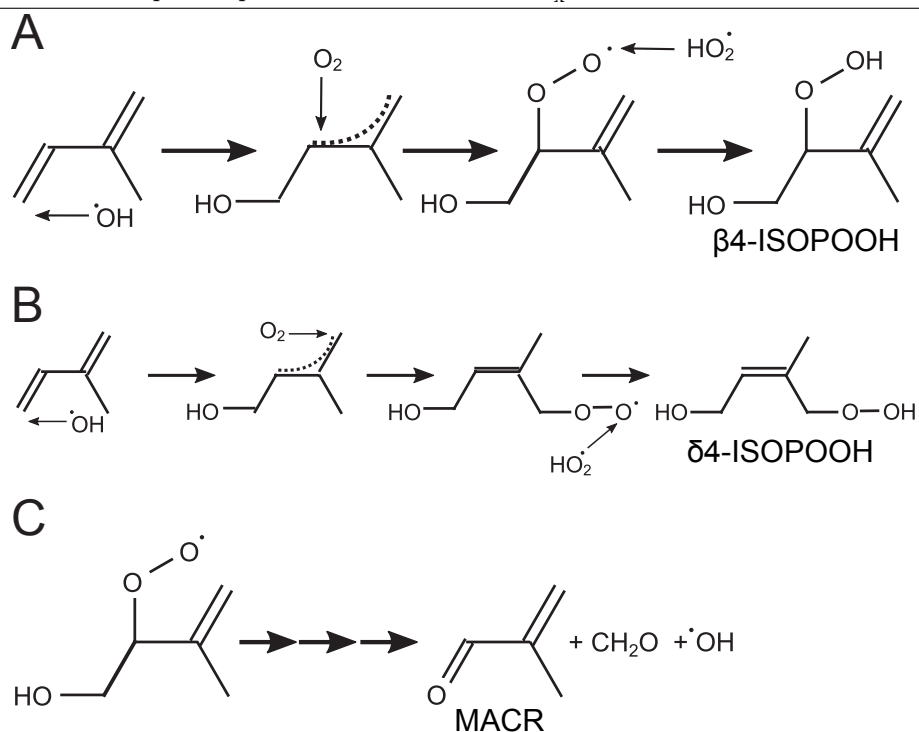
2008).

Analogous to Scheme 7.1, A to C, addition of OH on the other double bond yields similar hydrox-yhydroperoxides (β1- and δ1-ISOPOOH) and methylvinylketone (MVK) (see Supporting Material). Both unimolecular decomposition of the peroxy radical (Peeters et al., 2009) and reaction with HO$_2$ (Dillon and Crowley, 2008) have been proposed in Scheme 7.1C. Although OH reformation (15 to 65%) has been measured for the reactions of HO$_2$ with acylperoxy and β-carbonyl peroxy radicals, low OH yields ($< 6\%$) have been reported from the reactions of HO$_2$ with β-hydroxy peroxy radicals, structurally more similar to isoprene peroxy radicals (Dillon and Crowley, 2008).

We show here that ISOPOOH is formed in large yields ($> 70\%$) via the channels shown in Scheme 7.1, A and B, with concomitant formation of MVK and MACR in much smaller yields ($< 30\%$) via the channel shown in Scheme 7.1C. The branching through Scheme 7.1C yields OH, although substantially less than required to close the HO$_x$ budget (Lelieveld et al., 2008).

We show below that the oxidation of ISOPOOH by OH produces dihydroxyepoxides (IEPOX = β-IEPOX + δ-IEPOX). This HO$_x$ neutral mechanism produces IEPOX with yields exceeding 75% (Scheme 7.2, A and B). This mechanism is likely specific to isoprene and other polyalkenes. Analogous to liquid phase processes (Bell et al., 1950), it profoundly differs from gas-phase oxidation

Scheme 7.2 Isoprene hydroxyhydroperoxide (ISOPOOH) + OH.
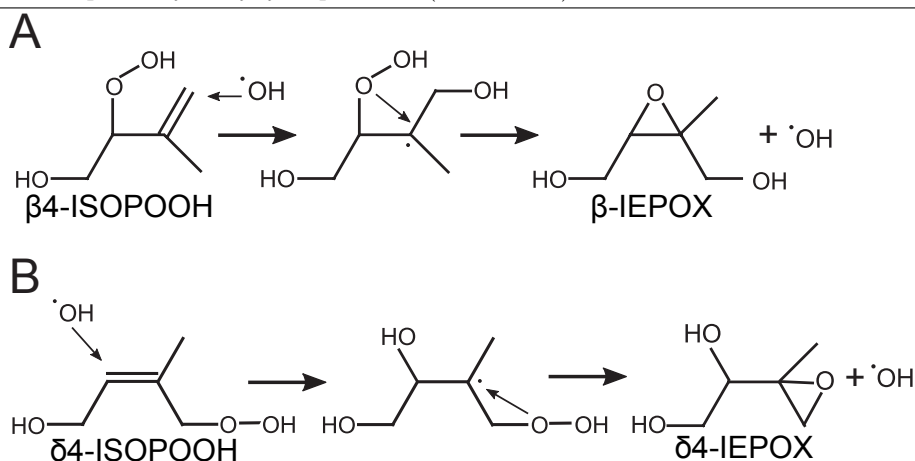
of simple alkenes by OH (e.g., Scheme 7.2, A and B), which would result in the formation of the dihydroxydihydroperoxides. Formation of these compounds is not observed in these experiments.

The gas-phase formation of IEPOX in high yields provides a suitable gas-phase precursor for Secondary Organic Aerosol from isoprene oxidation (iSOA) under low NO_x conditions (Wang et al., 2005; Surratt et al., 2006; Minerath and Elrod, 2009) and may help resolve an outstanding puzzle in atmospheric aerosol chemistry. Although epoxides have previously been speculated as a possible precursor for iSOA (Wang et al., 2005), no mechanism was known to produce them in either the gas or aerosol phase. Consistent with expectation that IEPOX can serve as a precursor to iSOA, we observe rapid and quantitative uptake of 1,4-dihydroxy-2,3-epoxybutane (BEPOX) – a compound structurally similar to IEPOX – on acidic aerosol.

7.3   Experiment and results

We monitor isoprene photooxidation products in the Caltech environmental chamber by chemical ionization mass spectrometry (CIMS) (Crounse et al., 2006), employing a triple-quadrupole mass filter that provides tandem mass spectra (MSMS) (Supporting Material). The reagent anion, CF_3O^-, provides sensitive detection of organic hydroperoxides by formation of ionmolecule clusters (Crounse et al., 2006). Detection of BEPOX by CIMS confirms its sensitivity to dihydroxyepoxides (Supporting Material). In the absence of native standards for many of the compounds described here, the calibration of the instrument was inferred from molecular properties of the analyte (Supporting Material; Paulot et al., 2009b).

Isoprene is oxidized by OH generated through the photolysis of hydrogen peroxide (H_2O_2) in a Teflon bag filled with 800 standard liters of ultrazero air. Known amounts of isoprene and H_2O_2 are introduced into the chamber before ultraviolet (UV) lights are energized. Isoprene is quantified using gas chromatography with flame ionization detection (GC-FID) (Supporting Material).

The products formed through Scheme 7.1, A and B, and Scheme 7.2, A and B–ISOPOOH and IEPOX–are isobaric and measured together by CIMS as the cluster of CF_3O^- with these compounds at the mass to charge ratio (m/z) 203 (Fig. 7.1, red curve). However, distinct daughter ions produced through collision-induced dissociation (CID) of these cluster ions allow for quantification of each compound (McLafferty, 1981). Clusters of CF_3O^- with hydroxyhydroperoxides, produced from the oxidation of simple alkenes, fragment to $m/z = 63$, whereas those with BEPOX exhibit loss of hydrofluoric acid (HF). The daughter $m/z = 63$ of 203 (Fig. 7.1, green curve), associated with the fragmentation of the ISOPOOH cluster clearly precedes the daughter $m/z = 183$ of 203 (Fig. 7.1, blue curve), associated with IEPOX, consistent with the proposed mechanism. Clusters of CF_3O^- with other plausible isomers of IEPOX are not known to exhibit efficient loss of HF (Supporting Material). The sum of the $m/z = 63$ and $m/z = 183$ daughters (Fig. 7.1, black dashed line) properly captures the shape of the parent signal (Fig. 7.1, red curve).

Experiments performed with ^{18}OH produced from the photolysis of $H^{18}O^{18}OH$ provide additional evidence for the conversion of ISOPOOH to IEPOX. With ^{18}OH as the primary oxidant, ISOPOOH and IEPOX are no longer isobaric: The ISOPOOH ion cluster is primarily monitored at $m/z = 205$ (Fig. 7.2, magenta circles) corresponding to the addition of one ^{18}OH on isoprene (Scheme 7.1, A and B), whereas IEPOX is detected at $m/z = 207$ (Fig. 7.2, blue squares) because its formation requires addition of a second ^{18}OH and simultaneous loss of ^{16}OH (Scheme 7.2, A and B) (Fig. 7.2). The coincidence between $m/z = 207$ and IEPOX fingerprint (daughter $m/z = 187$) suggests that $m/z = 207$ is derived almost entirely from the dilabeled IEPOX, consistent with the proposed mechanism.

7.4 Discussion

Quantum chemical calculations confirm that, after the addition of OH, ISOPOOH is connected to IEPOX by energetically favorable adiabatic pathways (Fig. 7.3 and Tables 7.4 and 7.5). β- and δ-IEPOX lie $\sim$50 kcal/mol below their ISOPOOH parent with the transition state connecting the alkyl radical and IEPOX $\sim$20 kcal/mol below the ISOPOOH reactant. The relative energies and structures of the stationary points along the surface are shown in Fig. 7.3 for the β4-ISOPOOH to β-
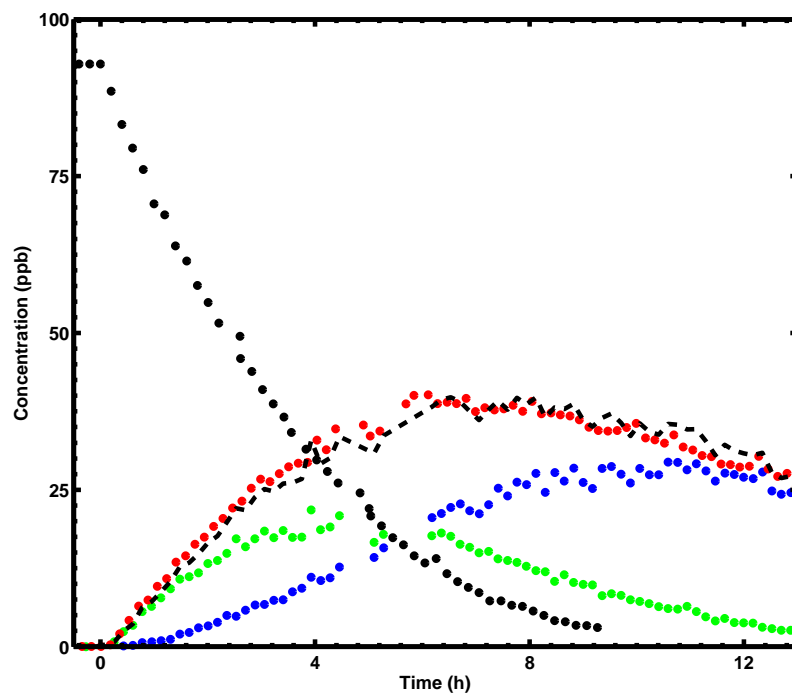
Figure 7.1 – Consecutive formation of ISOPOOH and IEPOX in the photooxidation of isoprene. Following the time when the photolysis of H_2O_2 [initially 1.66 parts per million by volume (ppmv)] begins ($t = 0$), isoprene (black dotted line) decays quickly. ISOPOOH and then IEPOX are detected as major products of the oxidation of isoprene [because they are isobaric, they both are detected at $m/z = 203$ (red), the cluster of these compounds with CF_3O^-]. Tandem mass spectroscopy provides for separation of the $m/z = 203$ signal: ISOPOOH (green) is observed as the $m/z = 63$ daughter, whereas IEPOX (blue) is observed as the $m/z = 183$ daughter. The sum of IEPOX and ISOPOOH is indicated by the dashed black line.
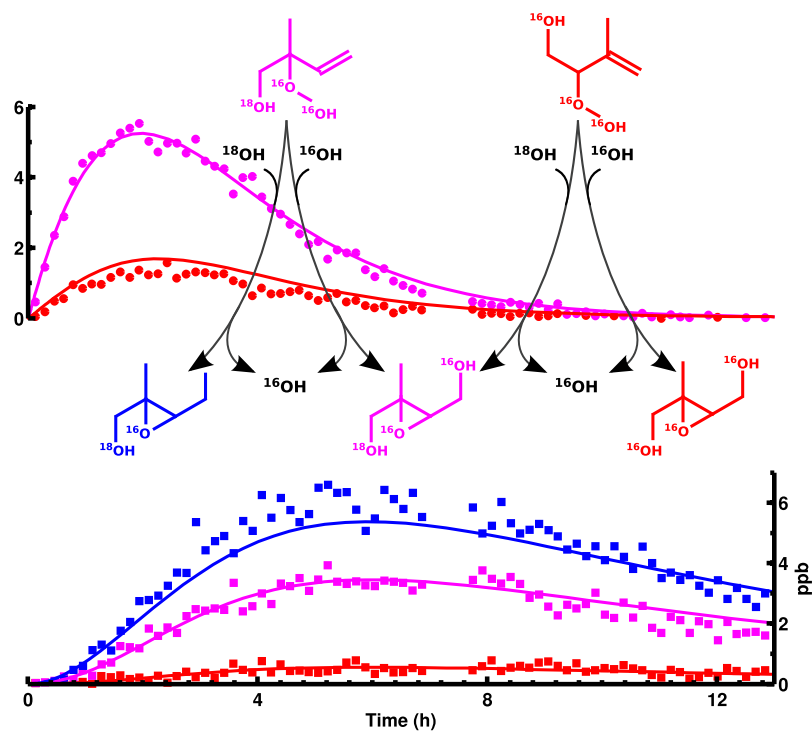
Figure 7.2 – Formation of light and heavy ISOPOOH and IEPOX in the oxidation of isoprene using $H^{18}O^{18}OH$ as the OH source. Formation of ISOPOOH is monitored via the daughter $m/z = 63$ (circles) of $m/z = 203$ (red) and $m/z = 205$ (magenta). Formation of IEPOX is monitored via the loss of HF (squares) from $m/z = 203$, $m/z = 205$, and $m/z = 207$ (blue). Formation of isotopically light ISOPOOH and IEPOX reflects OH reformation. Solid lines represent the modeled mixing ratios for the different isomers. Isoprene initial concentration was 23.5 parts per billion by volume (ppbv), and ^{18}OH was generated from the photolysis of $H^{18}O^{18}OH$ (1.75 ppmv initial concentration, UV lights on at $t = 0$).
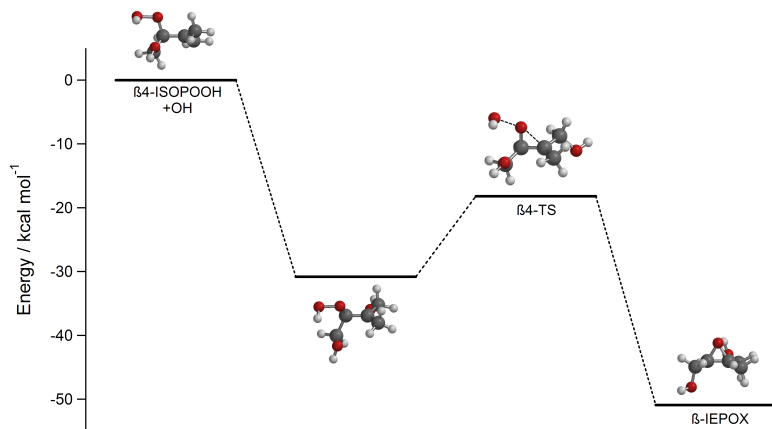
Figure 7.3 – Relative energies for the formation of β-IEPOX from β4-ISOPOOH (Scheme 7.2A). The alkylradical resulting from the addition of OH onto β4-ISOPOOH double bond is formed with enough excess energy ($\sim$30 kcal/mol) that it quickly decomposes to the β-IEPOX + OH via the β4- transition state. Energies are calculated with the CCSD(T)-F12/VDZ-F12 explicitly correlated method at the B3LYP/cc-pVTZ optimized structures (Supporting Material).

IEPOX reaction (Scheme 7.2A). The reaction paths and energetics for the analogous β1-ISOPOOH to β-IEPOX reaction and for the δ4-ISOPOOH to δ4-IEPOX reaction (Scheme7.2B) are similar (Figs. 7.7 and 7.8 and Tables 7.6 and 7.7).

The formation of isotopically-light ISOPOOH ($m/z = 203$) (Fig. 7.2, red circles) and IEPOX ($m/z = 203$ and 205) (Fig. 7.2, red and magenta squares) in the [18]OH-labeled experiment provides additional evidence for Scheme 7.2, A and B, because [16]OH is released through formation of IEPOX (Scheme 7.2, A and B). The [16]OH quickly reacts with isoprene and ISOPOOH, forming the observed isotopically-light compounds. The formation of light ISOPOOH ($m/z = 203$) in the first hour of the experiment cannot, however, be accounted for by Scheme 7.2, A and B, alone, suggesting a small but rapid [16]OH formation from Scheme 7.1C. This is consistent with the coincident production of MVK and MACR, measured together by proton transfer mass spectrometry at $m/z = 89$. Very little methyl-butenediol ($<2\%$) is observed, which suggests that cross-peroxy radical reactions (Ruppert and Becker, 2000) are unlikely to account for the formation of MVK and MACR. A prompt signal at $m/z = 201$ appears consistent with the recently hypothesized formation of (2Z)-hydroperoxymethylbutenol by a 1,6-H-shift. However, its yield ($<10\%$ of ISOPOOH) is much less than predicted theoretically (Peeters et al., 2009).

Using a kinetic model constrained by the observed yields of MVK/MACR and the ratios between light and heavy isotopes of ISOPOOH, we estimate that 12$\pm$12% of the isoprene peroxy radicals react with HO$_2$ to recycle OH by Scheme 7.1C. This estimate accounts for a small initial amount

of NO_x present initially in the chamber (Supporting Material). The balance of the isoprene peroxy radicals reacts with HO_2 to form ISOPOOH.

The lifetime of ISOPOOH with respect to OH (3 to 5 hours) is considerably shorter than IEPOX (18 to 22 hours) (calculated for [OH] = 10^6 radicals cm^{-3}). The formation of unlabeled hydroxyacetone as well as singly-labeled hydroxyacetone and glycolaldehyde in the photooxidation of isoprene by ^{18}OH suggests that the degradation of IEPOX by OH occurs primarily through hydrogen abstraction a to the alcohol (Supporting information).

In addition to the gas-phase oxidation, dihydroxyepoxides are lost to aerosol surfaces through reactive uptake. We monitor by CID-CIMS rapid and nearly quantitative uptake of BEPOX onto acidic aerosol seeds ($MgSO_4/H_2SO_4$). The resulting SOA composition can be readily related to the one identified for iSOA in pristine environments. In particular, analogs of dihydroxyenols, 2-methyltetrols, alkene-triols, and associated sulfate esters are detected (Supporting information), which suggests that IEPOX may explain their formation in both field (Claeys et al., 2004; Surratt et al., 2008) and chamber studies (Wang et al., 2005; Surratt et al., 2006). Epoxides are also known to polymerize easily, an essential process for SOA growth (Gao et al., 2004).

The atmospheric yield of IEPOX is directly related to the relative importance of the reactions of isoprene peroxy radicals with HO_2 and NO. Using the chemical transport model GEOS-CHEM (Bey et al., 2001) with an updated chemical mechanism (Table 7.9) (Paulot et al., 2009b), we find that globally about one-third of isoprene peroxy radicals undergo reaction with HO_2, with the remaining fraction reacting with NO. Over the Amazon, this ratio is almost inverted (Fig. 7.11). Including uncertainties in isoprene emissions, we estimate that 95±45 Tg C/year of IEPOX, a previously unknown class of compounds, are formed each year in the atmosphere. The largest concentrations of IEPOX are localized over the southern tropics, with substantial levels predicted over Canada and the Southeast United States during Northern Hemisphere summer (Fig. 7.4). The presence of high concentrations of ISOPOOH and IEPOX in the atmosphere are consistent with recent aircraft-borne observations of isoprene oxidation products (m/z = 203) over southeast Columbia [NASA Tropical Composition, Cloud, and Climate Coupling (TC4) campaign] and (m/z = 203 and its daughters) over Alberta and California [NASA Artic Research of the Composition of the Troposphere from Aircraft and Satellites (ARCTAS) campaign]. Preliminary study of the data collected in the boundary layer is consistent with the concentrations of these compounds calculated with GEOSCHEM (Fig. 7.12).

The variability in the yield and fate of IEPOX is expected to translate into highly variable iSOA yields. In particular, anthropogenic activities depress for IEPOX formation as IEPOX yield drops
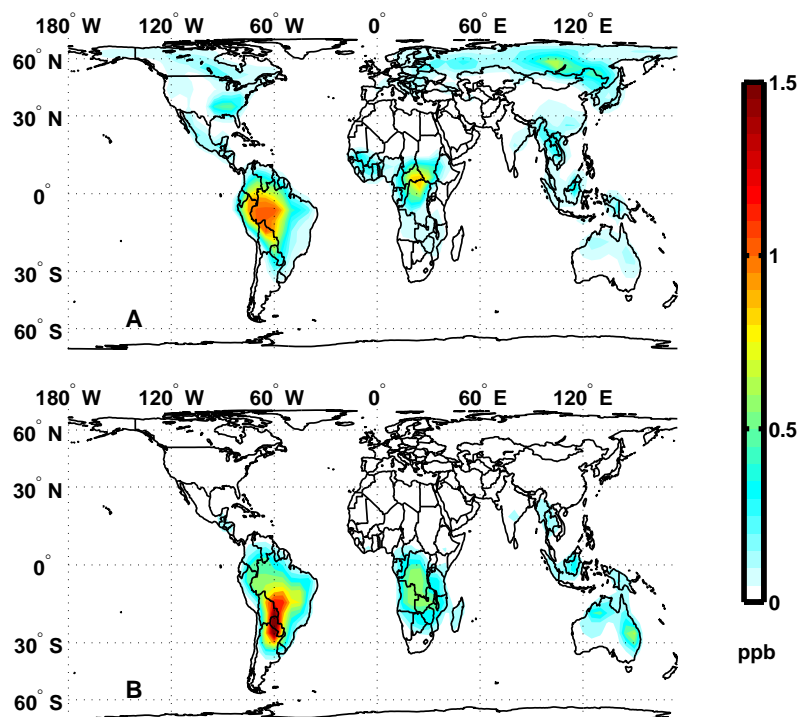
Figure 7.4 – Simulated daily distribution of IEPOX in the planetary boundary layer during the Northern Hemisphere summer (A) and winter (B). IEPOX seasonal cycle mirrors the isoprene emissions. The mixing ratio of IEPOX is higher in the tropics than in other isoprene production regions in the northern mid-latitudes (e.g., the southeast United States). This reflects the reduction in the yield of IEPOX from isoprene due to anthropogenic emissions of NO.

rapidly with increasing NO. Anthropogenic emissions, however, may enhance the iSOA yield from IEPOX because its uptake on surfaces is likely dependent on the aerosol pH and sulfur content (Minerath and Elrod, 2009; Surratt et al., 2007). This may explain part of the variability of the reported SOA biogenic yields, ranging from negligible (de Gouw et al., 2005) to potentially dramatic (Tunved et al., 2006). Given the enormous flux of IEPOX, the chemistry presented here may also resolve part of the intriguing discrepancy between bottom-up (10 to 70 Tg/year) and top-down (140 to 910 Tg/year) estimates of global SOA production (Goldstein and Galbally, 2007). Nevertheless, IEPOX is expected to undergo hundreds of collisions with aerosol surfaces before reacting with OH, and its detection in the atmosphere (Fig. 7.8) suggests that a complex suite of conditions likely controls its uptake to aerosols (e.g., the pH and chemical composition of aerosol). Furthermore, iSOA formation may depend on the unquantified differences in the yields and uptake characteristics of the β- and δ-IEPOX. Quantitative understanding of these complex interactions is required to assess the effect of this chemistry on the overall SOA abundance and its associated impacts [e.g., cloud condensation nuclei (Kerminen et al., 2005)].

7.5   Conclusions

The efficient formation of dihydroxyepoxides, a previously unknown class of gas-phase compounds, addresses many of the issues currently being debated about isoprene chemistry. Because their formation is accompanied by the reformation of OH, this chemistry contributes to the remarkable stability of HO_x in remote regions of the troposphere subjected to high isoprene emissions. The formation of IEPOX also provides a gas-phase precursor for the iSOA formation. Further investigation of the multiphase chemistry of IEPOX is needed to elucidate the complex interaction between emissions from the biosphere and atmospheric composition (Went, 1960; Andreae and Crutzen, 1997). In particular, the development of a proper chemical description of these interactions is essential for assessing the sensitivity of this chemistry to changes in isoprene emissions caused by environmental changes (e.g., climate change and deforestation) and to the further development of anthropogenic activities and the accompanying NO_x emissions in these regions.

7.6 Supporting information

7.6.1 Chemical ionization mass spectrometer (CIMS)

7.6.1.1 Overview

The Caltech Chemical Ionization Mass Spectrometer (CIMS) was originally designed for aircraft missions as a robust and lightweight instrument capable of detecting trace amounts of atmospherically-relevant substances with high selectivity and sensitivity. The reagent ion used in negative ion mode, CF_3O^-, reacts with a suite of peroxides and various other compounds, e.g., SO_2, HNO_3 and organic acids (Huey et al., 1996; Amelynck et al., 2000a; Crounse et al., 2006; Amelynck et al., 2000b).

There exist two versions of the flight instrument: 1) The original version that utilizes a single quadrupole mass filter as a mass spectrometerCrounse et al. (2006) and 2) a more recently developed instrument with the same ionization scheme but utilizing a commercial triple quadrupole mass spectrometer, thereby allowing for the differentiation of certain mass analogues using tandem MSMS. This latter instrument has been largely replicated for laboratory experiments at the Caltech environmental chamber. Additionally, this new instrument can be operated in positive ion mode similar to a classical proton transfer mass spectrometry (PTR-MS) instrument (Hansel et al., 1995). The instrument configuration allows for rapid switching between negative and positive ion chemistry. A brief general description of the CIMS follows here with a focus on the MSMS and PTR-MS capabilities, which are key features for the identification of IEPOX formation during isoprene photooxidation, and which have not been described in detail before.

The Caltech CIMS consists of a commercial triple quadrupole mass spectrometer (Varian 300-MS GC/MS, Varian, Inc.) and a custom ion source with a specially designed sample gas inlet system (Fig. 7.5). During an experiment the sample air is pulled (1 slm) from the chamber through a Teflon line to the instrument. Twenty percent of this sample flow is transferred to the CIMS instrument. The flow rate is controlled by a critical orifice made of glass that connects the sampling line with a 2.54 cm outer diameter glass flow tube coated with a thin layer of Teflon (Fluoropel 801A, Cytonix Corp.). The flow tube is operated at a constant pressure of 35 hPa. The sample flow entering the flow tube is diluted with nitrogen (ultra-high purity, 99.999 %) at a mixing ratio of 1:8.2. The exact value of the dilution flow is adjusted such that the pressure inside the flow tube is held constant at 35 hPa. With the exception of the sample flow, all gas flows are controlled by metal sealed mass flow controllers (SEC-4400, Horiba Stec) to minimize contamination.

The main modification to the Varian triple quadrupole mass spectrometer consists of the removal
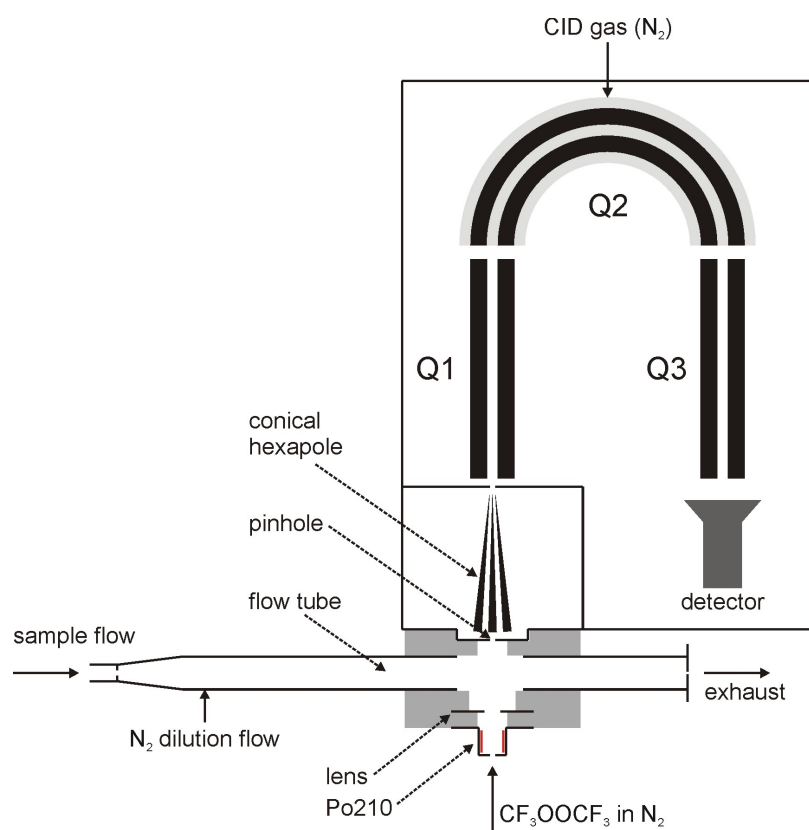
Figure 7.5 – Schematic diagram of the Caltech Chemical Ionization Mass Spectrometer (CIMS).

of the originally installed electron impact ionization source thereby making room for a conically-shaped hexapole ion guide that efficiently transfers ions from the flow tube to the first quadrupole (Q1). The section where the hexapole is mounted is differentially pumped and only connected to the flow tube and the high-vacuum chamber by small openings.

The three linear quadrupole mass filters (Q1, Q2, and Q3) can be used in different configurations allowing either the acquisition of single mass spectra (MS) or tandem mass spectra (MSMS). In the MSMS mode, a buffer gas, nitrogen, is added to the second quadrupole (Q2), which is partially enclosed. In Q2, the presence of several Pa of N_2 results in collision induced dissociation (CID) of the ions selected in Q1. The fragments (or daughter ions) produced in Q2 are filtered by m/z in Q3 before being detected with an electron multiplier operated simultaneously in both analog and ion-counting mode. For the experiments shown here, the following modes were used: (a) Single MS (SMS) – Operating Q1 as a mass filter to select a single m/z value at a time while operating Q2 (evacuated) and Q3 in RF-only mode such that virtually all ions selected by Q1 reach the detector. In this manner, a mass spectrum can be obtained if all m/z values of interest are scanned (b) MSMS – Operate Q1 as a mass filter to select a single m/z value for the parent ion. The pressure in the region of Q2 is increased to several Pa inducing the fragmentation of the selected ion. Fragment ions are then selected by Q3 and reach the detector. Mode (a) was conducted for both anions and cations, while mode (b) was conducted for anions only. For the experiments reported in this study, the following sequence was repeated throughout the experiments 1) negative ion SMS, 2) positive ion SMS, and 3) negative ion MSMS, with the total cycle duration being approximately 10 minutes.

7.6.1.2 Negative ion mode

In negative ion mode, 400 sccm of 10 ppmv CF_3OOCF_3 in N_2 passes through the ion source, which contains a radioactive material (^{210}Po foil, NRD, Inc.). The foil containing the ^{210}Po is housed in a stainless steel holder and emits α-particles that by ionizing nitrogen molecules lead to the release of electrons. The electrons are captured by CF_3OOCF_3, generating the reagent anion, CF_3O^-. Potentials of -240 V and -220 V (relative to the pinhole and the instrument housing, which are held at ground potential) are applied to the stainless steel ^{210}Po holder and -220 V to the lens, respectively, such that only negative ions are transmitted across the flow tube in a transverse direction to the diluted sample flow. Product ions are formed through reactions of neutral analyte molecules with reagent ions as they move across the flow tube. The anions (reagent and product ions) are then pushed towards the pinhole and enter the chamber containing the conical hexapole.

The ion-molecule reactions (with a trace compound R) that can occur are: proton transfer (R7.1), fluoride transfer (R7.2) or clustering with a CF_3O^- ion (R7.3) (Crounse et al., 2006; Paulot et al., 2009b).

$$R + CF_3O^- \rightarrow R^- + CF_3OH \tag{R7.1}$$

$$R + CF_3O^- \rightarrow R^-\cdot HF + CF_2O \tag{R7.2}$$

$$R + CF_3O^- \rightarrow R\cdot CF_3O^- + CF_2O \tag{R7.3}$$

When operating the instrument in negative SMS mode, anions were scanned sequentially for 0.5 seconds from m/z=50 to m/z=275. The acquisition of a full mass spectrum thus requires $\sim$2 min. The m/z of the reagent anion and its major clusters with water and hydrogen peroxide (m/z=85 (CF_3O^-), m/z=103 ($CF_3O^-\cdot H_2O$) and m/z=119 ($CF_3O^-\cdot H_2O_2$)) are omitted from the scans due to their high intensities; these anions are quantified at m/z +1 – mostly from the ^{13}C isotopologues.

7.6.1.3 Positive ion mode

In positive ion mode, 400 sccm of N_2 (without CF_3OOCF_3) is passed through the ion source. Residual H_2O in the gas stream reacts with N_2^+ ions (generated from the collisions of the α particles with the bath gas) to form $H^+\cdot(H_2O)_n$ reagent ions in the ion source. The positively charged ions are directed out of the source and across the flow tube by inverting the polarity of the potentials on the ion source and the lens from those used in negative ion mode. The most abundant positive ions detected by the spectrometer correspond to n $= 3, 4$. The pressure ($\sim$3$\times$10^{-3} hPa) inside the conical hexapole limits the transmission of ions with $m/z < 50$, so that the $n = 1$ and 2 water clusters cannot be detected.

The ion-molecule reactions that occur in positive ion mode are:

$$R + H^+\cdot(H_2O)_n \rightarrow R\cdot H^+(H_2O)_x + (n{-}x)H_2O \tag{R7.4}$$
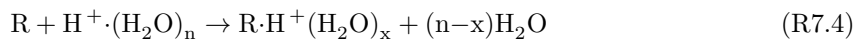
where, x$\leq$n, and generally equals 0, 1, or 2.

When operating the instrument in positive SMS mode, ions are scanned sequentially for 0.5 seconds from m/z=30 to m/z=235. The full mass spectrum requires approximately 1 min and 40 s. Ions with m/z=55 ($H^+\cdot(H_2O)_3$), m/z=73 ($H^+\cdot(H_2O)_4$) are omitted due to their high intensities.

7.6.1.4   Negative ion MSMS mode

The ion generation for the negative ion MSMS mode is identical to the negative ion SMS mode. The main difference of MSMS mode as compared to the SMS mode is the addition of a small flow of N_2 into the Q2 quadrupole such that the pressure inside Q2 reaches approximately 2.5×10^{-3} hPa. To increase the signal to noise ratio in MSMS mode, the resolution of Q3 is set to a full-width-half-maximum of approximately 1.5 amu. While this does give fairly broad peaks, the chance of distinct fragment ions (excluding isotopic pairs, e.g. ^{12}C and ^{13}C) occurring at adjacent masses (and thus being indistinguishable at this resolution) is small.

In many cases, the formation of the daughter ions induced by collisions of the parent ion (e.g., $R \cdot CF_3 O^-$) with the bath gas (M) can be explained through the following CID channels:

$R \cdot CF_3 O^-$ parent ions:

$$R \cdot CF_3 O^- + M \rightarrow CF_3 O^- + R + M \tag{R7.5}$$

$$R \cdot CF_3 O^- + M \rightarrow HF \cdot R^- + CF_2 O + M \tag{R7.6}$$

$$R \cdot CF_3 O^- + M \rightarrow R^-_{-H} + CF_2 O + HF + M \tag{R7.7}$$

$$R \cdot CF_3 O^- + M \rightarrow [CF_2 O \cdot R]^- + HF + M \tag{R7.8}$$

$$R \cdot CF_3 O^- + M \rightarrow HF \cdot F^- + HF + CO + R_{-2H} + M \tag{R7.9}$$

$$R \cdot CF_3 O^- + M \rightarrow (HF)_2 \cdot F^- + CO + R_{-2H} + M \tag{R7.10}$$

$$R \cdot CF_3 O^- + M \rightarrow FCO_2^- + 2HF + R_{-2H-O} + M \tag{R7.11}$$

$R^-_{-H} \cdot HF$ parent ions:

$$R^-_{-H} \cdot HF + M \rightarrow R^-_{-H} + HF + M \tag{R7.12}$$
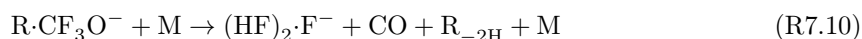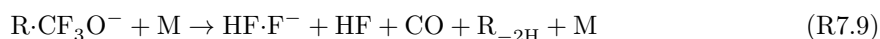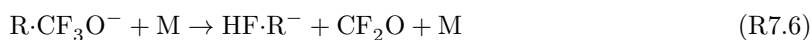
The distribution across the possible CID channels (R7.5–R7.11) for a given parent ion, $R \cdot CF_3 O^-$, vary greatly depending upon the nature of R (acidity, fluoride affinity, dipole moment, etc). This distribution can also be modified by changing the average collision energy in Q2, i.e., changing the kinetic energy (velocity) of the ion upon entering Q2. In this work, the ion energies (velocities) are tuned to be quite low (slow) to prevent CID from occurring in the conical hexapole. As a result, it is not possible to alter the collision energies in Q2 significantly without scattering most of the ions onto undetectable trajectories. For a given parent ion m/z, the collisional energy in Q2 was the same across all experiments, and was adjusted as a function of the parent ion mass in order to

place the parent ion (and latter the fragment ions) on detectable trajectories, namely those moving through Q2.

The MSMS spectrum of a parent ion is useful for determining the nature of the analyte R as well as distinguishing isobaric compounds, which are detected at the same parent m/z. For instance, compounds containing a hydroperoxy group (ROOH) often have a significant yield of the daughter ion at m/z=63 (R7.11), which seems to be a fragment specific to ROOH compounds, probably FCO_2^-. Fingerprints can also be used to distinguish glycolaldehyde from acetic acid. Both compounds are detected at m/z=145 in SMS. In MSMS mode, parent ions arising from acetic acid give daughter ions as m/z=79 (R7.6) with reasonable yield, while parent ions arising from glycolaldehyde do not give any daughter ions at m/z=79. Given calibrated MSMS fragment spectra for acetic acid and glycolaldehyde, one can quantify each compound separately in an unknown mixture.

7.6.2 Experiment

7.6.2.1 Reagents

All chemicals were purchased from Sigma Aldrich. Atmospheric chamber experiments were carried out in an 800 L FEP Teflon bag filled with ultrazero air (Air Liquide). $H^{18}O^{18}OH$ was purchased from ISOTECH as a 2–3% (by mass) solution in H_2O, and a stated purity of 90% ^{18}O by atom for the H_2O_2. The unlabeled H_2O_2 was prepared as a 3% solution (by mass) using 30% H_2O_2 (Fischer) and deionised water (MilliQue). The concentration of the unlabeled 3% H_2O_2 solution was measured by UV-VIS absorption in the liquid phase after standard dilution using published absorbance cross-sections at 240 nm (Sander, 2006). The concentration and purity of the labeled H_2O_2 was determined to be 2.2% $H^{18}O^{18}OH$ (by mass), and 97.2% ^{18}O (by atom) using the CIMS instrument.

7.6.2.2 H_2O_2 introduction

A known mass of H_2O_2 (an aliquot of the $\sim$3% solutions in H_2O) was evaporated into a 15 SLM stream of ultrazero air (controlled by a mass flow controller) as it filled the 800 L bag. For typical concentrations (1–2 ppmv H_2O_2), the evaporation was complete in 15–20 minutes.

7.6.2.3 Isoprene introduction

A known mass of isoprene was evaporated into 100 standard liters of N_2 by flowing N_2 over the isoprene and collecting in a 100 L Teflon bag. An aliquot (typically 120 mL) from the 100 L

Table 7.1 – Initial conditions (in ppb).

Experiment	Isoprene	H^{18}O^{18}OH	H^{18}O^{18}OH	H^{16}O^{16}OH	NO$_x$
Exp 1	70	1700	57.2	3.5	1.3
Exp 2	23.5	1750	58	3.76	.77
Exp 3	20.9	2860	94	5.9	.1

isoprene/N$_2$ mixture was taken using a gas-tight syringe for injection into the 800 L experiment bag. Final isoprene concentration was calculated from the initial mass, and the serial dilution, correcting for the temperature and pressure of the injected aliquot. This procedure was followed prior to each experiment.

7.6.2.4 Bag flushing

Between experiments, the 800 standard liter experiment bag was flushed with dry N$_2$ (taken from liquid N$_2$ boil off). Flushing typically consisted of 4–6 fill and evacuation cycles. After 4 fill/evacuation cycles, all detected compounds are less than 5% of their value at the end of the previous experiment.

7.6.2.5 Photolysis

The 800 L bag was placed on the floor of the Caltech environmental chamber (Cocker et al., 2001) between the existing 28 m^3 bags. All experiments were conducted using 50% of the UV lights corresponding to $J_{\text{H}_2\text{O}_2} = 2.15 \times 10^{-6}\,\text{s}^{-1}$. The ambient temperature was between 290 and 295 K.

7.6.2.6 Initial conditions

Three different experiments were carried out with labeled hydrogen (Table 7.1). The initial concentration of NO$_x$ was determined using the isoprene nitrate cluster signal at m/z=234 and the yields as determined in our earlier work (Paulot et al., 2009b).

7.6.2.7 Sythesis of BEPOX

cis-2,3-epoxy-1,4-butanediol (BEPOX) was synthesized by mixing *cis*-butene-1,4-diol and hydrogen peroxide under basic conditions and in the presence of tungstinic acid in a 50 °C water bath (Skinner et al., 1958). The final product was purified by recrystallization from hexanes.

7.6.2.8 Reactive uptake of BEPOX: Characterization of particle-phase reaction products and their implications for isoprene SOA

Chamber experiments were conducted in order to evaluate the SOA formation potential resulting from the reactive uptake of BEPOX in the presence of acidified sulfate aerosol.

Reactive uptake of BEPOX was monitored via CIMS at m/z=189. Gas-phase BEPOX is largely consumed following addition of the acidic aerosol ($MgSO_4$) to the chamber. The resulting SOA produced from this reaction were collected onto Teflon filters (PALL Life Sciences, 47 mm diameter, 1.0 μm pore size, teflo membrane) for off-line detailed chemical characterization efforts. Tetrols (i.e., erythritol and threitol) were characterized by GC/MS with prior trimethylsilylation (Surratt et al., 2006). Additionally, organosulfates (e.g., C_4-trihydroxy sulfates) of BEPOX were characterized by ultra performance liquid chromatography (UPLC) interfaced to an electrospray ionization (ESI) time-of-flight mass spectrometer (TOFMS) operated in the negative ion mode. Details of the Teflon filter extractions and subsequent UPLC/ESI-TOFMS analysis can be found elsewhere (Surratt et al., 2008).

The tetrols and organosulfates produced from the reactive uptake of BEPOX are analogues of the previously characterized 2-methyltetrols and organosulfates of isoprene, consistent with the hypothesis that the reactive uptake of IEPOX is likely responsible for some of the observed enhancements of isoprene SOA under low-NO_x and acidic conditions (Surratt et al., 2007).

BEPOX is stable in the Teflon bag suggesting that under the experimental conditions described here, wall losses are negligible. Nevertheless, experiments carried out under humid conditions or with acidified walls show immediate uptake of IEPOX to the walls. This may explain why this compound has been difficult to detect.

7.6.2.9 Calibrations

As detailed in a recent study, the calibration of the CIMS instrument for a specific compound can be estimated from the collision rate constant of the reagent ion (in this case CF_3O^-) with the analyte species (Paulot et al., 2009b). The thermal collision rate constant can be estimated from the dipole and polarizability of the analyte species using the parameterization of Su and Chesnavich (1982). The average dipole moment and polarizability were calculated with the B3LYP/6-31G(d) density functional method for the compounds of interest (Table 7.2) (Wavefunction, 2006; Garden et al., 2009). Theoretical calibrations show good agreement between the ratio of the calibration obtained for BEPOX, glycolaldehyde and hydroxyacetone (Table 7.3).

Table 7.2 – Theoretical weighted average dipole moments (μ) and polarizabilites (α) for conformers with abundance greater than 1%. *Cis* and *trans* refer to the position of the CH_2OH group with respect to the plane of the oxirane.

Compound	μ (D)	$\alpha(\text{Å}^3)$
β-IEPOX (*cis*)	2.47	8.98
β-IEPOX (*trans*)	1.00	9.01
δ1-IEPOX	2.39	9.98
δ4-IEPOX	2.30	8.93
β1-ISOPOOH	2.19	9.44
β4-ISOPOOH	2.20	9.44
δ1-ISOPOOH	2.85	9.63
δ4-ISOPOOH	3.34	9.66
BEPOX (cis)	2.71	7.52
BEPOX (trans)	0.55	7.47
(2Z)-but-2-ene-1,4-diol	2.93	7.28
but-3-ene-1,2-diol	2.29	7.21
2-methylbut-3-ene-1,2-diol	2.01	8.79
3-methylbut-3-ene-1,2-diol	2.30	8.76
(2Z)-2-methylbut-2-ene-1,4-diol	2.98	8.98

Table 7.3 – Comparison of the experimental and theoretical calibration for three representative compounds.

Compound	Theoretical calibration (normalized counts/pptv)	Experimental calibration (normalized counts/pptv)
BEPOX (*cis*)	2.0×10^{-4}	2.0×10^{-4}
Hydroxyacetone	2.7×10^{-4}	2.6×10^{-4}
Glycolaldehyde	2.2×10^{-4}	2.3×10^{-4}

Cis and *trans* conformers of β-IEPOX exhibit very different dipole moments. The CIMS is predicted to be $\sim$37% more sensitive to the *cis* than to the *trans* conformer. The conformation of IEPOX depends on the both the conformation of the ISOPOOH peroxy radical before OH adds and on the rotation about the carbon bond prior to the oxirane formation. Theoretical calculations show that the *cis* conformation of the carbon radical is largely favored over the *trans* conformation. Nevertheless, given the excess energy of the carbon radical, it is unclear that the radical will be sufficiently long-lived to reach an equilibrium structure before it decomposes to IEPOX. In other words the relative rate of formation of the conformers depends on the formation timescale of IEPOX versus the time scale of bond rotation. These experiments provide some constraints. It is non-physical for all the IEPOX to be *trans* as it would result in a yield exceeding 100%. In this study, we assume that IEPOX was entirely in its *cis* conformation. A racemic mixture would increase the yield by about 20%, well within the calibration uncertainty.

Experiments using isotopically-labeled OH are used to derive a calibration for the CID fragments of IEPOX and ISOPOOH. In particular the signal at $m/z=207$ can be associated with the dilabeled epoxide. We derive a ratio for the daughter $m/z=187$ to parent $m/z=207$ of 11.3. Using this ratio, the contribution of the epoxide from the parent $m/z=205$ signal can be removed. The resulting signal corresponds to the peroxide contribution:

$m/z(205)_{\text{CORRECTED}} = m/z(205) - 11.3 \times m/z(205 \rightarrow 185)$. The ratio of m/z $(205)_{\text{CORRECTED}}$ to $m/z(205 \rightarrow 63)$, the characteristic daughter of the peroxide, is then found to be 6.9. With these derived relationships between the characteristic daughters and the parent signals, the calibration for the parent signals previously derived from the dipole moments and polarizabilities can be used to infer the calibration factors for the characteristic daughter ion signals.

MVK and MACR are monitored together in positive ion mode at $m/z=89$ (via R7.4 with n=1). We calibrate for both compounds using native standards (Sigma Aldrich).

7.6.3 CID-Signature of the IEPOX and ISOPOOH

7.6.3.1 Negative mode

The combined use of CIMS and CID is new and therefore no published database is available against which the observed fragments can be compared. Instead, we build such a database using synthesis of these or related compounds. Although there are many daughters of m/z=203, the signal at all daughters can be described as a linear combination of two daughters nearly unique to the first and second generation products – m/z=63 and m/z=183 respectively. ISOPOOH makes only a minor contribution to m/z=183: $m/z(183)_{\text{ISOPOOH}} \sim 5\%$ of m/z=63.

The identification of ISOPOOH is supported by the daughter m/z=63. Using photooxidation of 3-methylbutene and 2-methylbutene in a fashion similar to that described in the isoprene study, we "synthesized" in the gas phase related β-hydroxyhydroperoxides. Each gives rise to a m/z=63 daughter analogous to ISOPOOH. This daughter is not seen in either hydroxyaldehydes or polyols.

As illustrated in Fig. 7.2 and similar to isoprene, the photooxidation of butadiene gives rise to the successive formation of hydroperoxides (loss of negative fragment 63 amu through R7.11) similar to ISOPOOH and epoxides similar to BEPOX (loss of neutral fragment 20 amu R7.6), consistent with our approach.

7.6.3.2 Positive mode

While the CF_3O^- based CIMS technique remains rare (Huey et al., 1996; Amelynck et al., 2000a; Crounse et al., 2006; Amelynck et al., 2000b), PTR-MS instruments are commonly used in chamber and field experiments, motivating the search for a potential fingerprint of IEPOX and ISOPOOH in positive mode.

As previously suggested (Crutzen et al., 2000; Williams et al., 2001; Warneke et al., 2001), ISOPOOH is detectable at m/z=101 (addition of H^+ followed by loss of water). Nevertheless, we find significant contamination of IEPOX at this mass, which may have affected previous measurements. Conversely, m/z=119 appears to be mostly representative of IEPOX. Concomitant measurements of both m/z=119 and m/z=101 should provide another proxy to measure the partitioning between IEPOX and ISOPOOH in field missions. We note, however, that this separation may not be possible with PTR-MS systems, which utilize an energetic ion de-clustering stage, as this may push product ions from both compounds to m/z=101. In any case, PTR-MS does not enable differentiation between IEPOX and ISOPOOH as clearly as negative ion CID MSMS.
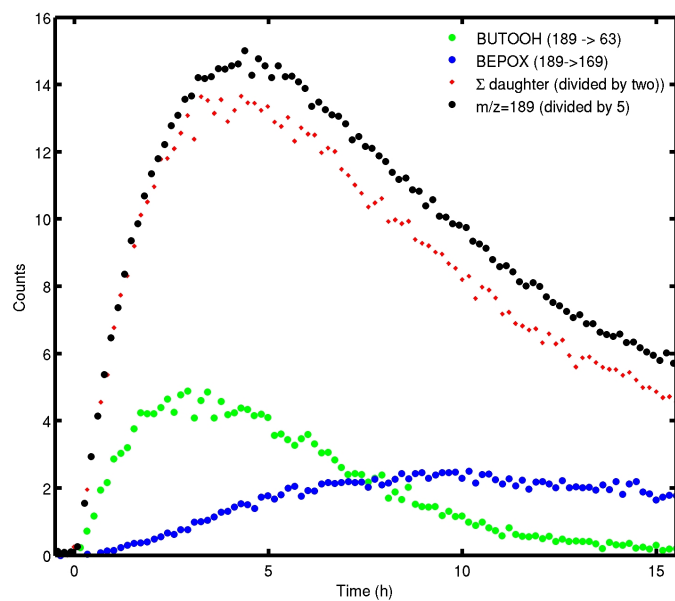
Figure 7.6 – Following the time when the photolysis of H_2O_2 (initially 1 ppmv) begins ($t = 0$), we observe the formation of BUTOOH and then BEPOX together detected at m/z=189 (black). Tandem mass spectroscopy provides for separation of the m/z=189 signal: BUTOOH (green) is observed as the m/z=63 daughter while BEPOX (blue) is observed as the m/z=169 daughter. The sum of the measurable daughters of m/z=189 (red) correctly captures the profile of the parent signal.

7.6.4 Theoretical method: Formation of β and δ-IEPOX

All stationary points in Scheme 7.2A and B and the analog β1-ISOPOOH reaction have been optimized with the B3LYP/6-31G(d) method. The transition state (TS) between the alkyl radical and the epoxide has a single imaginary frequency at 729 cm^{-1}, 689 cm^{-1} and 676 cm^{-1} for the β1-TS, β4-TS, and δ4-TS, respectively (Wavefunction, 2008). As expected, the imaginary mode is a vibration along the O-O bond. Intrinsic Reaction Coordinate (IRC) calculations were done in both the forward and backward direction (Frisch et al., 2004). We let the IRC calculation run 20 steps (each 0.01 a.u. along the reaction path) in each direction, which was sufficient to connect the TS to the optimized structures. For example, for the β1-channel, the 20 steps in backward reaction led to a structure very close to the optimized alkyl radical. The O-O distance in the final IRC step is only 0.02 Å longer than the O-O distance in the optimized structure. The final structure in the forward direction has the OH group loosely attached and the oxirane is not completely formed. The COC angle is 58° in the last step and is 62° in the optimized β-IEPOX. The CO distance is 1.62 Å whereas it is 1.44 Å in β-IEPOX. We also located a product complex with the OH radical hydrogen bound to the epoxide oxygen atom. With the amount of excess energy available this complex is unlikely to form and is of little importance for the reaction. Similar results are obtained for the β4- and δ4- channels.

We have calculated B3LYP single point energies with the correlation consistent polarized triple zeta (cc-pVTZ) basis set on the B3LYP/6-31G(d) optimized structures and have also optimized each structure with the B3LYP/cc-pVTZ method. The B3LYP/cc-pVTZ and B3LYP/6-31G(d) structures are similar. The B3LYP/cc-pVTZ optimized geometries of the TS has a single imaginary frequency at slightly lower frequency of 704 cm^{-1}, 658 cm^{-1} and 651 cm^{-1} for the β1-TS, β4-TS, and δ4-TS, respectively, in good agreement with the B3LYP/6-31G(d) results. The B3LYP/cc-pVTZ optimized geometries are shown in Figs. 7.3, 7.7, and 7.8 and the B3LYP relative energies are given in Tables 7.4, 7.6, and 7.7. For all three reactions, the B3LYP/cc-pVTZ optimized relatives energies are very close to the B3LYP/cc-pVTZ single point relative energies on the 6-31G(d) structure and within 2 kcal/mol of the B3LYP/6-31G(d) energies.

To corroborate the B3LYP results we have, for the four B3LYP/cc-pVTZ optimized stationary points on the β4-ISOPOOH to β-IEPOX reaction, calculated single point energies with second order perturbation Møller-Plesset (MP2) and the recently developed explicitly correlated coupled cluster (CCSD(T)-F12) methods, as implemented in MOLPRO 2008.1 (Werner et al., 2008; Tew et al., 2007). We have used the VDZ-F12 orbital basis sets of Peterson et al. (2008) that have been specifically
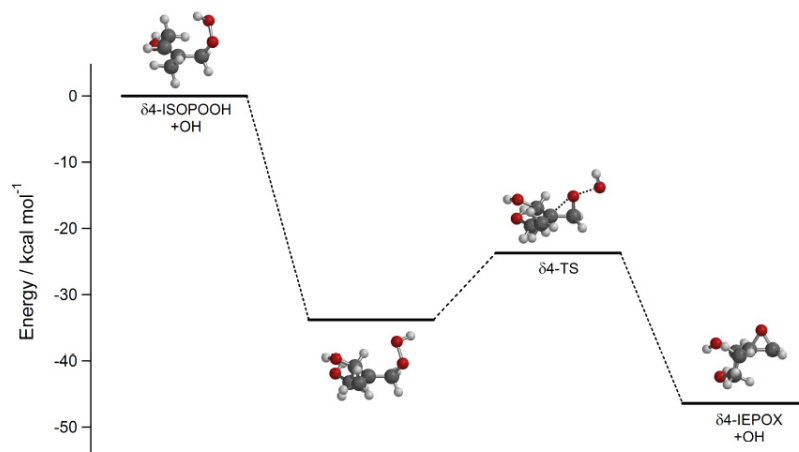
Figure 7.7 – Relative energies of the B3LYP/cc-pVTZ optimized geometries for the formation of δ4-IEPOX from δ4-ISOPOOH.

Table 7.4 – Calculated relative energies (kcal/mol) of the stationary points in the β4-ISOPOOH to β-IEPOX reaction (Scheme 7.2A and Fig. 7.3).

Species	B3LYP/6-31G(d)	B3LYP/cc-pVTZ// B3LYP/6-31G(d)	B3LYP/cc-pVTZ
β4-ISOPOOH	0	0	0
Alkyl radical	-32.9	-30.4	-30.6
β4-TS	-21.1	-19.7	-20.0
β-IEPOX	-47.8	-47.4	-47.4

Table 7.5 – Calculated relative energies (kcal/mol) of the stationary points in the β4-ISOPOOH to β-IEPOX reaction (Scheme 7.2A and Fig. 7.3). All single point energies on the B3LYP/cc-pVTZ optimized geometries.

Species	RMP2/ cc-pVTZ	RMP2/ aug-cc-pVTZ	MP2-F12b/ VDZ-F12	CCSD(T)-F12b/ VDZ-F12
β4-ISOPOOH	0	0	0	0
Alkyl radical	-33.6	-34.1	-34.8	-30.9
β4-TS	-28.7	-31.3	-31.8	-18.2
β-IEPOX	-54.1	-54.6	-55.5	-50.9
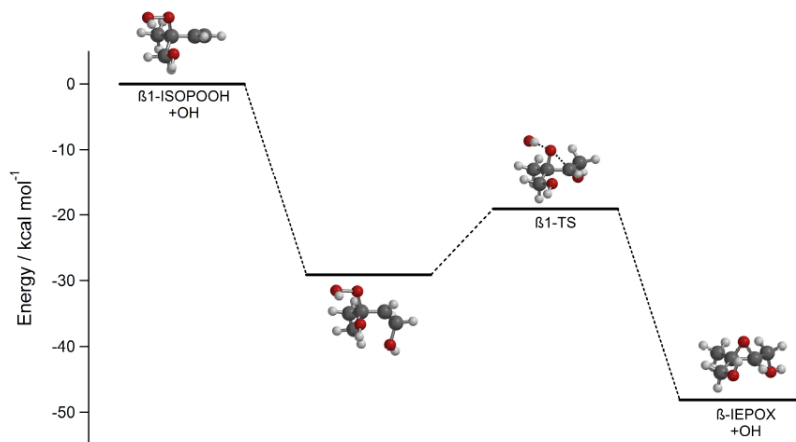
Figure 7.8 – Relative energies of the B3LYP/cc-pVTZ optimized geometries for the formation of β-IEPOX from β1-ISOPOOH.

Table 7.6 – Calculated relative energies (kcal/mol) of the stationary points in the δ4-ISOPOOH to δ4-IEPOX reaction (Scheme 7.2B and Fig. 7.7).

Species	B3LYP/6-31G(d)	B3LYP/cc-pVTZ// B3LYP/6-31G(d)	B3LYP/cc-pVTZ
δ4-ISOPOOH	0	0	0
Alkyl radical	-37.4	-33.9	-33.8
δ4-TS	-25.9	-23.7	-23.7
δ4-IEPOX	-48.1	-46.5	-46.4

optimized for use with explicitly correlated F12 methods (Peterson et al., 2008). The VDZ-F12 basis sets is of similar size to the aug-cc-pVDZ basis set. Density fitting approximations (Manby, 2003; Werner et al., 2007) were used in all explicitly correlated calculations using the VDZ/JKFIT and the AVDZ/MP2FIT auxiliary basis sets of Weigend et al. (Weigend et al., 2002; Weigend, 2002). We have used the resolution of the identity (RI) auxiliary basis sets of Yousaf and Peterson (2008) for all RI approximations. In the MP2 calculations we have used used the cc-pVTZ and aug-cc-pVTZ basis sets. We found that the unrestricted MP2 (UMP2) calculation on β4-TS, led to a large spin contamination ($S^2 = 1.27$ with UMP2/aug-cc-pVTZ), which is unreasonable, and hence the UMP2 results are not included. Instead we have used the restricted open (ROMP2) for the two radicals and RMP2 for the β4-ISOPOOH to β-IEPOX structures.

The calculated relative MP2 and CCSD(T) energies are given in Table 7.5. These higher level correlated results for the β4-ISOPOOH reaction corroborate the B3LYP results. The noticeable

Table 7.7 – Calculated relative energies (kcal/mol) of the stationary points in the $\beta1$-ISOPOOH to β-IEPOX reaction (Scheme 7.2A analog and Fig. 7.8).

Species	B3LYP/6-31G(d)	B3LYP/cc-pVTZ// B3LYP/6-31G(d)	B3LYP/cc-pVTZ
$\beta1$-ISOPOOH	0	0	0
Alkyl radical	-31.8	-29.1	-29.1
$\beta1$-TS	-20.6	-19.0	-19.1
β-IEPOX	-48.8	-48.2	-48.1

difference between the B3LYP and correlated results is in the barrier between the alkyl radical and the TS, which is about 10 kcal/mol with B3LYP and CCSD(T)-F12 and about 3–5 kcal/mol with the RMP2 method. The explicitly correlated F12 method with the VDZ-F12 basis set is known to give near basis set limit CCSD(T) results (Tew et al., 2007) and are as such considered to approach chemical accuracy (Lane and Kjaergaard, 2007; Voehringer-Martinez et al., 2007). These higher level calculations corroborate the B3LYP result, that the reaction to form the epoxide is energetically favorable and proceeds through a small barrier.

7.6.5   Possible interferences from isomers of IEPOX

We have shown in the previous section that the identification of ISOPOOH and IEPOX was supported by CIMS-CID, via their unique fragmentation pattern. Other observations confirm our attribution.

From the ratio of m/z=204 to m/z=203 (largely a measure of the ^{13}C content of the ion), we find that both the first and second generation MW=118 compounds have five carbons, consistent with IEPOX formation.

Because of the high yield, the candidate isomers need to be formed from ISOPOOH via a mechanism that incorporates one ^{18}OH while releasing one ^{16}OH. The reaction of OH with ISOPOOH will proceed almost exclusively by addition of OH to the remaining double bond. The measured lifetime of ISOPOOH is completely consistent with this understanding. In a previous section, we showed using quantum mechanical calculations that following the addition of the OH, the energetic barrier to formation of IEPOX lies significantly below the OH + ISOPOOH entrance channel energy. This implies that the lifetime of the highly excited alkylradical HO·ISOPOOH will be very short before fragmentation to the epoxide and OH. To form a peroxy radical (RO_2), many nanoseconds will be
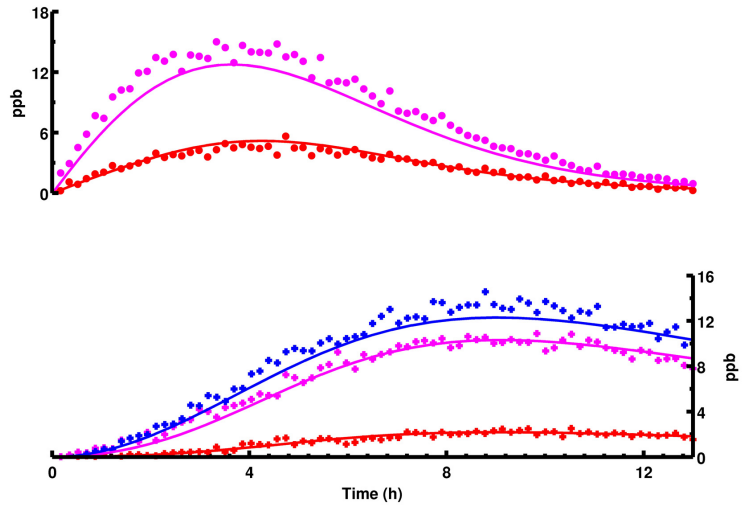
Figure 7.9 – Same as Fig. 2 for Exp 1.
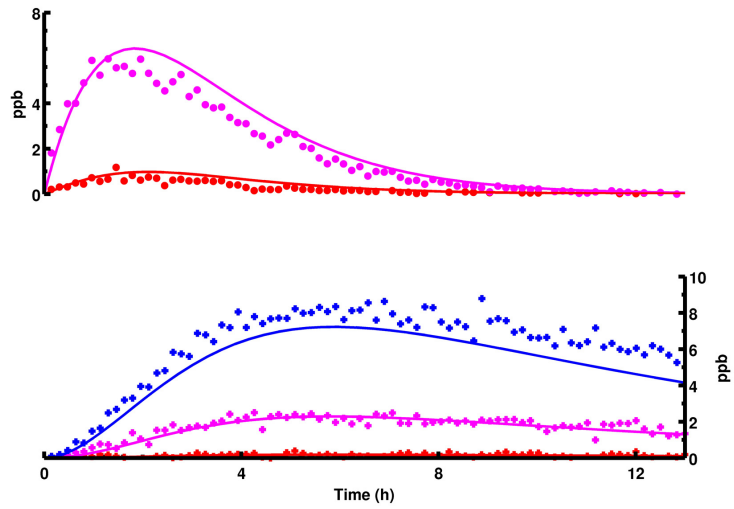
Figure 7.10 – Same as Fig. 2 for Exp 3.

Table 7.8 – Isomers of IEPOX previously observed in the aerosol phase.

Possible isomer	Example	Incompatibility with measurements
alkene triols		Alkene triol formation has been reported in the aerosol phase (Wang et al., 2005). Proposed formation schemes involve enol/ketone equilibrium with dihydroxycarbonyl (Surratt et al., 2006) or acid catalyzed rearrangement of dihydroxyepoxide (Wang et al., 2005). In both mechanisms, formation of alkene triols requires a solvent. The proposed mechanisms cannot take place in the gas-phase. Furthermore, such a compound features a double bond and thus is not consistent with the observed lifetime of the second generation product.
dihydroxycarbonyls		Formation of isobaric dihydroxycarbonyl has previously been proposed through a keto/enol mechanism with the previous isomer (Surratt et al., 2006). CIMS has been shown to be sensitive to this class of compounds (Paulot et al., 2009b). CID of hydroxyacetone and glycolaldehyde standards show a daughter of $m/z=85$ of (CF_3O^-) exclusively with no measurable loss of HF (20 amu) or FCO_2^- (fragment at $m/z=63$). Therefore they cannot account for the formation of daughter $m/z=183$ which is specific to IEPOX.
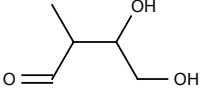
required as only one in five collisions will be with O_2 and few of these will be reactive. Consistent with the lack of formation of the RO_2 following the OH addition to ISOPOOH, we do not observe any dihydroxydihydroperoxide. The [18]OH experiments further confirms that the second generation product results from the addition of a second OH radical and, by mass balance, loss of OH. This can be seen in Fig. 7.2 where the 205 signal (one ^{18}O) is converted mostly to a second generation product with two [18]OH ($m/z=207$). Again, these observations are consistent with the formation of IEPOX.

The isomers of IEPOX which have been previously proposed based on iSOA speciation (Surratt et al., 2006; Wang et al., 2005) cannot explain our observations (Table 7.8). However, they may have resulted from IEPOX heterogeneous chemistry (Wang et al., 2005).

7.6.6 Additional mechanisms

7.6.6.1 Addition of OH on isoprene second double bond

In the main body of the manuscript, we have described the addition of OH onto the double bond which does not carry the methyl group. Addition also occurs on the other double bond as described

Scheme 7.3 Additional isoprene + OH oxidation pathway under low NO$_x$ conditions.
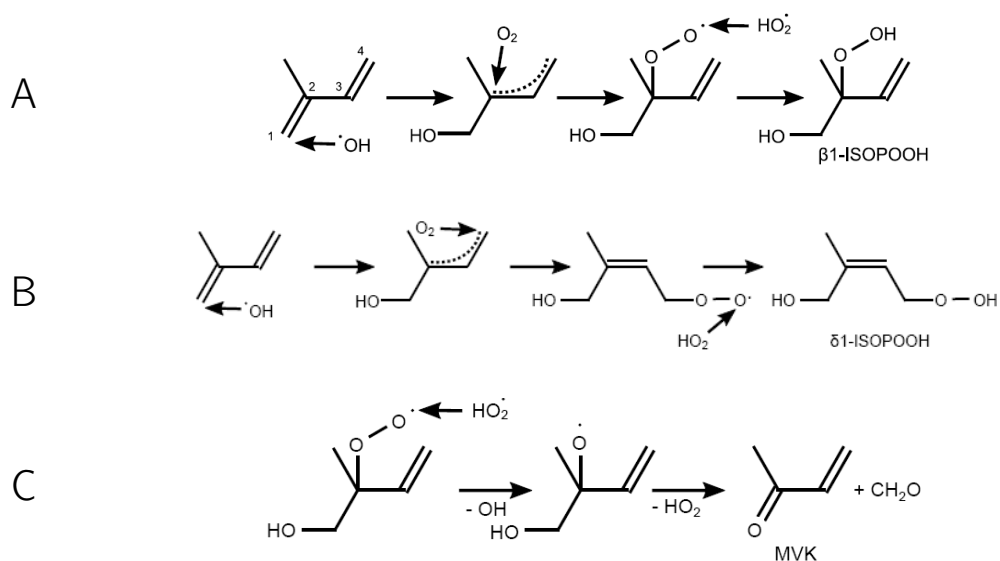
below.

Given the yield of IEPOX, δ1-ISOPOOH produced by Scheme 7.10B is likely to lead, at least partly, to δ1-IEPOX. This would suggest that OH can add substantially on the side of the double bond bearing the methyl group ($\sim$50%).

Addition of OH on carbons 2 and 3 (cf. Scheme 7.3A) is less than 10% and was not considered in this study (Fan and Zhang, 2004).

7.6.6.2 Fate of IEPOX

We investigated this reaction using synthesized BEPOX reacting with labeled ^{18}OH. It appears that the reaction of IEPOX with OH occurs mostly by abstraction of the H–α to the alcohol followed by the opening of the oxirane C-O bond. Five different channels were considered:

⋄ Abstraction of the epoxidic H (Scheme 7.4A).

⋄ Abstraction of the H–α to the alcohol followed by reaction with O$_2$ (Scheme 7.4B).

⋄ Abstraction of the H–α of the alcohol followed by opening of C-O bond of the oxirane (Scheme 7.4C). DM refers to the mechanism first suggested by Dibble (Dibble, 2004a,b).

⋄ Abstraction of the H–α of the alcohol followed by opening of C-C bond of the oxirane (Scheme 7.4D).

227

Scheme 7.4 Potential epoxide + OH oxidation pathways.
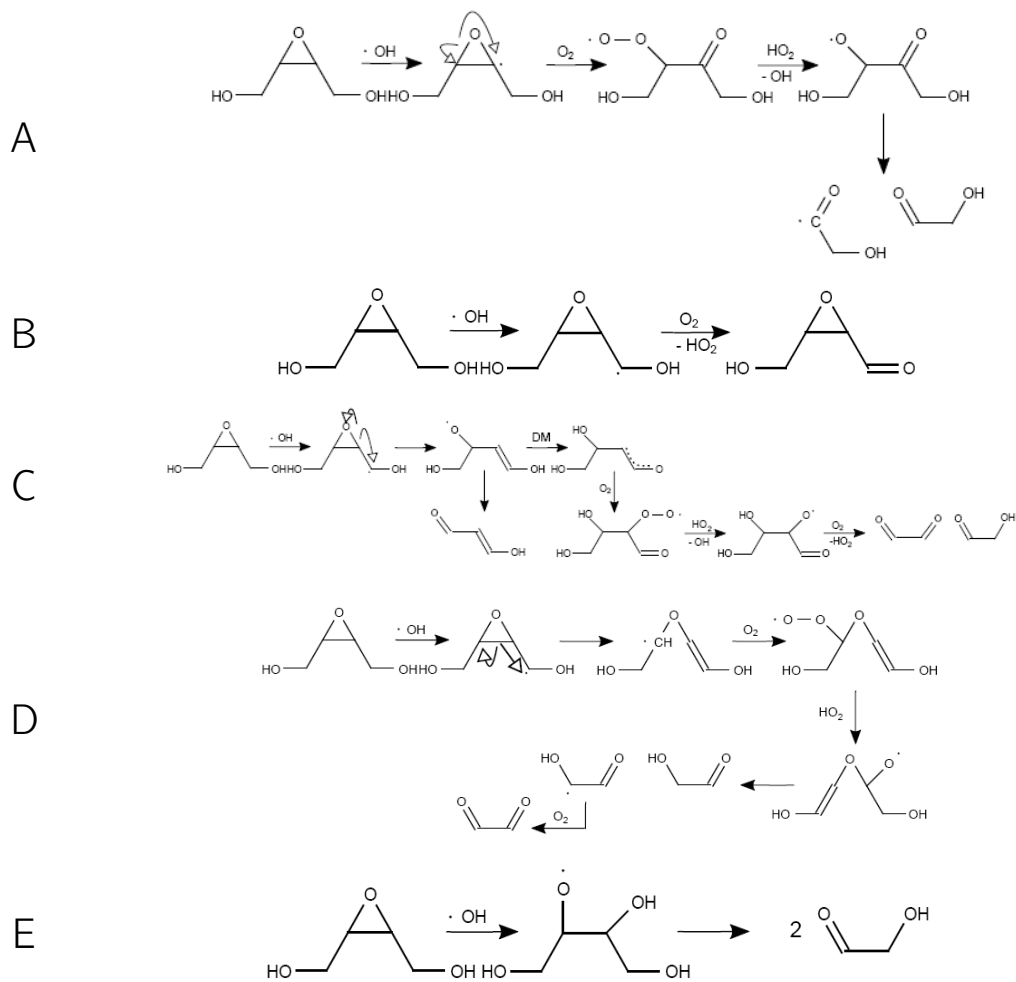
⋄ Addition of OH to the oxirane (Scheme 7.4E).

The only mechanism yielding singly labeled glycolaldehyde is Scheme 7.4E. Very little signal is recorded at this mass suggesting that OH is not incorporated into the oxirane. This is also consistent with the absence of dilabeled hydroxyacetone and glycolaldehyde in the isoprene $+$ ^{18}OH experiments.

The signal recorded at $m/z=187$ corresponding to the product of Scheme 7.4B also represents a minor contribution to the total signal. This is consistent with the unlabeled isoprene experiment where little signal is recorded at $m/z=201$, the analog of $m/z=187$ in the isoprene system.

Scheme 7.4A (Meleshevich, 1970), Scheme 7.4C and Scheme 7.4D all yield non-labeled glyco-laldehyde and are difficult to distinguish directly because of the BEPOX symmetry. However, data from ^{18}OH $+$ isoprene suggest high yields of both singly-labeled hydroxyacetone and glycolaldehyde from IEPOX photoxidation. This suggests that the analogue of Scheme 7.4A for isoprene is not the main oxidation channel, as no glycolaldehyde can result from this channel. Furthermore if Scheme 7.4A is an important decomposition pathway, dilabeled glycolaldehyde from δ4-IEPOX would be formed. However, dilabeled glycolaldehyde is not observed.

Scheme 7.4, C and D are mostly indistinguishable and further studies are required to investigate these mechanisms in more detail. It is suggested here that the reaction of IEPOX with OH occurs mostly by abstraction of the H α to the alcohol followed by the opening of the oxirane C-O bond (Scheme 7.4D). The signal recorded at $m/z=91$ in PTR-MS mode may be associated with the formation of the enol (3-hydroxy-2-propenal). Furthermore the analogue of Scheme 7.4C applied to the IEPOX seems thermodynamically unfavorable as it requires a rearrangement which involves the formation of a primary radical from a secondary radical.

δ1-IEPOX cannot undergo Scheme 7.4D and its fate remains uncertain. For simplicity we have assumed in our kinetic model and in the proposed GEOS-CHEM mechanism that δ1-IEPOX shares the fate of δ4 - IEPOX, yielding hydroxyacetone.

7.6.7 Kinetic mechanism

In our simulations of the laboratory experiments, we used a simplified chemical scheme focusing on the first few hours. The different isotopes for each species are explicitly treated but we neglect any kinetic isotope effect on the reaction rate constants or the yields of the reactions. Cross-reactions of peroxy radicals are treated using a class approach (Madronich and Calvert, 1990; Jenkin et al., 1997; Saunders et al., 2003). This approach was modified to account for the possibility of homomolecular

biradical cross-reactions. The reaction of a peroxy radical (RO_2) with a class of peroxy radical CLO_2 is defined as:

$$\frac{d[RO_2]}{dt} = -k_{CLO_2}^{RO_2}[RO_2][CLO_2](1 + \frac{[RO_2]}{[CLO_2]}\delta(RO_2, CLO_2)) \tag{7.1}$$

where $\delta(x, y)$ is the Dirac function. A simplified scheme is used to treat the products of the RO_2 + RO_2 channel. This approximation is justified as the experiment was designed to limit the role of these reactions.

Peroxy radicals formed by the reaction of OH with isoprene were divided into two classes: β (70%) and δ peroxy radicals (30%). Addition of OH on the internal carbons are neglected as they account for less than 10% of the carbon (Paulot et al., 2009b).

The expected product of Scheme 7.1C for the δ channels (isomer of 1-hydroxy-4-oxo-2-methylbut-2-ene) is not observed in large yields. Therefore we assume that Scheme 7.1C is only occurring for the β peroxy radicals, consistent with the formation of MVK and MACR. The fraction of β peroxy radicals undergoing analog of Scheme 7.1C is ~17%. The ratio between the yields of MVK and MACR is assumed to be equal to the one derived under high NO_x conditions.

In addition to the ^{16}OH regenerated from the VOC photooxidation, an additional conversion of ^{18}OH to ^{16}OH of ~$7\,s^{-1}$ takes place in our experiments. A minor fraction of this conversion can be attributed to the reaction of OH with water (13%) (Dubey et al., 1997). Experiments at reduced oxygen concentration suggest that the reaction of OH with O_2 could account for the bulk of this conversion (k~$1.3{\times}10^{-18}\,cm^3\,molecule^{-1}\,s^{-1}$) (Greenblatt and Howard, 1989). For the conditions of this experiment, the production of ^{18}OH from hydrogen peroxide photolysis, ~$2.2{\times}10^8\,s^{-1}$ ($[H_2O_2] = 2\,ppmv$) largely exceeds the conversion of ^{18}OH to ^{16}OH.

Uncertainties regarding the fate of IEPOX as described in the previous section have little effect on our conclusions since Scheme 7.4A and B reactions pathways share the same products.

Comparison between modeled and measured ISOPOOH and IEPOX are shown in Figs. 7.9 (Experiment 1, cf. Table 7.1) and 7.10 (Experiment 3). For Experiment 2, modeled ^{16}OH is about $4.5{\times}10^5\,molec\,cm^{-3}$, ^{18}OH ~ $1.8{\times}10^6\,molec\,cm^{-3}$, $H^{16}O^{16}O$ ~ $2.0{\times}10^9\,molec\,cm^{-3}$, $H^{16}O^{18}O$ ~ $1.1{\times}10^8\,molec\,cm^{-3}$, and $H^{18}O^{18}O$ ~ $2.8{\times}10^9\,molec\,cm^{-3}$.

7.6.8   GEOS-CHEM

GEOS-CHEM v8.01.04 (`http://www-as.harvard.edu/chemistry/trop/geos/`) driven by assimilated meteorological observations from the Goddard Earth Observing System (GEOS-4) of the NASA Global Modeling and Assimilation Office (GMAO) (Bey et al., 2001) is used to assess the global

Table 7.9 – Low NO_x mechanism for the photooxidation of isoprene.

									$A \times 10^{11}$ $(cm^3\,molec^{-1}\,s^{-1})$	$-E_a/R$ (K)
ISOP	+	OH	→	ISOPOO					2.7	390
ISOPOO	+	HO_2	→	0.88 0ISOPOOH	+	0.120 OH	+	0.047 MACR	0.074	700
				+ 0.073 MVK	+	0.120 HO_2	+	0.120 HCHO		
ISOPOOH	+	OH	→	IEPOX	+	OH			1.9	390
ISOPOOH	+	OH	→	0.70 ISOPOO	+	0.300 HC5	+	0.300 OH	0.38	200
IEPOX	+	OH	→	IEPOXOO					5.78	-400
IEPOXOO	+	HO_2	→	0.725 HAC	+	0.275 GLYC	+	0.275 GLYX	0.074	700
				+ 0.275 MGLY	+	1.125 OH	+	0.825 HO_2		
				+ 0.200 CO_2	+	0.375 HCHO	+	0.074 HC(O)OH		
				+ 0.251 CO						

impact of the isoprene chemistry described herein. The model is run with a spatial resolution of 4° latitude and 5° longitude and 30 vertical levels (22 in the troposphere).

Isoprene emissions are taken from the Global Emission Inventory Activity (GEIA) inventory (Guenther et al., 1995). The default chemical mechanism is updated to incorporate recently proposed modification to the high NO_x chemistry (Paulot et al., 2009b) as well as the low NO_x regime derived in this study (Table 7.9). Dry deposition for IEPOX and ISOPOOH is modeled using H_2O_2, while hydroxymethylhydroperoxide (HMHP) parameters are used to model their wet deposition.

A model spin-up of 15 months is done before the results are retained. The results presented in this study are for northern hemisphere summer 2002 and northern hemisphere winter 2001. Isoprene emissions from GEIA are scaled in GEOS-CHEM so that the flux of isoprene to the atmosphere is ∼342 TgC/yr. This yields a yearly IEPOX formation of ∼65 TgC/yr. Estimates of isoprene emissions range from 250 – 750 TgC/yr. Assuming that IEPOX formation scales with isoprene emissions, this leads to our global estimate of yearly production of IEPOX: 95±45 TgC/yr (167 Tg/yr).

The formation of IEPOX from isoprene is predicted to be asymmetric with a larger yield in the southern hemisphere (Fig. 7.11). More than 60% of IEPOX is formed in the tropics (−15° to +15°) reflecting the influence of anthropogenic activities on the chemistry of isoprene.
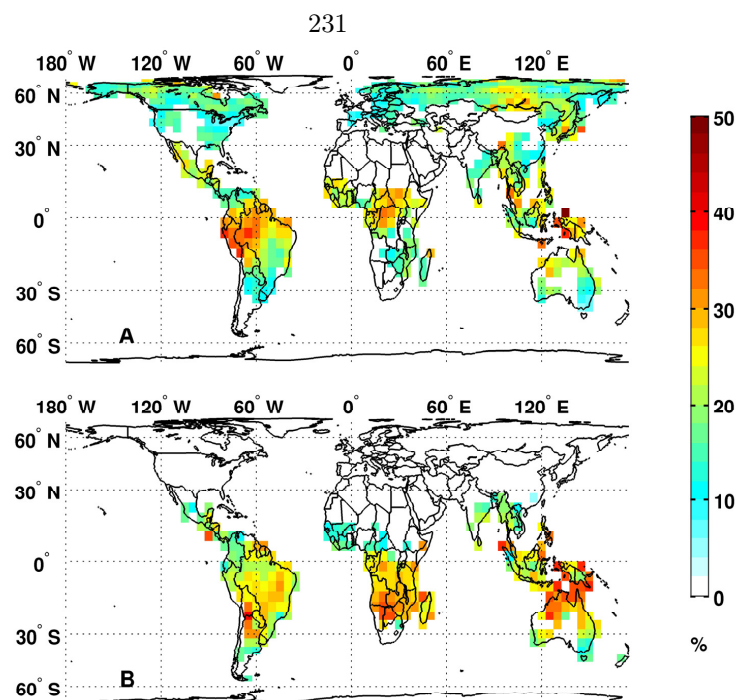
Figure 7.11 – Modeled yield of IEPOX from the reaction of isoprene + OH in the planetary boundary layer. Grid cells where isoprene mixing ratio is lower than 50 pptv are not shown.

7.6.9   Field measurements

7.6.9.1   TC4

The NASA Tropical Composition, Cloud and Climate Coupling (TC4) mission was designed to investigate the atmospheric structure, properties, and processes in the tropical troposphere. This mission, based out of San Jose, Costa Rica, was conducted during July and August 2007 and consisted of coordinated flights between several NASA aircraft including the DC-8, ER-2, and WB-57. Two Caltech CIMS instruments (single quadrupole instrument and the Varian tandem-MS instrument) were deployed on the DC-8.

Low-level legs were flown over the Columbian jungle during several flights. During these legs large signals at m/z=203 were observed with the single quadrupole instrument. Quantification of ISOPOOH and IEPOX is not possible due to uncertainties regarding the ion transmission efficiency for the quadrupole at these high masses as well as the inability of the single quadrupole to separate these mass analogues. The tandem-MS did not monitor m/z=203 during this experiment.

7.6.9.2 ARCTAS

The primary scientific focus of the 2008 summer NASA Arctic Research of the Composition of the Troposphere from Aircraft and Satellites (ARCTAS) mission was to study boreal forest fire emissions. ARCTAS was a NASA contribution within the greater Third International Polar Year effort (POLARCAT). The NASA DC-8 aircraft was based in Cold Lake, Alberta, during the summer phase of ARCTAS, with nine total flights: two transit flights between Cold Lake and Southern California, four local flights from Cold Lake, two flights between Cold Lake and Thule, Greenland, and one local flight from Thule. More information about the ARCTAS mission, including details of the DC-8 instrument payload and an overview of the mission scientific objectives, is available at http://www.espo.nasa.gov/arctas/.

Two Caltech-CIMS instruments were flown aboard the DC-8 during ARCTAS: the single quadrupole (Crounse et al., 2006) and the triple quadrupole (identical to the instrument in the chamber). The triple quadrupole was operated exclusively in CID-MSMS mode while in flight. Both flight instruments monitored $m/z=203$, though the tandem MS did so for only five of the nine flights.

A subset of the $m/z=203$ daughters ($m/z=63$, $m/z=85$, $m/z=137$, $m/z=203$) were measured by the tandem MS for the last five flights of summer ARCTAS. By assuming that the only source of $m/z=203$ is ISOPOOH and IEPOX, we can infer ISOPOOH and IEPOX respective signals from the flight data. As discussed in the text, ISOPOOH·CF_3O was determined to be the source of $m/z=63$ daughter ion in the chamber experiments. The $m/z=183$ daughter ion, used in the chamber study as the fingerprint for IEPOX, was not measured during flight. Signal potentially attributable to IEPOX was determined for the flight data by removing the ISOPOOH contribution to the $m/z=137$ daughter ion signal, using the relationship between the $m/z=203$ daughters derived from an OH + isoprene chamber experiment where the aircraft tandem MS instrument monitored all relevant $m/z=203$ daughter masses: $(m/z = 203{\rightarrow}137) = (1.49{\pm}0.03){\times}(m/z = 203{\rightarrow}63) + (1.43{\pm}0.03){\times}(m/z = 203{\rightarrow}183)$ where the coefficients and 2σ uncertainties (of the fit) are obtained from a multivariate linear regression.

Both tandem MS instruments sampled from the same chamber during this calibration experiment. By determining the IEPOX contribution to the $m/z = 203{\rightarrow}137$ ion signal in terms of the $m/z = 203{\rightarrow}183$ ion signal and also determining the scaling factor between the $m/z = 203{\rightarrow}183$ ion signals of the two instruments, the IEPOX sensitivity used for the chamber experiments can be applied to the ARCTAS data to obtain in situ IEPOX mixing ratios. Determination of *in situ* ISOPOOH mixing ratios required only obtaining the scaling factor between the $m/z = 203{\rightarrow}63$ ion signals of

the two instruments before applying the ISOPOOH sensitivity used for the chamber experiments.

The possibility of mass interferences at m/z=203 *in situ* precludes the definitive attribution of the m/z=203 signal, in its entirety, to ISOPOOH and IEPOX. One known interferent at m/z=203 was identified from data not yet published from a chamber study of the OH oxidation of 2-methyl-3-buten-2-ol (MBO). The MBO oxidation product at m/z=203 yields no daughter ion at m/z=63 but does yield a daughter ion mass at m/z=137. Consequently, the presence of MBO oxidation products may influence the calculated ARCTAS IEPOX mixing ratios, but not the ARCTAS ISOPOOH mixing ratios. We currently know of no mass interferences for the m/z=63 daughter ion of m/z=203. In recognition of the potential for interferences, however, the ARCTAS data for ISOPOOH and IEPOX will be hereafter referred to as ISOPOOH_flt and IEPOX_flt, respectively, to distinguish the *in situ* data from the chamber data.

Both ISOPOOH_flt and IEPOX_flt were observed during four of the last five ARCTAS flights, as shown in Fig. 7.12. All of the ISOPOOH_flt and most of the IEPOX_flt were detected below 1.5 km above ground level (Fig. 7.9). The highest mixing ratios of both ISOPOOH_flt and IEPOX_flt during the mission, 1.2 ppbv and 3.4 ppbv respectively, were encountered while flying 0.7 km above ground level at 40.7319°N, 122.0492°W. Signal for ISOPOOH_flt was always accompanied by IEPOX_flt signal, but IEPOX_flt was observed without concurrent ISOPOOH_flt signal, consistent with IEPOX having a significantly longer lifetime than ISOPOOH.

Acknowledgments

Figure 7.12 – Flight tracks for 2008 summer ARCTAS flights on July 5, 8, 10, and 12 indicating the location of data and the mixing ratio for ISOPOOH_flt (top panel) and IEPOX_flt (bottom panel).
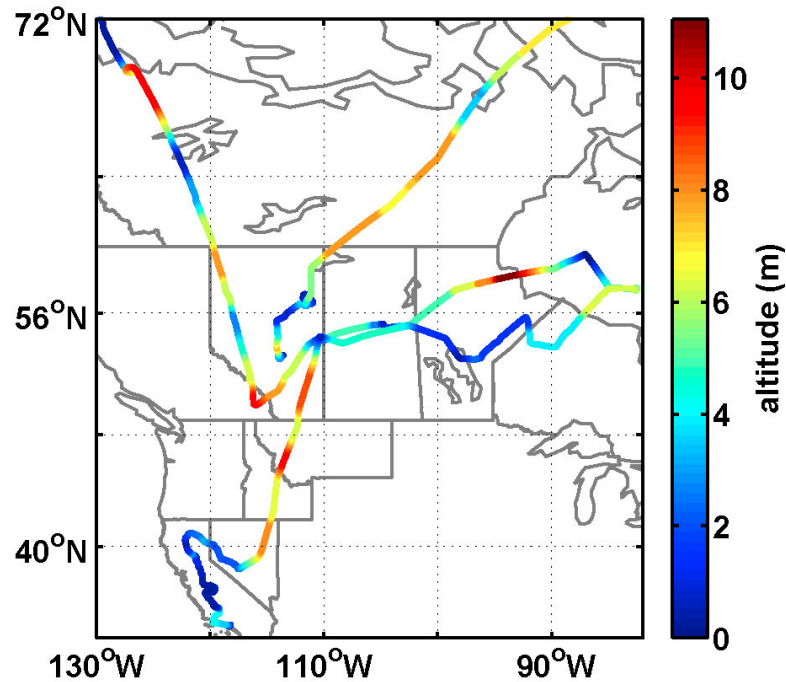
Figure 7.13 – Flight tracks for 2008 summer ARCTAS flights on July 5, 8, 10, and 12 with color indicating the altitude of the DC-8 aircraft.

Bibliography

Amelynck, C., Schoon, N., and Arijs, E.: Gas phase reactions of CF_3O^- and $CF_3O^- \cdot H_2O$ with nitric, formic, and acetic acid, Int. J. Mass. Spectrom., 203, 165–175, 2000a.

Amelynck, C., Van Bavel, A. M., Schoon, N., and Arijs, E.: Gas phase reactions of CF_3O^- and $CF_3O^- \cdot H_2O$ and their relevance to the detection of stratospheric HCl, Int. J. Mass. Spectrom., 202, 207–216, 2000b.

Andreae, M. O. and Crutzen, P. J.: Atmospheric aerosols: biogeochemical sources and role in atmospheric chemistry, Science, 276, 1052–1058, 1997.

Bell, E. R., Rust, F. F., and Vaughan, W. E.: Decompositions of di-tert-alkyl peroxides: 4. Decomposition of pure liquid peroxide, J. Am. Chem. Soc., 72, 337–338, 1950.

Bey, I., Jacob, D. J., Yantosca, R. M., Logan, J. A., Field, B. D., Fiore, A. M., Li, Q. B., Liu, H. G. Y., Mickley, L. J., and Schultz, M. G.: Global modeling of tropospheric chemistry with assimilated meteorology: model description and evaluation, J. Geophys. Res.-Atmos., 106, 23 073–23 095, 2001.

Claeys, M., Graham, B., Vas, G., Wang, W., Vermeylen, R., Pashynska, V., Cafmeyer, J., Guyon, P., Andreae, M. O., Artaxo, P., and Maenhaut, W.: Formation of secondary organic aerosols through photooxidation of isoprene, Science, 303, 1173–1176, 2004.

Cocker, D. R., Flagan, R. C., and Seinfeld, J. H.: State-of-the-art chamber facility for studying atmospheric aerosol chemistry, Environ. Sci. Technol., 35, 2594–2601, doi:10.1021/es0019169, 2001.

Crounse, J. D., McKinney, K. A., Kwan, A. J., and Wennberg, P. O.: Measurement of gas-phase hydroperoxides by chemical ionization mass spectrometry, Anal. Chem., 78, 6726–6732, doi:10.1021/ac0604235, 2006.

Crutzen, P. J., Williams, J., Poschl, U., Hoor, P., Fischer, H., Warneke, C., Holzinger, R., Hansel, A., Lindinger, W., Scheeren, B., and Lelieveld, J.: High spatial and temporal resolution measurements of primary organics and their oxidation products over the tropical forests of Surinam, Atmos. Environ., 34, 1161–1165, 2000.

de Gouw, J. A., Middlebrook, A. M., Warneke, C., Goldan, P. D., Kuster, W. C., Roberts, J. M., Fehsenfeld, F. C., Worsnop, D. R., Canagaratna, M. R., Pszenny, A. A. P., Keene, W. C.,

Marchewka, M., Bertman, S. B., and Bates, T. S.: Budget of organic carbon in a polluted atmosphere: Results from the New England Air Quality Study in 2002, J. Geophys. Res.-Atmos., 110, doi:10.1029/2004JD005623, 2005.

Dibble, T. S.: Prompt chemistry of alkenoxy radical products of the double H-atom transfer of alkoxy radicals from isoprene, J. Phys. Chem. A, 108, 2208–2215, doi:10.1021/jp0312161, 2004a.

Dibble, T. S.: Intramolecular hydrogen bonding and double H-atom transfer in peroxy and alkoxy radicals from isoprene, J. Phys. Chem. A, 108, 2199–2207, doi:10.1021/jp0306702, 2004b.

Dillon, T. J. and Crowley, J. N.: Direct detection of OH formation in the reactions of HO_2 with $CH_3C(O)O_2$ and other substituted peroxy radicals, Atmos. Chem. Phys., 8, 4877–4889, 2008.

Dubey, M. K., Mohrschladt, R., Donahue, N. M., and Anderson, J. G.: Isotope specific kinetics of hydroxyl radical (OH) with water (H_2O): Testing models of reactivity and atmospheric fractionation, J. Phys. Chem. A, 101, 1494–1500, 1997.

Fan, J. and Zhang, R.: Atmospheric Oxidation Mechanism of Isoprene, Environ. Chem., 1, 140–149, doi:10.1071/EN04045, 2004.

Frisch, M. J., Trucks, G. W., Schlegel, H. B., Scuseria, G. E. Robb, M. A., Cheeseman, J. R., Montgomery, Jr., J. A., Vreven, T., Kudin, K. N., Burant, J. C., Millam, J. M., Iyengar, S. S., Tomasi, J. Barone, V., Mennucci, B., Cossi, M., Scalmani, G., Rega, N., Petersson, G. A., Nakatsuji, H. Hada, M., Ehara, M., Toyota, K., Fukuda, R., Hasegawa, J., Ishida, M., Nakajima, T., Honda, Y., Kitao, O., Nakai, H., Klene, M., Li, X., Knox, J. E., Hratchian, H. P., Cross, J. B., Bakken, V., Adamo, C., Jaramillo, J., Gomperts, R., Stratmann, R. E., Yazyev, O., Austin, A. J., Cammi, R., Pomelli, C., Ochterski, J. W., Ayala, P. Y., Morokuma, K., Voth, G. A., Salvador, P., Dannenberg, J. J., Zakrzewski, V. G., Dapprich, S., Daniels, A. D., Strain, M. C., Farkas, O., Malick, D. K., Rabuck, A. D., Raghavachari, K., Foresman, J. B., Ortiz, J. V., Cui, Q., Baboul, A. G., Clifford, S., Cioslowski, J., Stefanov, B. B., Liu, G., Liashenko, A., Piskorz, P., Komaromi, I., Martin, R. L., Fox, D. J., Keith, T., Al-Laham, M. A., Peng, C. Y., Nanayakkara, A., Challacombe, M., Gill, P. M. W., Johnson, B., Chen, W., Wong, M. W., Gonzalez, C., and Pople, J. A.: Gaussian 03, Revision C.02, 2004.

Fuentes, J. D., Lerdau, M., Atkinson, R., Baldocchi, D., Bottenheim, J. W., Ciccioli, P., Lamb, B., Geron, C., Gu, L., Guenther, A., Sharkey, T. D., and Stockwell, W.: Biogenic hydrocarbons in the atmospheric boundary layer: A review, B. Am. Meteorol. Soc., 81, 1537–1575, 2000.

238

Gao, S., Ng, N. L., Keywood, M., Varutbangkul, V., Bahreini, R., Nenes, A., He, J. W., Yoo, K. Y., Beauchamp, J. L., Hodyss, R. P., Flagan, R. C., and Seinfeld, J. H.: Particle phase acidity and oligomer formation in secondary organic aerosol, Environ. Sci. Technol., 38, 6582–6589, doi: 10.1021/es049125k, 2004.

Garden, A. L., Paulot, F., Crounse, J. D., Maxwell-Cameron, I. J., Wennberg, P. O., and Kjaergaard, H. G.: Calculation of conformationally weighted dipole moments useful in ion-molecule collision rate estimates, Chem. Phys. Lett., 474, 45–50, doi:10.1016/j.cplett.2009.04.038, 2009.

Goldstein, A. H. and Galbally, I. E.: Known and unexplored organic constituents in the Earth's atmosphere, Environ. Sci. Technol., 41, 1514–1521, 2007.

Greenblatt, G. D. and Howard, C. J.: Oxygen atom exchange in the interaction of (^{18}OH) with several small molecules, J. Phys. Chem., 93, 1035–1042, 1989.

Guenther, A., Hewitt, C. N., Erickson, D., Fall, R., Geron, C., Graedel, T., Harley, P., Klinger, L., Lerdau, M., McKay, W. A., Pierce, T., Scholes, B., Steinbrecher, R., Tallamraju, R., Taylor, J., and Zimmerman, P.: A global-model of natural volatile organic-compound emissions, J. Geophys. Res.-Atmos., 100, 8873–8892, 1995.

Guenther, A., Karl, T., Harley, P., Wiedinmyer, C., Palmer, P. I., and Geron, C.: Estimates of global terrestrial isoprene emissions using MEGAN (Model of Emissions of Gases and Aerosols from Nature), Atmos. Chem. Phys., 6, 3181–3210, 2006.

Hansel, A., Jordan, A., Holzinger, R., Prazeller, P., Vogel, W., and Lindinger, W.: Proton-transfer reaction mass-spectrometry – online trace gas-analysis at the ppb level, Int. J. Mass. Spectrom., 149, 609–619, 1995.

Harley, P. C., Monson, R. K., and Lerdau, M. T.: Ecological and evolutionary aspects of isoprene emission from plants, Oecologia, 118, 109–123, 1999.

Huey, L. G., Villalta, P. W., Dunlea, E. J., Hanson, D. R., and Howard, C. J.: Reactions of CF_3O^- with atmospheric trace gases, J. Phys. Chem., 100, 190–194, 1996.

Jenkin, M. E., Saunders, S. M., and Pilling, M. J.: The tropospheric degradation of volatile organic compounds: a protocol for mechanism development, Atmos. Environ., 31, 81–104, 1997.

Kerminen, V. M., Lihavainen, H., Komppula, M., Viisanen, Y., and Kulmala, M.: Direct observational evidence linking atmospheric aerosol formation and cloud droplet activation, Geophys. Res. Lett., 32, doi:10.1029/2005GL023130, 2005.

Lane, J. R. and Kjaergaard, H. G.: Fluorosulfonic acid and chlorosulfonic acid: Possible candidates for OH-Stretching overtone-induced photodissociation, J. Phys. Chem. A, 111, 9707–9713, doi: 10.1021/jp074436d, 2007.

Lelieveld, J., Butler, T. M., Crowley, J. N., Dillon, T. J., Fischer, H., Ganzeveld, L., Harder, H., Lawrence, M. G., Martinez, M., Taraborrelli, D., and Williams, J.: Atmospheric oxidation capacity sustained by a tropical forest, Nature, 452, 737–740, doi:10.1038/nature06870, 2008.

Madronich, S. and Calvert, J. G.: Permutation reactions of organic peroxy-radicals in the troposphere, J. Geophys. Res.-Atmos., 95, 5697–5715, 1990.

Manby, F. R.: Density fitting in second-order linear-r(12) Moller-Plesset perturbation theory, J. Chem. Phys., 119, 4607–4613, doi:10.1063/1.1594713, 2003.

McLafferty, F. W.: Tandem mass-spectrometry, Science, 214, 280–287, 1981.

Meleshevich, A. P.: Reactions of epoxy-compounds by a radical mechanism, Russ. Chem. Rev., 39, 213–226, 1970.

Minerath, E. C. and Elrod, M. J.: Assessing the potential for diol and hydroxy sulfate ester formation from the reaction of epoxides in tropospheric aerosols, Environ. Sci. Technol., 43, 1386–1392, doi: 10.1021/es8029076, 2009.

Paulot, F., Crounse, J. D., Kjaergaard, H. G., Kroll, J. H., Seinfeld, J. H., and Wennberg, P. O.: Isoprene photooxidation: new insights into the production of acids and organic nitrates, Atmos. Chem. Phys., 9, 1479–1501, 2009.

Peeters, J., Nguyen, T. L., and Vereecken, L.: HO_x radical regeneration in the oxidation of isoprene, Phys. Chem. Chem. Phys., 11, 5935–5939, doi:10.1039/b908511d, 2009.

Peterson, K. A., Adler, T. B., and Werner, H.-J.: Systematically convergent basis sets for explicitly correlated wavefunctions: the atoms H, He, B-Ne, and Al-Ar, J. Chem. Phys., 128, doi:10.1063/1.2831537, 2008.

Reeves, C. E. and Penkett, S. A.: Measurements of peroxides and what they tell us, Chem. Rev., 103, 5199–5218, doi:10.1021/cr0205053, 2003.

Ren, X., Olson, J. R., Crawford, J. H., Brune, W. H., Mao, J., Long, R. B., Chen, Z., Chen, G., Avery, M. A., Sachse, G. W., Barrick, J. D., Diskin, G. S., Huey, L. G., Fried, A., Cohen, R. C., Heikes, B., Wennberg, P. O., Singh, H. B., Blake, D. R., and Shetter, R. E.: HO_x chemistry during INTEX-A 2004: Observation, model calculation, and comparison with previous studies, J. Geophys. Res.-Atmos., 113, doi:10.1029/2007JD009166, 2008.

Rosenstiel, T. N., Potosnak, M. J., Griffin, K. L., Fall, R., and Monson, R. K.: Increased CO_2 uncouples growth from isoprene emission in an agriforest ecosystem, Nature, 421, 256–259, doi: 10.1038/nature01312, 2003.

Ruppert, L. and Becker, K. H.: A product study of the OH radical-initiated oxidation of isoprene: formation of C_5-unsaturated diols, Atmos. Environ., 34, 1529–1542, 2000.

Sander, S.: Chemical kinetics and photochemical data for use in atmospheric studies evaluation number 15, 2006.

Saunders, S. M., Jenkin, M. E., Derwent, R. G., and Pilling, M. J.: Protocol for the development of the Master Chemical Mechanism, MCM v3 (Part A): tropospheric degradation of non-aromatic volatile organic compounds, Atmos. Chem. Phys., 3, 161–180, 2003.

Skinner, J. R., Wilkoxen, Jr, C. H., and Carlson, G. J.: Production of Epoxides, 1958.

Su, T. and Chesnavich, W. J.: Parameterization of the ion-molecule collision rate-constant by trajectory calculations, J. Chem. Phys., 76, 5183–5185, 1982.

Surratt, J. D., Murphy, S. M., Kroll, J. H., Ng, a. L. N., Hildebrandt, L., Sorooshian, A., Szmigielski, R., Vermeylen, R., Maenhaut, W., Claeys, M., Flagan, R. C., and Seinfeld, J. H.: Chemical composition of secondary organic aerosol formed from the photooxidation of isoprene, J. Phys. Chem. A, 110, 9665–9690, doi:10.1021/jp061734m, 2006.

Surratt, J. D., Lewandowski, M., Offenberg, J. H., Jaoui, M., Kleindienst, T. E., Edney, E. O., and Seinfeld, J. H.: Effect of acidity on secondary organic aerosol formation from isoprene, Environ. Sci. Technol., 41, 5363–5369, doi:10.1021/es0704176, 2007.

Surratt, J. D., Gomez-Gonzalez, Y., Chan, A. W. H., Vermeylen, R., Shahgholi, M., Kleindienst, T. E., Edney, E. O., Offenberg, J. H., Lewandowski, M., Jaoui, M., Maenhaut, W., Claeys, M., Flagan, R. C., and Seinfeld, J. H.: Organosulfate formation in biogenic secondary organic aerosol, J. Phys. Chem. A, 112, 8345–8378, doi:10.1021/jp802310p, 2008.

Tew, D. P., Klopper, W., Neiss, C., and Haettig, C.: Quintuple-zeta quality coupled-cluster correlation energies with triple-zeta basis sets, Phys. Chem. Chem. Phys., 9, 1921–1930, doi: 10.1039/b617230j, 2007.

Thornton, J. A., Wooldridge, P. J., Cohen, R. C., Martinez, M., Harder, H., Brune, W. H., Williams, E. J., Roberts, J. M., Fehsenfeld, F. C., Hall, S. R., Shetter, R. E., Wert, B. P., and Fried, A.: Ozone production rates as a function of NO_x abundances and HO_x production rates in the Nashville urban plume, J. Geophys. Res.-Atmos., 107, doi:10.1029/2001JD000932, 2002.

Tunved, P., Hansson, H. C., Kerminen, V. M., Strom, J., Dal Maso, M., Lihavainen, H., Viisanen, Y., Aalto, P. P., Komppula, M., and Kulmala, M.: High natural aerosol loading over boreal forests, Science, 312, 261–263, doi:10.1126/science.1123052, 2006.

Voehringer-Martinez, E., Hansmann, B., Hernandez, H., Francisco, J. S., Troe, J., and Abel, B.: Water catalysis of a radical-molecule gas-phase reaction, Science, 315, 497–501, doi: 10.1126/science.1134494, 2007.

von Kuhlmann, R., Lawrence, M. G., Poschl, U., and Crutzen, P. J.: Sensitivities in global scale modeling of isoprene, Atmos. Chem. Phys., 4, 1–17, 2004.

Wang, W., Kourtchev, I., Graham, B., Cafmeyer, J., Maenhaut, W., and Claeys, M.: Characterization of oxygenated derivatives of isoprene related to 2-methyltetrols in Amazonian aerosols using trimethylsilylation and gas chromatography/ion trap mass spectrometry, Rapid Commun. Mass. Sp., 19, 1343–1351, doi:10.1002/rcm.1940, 2005.

Warneke, C., Holzinger, R., Hansel, A., Jordan, A., Lindinger, W., Poschl, U., Williams, J., Hoor, P., Fischer, H., Crutzen, P. J., Scheeren, H. A., and Lelieveld, J.: Isoprene and its oxidation products methyl vinyl ketone, methacrolein, and isoprene related peroxides measured online over the tropical rain forest of Surinam in March 1998, J. Atmos. Chem., 38, 167–185, 2001.

Wavefunction: Spartan '06, 2006.

Wavefunction: Spartan '08, 2008.

Weigend, F.: A fully direct RI-HF algorithm: Implementation, optimised auxiliary basis sets, demonstration of accuracy and efficiency, Phys. Chem. Chem. Phys., 4, 4285–4291, doi:10.1039/b204199p, 2002.

Weigend, F., Kohn, A., and Hattig, C.: Efficient use of the correlation consistent basis sets in resolution of the identity MP2 calculations, J. Chem. Phys., 116, 3175–3183, doi:10.1063/1.1445115, 2002.

Went, F. W.: Blue hazes in the atmosphere, Nature, 187, 641–643, 1960.

Werner, H.-J., Adler, T. B., and Manby, F. R.: General orbital invariant MP2-F12 theory, J. Chem. Phys., 126, doi:10.1063/1.2712434, 2007.

Werner, H.-J., Knowles, P. J., Manby, F. R., Schütz, M., Celani, P., Knizia, G., Korona, T., Lindh, R., Mitrushenkov, A., Rauhut, G., Adler, T. B., Amos, R. D., Bernhardsson, A., Berning, A., Cooper, D. L., Deegan, M. J. O., Dobbyn, A. J., Eckert, F., Goll, E., Hampel, C., Hesselmann, A., Hetzer, G., Hrenar, T., Jansen, G., Köppl, C., Liu, Y., Lloyd, A. W., Mata, R. A., May, A. J., McNicholas, S. J., Meyer, W., Mura, M. E., Nicklass, A., Palmieri, P., Pflüger, K., Pitzer, R., Reiher, M., Shiozaki, T., Stoll, H., Stone, A. J., Tarroni, R., Thorsteinsson, T., Wang, M., and Wolf, A.: MOLPRO, version 2008.1, a package of ab initio programs, URL `http://www.molpro.net`, 2008.

Wiedinmyer, C., Tie, X., Guenther, A., Neilson, R., and Granier, C.: Future changes in biogenic isoprene emissions: How might they affect regional and global atmospheric chemistry?, Earth Interactions, 10, international Young Scientists Global Change Conference 2003, Trieste, ITALY, NOV 16-19, 2003, 2006.

Williams, J., Poschl, U., Crutzen, P. J., Hansel, A., Holzinger, R., Warneke, C., Lindinger, W., and Lelieveld, J.: An atmospheric chemistry interpretation of mass scans obtained from a proton transfer mass spectrometer flown over the tropical rainforest of Surinam, J. Atmos. Chem., 38, 133–166, 2001.

Yousaf, K. E. and Peterson, K. A.: Optimized auxiliary basis sets for explicitly correlated methods, J. Chem. Phys., 129, doi:10.1063/1.3009271, 2008.

Chapter 8

Peroxy radical isomerization in the oxidation of isoprene*

8.1 Abstract

We report experimental evidence for the formation of C_5-hydroperoxy-aldehydes (HPALDs) from 1,6-H-shift isomerizations in peroxy radicals formed from the hydroxyl radical (OH) oxidation of 2-methyl-1,3-butadiene (isoprene). At 295 K, the isomerization rate of isoprene peroxy radicals ($\mathrm{ISO}_2^\bullet$) relative to the rate of reaction of $\mathrm{ISO}_2^\bullet + \mathrm{HO}_2$ is $\frac{k_{\mathrm{isom}}^{295}}{k_{\mathrm{ISO}_2^\bullet + \mathrm{HO}_2}^{295}} = (1.2 \pm 0.6) \times 10^8$ molec. cm^{-3}, or $k_{\mathrm{isom}}^{295} \simeq 0.002\,\mathrm{s}^{-1}$. The temperature dependence of this rate was determined through experiments conducted at 295, 310 and 318 K and is well described by $\frac{k_{\mathrm{isom}}(T)}{k_{\mathrm{ISO}_2^\bullet + \mathrm{HO}_2}(T)} = 2.0 \times 10^{21} \exp(-9000/T)$ molec. cm^{-3}. The overall uncertainty in the isomerization rate (relative to $k_{\mathrm{ISO}_2^\bullet + \mathrm{HO}_2}$) is estimated to be 50%. Peroxy radicals from the oxidation of the fully deuterated isoprene analog isomerize at a rate ~ 15 times slower than non-deuterated isoprene. The fraction of isoprene peroxy radicals reacting by 1,6-H-shift isomerization is estimated to be 8-11% globally, with values up to 20% in tropical regions.

8.2 Introduction

Approximately 500 Tg of isoprene (C_5H_8) originating primarily from plants is realeased to Earth's atmosphere each year (Guenther et al., 2006). The oxidation of isoprene in the atmosphere is largely initiated by reaction with hydroxyl radicals (OH). The bulk of this reaction proceeds through addition of the OH to one of the two external olefinic carbon atoms. In the presence of oxygen, 6 different peroxy radicals (collectively $\mathrm{ISO}_2^\bullet$) are formed from reaction with O_2 (R8.1).

$$\text{isoprene} + \text{OH} \xrightarrow{\mathrm{O}_2} \mathrm{ISO}_2^\bullet \qquad\qquad \text{R8.1}$$

In nearly all chemical mechanisms used to describe atmospheric photochemistry, the subsequent fate of $\mathrm{ISO}_2^\bullet$ is determined by reaction with either NO (R8.2a and R8.2b) or HO_2 (R8.3).

$$\mathrm{ISO}_2^\bullet + \mathrm{NO} \xrightarrow{k_{\mathrm{ISO}_2^\bullet + \mathrm{NO}} \times (1 - \mathrm{NY})} \mathrm{ISO}^\bullet + \mathrm{NO}_2 \qquad\qquad \text{R8.2a}$$

$$\mathrm{ISO}_2^\bullet + \mathrm{NO} \xrightarrow{k_{\mathrm{ISO}_2^\bullet + \mathrm{NO}} \times \mathrm{NY}} \mathrm{ISONO}_2, \qquad\qquad \text{R8.2b}$$

where, NY = nitrate yield.

$$\mathrm{ISO_2^{\bullet} + HO_2} \xrightarrow{k_{\mathrm{ISO_2^{\bullet}+HO_2}}} \mathrm{ISOPOOH + O_2} \qquad \text{R8.3}$$

This representation is consistent with a wealth of laboratory studies of the reactivity of peroxy radicals. Such studies have typically been performed with sufficient concentrations of NO or HO_2 that the lifetimes of the peroxy radicals are very short – often less than 0.1 sec. For vast regions of the atmosphere (including most of the tropics), however, the peroxy radicals are estimated to live for 10's of seconds before finding a reactive partner in either NO or HO_2 (e.g., for observed NO and HO_2 levels over Amazonia (Lelieveld et al., 2008), $\mathrm{ISO_2^{\bullet}}$ lifetime with respect to R8.2a-R8.3 is calculated to be 30-60 s).

A number of recent analyses have cast doubt on the traditional representation of peroxy radical chemistry (R8.2a-R8.3). In particular, motivated by the inability to explain measured concentrations of OH in regions with elevated levels of biogenically-derived hydrocarbons (Tan et al., 2001; Thornton et al., 2002; Ren et al., 2008; Lelieveld et al., 2008; Hofzumahaus et al., 2009), investigators have hypothesized that the peroxy radicals of the dominant VOC, isoprene, may not follow the traditional reactive pathways R8.2a-R8.3. Most recently, Peeters et al. (2009) and da Silva et al. (2010) have estimated from quantum mechanical calculations that intramolecular hydrogen transfer reactions of the isoprene peroxy radicals (R8.4) substantially alter the trajectory of the isoprene chemistry, significantly diminishing the impact of isoprene oxidation on HO_x concentrations.

$$\mathrm{ISO_2^{\bullet}} \xrightarrow{k_{\mathrm{isom}}} \mathrm{HO_x + carbonyl(s)} \qquad \text{R8.4}$$

Here, we report product yields in the oxidation of isoprene and its fully deuterated analog by OH in the presence of NO and HO_2 concentrations similar to those encountered in the environment. We report temperature dependent formation rates for unsaturated C_5-hydroperoxyaldehydes (HPALDs) (Peeters et al., 2009) generated through 1,6-H-shift isomerization of two of the six peroxy radical isomers, *Z*-1-OH-4-OO (R8.5) and *Z*-4-OH-1-OO (R8.6). We assess the extent to which these intramolecular hydrogen transfer reactions occur in the atmosphere using the GEOS-Chem chemical

transport model.
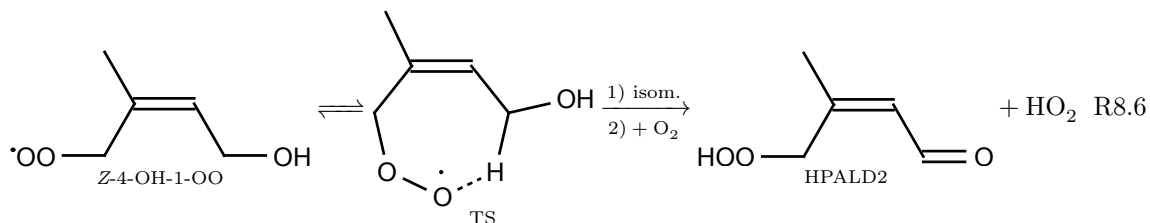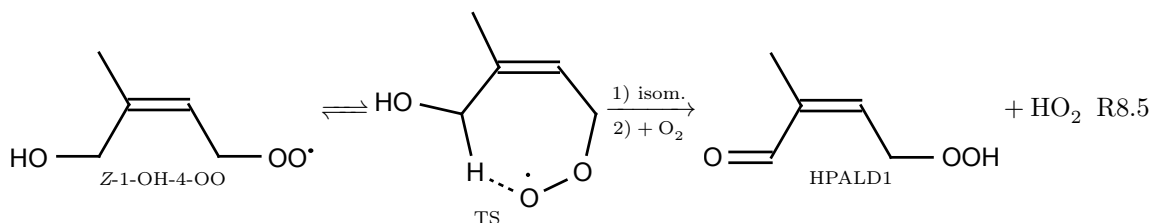
8.3 Experiment

Experiments were conducted within a $\sim 1\,\mathrm{m}^3$ bag composed of fluorinated ethylene propylene copolymer (Teflon-FEP, DuPont). The bag was enclosed in a chamber that is painted black on the inside and equipped with ultra-violet (UV) lights (Sylvania F40/350BL) mounted to one wall. Photolysis of CH_3ONO provided the primary HO_x source as described in R8.7-R8.8 (Cox et al., 1980). In order to achieve the slow chemistry required to study the RO_2 isomerization reactions, only a single UV bulb was used. In addition, the direct emission from this UV-bulb was blocked, such that only photons reflected from the fixture back-reflector contributed to the light flux. The photon intensity as a function of wavelength (300-850 nm) was measured using a Licor (LI-1800) spectroradiometer. Using published CH_3ONO cross-sections (Taylor et al., 1980), and assuming a quantum yield of 1 for all wavelengths, we calculate $J_{CH_3ONO} = 0.9\times10^{-5}\,\mathrm{s}^{-1}$ ($J_{NO_2} = 2.8\times10^{-5}\,\mathrm{s}^{-1}$) for the measured light intensity.

$$CH_3ONO + hv \xrightarrow{O_2} HO_2 + NO + HCHO \qquad\qquad R8.7$$

$$HO_2 + NO \longrightarrow OH + NO_2 \qquad\qquad R8.8$$

High purity isoprene-H_8 (C_5H_8) and methacrolein were purchased from Sigma-Aldrich and used without further purification. Fully deuterated isoprene (isoprene-D_8, C_5D_8, $\frac{D}{D+H} > 0.98$, Polymer Source, Inc.) was used without purification. Gas-phase standards of ~ 200 ppmv of each compound were created by evaporating a known mass of liquid material into a known volume of N_2. The concentration of this mixture was verified for isoprene-H_8 by FTIR spectroscopy using tabulated cross-sections (Sharpe et al., 2004). The concentration determined from the mass and volume measurements and the IR measurements agree to within 5%. Generally, 100 cm^3 of the 200 ppmv VOC mixture was transferred to the 1 m^3 experiment bag using a gas-tight ground-glass syringe.

Methylnitrite (CH_3ONO) was synthesized by slowly adding concentrated sulphuric acid to a solution of sodium nitrite in methanol and water with vigorous stirring. A stream of dry N_2 carried vapors above the reaction mixture through a saturated sodium hydroxide solution, and then through a trap containing Dryrite before entering a cold trap at -60° C where the CH_3ONO was condensed. CH_3ONO was purified first by pumping on the trap at -60° C, and then through several thaw-freeze-pump cycles. After purification the trap containing the CH_3ONO was stored in liquid nitrogen. For use in experiments, the CH_3ONO trap was removed from the liquid nitrogen and allowed to warm, releasing ~ 5 hPa CH_3ONO vapor into an evacuated 500 cm^3 bulb. The contents of the bulb were discarded. After a second fill, the bulb pressure was reduced to ~ 0.1 hPa, and then its contents were transferred to the experiment bag.

For experiments with initial NO, a 500 cm^3 bulb was filled with ~ 15 hPa of gas from a primary standard tank containing 1993 ± 20 ppmv NO in N_2 (Matheson). The contents of the bulb are then transferred to the experiment bag.

Clean, dry air was generated from compressed house air using a FT-IR purge gas generator (Perkin, Model 75-52). A known amount (~ 980L) of zero air was added to the bag using a mass flow meter (MKS).

Upon illumination, very slow photochemistry is initiated. After ~ 4 hours of slow photochemistry, six additional unblocked UV bulbs were energized, increasing the photon flux by a factor of ~ 30. This rapidly completed the isoprene oxidation and allowed for mass balance to be evaluated.

Reaction products are monitored using chemical ionization mass spectrometry (CIMS) (Crounse et al., 2006; Paulot et al., 2009b) triple quadrupole instrument (Paulot et al., 2009b; St Clair et al., 2010). The CF_3O^- ion chemistry and instrumentation has been described in detail previously (Crounse et al., 2006; Paulot et al., 2009a,b; St Clair et al., 2010), and will only briefly be described here. Air is drawn from the experiment bag at a rate of ~ 1.8 standard liters per minute (slpm)

through ~1 m of 6.35 mm O.D. Teflon (PFA) tubing, where 260 standard cubic centimeters (sccm) of gas sub-sampled into the CIMS flowtube. The remainder of flow is routed to commercial ozone and NO_x monitors. Within the CIMS flowtube, air from the experiment bag is diluted with 1540 sccm of dry N_2 (from liquid nitrogen boiloff).

Neutral analytes react with CF_3O^- ions primarily through CF_3O^- clustering and/or fluoride transfer reactions to form product ions observed at $m/z = \mathrm{mass_{neutral}} + 85$ amu, and $m/z = \mathrm{mass_{neutral}} + 19$ amu, respectively. For certain isobaric analytes, CF_3O^- tandem MS analysis provides separate quantification. Several analytes which are undetectable using CF_3O^- ion chemistry were monitored using positive mode via $H^+ \cdot (H_2O)_n$ ion chemistry.

H_2O_2 was monitored using the CF_3O^- cluster ion at $m/z = 119$ and quantified using calibration factors obtained from gas phase standard addition (Crounse et al., 2006). Hydroperoxides, hydroxycarbonyls, and hydroxynitrates were monitored using the sum of cluster and transfer product ions, and were quantified using calculated relative ion-molecule collision rates (Section 8.6.1). HNO_3, HONO, and HO_2NO_2 were monitored at transfer product ions and quantified using calibration factors obtained from standard additions. H_2O concentrations were monitored using the $^{13}CF_3O^- \cdot H_2O$ ion cluster observed at $m/z = 104$, and quantified using calibration factors from standard additions of H_2O. Water vapor mixing ratios generally increased from 100 to 1000 ppmv over the course of the experiment from diffusion and/or leaks into the teflon bag. The sum of methylvinylketone (MVK) and methacrolein (MACR) are monitored using the positive mode product ion observed at $m/z = 71$ and quantified using calibration factors from standard additions of MACR.

Experiments were performed at three different temperatures. Using a resistive heater, steady-state temperatures of 295, 310, 318 K were maintained. A box fan was used to circulate air within the chamber. The temperature uniformity and stability was ±2 K.

8.4 Results and discussion

8.4.1 Determination of isomerization rates

The observations of H_2O_2, ISOPOOH, and HPALD over the first 2 hours of slow oxidation along with recommended rate constant for $HO_2 + HO_2$ are used to evaluate the isomerization rate for isoprene peroxy radicals relative to their reaction with HO_2. In the absence of secondary chemistry, the observed time-rate-of-change for each product is equal to the production rate, defined in eqns

Table 8.1 – Summary of experiments. All experiments were conducted at atmospheric pressure (993±7 hPa). Product growth rates are given in units of pptv min^{-1}. The 1σ precision from the linear fits are listed for product growth rates and propagated through eqn (8.5) to determine the $\frac{k_{\text{isom}}}{k_{\text{ISO}_2+\text{HO}_2}}$ precision.

Exp.-VOC	T	[VOC]$_0$	[NO]$_0$	$\frac{d[\text{H}_2\text{O}_2]}{dt}$	$\frac{d[\text{ISOPOOH}]}{dt}$ a	$\frac{d[\text{HPALD}]}{dt}$ b	$\frac{d[\text{ISONO}_2]}{dt}$ c	$\frac{d[\text{MVK+MACR}]}{dt}$ d	$\frac{k_{\text{isom}}}{k_{\text{ISO}_2+\text{HO}_2}}$ f
	(K)	(ppbv)	(ppbv)						(10^8 molec. cm^{-3})
1-isop-H$_8$	295.2±1.4	21.1	0	2.33±0.10	4.27±0.62	1.02±0.03	0.53±0.02	7.53±0.33	1.18±0.18
2-isop-H$_8$	310.2±1.4	22.6	0	3.61±0.13	3.78±0.53	2.78±0.08	0.36±0.02	5.31±0.28	4.81±0.69
3-isop-H$_8$	318.2±1.4	21.2	0	5.21±0.22	3.10±0.31	4.06±0.07	0.16±0.07	4.76±0.23	10.7±1.1
4-isop-H$_8$	295.1±1.4	19.0	19	0.01±0.05	0.01±0.01	0.35±0.12	6.71±0.13	50.9±0.63	-
5-isop-D$_8$	295.3±1.4	21.4	0	1.65±0.10	3.81±0.41	0.073±0.012	0.72±0.02	6.19±0.26	0.08±0.02
6-isop-D$_8$	310.2±1.4	21.3	0	2.00±0.10	3.26±0.41	0.24±0.09	0.51±0.03	5.87±0.27	0.36±0.06
7-isop-D$_8$	316.8±1.4	19.1	0	2.10±0.14	4.04±0.75	0.57±0.06	0.46±0.05	4.89±0.18	0.71±0.16
8-isop-D$_8$	294.9±1.4	21.3	20	0.04±0.08	0.02±0.03	0.06±0.02	5.35±0.13	28.3±0.68	-

a C$_5$-hydroxyhydroperoxide isomers observed at CF$_3$O$^-$-cluster mass of $m/z = 203$ for isoprene-H$_8$ and $m/z = 211$ for isoprene-D$_8$

b C$_5$-hydroperoxyaldehyde isomers (HPALD) attributed to form from isomerization reactions and observed at CF$_3$O$^-$-cluster mass of $m/z = 201$ for isoprene-H$_8$ and $m/z = 208$ for isoprene-D$_8$.

c C$_5$-hydroxynitrate isomers observed at CF$_3$O$^-$-cluster mass of $m/z = 232$ for isoprene-H$_8$ and $m/z = 240$ for isoprene-D$_8$.

d Sum of MVK and MACR carbonyls observed at H$^+$-cluster mass of $m/z = 71$ for isoprene-H$_8$ and $m/z = 77$ for isoprene-D$_8$ (MVK-D$_6$+MACR-D$_6$).

f Bulk isomerization rate for sum of ISO$_2^\bullet$ isomers, including ISO$_2^\bullet$ interconversion processes.

(8.1-8.3).

$$P_{\text{H}_2\text{O}_2} = k_{\text{HO}_2+\text{HO}_2}[\text{HO}_2]^2 \tag{8.1}$$

$$P_{\text{ISOPOOH}} = Y_{\text{ISOPOOH}} k_{\text{ISO}_2^\bullet+\text{HO}_2}[\text{HO}_2][\text{ISO}_2^\bullet] \tag{8.2}$$

$$P_{\text{HPALD}} = k_{\text{isom}}[\text{ISO}_2^\bullet] \tag{8.3}$$

Here we assume $Y_{\text{ISOPOOH}} = 0.88\pm0.12$ (Paulot et al., 2009b) and use the recommended expression (Atkinson et al., 2004) for the rate of HO$_2$ self-reaction shown in eqn (8.4).

$$k_{\text{HO}_2+\text{HO}_2} = \{2.2 \times 10^{-13}\exp(600/\text{T}) \tag{8.4}$$
$$+ 2.8 \times 10^{-33}[\text{M}]\exp(980/\text{T})\}$$
$$\times \{1 + 1.4 \times 10^{-21}[\text{H}_2\text{O}]\exp(2200/\text{T})\}$$

Combining eqns (8.1-8.3),

$$\frac{k_{\text{isom}}}{k_{\text{ISO}_2^\bullet+\text{HO}_2}} = \frac{Y_{\text{ISOPOOH}}\, P_{\text{HPALD}}}{\left\{\frac{k_{\text{HO}_2+\text{HO}_2}}{P_{\text{H}_2\text{O}_2}}\right\}^{1/2} P_{\text{ISOPOOH}}} \tag{8.5}$$

The determination of k_{isom} relative to $k_{\text{ISO}_2^\bullet+\text{HO}_2}$ relies only on experimental observations and the well-known $k_{\text{HO}_2+\text{HO}_2}$. As illustrated below, knowledge of the ratio of these rates is largely sufficient to describe the importance of this reaction in the atmosphere, as the regions where isomerization reactions become important (long $\text{ISO}_2^\bullet$ lifetimes) are dominated by HO_2 chemistry. Nevertheless, using the $k_{\text{ISO}_2^\bullet+\text{HO}_2}$ recommendation from Saunders et al. (2003) (eqn (8.6)), k_{isom} can be estimated. We note that at 298 K, this recommendation (Saunders et al., 2003) agrees well with the only experimental determination of this rate (Boyd et al., 2003a).

$$k_{\text{ISO}_2^\bullet+\text{HO}_2} = 2.06 \times 10^{-13} \exp(1300/\text{T}) \tag{8.6}$$

OH and NO levels are estimated using an explicit photochemical model (Paulot et al., 2009a). Observations of NO using the commercial NO_x monitor are precluded by interferences from CH_3ONO, and HONO. The perfomance of the model is evaluated through comparison with a number of observed species including H_2O_2, ISOPOOH, MVK+MACR, ISONO_2, HONO, HO_2NO_2, and HNO_3.

8.4.2 Slow chemistry.

The very slow chemistry ([OH]$\sim$1-2$\times10^5$ molec. cm^{-3}, for experiments with no initial NO) established in these experiments enables long $\text{ISO}_2^\bullet$ lifetimes, similar to those in the pristine atmosphere (Lelieveld et al., 2008). HO_2 concentrations range from 20-40 pptv. NO levels range from 30-60 pptv. The combined low HO_2 and NO concentrations produces $\text{ISO}_2^\bullet$ lifetimes up to $\sim$50 s. A summary of the experiments is given in Table 8.1.

Fig. 8.1 shows time traces of H_2O_2, ISOPOOH, and HPALD (sum of HPALD1 and HPALD2) are shown for isoprene oxidation experiments conducted at two temperatures. The sum of ISOPOOH isomers were monitored using the CF_3O^- cluster ion observed at $m/z = 203$ (isoprene-H_8) and $m/z = 211$ (isoprene-D_8), and distinguished from the later generation isobaric epoxide using tandem MS mode ($m/z = 203 \rightarrow m/z = 63$ or $m/z = 211 \rightarrow m/z = 63$) (Paulot et al., 2009b). The sum of HPALD isomers were monitored at $m/z = 201$ (isoprene-H_8) and $m/z = 208$ (isoprene-D_8).
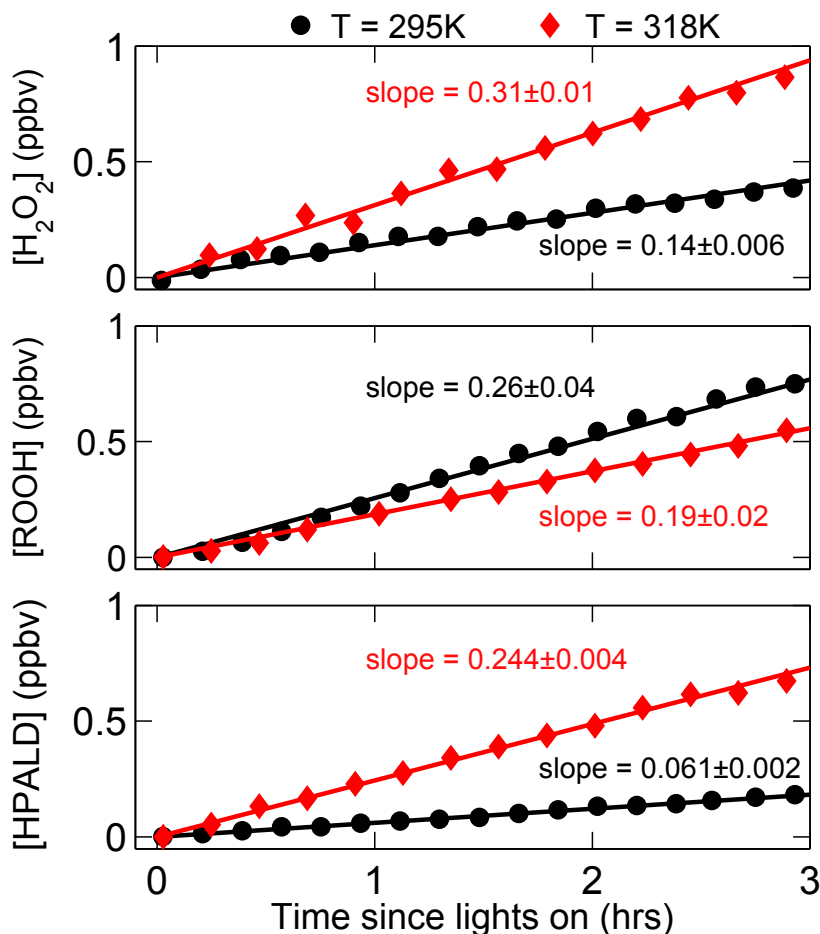
Figure 8.1 – Observations of H_2O_2 (top), ISOPOOH (middle), and HPALD (bottom) species during oxidation of normal isoprene (C_5H_8). Results from experiments #1 (black circles, T=295.2 K) and #3 (red diamonds, T=318.2 K) are shown. Lines represent the best fit parameters from linear ordinary least-squares regression.

Although HPALD compounds formed from isoprene-D_8 initially contain a deuterated hydroperoxide group (-OOD) ($m/z = 209$), we observe the product at $m/z = 208$. This is due to fast D-H exchange of the hydroperoxide hydrogen atom with hydrogen atoms in the background H_2O on the walls of the bag and the gas sampling system. We have observed such rapid exchange in previous experiments for both hydroxy and hydroperoxy hydrogen atoms. Tandem MS investigation of both $m/z = 201$ and 208 product ions gave a significant yield of the daughter ion with $m/z = 63$, similar to the tandem MS of the ISOPOOH product ions, supporting the attribution of these signals to a hydroperoxide species (Paulot et al., 2009b).

The isoprene oxidation rate is quite similar for both experiments shown in Fig. 8.1. The growth rate for H_2O_2 is substantially greater for the warmer experiment, however, indicating higher HO_2 levels. This is consistent with enhanced HO_2 production from the isomerization processes, reduced

HO_2 loss from $ISO_2^\bullet + HO_2$, and lower NO concentrations (due to the higher HO_2).

The observed product growth rates listed in Table 8.1 are obtained from the slope of the ordinary least-squares fit to the CIMS observations over the first 2 hrs of photooxidation for experiments with no initial NO (0.7 hrs for NO expts.), along with the standard 1σ uncertainty to the fit. In experiments with no initial NO, $\sim$8% of the initial isoprene is oxidized over this period. No correction is made for the oxidation of the product species. Neglecting this loss for a product which reacts with OH at the same rate as isoprene produces an error of $< 10\%$ using the method of Atkinson et al. (1982). For these experimental conditions, photolysis of HPALD is also negligible. Using the photolysis cross-section of MACR with a quantum yield $= 1$ (recommended by Peeters et al. (2009)), we estimate $J_{\mathrm{HPALD}} = 2\times10^{-6}\,\mathrm{s}^{-1}$. An explicit photochemical model of this system shows that the error in equating the observed linear increase to the average rate of production for these products over this time-frame is small ($<$5%) due to the slow chemistry. No correction is made for heterogeneous loss of the product species. In general, however, unaccounted product loss rates only impact our derivation of k_{isom} by the relative difference in the loss rates of ISOPOOH and HPALD. As ISOPOOH and HPALD species are structurally similar, the heterogeneous loss processes are also likely similar.

HPALD products are preferentially formed at warmer temperature, consistent with the proposed origin involving a primary H-shift over or through a significant barrier (Fig. 8.1 and Table 8.1). In addition, HPALD formation for isoprene-D_8 is observed to be slower than for isoprene-H_8 by factors of 15.4 and 13.0 at $T =$295 and 318 K, respectively.

Fig. 8.2 shows the isoprene peroxy radical isomerization data listed in Table 8.1 on an Arrhenius plot. Also shown are the best-fit equations to the data which are derived using a York-type fit (York et al., 2004), accounting for uncertainties (Table 8.1) in both coordinates. While the observed isomerization rates are well-represented by the functional parameters shown in Fig. 8.2 (reproduce observations to within 5%), these parameters are only valid for 295-318 K temperature range. Large uncertainties in these parameters limit their interpretation in the traditional context of entropic and enthalpic constraints.

8.4.3   Overall uncertainty in 1,6-H-shift isomerization rate

The uncertainty values for $\frac{k_{\mathrm{isom}}}{k_{\mathrm{ISO}_2^\bullet+HO_2}}$ listed in Table 8.1 reflect only the propagated 1σ standard precision from the ordinary least-square fits to the production rates of H_2O_2, ISOPOOH, and HPALD. Using the standard precision listed in Table 8.1 and 0.15, 0.14, 0.2, and 0.4 for uncertainties in
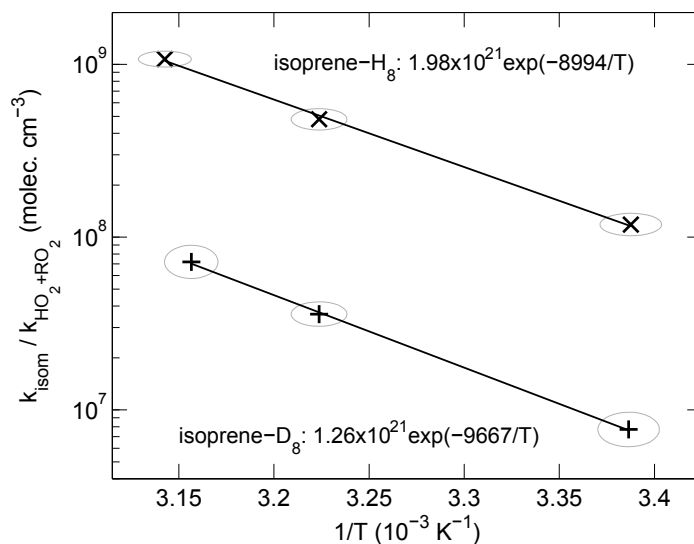
Figure 8.2 – Temperature dependence of 1,6-H-shift isomerization rates yielding HPALD compounds relative to the rate of $ISO_2 + HO_2$ reaction, constrained through simultaneous observations of HPALD (HPALD1 + HPALD2), ISOPOOH, and H_2O_2 (eqn (8.5)) for normal (C_5H_8, × symbols) and deuterated (C_5D_8, + symbols) isoprene. The axes of the elipses surrounding each data point show the 1σ uncertainty in each coordinate (Table 8.1).

$k_{HO_2+HO_2}$, $Y_{ISOPOOH}$, $P_{H_2O_2}$, and in the relative calibration between ISOPOOH and HPALD, respectively, we estimate the overall uncertainty in $\frac{k_{isom}}{k_{ISO_2^{\bullet}+HO_2}}$ to be $\sim 50\%$.

8.4.4 Comparison with theory

The isomerization rate for 1,6-H-shift for the δ-isoprene peroxy radicals is substantially slower than predicted in the theoretical calculations of Peeters et al. (2009) and later refined in subsequent works (Stavrakou et al., 2010; Peeters and Muller, 2010; Nguyen et al., 2010). A direct comparison to the theoretical rate is not, however, straightforward as we only observe the end product of two important processes, namely: a) interconversion between the β-OH-OO, Z-δ-OH-OO, and E-δ-OH-OO peroxy radicals (shown for 1-OH isomers in R8.9); and b) the 1,6-H-shift isomerization reactions from the two Z-δ-OH-OO peroxy radicals (R8.5 and R8.6):

R8.9
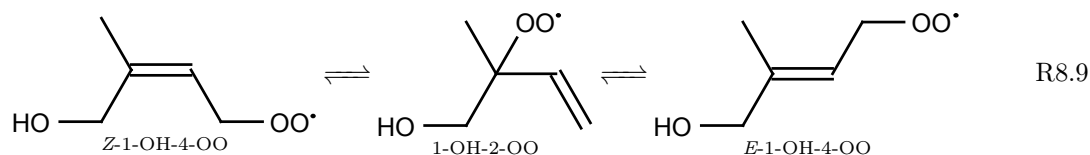
Using Peeters et al. (2009) estimates of $ISO_2^{\bullet}$ interconversion rates and the refined isomerization

rate for the Z-δ-OH-OO from Peeters and Muller (2010), we calculate a bulk isomerization rate $\sim$50 times faster than measured. The theoretical ratio $\frac{k_{\text{isom-H}}}{k_{\text{isom-D}}}$ from Nguyen et al. (2010) is a factor of 2.3 (295 K) and 1.3 (318 K) higher than experimentally observed here.

8.4.5 Subsequent fate of HPALD unknown

The maximum HPALD concentrations achieved during these experiments did not exceed 1 ppbv. The total yield was limited by the slow chemistry required for observation of the peroxy radical isomerization reactions and by the volume of the bag. Due to the low HPALD concentrations, products from its subsequent photooxidation could not be clearly identified. We intend to undertake future experiments to probe this chemistry.

8.4.6 1,5-H-shift (from alcohol)

Peeters et al. (2009) and da Silva et al. (2010) also calculated rates for 1,5-H-shift isomerization/decomposition reactions, where an alkoxy radical is formed as the alcohol hydrogen is abstracted by the peroxy group in the dominant β-hydroxyperoxy radicals formed from isoprene oxidation by OH (1-OH-2-OO and 4-OH-3-OO). The alkoxy radicals are expected to rapidly decompose, forming OH+HCHO+C_4-carbonyl (MVK or MACR). Both calculations predict the same products, though with significantly different rates (Peeters et al. (2009) is $\sim 8\times$ faster at T=298K). Based on the assumption that the observed yield of MVK+MACR reported by Paulot et al. (2009b) came from this process, the rate of Peeters et al. (2009) was adjusted upwards by a factor of 5 in the more recent study of Peeters and Muller (2010). Paulot et al. (2009b), however, attributed the observed MVK+MACR yield ($[12\pm12]\%$) a radical channel in the $\text{ISO}_2^{\bullet}+\text{HO}_2$ reaction. In addition, uncertainties in the $\text{ISO}_2^{\bullet}+\text{ISO}_2^{\bullet}$ reaction rates as well as in the determination of the fraction of $\text{ISO}_2^{\bullet}$ radicals reacting with NO could very well account for all the observed MVK+MACR reported in the Paulot et al. (2009b) study.

We are unable to experimentally estimate the rate of the 1,5-H-shift in this study primarily due to large uncertainties in the $\text{ISO}_2^{\bullet}+\text{ISO}_2^{\bullet}$ reaction rate constants and product branching ratios, as well as uncertainties in the $\text{ISO}_2^{\bullet}$-isomer specific nitrate yields from $\text{ISO}_2^{\bullet}$ + NO, and unknown temperature dependencies for all these parameters. Using the $\text{ISO}_2^{\bullet}+\text{ISO}_2^{\bullet}$ parameters recommended by Jenkin et al. (1998), and the nitrate yields of Paulot et al. (2009a) coupled with the temperature dependence recommended by Carter and Atkinson (1989), the observed isoprene-nitrate/(MVK+MACR) ratio is not, however, compatible with 1,5-H-shift rate recommended by Peeters and Muller (2010). The

rate calculated by da Silva et al. (2010) ($\sim$ factor of 40 slower) is consistent with our observations, but also not well-constrained (Fig. 8.4). In any case, this isomerization channel is likely only of minor importance in the atmosphere.

8.4.7 Nitrate yields and ISO$_2$ interconversion

Isoprene nitrate yields are observed to decrease relative to MVK+MACR with increasing temperature. This is consistent with previous studies of the temperature dependence of organic nitrate formation (e.g., Carter and Atkinson (1989)) and is attributed to a longer lifetime of the excited ROONO* (and/or RONO$_2$*) complex at cooler temperatures allowing for increased collisional deactivation (Barker et al., 2003). Similarly, we attribute the much higher isoprene-D$_8$ hydroxy nitrate yields relative to those from isoprene-H$_8$ (a factor of 1.7 and 1.4 for low and high NO conditions, expts. 1,5 and 4,8; Table 8.1) to increased stabilization of the ROONO* (and/or RONO$_2$*) complex from nearby deuterium atoms as compared with hydrogen atoms.

There is a significant difference in the ratio of ISONO$_2$/(MVK+MACR) between the high and low NO experiments at 295 K. While this difference could result from more heterogeneous nitrate loss in the slow experiment, it may reflect differences in the peroxy radical distribution between these two experiments as the high NO experiment would be closer to the initial kinetic distribution of ISO$_2^\bullet$ (higher fraction in δ) and the slow experiment closer to the thermodynamic equilibrium for ISO$_2^\bullet$ (lower fraction in δ) (Peeters et al., 2009). Giacopelli et al. (2005) and Paulot et al. (2009a) estimate significantly higher nitrate yields from the δ-hydroxy peroxy radicals as compared to the β-hydroxy peroxy radicals. The large (up to $\sim$30%), and continued increase in HPALD yields with temperature provide evidence that the isoprene peroxy radicals do indeed interconvert on the timescale of the estimated lifetime of the peroxy radicals in these experiments ($\sim$50 s).

8.5 Atmospheric implications

The fraction of isoprene peroxy radicals undergoing isomerization in Earth's atmosphere was estimated using the GEOS-Chem (v8.3.2) 3-D global model (Bey et al., 2001) with a modified chemical mechanism including updated isoprene chemistry as described previously (Paulot et al., 2009a,b, 2011). Simulations were conducted with and without the isoprene peroxy radical isomerization for the June 2006 - May 2007 time period with a 1.5 year model spin-up. We implemented the isomerization process through the addition of R8.10. Due to uncertainties regarding the fate of HPALD

we did not consider the further oxidation chemistry of this compound. This is equivalent to considering the subsequent chemistry as HO_x-neutral. In addition, the sensitivity of the model to the rate coefficient for the reaction of isoprene peroxy radicals with HO_2 was investigated. In the standard GEOS-Chem mechanism, the rate of $ISO_2^\bullet + HO_2$ is $k_{ISO_2^\bullet + HO_2} = 7.40 \times 10^{-13} \exp(700/T)$. At $T = 298\,\mathrm{K}$, this rate is $\sim \frac{1}{2}$ that calculated from eqn (8.6). While this does not change the ratio of k_{isom} relative to $k_{ISO_2^\bullet + HO_2}$ (as we determined only the relative value), it does reduce both rates relative to $k_{ISO_2^\bullet + NO}$.

$$ISO_2^\bullet \xrightarrow{k_{isom}} HO_2 \qquad\qquad \text{R8.10}$$

Isoprene peroxy radicals are predicted to react 44.1% with NO, 42.6% with HO_2, with 7.4% isomerizating to form HPALD using the slow $ISO_2^\bullet + HO_2$ rate. Simulations using the faster $ISO_2^\bullet + HO_2$ rate (eqn (8.6)) result in the following isoprene $ISO_2^\bullet$ loss distribution: 33.5% reaction with NO, 53.5% reaction with HO_2, and 9.6% isomerization. As expected, the ratio between the HO_2/isomerization loss processes remains about the same in these two simulations. The spatial distribution of the fraction of isoprene peroxy radicals predicted to undergo isomerization reaction is shown in Fig. 8.3. While not the dominant process suggested previously (Peeters et al., 2009; Stavrakou et al., 2010; Archibald et al., 2010; Peeters and Muller, 2010), peroxy radical isomerization is an important process for isoprene oxidation in the atmosphere even with the slow isomerization rate reported here. Goals for future studies include the elucidation of the oxidation mechanisms and products for HPALD compounds, as well as better constraints for the relative rates of reaction of isoprene peroxy radicals with NO and HO_2.

In a series of manuscripts (Jorand et al., 1996; Perrin et al., 1998b,a; Blin-Simiand et al., 1998; Jorand et al., 2000; Blin-Simiand et al., 2001), Jorand, Perrin, Blin-Simiand and co-workers have reported peroxy radical isomerizations in several systems at elevated temperatures. They have suggested that such isomerization reactions may be important for atmospheric chemistry. Until now, however, such mechanisms have not been studied under conditions relevant for atmospheric chemistry, nor have they been incorporated into the mechanisms of atmospheric chemistry models. In this work, we provide experimental evidence for the importance of such peroxy radical isomerization reactions under atmospherically relevant conditions. From the isomerization rates determined here, isoprene peroxy radical isomerization reactions are unlikely to reconcile the differences in HO_x levels between observations and model simulations (Archibald et al., 2010). It is possible, however, that
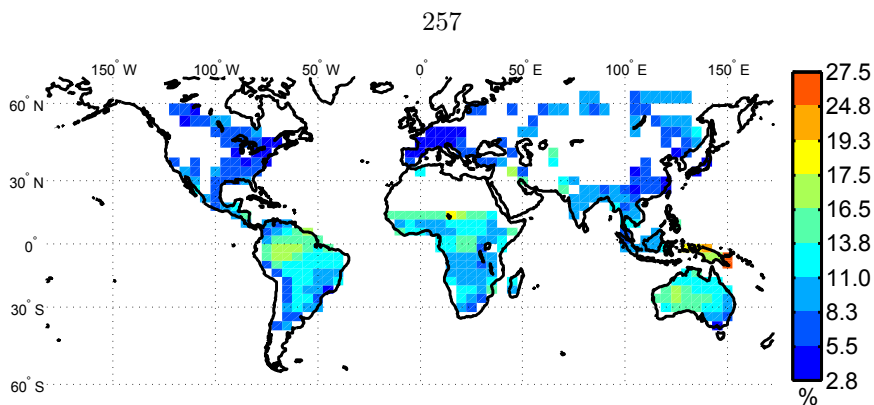
Figure 8.3 – Annual boundary layer ($P > 800$ hPa) percentage of isoprene peroxy radicals undergoing isomerization simulated using the GEOS-Chem chemical transport model at a resolution of $4°$ lat.$\times 5°$ long. Regions where isoprene mean monthly emissions are $< 1 \times 10^{11}$ molec. cm^{-2} s^{-1} are excluded. Data from simulations using $\frac{k_{\text{isom-H}_8}}{k_{\text{ISO}_2+\text{HO}_2}}$ given in Fig. 8.2 and $k_{\text{ISO}_2+\text{HO}_2}$ from Saunders et al. (2003) (eqn (8.6)).

other similar isomerization reactions contribute to HO$_x$ reformation. For example, similar studies on the oxidation of MACR performed in our laboratory (Crounse, *et al.*, in preparation) provide evidence for a fast 1,4-H-shift isomerization from the peroxy radical formed after OH addition to the external olefinic carbon, yielding OH and hydroxyacetone. It is likely that similar processes occur in the gas phase oxidation of other organic compounds for conditions where RO$_2$ lifetimes become sufficiently long. The methods described in this work should be generally useful for the future investigation of RO$_2$ isomerization reactions under such atmospherically relevant conditions.

8.6 Supporting information

8.6.1 CIMS sensitivity.

We estimate the CIMS sensitivity for the hydroxyhydroperoxides (ISOPOOH) and hydroperoxyaldehydes (HPALD) from the ion-molecule collision rate, calculated using the parameterization of Su and Chesnavich (1982). This requires knowledge of the average dipole moment and polarizibility of the neutral species. We obtain these parameters for the species of interest from *ab initio* calulations. For accurate results, all conformers with significant populations at the temperature of interest must be considered. We calculate conformer-specific dipoles for all conformers with a relative population of $>1\%$ at T=298K, as estimated from a Boltzman weighting to the conformer energies. The conformer-specific dipoles, weighted by their relative population, are averaged to yield the overall dipole moment for the species of interest. This methodology has been described in more detail by

Garden et al. (2009).

Table 8.2 lists the isomer-specific average dipole moments and polarizibilities for the four important ISOPOOH isomers and both HPALD isomers. In this work we use values calculated at the B3LYP/cc-pVTZ level. The same values calculated at the lower B3LYP/6-31G(d) level, used in the study of Paulot et al. (2009b), are listed for comparison.

The CIMS instrument measures the sum of isomers appearing at a specific mass. Thus to calculate the average CIMS sensitivity, we weight the four major ISOPOOH isomers according to the relative initial ISO_2 distribution (at 303 K) as calculated by Peeters et al. (2009) (1-OH-2-OO: 0.45, Z-1-OH-4-OO: 0.21, 4-OH-3-OO: 0.23, 4-OH-1-OO: 0.11). We give the HPALD isomers equal weight. Weighting the ISOPOOH sensitivity by the near-equilibrium ISO_2 distribution predicted for our experimental conditions at 295 K (1-OH-2-OO: 0.67, Z-1-OH-4-OO: 0.04, 4-OH-3-OO: 0.27, 4-OH-1-OO: 0.02) (Peeters et al., 2009) changes the inferred sensitivity by only $\sim$3%. As both HPALD isomers have similar dipole moments, our determinations are insensitive to this weighting scheme.

Absolute sensitivities for both ISOPOOH and HPALD are determined from the calculated ion-molecule collision rates using the average between the ratios of the experimentally determined sensitivities for glycolaldehyde and hydroxyacetone to their respective calculated-collision rate:

$$\overline{R}_{\mathrm{GH}} = \frac{\frac{S_{\mathrm{expt}}^{\mathrm{GLYC}}}{k_{\mathrm{coll}}^{\mathrm{GLYC}}} + \frac{S_{\mathrm{expt}}^{\mathrm{HAC}}}{k_{\mathrm{coll}}^{\mathrm{HAC}}}}{2}$$

$$S_{\mathrm{calc}}^{X} = k_{\mathrm{coll}}^{X} \times \overline{R}_{\mathrm{GH}}$$

The sensitivity for the isoprene hydroxynitrates is determined relative to nitric acid following Paulot et al. (2009a).

8.6.2   Rate of 1,5-H-shift (from alcohol).

Fig. 8.4 shows CIMS observations of MVK+MACR and isoprene nitrates as a function of time for experiment #3 (main paper, Table 1, T=318 K). Also shown are results from a kinetic model simulation for this isoprene oxidation experiment for MVK+MACR and isoprene nitrates using several values for the 1,5-H-shift isomerization rate ($k_{1,5\text{-isom}}$) within the model. Simulations were run using the rate for the 1,6-H-shift determined in this study, isomer-dependant nitrate yields from Paulot et al. (2009a), the temperature dependance for nitrate yields from Carter and Atkinson (1989), with several theoretical values for the 1,5-H-shift isomerization rates reported by Peeters

Table 8.2 – Average dipole moments and polarizibilities for ISOPOOH and HPALD isoprene oxidation products, for $T = 298$ K. Collision rates have units of 10^{-9} cm^3 molec.$^{-1}$ s^{-1}.

Molecule	Structure	B3LYP/6-31G(d)			B3LYP/cc-pVTZ		
		$\overline{\text{Dipole}}$	Polarizability	$k_{\text{coll}}^{\text{x}}$	$\overline{\text{Dipole}}$	Polarizability	$k_{\text{coll}}^{\text{x}}$
		(D)	(Å^3)		(D)	(Å^3)	
β1-ISOPOOH		2.19	9.44	1.85	2.32	10.8	1.96
β4-ISOPOOH		2.20	9.44	1.85	2.29	11.0	1.95
δ1-ISOPOOH		2.85	9.63	2.23	2.54	11.0	2.09
δ4-ISOPOOH		3.34	9.66	2.49	3.22	11.06	2.47
HPALD1		2.51	9.5	2.03	2.54	10.9	2.10
HPALD2		1.90	9.6	1.70	2.36	10.9	2.00
Glycolaldehyde		2.3	4.5	2.0	2.33	4.64	2.06
Hydroxyacetone		3.1	5.5	2.5	3.08	6.40	2.49
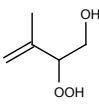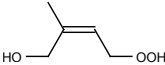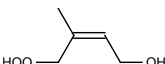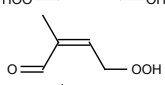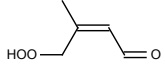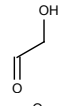
et al. (2009); da Silva et al. (2010); Peeters and Muller (2010). The rate calculated by Peeters et al. (2009)($k_{1,5\text{-isom}}^{318} = 0.026\,\text{s}^{-1}$) and increased by 5× in Peeters and Muller (2010) ($k_{1,5\text{-isom}}^{318} = 0.13\,\text{s}^{-1}$) predicts that the isoprene chemistry at the long ISO$_2{}^\bullet$ lifetimes and elevated temperature in this experiment should be dominated by this mechanism. This however, is not consistent with the CIMS observations. The geometric average of the rates for the two 1,5-H-shift isomerization channels calculated by da Silva et al. (2010) ($k_{1,5\text{-isom}}^{318} = 0.005\,\text{s}^{-1}$) is consistent with our results, but also is not well constrained, as errors in the assumed ISO$_2$ distribution, ISO$_2$ + ISO$_2$ reaction rates, and isomer-specific nitrate yields, all can impact the modeled MVK+MACR and ISONO$_2$.
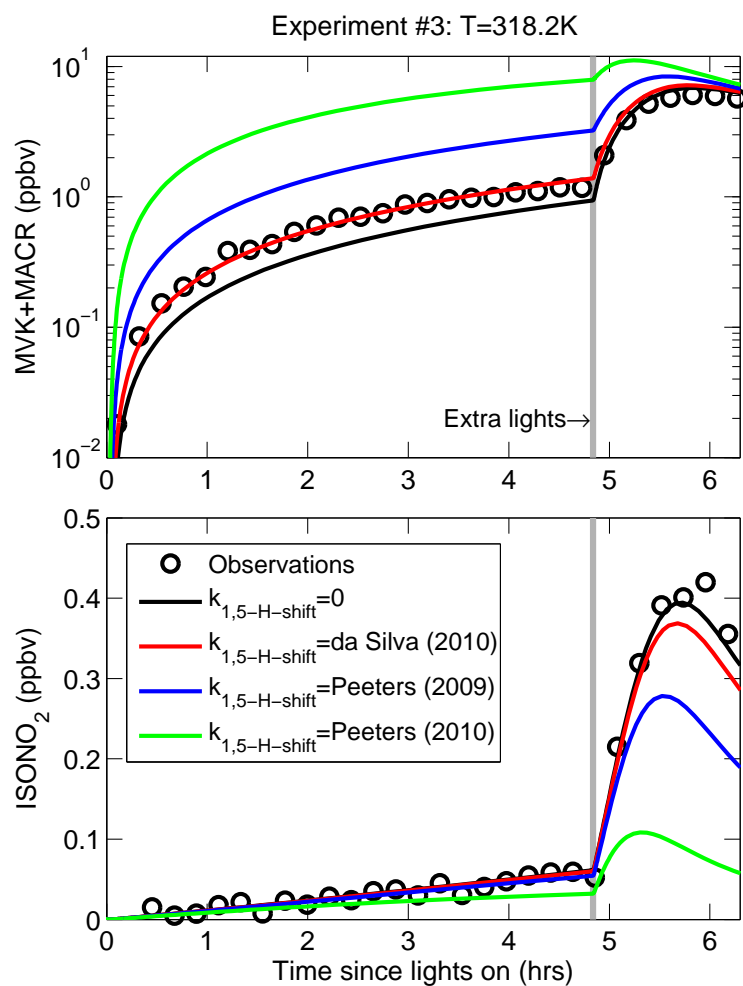
Figure 8.4 – CIMS observations (black circles) of MVK+MACR (top) and ISONO$_2$ (bottom) during isoprene oxidation experiment (#3 - main paper, T = 318 K). Kinetic model results are shown using a range of 1,5-H-shift isomerization rates.

Acknowledgements

Bibliography

Archibald, A. T., Cooke, M. C., Utembe, S. R., Shallcross, D. E., Derwent, R. G., and Jenkin, M. E.: Impacts of mechanistic changes on HO_x formation and recycling in the oxidation of isoprene, Atmos. Chem. Phys., 10, 8097–8118, doi:10.5194/acp-10-8097-2010, URL `http://www.atmos-chem-phys.net/10/8097/2010/`, 2010.

Atkinson, R., M, A. S., Carter, W. P. L., Winer, A. M., and Pitts, J. N.: Alkyl nitrate formation from the NO_x-air photooxidations of C_2-C_8 *n*-alkanes, J. Phys. Chem., 86, 4563–4569, 1982.

Atkinson, R., Baulch, D. L., Cox, R. A., Crowley, J. N., Hampson, R. F., Hynes, R. G., Jenkin, M. E., Rossi, M. J., and Troe, J.: Evaluated kinetic and photochemical data for atmospheric chemistry: Volume I - gas phase reactions of Ox, HOx, NOx and SOx species, Atmos. Chem. Phys., 4, 1461–1738, 2004.

Barker, J. R., Lohr, L. L., Shroll, R. M., and Reading, S.: Modeling the organic nitrate yields in the reaction of alkyl peroxy radicals with nitric oxide. 2. Reaction simulations, J. Phys. Chem. A, 107, 7434–7444, doi:10.1021/jp034638j, 2003.

Bey, I., Jacob, D. J., Yantosca, R. M., Logan, J. A., Field, B. D., Fiore, A. M., Li, Q. B., Liu, H. G. Y., Mickley, L. J., and Schultz, M. G.: Global modeling of tropospheric chemistry with assimilated meteorology: Model description and evaluation, J. Geophys. Res.-Atmos., 106, 23 073–23 095, 2001.

Blin-Simiand, N., Jorand, F., Keller, K., Fiderer, M., and Sahetchian, K.: Ketohydroperoxides and ignition delay in internal combustion engines, Combust. Flame, 112, 278–282, 1998.

Blin-Simiand, N., Jorand, F., Sahetchian, K., Brun, M., Kerhoas, L., Malosse, C., and Einhorn, J.: Hydroperoxides with zero, one, two or more carbonyl groups formed during the oxidation of n-dodecane, Combust. Flame, 126, 1524–1532, 2001.

Boyd, A. A., Flaud, P. M., Daugey, N., and Lesclaux, R.: Rate constants for RO_2 + HO_2 reactions measured under a large excess of HO_2, J. Phys. Chem. A, 107, 818–821, doi:10.1021/jp026581r, 2003a.

Butkovskaya, N., Pouvesle, N., Kukui, A., Mu, Y., and Le Bras, G.: Mechanism of the OH-initiated oxidation of hydroxyacetone over the temperature range 236-298 K, J. Phys. Chem. A, 110, 6833–6843, doi:10.1021/jp056345r, 2006a.

Butkovskaya, N. I., Pouvesle, N., Kukui, A., and Le Bra, G.: Mechanism of the OH-initiated oxidation of glycolaldehyde over the temperature range 233-296 K, J. Phys. Chem. A, 110, 13 492–13 499, doi:10.1021/jp064993k, 2006b.

Carter, W. P. L. and Atkinson, R.: Alkyl nitrate formation from the atmospheric photooxidation of alkanes - A revised estimation method, J. Atmos. Chem., 8, 165–173, 1989.

Cox, R. A., Derwent, R. G., Kearsey, S. V., Batt, L., and Patrick, K. G.: Photolysis of methyl nitrite - Kinetics of the reaction of the methoxy radical with O_2, J. Photochem., 13, 149–163, 1980.

Crounse, J. D., McKinney, K. A., Kwan, A. J., and Wennberg, P. O.: Measurement of gas-phase hydroperoxides by chemical ionization mass spectrometry, Anal. Chem., 78, 6726–6732, doi:10.1021/ac0604235, 2006.

da Silva, G., Graham, C., and Wang, Z.-F.: Unimolecular β-hydroxyperoxy radical decomposition with OH recycling in the photochemical oxidation of isoprene, Environ. Sci. Technol., 44, 250–256, doi:10.1021/es900924d, 2010.

Garden, A. L., Paulot, F., Crounse, J. D., Maxwell-Cameron, I. J., Wennberg, P. O., and Kjaergaard, H. G.: Calculation of conformationally weighted dipole moments useful in ion-molecule collision rate estimates, Chem. Phys. Lett., 474, 45–50, doi:10.1016/j.cplett.2009.04.038, 2009.

Giacopelli, P., Ford, K., Espada, C., and Shepson, P. B.: Comparison of the measured and simulated isoprene nitrate distributions above a forest canopy, J. Geophys. Res.-Atmos., 110, 10.1029/2004JD005 123, doi:10.1029/2004JD005123, 2005.

Guenther, A., Karl, T., Harley, P., Wiedinmyer, C., Palmer, P. I., and Geron, C.: Estimates of global terrestrial isoprene emissions using MEGAN (Model of Emissions of Gases and Aerosols from Nature), Atmos. Chem. Phys., 6, 3181–3210, 2006.

Hofzumahaus, A., Rohrer, F., Lu, K., Bohn, B., Brauers, T., Chang, C.-C., Fuchs, H., Holland, F., Kita, K., Kondo, Y., Li, X., Lou, S., Shao, M., Zeng, L., Wahner, A., and Zhang, Y.: Amplified trace gas removal in the troposphere, Science, 324, 1702–1704, doi:10.1126/science.1164566, 2009.

Jenkin, M. E., Boyd, A. A., and Lesclaux, R.: Peroxy radical kinetics resulting from the OH-Initiated oxidation of 1,3-butadiene, 2,3-dimethyl-1,3-butadiene and isoprene, J. Atmos. Chem., 29, 267–298, 1998.

Jorand, F., Heiss, A., Sahetchian, K., Kerhoas, L., and Einhorn, J.: Identification of an unexpected peroxide formed by successive isomerization reactions of the n-butoxy radical in oxygen, J. Chem. Soc. Faraday T., 92, 4167–4171, 1996.

Jorand, F., Kerhoas, L., Heiss, A., Einhorn, J., and Sahetchian, K.: Determination of the ultra violet absorption cross section of hexyl-ketohydroperoxides in solution in acetonitrile, J. Photoch. Photobio. A, 134, 119–125, 2000.

Karl, T., Guenther, A., Turnipseed, A., Tyndall, G., Artaxo, P., and Martin, S.: Rapid formation of isoprene photo-oxidation products observed in Amazonia, Atmos. Chem. Phys., 9, 7753–7767, 2009.

Lelieveld, J., Butler, T. M., Crowley, J. N., Dillon, T. J., Fischer, H., Ganzeveld, L., Harder, H., Lawrence, M. G., Martinez, M., Taraborrelli, D., and Williams, J.: Atmospheric oxidation capacity sustained by a tropical forest, Nature, 452, 737–740, doi:10.1038/nature06870, 2008.

Nguyen, T. L., Vereecken, L., and Peeters, J.: HO_x Regeneration in the oxidation of isoprene III: Theoretical study of the key isomerisation of the Z-δ-hydroxy-peroxy isoprene radicals, Chem. Eur. J. of Chem. Phys., 11, 3996–4001, URL `http://dx.doi.org/10.1002/cphc.201000480`, 2010.

Park, J., Jongsma, C. G., Zhang, R. Y., and North, S. W.: OH/OD initiated oxidation of isoprene in the presence of O_2 and NO, J. Phys. Chem. A, 108, 10 688–10 697, doi:10.1021/jp040421t, 2004.

Paulot, F., Crounse, J. D., Kjaergaard, H. G., Kroll, J. H., Seinfeld, J. H., and Wennberg, P. O.: Isoprene photooxidation: new insights into the production of acids and organic nitrates, Atmos. Chem. Phys., 9, 1479–1501, 2009a.

Paulot, F., Crounse, J. D., Kjaergaard, H. G., Kuerten, A., St Clair, J. M., Seinfeld, J. H., and Wennberg, P. O.: Unexpected epoxide formation in the gas-phase photooxidation of isoprene, Science, 325, 730–733, doi:10.1126/science.1172910, 2009b.

Paulot, F., Wunch, D., Crounse, J. D., Toon, G. C., Millet, D. B., DeCarlo, P. F., Vigouroux, C., Deutscher, N. M., González Abad, G., Notholt, J., Warneke, T., Hannigan, J. W., Warneke, C., de Gouw, J. A., Dunlea, E. J., De Mazière, M., Griffith, D. W. T., Bernath, P., Jimenez, J. L., and Wennberg, P. O.: Importance of secondary sources in the atmospheric budgets of formic and acetic acids, Atmos. Chem. Phys., 11, 1989–2013, doi:10.5194/acp-11-1989-2011, URL `http://www.atmos-chem-phys.net/11/1989/2011/`, 2011.

Peeters, J. and Muller, J.-F.: HO$_x$ radical regeneration in isoprene oxidation via peroxy radical isomerisations. II: experimental evidence and global impact, Phys. Chem. Chem. Phys., 12, 14 227–14 235, doi:10.1039/c0cp00811g, 2010.

Peeters, J., Nguyen, T. L., and Vereecken, L.: HO$_x$ radical regeneration in the oxidation of isoprene, Phys. Chem. Chem. Phys., 11, 5935–5939, doi:10.1039/b908511d, 2009.

Perrin, O., Heiss, A., Doumenc, F., and Sahetchian, K.: Homogeneous and heterogeneous reactions of the n$-$C$_5$H$_{11}$O, n$-$C$_5$H$_{10}$OH and OOC$_5$H$_{10}$OH radicals in oxygen. Analytical steady state solution by use of the Laplace transform, J. Chem. Soc. Faraday T., 94, 2323–2335, 1998a.

Perrin, O., Heiss, A., Sahetchian, K., Kerhoas, L., and Einhorn, J.: Determination of the isomerization rate constant HOCH$_2$CH$_2$CH$_2$CH(OO$^.$)CH$_3$ → HOC$^.$HCH$_2$CH$_2$CH(OOH)CH$_3$. Importance of intramolecular hydroperoxy isomerization in tropospheric chemistry, Int. J. Chem. Kinet., 30, 875–887, 1998b.

Ren, X., Olson, J. R., Crawford, J. H., Brune, W. H., Mao, J., Long, R. B., Chen, Z., Chen, G., Avery, M. A., Sachse, G. W., Barrick, J. D., Diskin, G. S., Huey, L. G., Fried, A., Cohen, R. C., Heikes, B., Wennberg, P. O., Singh, H. B., Blake, D. R., and Shetter, R. E.: HO$_x$ chemistry during INTEX-A 2004: Observation, model calculation, and comparison with previous studies, J. Geophys. Res.-Atmos., 113, Doi: 10.1029/2007JD009 166, doi:10.1029/2007JD009166, 2008.

Saunders, S. M., Jenkin, M. E., Derwent, R. G., and Pilling, M. J.: Protocol for the development of the Master Chemical Mechanism, MCM v3 (Part A): tropospheric degradation of non-aromatic volatile organic compounds, Atmos. Chem. Phys., 3, 161–180, 2003.

Sharpe, S. W., Johnson, T. J., Sams, R. L., Chu, P. M., Rhoderick, G. C., and Johnson, P. A.: Gas-phase databases for quantitative infrared spectroscopy, Appl. Spectrosc., 58, 1452–1461, 2004.

St Clair, J. M., McCabe, D. C., Crounse, J. D., Steiner, U., and Wennberg, P. O.: Chemical ionization tandem mass spectrometer for the in situ measurement of methyl hydrogen peroxide, Rev. Sci. Instrum., 81, 094 102, doi:10.1063/1.3480552, 2010.

Stavrakou, T., Peeters, J., and Muller, J. F.: Improved global modelling of HO$_x$ recycling in isoprene oxidation: evaluation against the GABRIEL and INTEX-A aircraft campaign measurements, Atmos. Chem. Phys., 10, 9863–9878, doi:10.5194/acp-10-9863-2010, 2010.

Su, T. and Chesnavich, W. J.: Parameterization of the ion-molecule collision rate-constant by trajectory calculations, J. Chem. Phys., 76, 5183–5185, 1982.

Tan, D., Faloona, I., Simpas, J. B., Brune, W., Shepson, P. B., Couch, T. L., Sumner, A. L., Carroll, M. A., Thornberry, T., Apel, E., Riemer, D., and Stockwell, W.: HO_x budgets in a deciduous forest: Results from the PROPHET summer 1998 campaign, J. Geophys. Res.-Atmos., 106, 24 407–24 427, 2001.

Taylor, W. D., Allston, T. D., Moscato, M. J., Fazekas, G. B., Kozlowski, R., and Takacs, G. A.: Atmospheric photo-dissociation lifetimes for nitromethane, methyl nitrite, and methyl nitrate, Int. J. Chem. Kinet., 12, 231–240, 1980.

Thornton, J. A., Wooldridge, P. J., Cohen, R. C., Martinez, M., Harder, H., Brune, W. H., Williams, E. J., Roberts, J. M., Fehsenfeld, F. C., Hall, S. R., Shetter, R. E., Wert, B. P., and Fried, A.: Ozone production rates as a function of NO_x abundances and HO_x production rates in the Nashville urban plume, J. Geophys. Res.-Atmos., 107, Doi: 10.1029/2001JD000 932, doi:10.1029/2001JD000932, 2002.

York, D., Evensen, N. M., Martinez, M. L., and Delgado, J. D.: Unified equations for the slope, intercept, and standard errors of the best straight line, Am. J. Phys., 72, 367–375, doi:10.1119/1.1632486, 2004.

Chapter 9

Conclusions and outlook

This thesis describes methods for the fast, sensitive, specific, and direct detection of functionalized organic and inorganic reactive trace gases in the atmosphere. This technology is demonstrated from aircraft and ground platforms for making robust observations that have been used successfully for partitioning atmospheric pollution into specific source categories. When applied to chamber studies, the CIMS instrumentation has proven to be a powerful tool for the detection of the gas-phase oxidation products of volatile organic compounds. The specific detection and quantification of intermediate oxidation products provide valuable information for elucidating oxidation mechanisms, and organic aerosol formation pathways.

It is likely that continued use of CF_3O^--CIMS will provide fruitful results from application to both *in situ* atmospheric studies and environmental chamber studies. Important uncertainties remain in the gas-phase oxidation of– and organic aerosol formation from– many volatile organic compounds. A mechanistic understanding of these processes will enable their proper simulation in atmospheric models across the wide range of conditions that are present in the atmosphere. In conjunction with a number of other emerging advanced analytical techniques, CF_3O^--CIMS, will help to reduce these uncertainties and increase our understanding of atmospheric composition and chemistry. Several potential ideas for future research and instrumental development are mentioned below.

The high sensitivity of CF_3O^--CIMS lends itself to laboratory experiments conducted at chemical concentrations that approach those encountered in the Earth's atmosphere. The importance of conducting experiments at or near atmospheric conditions has been recognized for sometime, however, instrumental detection limits often prevent experiments from being conducted under these conditions. It has recently been postulated that certain RO_2 radicals, particularly those formed from the reaction of OH and O_2 with isoprene, can undergo H-shift isomerization reactions that

are calculated to occur at rates fast enough to be important under pristine atmospheric conditions (low HO_2 and NO mixing ratios). To measure such rates in the laboratory, experiments must be designed that have low HO_2 and NO mixing ratios, and, to minimize RO_2 self-reaction, low RO_2 mixing ratios. Achieving such conditions requires slow chemistry, and thus sensitive instrumentation. Chapter 8 discusses initial experiments probing this chemistry using the CIMS methods described in this thesis.

CF_3O^--MSMS-CIMS is a promising analytical method that almost certainly has many more applications than those described in this thesis. Currently, only a small range of collision energies and CID-pressures for only a few parent ions have been investigated. It is possible that more structural information pertaining to the parent analyte can be gleaned by utilizing higher collision energies. PTR-MSMS has not been investigated with these instruments; however, initial results from other groups show this technique can likewise provide useful structural information (e.g., the separate quantification of a mixture of the isobaric methylvinylketone and methacrolein compounds).

A current limitation of the CIMS instrumentation is that product ions are detected serially (one at a time) by changing the electric fields applied to the quadrupole mass filters. After changing the electric fields, a period of time is required to permit the new electric fields to stabilize. During this time, no data can be collected. This dead-time limits the rate at which masses can be switched with the quadrupole mass filter. An alternative approach that would circumvent this issue is the use of a time-of-flight (TOF) mass analyzer in place of the quadrupole mass filter. In a TOF mass analyzer, a packet of ions is accelerated into a field free drift tube before reaching the detector. Ions with different masses are accelerated to different velocities and thus reach the detector at different times, allowing for mass separation. State-of-the-art TOF analyzers allow for fast duty cycles (10,000's of ion packets per second), and out-perform quadrupole mass filters when many masses are to be monitored. An important benefit provided by a TOF mass analyzer is that quasi-continuous data is collected over the full mass range. A CF_3O^--TOF-CIMS would be especially useful for observations made from aircraft platforms, where the concentrations of ambient species can change rapidly.

It is feasible that CIMS instruments, similar to those described here, can be fabricated thath will fit onto unmanned aircraft (such as NASA's Global Hawk aircraft). Unmanned aircraft are just beginning to be utilized extensively for *in situ* atmospheric observations, and show great promise for future research opportunities. Benefits of such aircraft include autonomous operation, long duration (over 30 h flight duration) and extensive horizontal (20,000 km) and vertical (0–18.3 km) range. The payload of these aircraft is somewhat reduced as compared with the larger aircraft traditionally

used for atmospheric research, but is still capable of carrying the instrumentation required for *in situ* atmospheric studies. However, given the reduced payload, instruments like the CIMS, which can measure a number of interesting species from a single package, will likely be a desirable addition for studies of atmospheric chemistry from these unmanned platforms.

In conclusion, the outlook for this technology seems very bright – the possibilities for new scientific insights that can be gained through its application are numerous, especially considering the potential for instrumental improvements.